Fabrication Routes for Thin-Film Solid-State Batteries



Stephen Turrell

St Catherine's College

University of Oxford

A thesis submitted for the degree of

Doctor of Philosophy

Michaelmas 2022

Abstract

Thin-film solid-state batteries have been studied since the 1950s, but it was the demonstration of remarkable cycling stability in an all-thin-film Li/LiPON (lithium phosphorus oxynitride)/LCO ($LiCoO_2$) cell in the mid-1990s that captured the attention of the solid-state battery research community. Although these cells were commercialized on a small scale, their utility is limited by their low areal capacities. Nevertheless, there is a growing realization that thin-film processing techniques such as RF (radio frequency) magnetron sputtering offer various advantages over the traditional powder processing routes commonly used to fabricate solid-state cell components.

The first investigation reported here looked at a strategy to improve the performance of the "traditional" all-thin-film cell by optimizing the processing of the LCO cathode. Most previous studies on thin-film LCO cathodes have reported similar processing conditions, and these are not optimal for large-scale manufacturing. In this work, the process pressure used for RF magnetron sputtering was reduced while the power density was increased relative to typical conditions from the literature. Several other changes were made, including the omission of an oxygen gas flow during deposition, until ~3 μm thick films well-crystallized in the targeted HT-LCO (high temperature LCO) structure were achieved at a deposition rate 3-4 times higher than obtained using the reference conditions. Characterization by X-ray diffraction (XRD) revealed strong parallel alignment of the (104), (101) and (110) planes with the film surface, as desired for efficient lithium transfer to the electrolyte. Notably, a maximum areal discharge capacity of 172 μAh cm^{-2} was measured during galvanostatic cycling between 3.0 and 4.3 V at a current density of 18 μA cm^{-2}, which is one of the highest values reported. This can be attributed to the greater film thicknesses reported here compared to those of most previous studies (generally below 1 μm) and the use of processing conditions optimized both for manufacturability and electrochemical performance.

The second investigation looked at the synthesis of Li_3OCl, a member of the recently discovered class of lithium-rich antiperovskite electrolyte materials. This compound has attracted interest because of its predicted stability in contact with lithium metal anodes, raising the prospect of future application in all-solid-state lithium metal batteries. However, its thermodynamic instability at room temperature and extreme hygroscopicity appear to preclude synthesis by traditional solid state and melt processing routes since the more stable Li_2OHCl compound is likely to form instead. This work attempted to synthesize Li_3OCl using RF magnetron sputtering, taking advantage of the moisture-free environment and high cooling rates associated with this technique. Sputtering was performed from an equimolar powdered mixture of the precursor compounds Li_2O and LiCl. After optimizing the sputtering conditions for target stability, XRD, Fourier transform infrared spectroscopy and electrochemical impedance spectroscopy were used to show that a small volume fraction of a phase with the properties expected for Li_3OCl was present in the as-deposited films. The results were compared to those of films deposited from Li_2OHCl powder to prove that Li_2OHCl had not been produced inadvertently. Both sets of films exhibited low ionic conductivities (on the order of 10^{-8} S cm^{-1}) owing to their low antiperovskite phase purities. Nevertheless, an increased understanding of the processing-structure-properties relationships pertaining to these compounds allowed several promising directions for future research to be proposed.

Acknowledgements

I am grateful to my supervisors, Professor Chris Grovenor and Professor Susie Speller for their guidance throughout my time as a DPhil student and for providing the opportunity to work on this less researched yet highly important topic within the broader solid-state battery field.

I would like to acknowledge those with whom I have collaborated in performing some of the experimental work reported here. First, I would like to thank Dr Hyeon Jeong Lee for imparting her knowledge of lithium-rich antiperovskite compounds and for helpful discussions on the designs of the experiments reported in Chapter 4. Dr Lee also contributed to the experimental work reported in this chapter by synthesizing Li_2OHCl powder (and characterizing it by FT-IR and XRD), producing Li_2O + LiCl precursor powder mixtures, annealing the sputter-deposited films and performing XRD data collection. I would also like to acknowledge the help of Marco Siniscalchi and Dr Sudarshan Narayanan, who collected the PFIB and XPS data, respectively, for this chapter. Regarding the work on thin-film LCO cathodes in Chapter 3, I would like to acknowledge the help of Dr Stefanie Zekoll and Dr Tayebeh Mousavi in developing experimental protocols, processing LCO films and performing characterization by surface profilometry, XRD and microscopy in the early stages of the investigation (up to Section 3.3.1.5). I am also grateful for the contributions of Dr Junliang Liu, who collected the PFIB data for this chapter, and Dr Robert House, who provided helpful advice on protocols for galvanostatic cycling.

I am grateful to my assessors, Professor Mauro Pasta and Professor Jonathan Yates, for their helpful feedback on my early results and progress.

The work reported in this thesis was supported by funding from an EPSRC studentship (project reference 2114670 related to EP/R513295/1) and the University's COVID-19 Scholarship Extensions Fund. I have also benefited from conference travel funding provided

by St Catherine's College and the Armourers & Brasiers' Company Conference Travel Grant programme.

I wish to express my thanks to the members of the "thin-film batteries group" – Marco Siniscalchi, Dr Jin Su and Dr Clara Barker – for their helpful advice, practical assistance and interesting conversation.

I would like to thank my family for all their support.

Finally I would like to thank my partner, Kaiyi, for her advice and support, and for keeping me motivated when writing this thesis.

Publications and Conference Presentations

1. Pasta, M., …, Turrell, S. J., *et al.* 2020 roadmap on solid-state batteries. *J. Phys. Energy* **2**, 032008 (2020).
2. Turrell, S. J., Zekoll, S., Liu, J., Grovenor, C. R. M. & Speller, S. C. Optimization of a potential manufacturing process for thin-film $LiCoO_2$ cathodes. *Thin Solid Films* **735**, 138888 (2021).
3. "Development of a Fabrication Process for Antiperovskite Li_3OCl Thin Films", EN06.16.02, MRS Spring Meeting, Honolulu, Hawaii, 13th May 2022 [In-person oral presentation].
4. Turrell, S. J., Lee, H. J., Siniscalchi, M., Narayanan, S., Pasta, M., Speller, S. C. & Grovenor, C. R. M. Fabrication of thin solid electrolytes containing a small volume of an Li_3OCl-type antiperovskite phase by RF magnetron sputtering. *Materials Advances* **3**, 8995–9008 (2022).

Abbreviations

AC	Alternating current
AP	Antiperovskite
ASSB	All-solid-state battery
ATR	Attenuated total reflectance
CIF	Crystallographic information file
CPE	Constant phase element
CV	Cyclic voltammetry
DC	Direct current
EDX	Energy dispersive X-ray spectroscopy
EIS	Electrochemical impedance spectroscopy
FIB	Focused ion beam
FT-IR	Fourier transform infrared spectroscopy
HT-LCO	High-temperature lithium cobalt oxide
ICSD	Inorganic crystal structure database
ICP-OES	Inductively coupled plasma optical emission spectroscopy
IR	Infrared
LCO	Lithium cobalt oxide
LIB	Lithium-ion battery
LiPON	Lithium phosphorus oxynitride
LiRAP	Lithium-rich antiperovskite
LMNO	Lithium manganese nickel oxide
LT-LCO	Low-temperature lithium cobalt oxide
NMC	Lithium nickel manganese cobalt oxide
OCV	Open circuit voltage
PFIB	Plasma focused ion beam

PLD	Pulsed laser deposition
PVD	Physical vapour deposition
RF	Radio frequency
RT	Room temperature
SE	Solid electrolyte
SEI	Solid electrolyte interphase
SEM	Scanning electron microscopy/microscope
UHV	Ultra high vacuum
XPS	X-ray photoelectron spectroscopy
XRD	X-ray diffraction

Table of Contents

Abstract iii

Acknowledgements v

Publications and Conference Presentations vii

Abbreviations viii

1 Introduction 1

1.1 Overview 1

1.2 Lithium-Ion Batteries 1

1.2.1 Background 1

1.2.2 Structure and Operation 2

1.2.3 Performance 4

1.2.4 Ongoing Challenges 8

1.3 All-Solid-State Batteries 9

1.3.1 Background 9

1.3.2 Solid Electrolytes 12

1.3.3 Challenges Hindering the Commercialization of Solid-State Cells 15

1.4 Thin-Film Solid-State Batteries 20

1.4.1 Background 20

1.4.2 LiPON and the Li/LiPON/LCO All-Thin-Film Cell 21

1.4.3 Benefits over Powder Processing 24

1.4.4 Current Research Directions 26

1.5 Summary and Aims of This Work 34

2 Experimental Techniques 36

2.1 Introduction 36
2.2 Fabrication Techniques 36
2.2.1 RF Magnetron Sputter Deposition 36
2.2.2 Post-Deposition Annealing 40
2.2.3 Fabrication of Airtight Cells for Galvanostatic Cycling and Impedance Measurements 42
2.3 Structural Characterization 44
2.3.1 X-Ray Diffraction 44
2.3.2 Scanning Electron Microscopy and Focused Ion Beam Milling 46
2.4 Chemical Characterization 50
2.4.1 Energy Dispersive X-Ray Spectroscopy 50
2.4.2 X-Ray Photoelectron Spectroscopy 53
2.4.3 Fourier Transform Infrared Spectroscopy 55
2.4.4 Inductively Coupled Plasma Optical Emission Spectroscopy 58
2.5 Electrochemical Characterization 59
2.5.1 Electrochemical Impedance Spectroscopy 59
2.5.2 Cyclic Voltammetry 65
2.5.3 Galvanostatic Cycling 65
3 Improving the Processing and Performance of $LiCoO_2$ (LCO) Thin Film Cathodes 67
3.1 Introduction 67
3.2 Experimental Methods 71
3.2.1 Sputtering Target and Substrate Preparation 71
3.2.2 Thin Film Deposition and Post-Deposition Annealing 72

3.2.3 Structural and Chemical Characterization 73
3.2.4 Electrochemical Characterization 74
3.3 Results and Discussion 74
3.3.1 Structural Characterization 74
3.3.2 Chemical Composition 96
3.3.3 Electrochemical Characterization 98
3.4 Conclusions 116
4 Fabrication of Lithium-Rich Antiperovskite Chloride Electrolytes by RF Magnetron Sputtering 120
4.1 Introduction and Aims of This Work 120
4.2 Experimental Methods 124
4.2.1 Preparation of Substrates and Sputtering Targets 124
4.2.2 Thin Film Deposition and Post-Deposition Annealing 126
4.2.3 Structural Characterization 128
4.2.4 Chemical Characterization 128
4.2.5 Ionic Conductivity Measurements 129
4.3 Results and Discussion 130
4.3.1 Stabilization of the Li_2O + LiCl Sputtering Target 130
4.3.2 Optimization of Films Deposited from Li_2O + LiCl Sputtering Targets 139
4.3.3 Deposition of Films from an Li_2OHCl Target 155
4.3.4 Characterization of Ionic Conductivity 160
4.3.5 Additional Structural and Chemical Characterization 168
4.4 Conclusions 171

5 Conclusions and Further Work 175

References 179

Appendices 203

Appendix A: Variability of cycling performance between cells 203

Appendix B: Equivalent Circuit Model Properties 204

Appendix C: Electrical Contact Area Measurements 205

1 Introduction

1.1 Overview

This chapter is intended to provide a technical background to the research reported in subsequent chapters. Starting with a broad overview of rechargeable, or secondary, lithium-ion batteries, fundamental aspects of their design, operation and performance are discussed. The focus then shifts to a potential successor technology: all-solid-state batteries. An historical overview of the development of these batteries is provided to explain their perceived advantages over lithium-ion batteries with liquid electrolytes. The challenges to outperforming the current commercial lithium-ion batteries are then presented, along with the observation that these can be placed into the broad categories of 'chemical' and 'processing'. The remainder of the chapter focuses on a sub-category of solid-state batteries: thin-film batteries. It is proposed that the use of physical vapour deposition techniques such as RF magnetron sputtering could be used to overcome most, if not all, of the processing challenges associated with all-solid-state cells. However, all-thin-film cells are currently suitable only for very low power applications. Ongoing efforts to improve the performance of these cells are discussed before the specific aims of this work are presented.

1.2 Lithium-Ion Batteries

1.2.1 Background

Since their commercialization by Sony in 1991, rechargeable, or 'secondary', lithium-ion batteries have become the ubiquitous power source for portable electronic devices such as mobile phones, laptops, and tablet computers[1]. Only lithium-ion technology can provide the charge capacities and power densities required by these applications, which is largely attributable to the fact that lithium is the third lightest element and is highly electropositive[2].

1.2.2 Structure and Operation

A lithium-ion battery consists of an array of cells connected in a configuration that achieves the optimum voltage and current for the intended application. The structure of the archetypal rechargeable lithium-ion cell is shown in Figure 1.1[1]. It features a graphite anode (negative electrode) with a copper current collector, a porous separator impregnated with an organic liquid electrolyte and an $LiCoO_2$ (LCO) cathode (positive electrode) with an aluminium current collector. A similar structure is used in most of the lithium-ion cells manufactured today, although various transition metal oxide cathode materials are now used (Table 1.1) and silicon is added to the graphite-based anode to increase the charge storage capacity[3,4]. In the discharged state, the oxide cathode acts as a "host" for lithium ions (Li^+). On charging, transition metal atoms in the cathode are oxidized. The electrons move to the anode though the external circuit, causing reduction, while a flow of Li^+ in the same direction through the electrolyte maintains charge neutrality. The Li^+ are extracted, or 'deintercalated', from the layers of the cathode host structure and inserted, or 'intercalated', between the layers of carbon atoms in the graphite anode. The electrolyte-separator combination must be an ionic conductor but an electronic insulator to avoid an internal short circuit. When the charged cell is connected to a load it begins to discharge and the reverse of the charging process occurs. The half reactions that occur in the cathode and anode of the Li / organic electrolyte / LCO cell, and the overall redox reaction, are represented by equations 1.1, 1.2, and 1.3, respectively[5].

$$Li_{1-x}CoO_2 + xLi^+ + xe^- \rightleftharpoons LiCoO_2 \qquad \textbf{Equation 1.1}$$

$$xC_6 + xLi^+ + xe^- \rightleftharpoons xLiC_6 \qquad \textbf{Equation 1.2}$$

$$Li_{1-x}CoO_2 + xLiC_6 \rightleftharpoons LiCoO_2 + xC_6 \qquad \textbf{Equation 1.3}$$

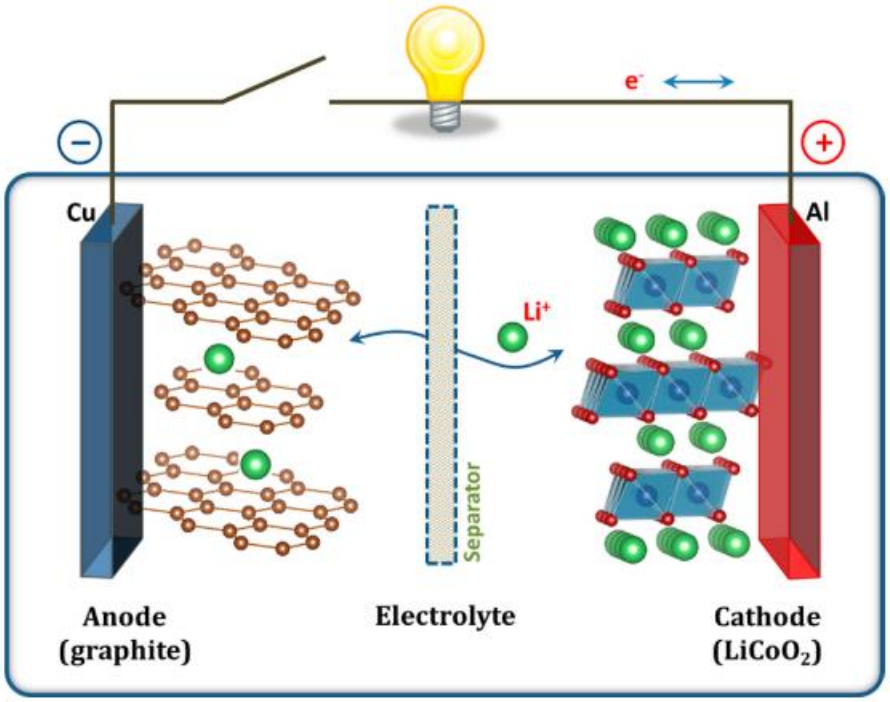


Figure 1.1 Structure of the archetypal lithium-ion cell. This basic structure is common to most lithium-ion cells manufactured today, although a variety of cathode materials are now in use. The brown, red and blue species are carbon atoms, oxygen ions and cobalt ions, respectively. Reproduced with permission from *J. Am. Chem. Soc.* 2013, 135, 4, 1167–1176[1]. Copyright 2013 American Chemical Society.

Table 1.1 Properties of cathode materials found in commercial lithium-ion cells.

Cathode Material	Average discharge potential *vs* Li^+/Li (V)	Specific Capacity (mAh g^{-1})	Year first reported
$LiCoO_2$ (LCO)	3.8[6]	145[6]	1980[7]
$LiMn_2O_4$ (LMO)	4.0[3]	120[3]	1983[8]
$LiFePO_4$ (LFP)	3.4[6]	160[9]	1997[10]
$LiNi_{0.8}Co_{0.15}Al_{0.05}O_2$ (NCA)	3.7[6]	200[11]	2000[12]
$LiNi_{1/3}Mn_{1/3}Co_{1/3}O_2$ (NMC-111)	3.7[6]	170[6]	2001[13]
$LiNi_{0.8}Mn_{0.1}Co_{0.1}O_2$ (NMC-811)	3.7[14]	>200[14]	2006[15]

1.2.3 Performance

1.2.3.1 Figures of Merit

A key property of an electrochemical cell is its open circuit voltage (V_{OC} or OCV). In lithium-ion cells under open circuit conditions, this is given by the difference in chemical potential of the lithium in the anode (μ_{Li}^{anode}) and cathode ($\mu_{Li}^{cathode}$) materials divided by the elementary charge, e (equation 1.4). The cell voltage will change with the state of charge according to the phases present in the cathode and anode materials and their dependence on lithium concentration. When current is drawn from the cell, a proportion of the voltage is dropped across the internal impedance, polarizing the cell voltage by η[5]. During discharging the cell voltage, V_{dis}, is reduced by η; during charging the applied voltage required, V_{ch}, is increased by η, as shown by equations 1.5 and 1.6.[5]

$$V_{OC} = -\frac{\mu_{Li}^{cathode} - \mu_{Li}^{anode}}{e} \qquad \textbf{Equation 1.4}$$

$$V_{dis} = V_{OC} - \eta \qquad \textbf{Equation 1.5}$$

$$V_{ch} = V_{OC} + \eta \qquad \textbf{Equation 1.6}$$

Another key figure of merit is charge storage capacity, since this determines the length of time that the cell can provide a given current before recharging is required. The theoretical specific capacity, Q_{th}, of a cathode or anode material is calculated using equation 1.7[5], where x is the number of moles of Li^+ inserted or extracted, *F* is the Faraday constant and *M* is the molar mass of the material.

$$Q_{th}\ (mAh\ g^{-1}) = \frac{xF}{3.6M} \qquad \textbf{Equation 1.7}$$

In the case of $LiCoO_2$, it might be assumed that x = 1 for a complete discharge. This would give a specific capacity of 274 mAh g^{-1}. However, the maximum practical specific capacity of $LiCoO_2$ is about 137 mAh g^{-1} because only ~0.5 moles of Li^+ can be extracted before the

onset of structural degradation[5]. In commercial lithium-ion cells, the charge capacity is limited by the cathode since the maximum specific capacity of the graphite (C_6) anode (372 mAh g^{-1}) is significantly higher than any of the values for the commercial cathode materials (Table 1.1).

Four further figures of merit can be calculated from those described above: the specific energy and energy density and specific power and power density of individual electrode materials and entire cells (by convention, 'specific' refers to a mass-normalized quantity and 'density' refers to a volume-normalized quantity). By measuring the cell voltage during discharge from full charge as a function of the charge released, $V(q)$, until the available capacity, Q, has been released, the available energy stored per unit mass or volume can be calculated using equation 1.8[5].

$$\text{Available Energy} = \int_0^Q V(q)dq \qquad \textbf{Equation 1.8}$$

This value can then be normalized by mass or volume to obtain specific energy or energy density, respectively. Further dividing by the discharge time gives values for the specific power or power density. The rate of charging or discharging can be described by the 'C-rate', which is the reciprocal of the time taken in hours for a cell to charge or discharge completely: a rate of 1 C means that a full charge/discharge takes 1 hour.

Aside from the maximum electrical output of a cell, the changes in performance with cycling conditions and over time must be evaluated. Cycle life is conventionally defined as the number of charge-discharge cycles a cell can undergo before its capacity falls to 80% of the initial value[1], and the rate at which this occurs depends on the rate of structural and chemical changes within the cell. Furthermore, electrochemical cells display a lower capacity during discharge than during charge for any given cycle over most of the cycle life. This is generally due to the occurrence of side reactions between the electrolyte and one or both of the electrodes[16]. The discrepancy between the discharge and charge capacities is captured at

any point during cycling by the Coulombic efficiency (equation 1.9), which is the percentage of capacity measured on charging, Q_{charge}, that is released in the subsequent discharge, $Q_{discharge}$.

$$Coulombic\ efficiency\ (\%) = \frac{Q_{discharge}}{Q_{charge}} \times 100 \qquad \textbf{Equation 1.9}$$

1.2.3.2 Factors Which Affect Performance

Several features of the design of a practical lithium-ion cell limit the performance, both at the start of cycling and in later stages. Properties normalized by mass or volume, for example specific capacity or power density, must take account of the masses or volumes of non-active components in the electrodes or cell, such as binders and conductive additives as well as the electrolyte, separator and current collectors. Thus, the actual performance is generally somewhat lower than that achievable in theory, even at the start of cycling. Furthermore, all cells display a deterioration in performance with repeated cycling, which is a consequence of structural and chemical changes.

The irreversible loss of capacity generally seen on the first charge is a result of the lithiated graphite anode reducing the electrolyte and forming a layer of reaction products known as a solid-electrolyte interphase (SEI)[1]. The Li^+ consumed in this reaction is strongly bonded within the SEI layer so it can no longer take part in the main cell redox reaction. The propensity for oxidation and reduction side reactions at the electrode-electrolyte interfaces is determined by the 'electrochemical window' of the electrolyte, defined as the difference between the energies of the lowest unoccupied molecular orbital (LUMO) and the highest occupied molecular orbital (HOMO) of the electrolyte, E_g, as illustrated in Figure 1.2[1]. For solid electrolytes, which will be introduced in Section 1.3, the relevant energy gap is that between the conduction and valence bands of the material[1].

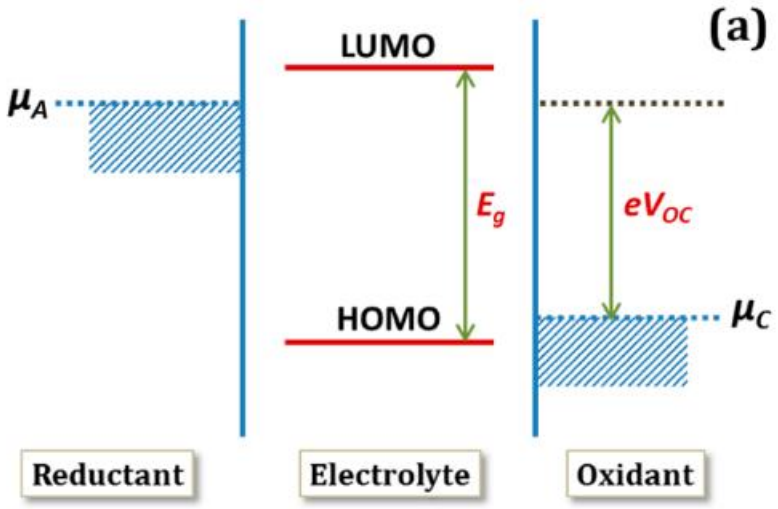


Figure 1.2 Energy level diagram of an electrochemical cell with a liquid electrolyte. E_g is the 'electrochemical window'; μ_A and μ_C are the electrochemical potentials of the anode and cathode materials, respectively. LUMO stands for Lowest Unoccupied Molecular Orbital; HOMO stands for Highest Occupied Molecular Orbital. The blue shaded regions represent the occupied electron states below μ_A and μ_C. Adapted with permission from *J. Am. Chem. Soc.* **135**, 1167–1176 (2013)[1]. Copyright 2013 American Chemical Society.

For a long cycle life, electrode and electrolyte material combinations should be chosen such that the electrochemical potential of the anode, μ_A, lies below the LUMO and the electrochemical potential of the cathode, μ_C, lies above the HOMO. If this condition is not satisfied, reduction and oxidation of the electrolyte will occur at the anode and cathode interfaces, respectively. These reactions may form stable SEI layers which passivate the electrodes and block further reaction, as in most commercial lithium-ion cells[1]. However, if the layer is non-passivating due to a high electronic conductivity or is repeatedly disrupted during cycling (for example by electrode volume changes), then a severe degradation of cell performance can occur, resulting in a poor cycle life[17]. The formation of these layers of reaction product tends to increase cell impedance since they generally have lower ionic conductivities than the electrolyte, which can lead to increasing polarization of the cell potential over the course of cycling. Another cause of capacity loss and increased

impedance during cycling is structural changes within the electrode materials; these can reduce the efficiency with which lithium is transferred to and from the electrodes.

1.2.4 Ongoing Challenges

Since the large-scale commercialization of lithium-ion batteries 30 years ago, the specific energies and energy densities of the commercial batteries have increased as a result of improved cell materials and designs[1,5,18]. However, most commercial cells still use graphite (often with added silicon)[3,4] as the anode material. Graphite has an average discharge potential of about 0.2 V versus lithium metal and a theoretical specific capacity of 372 mAh g^{-1}. Using lithium metal as the anode increases the cell voltage by about 0.2 V and the specific capacity of the anode tenfold to 3862 mAh g^{-1}. However, there are significant challenges associated with the adoption of lithium metal anodes which have so far limited their use to the research laboratory.

As for graphite, an SEI layer forms at the interface between a lithium metal anode and organic liquid electrolyte on the first charge. However, during cycling the lithium metal anode undergoes significant volume changes[17] which continually disrupt the SEI layer and expose lithium metal, leading to further reaction and growth of the layer. This consumes lithium, resulting in a poor Coulombic efficiency and an increasing internal impedance. Furthermore, uneven plating of lithium across the anode due to the heterogeneous SEI layer can create protrusions of lithium metal[19]. The electric field, and hence ionic current, concentrate in these regions, resulting in preferential plating and the growth of dendritic structures into the electrolyte, as illustrated in Figure 1.3[19]. There are two main consequences of this. First, dendrite pieces can break away and become electronically isolated from the anode. These pieces are referred to as “dead lithium” because they no longer contribute to the cell capacity[19]. Second, catastrophic failure occurs when dendrites grow across the electrolyte to the cathode and short the cell internally. Aside from causing cell failure, the resulting discharge current can generate enough heat to ignite the organic liquid electrolyte[4].

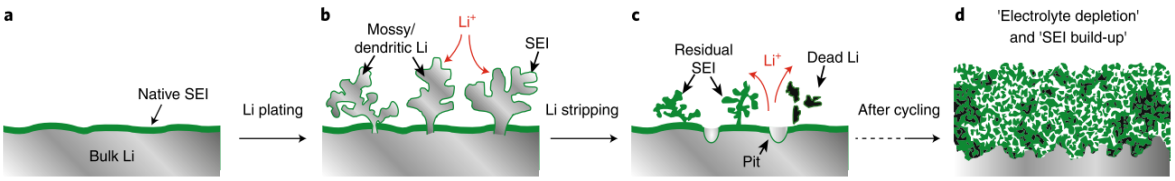


Figure 1.3 Illustration of the degradation processes that occur at the anode-electrolyte interface in Li metal batteries: a) a planar SEI layer forms on the first charge; b) dendrites grow from the lithium metal anode due to uneven plating of lithium during charging; c) during discharging, lithium metal is stripped from the dendrites leaving some parts isolated from the anode; d) over extended periods of cycling a thick, porous layer of reaction products forms. Adapted with permission from *Nat Energy* **4**, 180–186 (2019)[19]. Copyright 2019 Springer Nature.

Therefore, to enable the safe, efficient use of lithium metal anodes in commercial cells, pairing with non-flammable, non-reactive and dendrite-resistant electrolyte materials is required. One of the most promising research directions is the replacement of organic liquid electrolytes with solid electrolytes.

1.3 All-Solid-State Batteries

1.3.1 Background

In a cell of an all-solid-state battery (ASSB), an ionically-conductive and electronically-insulative solid material is used in place of a liquid electrolyte and separator[20]. The present interest in solid state systems stems from the hope that they will provide higher-performance successors to lithium-ion batteries. However, the current research activity is in fact a resurgence of earlier efforts which began in earnest in the middle of the 20th century and dwindled with the rise of lithium-ion technology in the early 1990s. Many of the benefits and challenges of solid-state cells are the same now as they were three decades ago; therefore, this section starts with some brief historical context.

Most of the solid-state cells under investigation in the first half of the 20th century were primary (non-rechargeable) and based on the transport of silver cations through silver halides[21]. A key discovery was made in 1914 by Tubandt and Lorenz[22], who observed that

solid AgI has an ionic conductivity comparable to that of the best contemporaneous liquid electrolyte in the 150-550 °C temperature range[23]. Most studies sought to improve understanding of reaction thermodynamics rather than to develop a device to store energy[24]. The pace of research was fairly slow until the early 1950s when Sator[25] reported the first all-thin-film vacuum deposited cell, $Pb/PbCl_2/AgCl/Ag$, which had a maximum OCV of 0.523 V and could deliver a current of several microamps for a few minutes[24]. It was also rechargeable, albeit poorly. At this time it was widely believed that batteries containing liquid electrolytes would not be suitable for emerging biomedical devices and consumer electronics due to internal corrosion, electrolyte leakage and limited temperature stability[26]. Nevertheless, a major challenge was the low ionic conductivity of solid electrolytes at room temperature (between 10^{-5} and 10^{-6} S cm^{-1} at best[27]), compared to the aqueous liquid electrolytes which were commonly used at the time (~5×10^{-1} S cm^{-1})[28]. This changed in the early 1960s with the remarkable discovery of a ~10^{-2} S cm^{-1} room temperature ionic conductivity in Ag_3SI[27]. Then in 1967 a room temperature ionic conductivity of 1.2×10^{-1} S cm^{-1} was reported for polycrystalline $RbAg_4I_5$[29]; this value has been surpassed by few, if any, solid electrolytes investigated subsequently[23,30]. Notwithstanding these remarkable conductivity values, the OCVs delivered by silver cells are rather low (~0.5-1.0 V)[26], resulting in low power densities. Along with the limited rechargeability of these cells and the high cost of silver, this was a major driver of the shift towards batteries based on other conducting ions, particularly lithium[26].

In 1969 Liang and Bro[31,32] reported the use of vacuum evaporation to deposit the electrolyte and lithium anode of an all-thin-film Li/LiI/AgI cell, one of the first lithium-based primary microbatteries[33]. This cell had an OCV of 2.1 V – a significant improvement on silver halide cells – although the electrolyte conductivity was only 8.55×10^{-8} S cm^{-1}, which is why a thin film format that minimized the contribution of the electrolyte to the internal resistance was investigated. A 2.8 V cell with a lithium metal anode, LiI solid electrolyte and an iodide

cathode were implemented in a cardiac pacemaker by Wilson Greatbatch Ltd.[34], which was first implanted into patients in 1973[35].

By the late 1970s, reports of Li^+-conducting glass electrolytes were beginning to emerge. These had several perceived benefits over polycrystalline conductors, including higher and more isotropic ionic conductivities[36–38]. In 1978, Glass *et al.*[39] showed that $LiNbO_3$ and $LiTaO_3$ glasses fabricated by twin-roller quenching possessed a Li^+ conductivity up to 10^{-5} S cm^{-1} and an electronic conductivity below 10^{-11} S cm^{-1}. Research on Li^+-conducting glass and amorphous electrolytes continued through the 1980s[40]. Levasseur *et al.*[41] investigated the B_2O_3-Li_2O-Li_nX (n = 1, X = F, Cl, Br, I; n = 2, X = SO_4) glass systems by melting and quenching and found that the best samples had ionic conductivities of ~10^{-6} S cm^{-1} at 25 °C[42]. Developments in thin film deposition technologies during the 1970s and 1980s[43] such as RF sputtering (see Chapter 2 for a detailed description of this technique) led to a growing interest in thin film electrolytes and full thin film cells, partly in an attempt to cater for the development of ever smaller electronic devices[44] but also to compensate for the generally low ionic conductivities of the state-of-the art Li^+ conductors[45]. Indeed, the highest room temperature ionic conductivities for amorphous or semicrystalline films from prominent systems such as Li_2O-SiO_2-ZrO_2, B_2O_3-SiO_2-Li_2O, $Li_{3.6}Si_{0.6}P_{0.4}O_4$ and Li_2O-V_2O_5-SiO_2, reported by Miyauchi *et al.*[45], Levasseur *et al.*[42], Kanehori *et al.*[46] and Ohtsuka *et al.*[47], respectively, were all on the order of 10^{-6} S cm^{-1}. It soon became apparent that the ionic conductivities of glasses based on sulphide compounds are vastly superior to those of the oxide glasses. Early work on Li^+-conducting sulphide electrolytes was performed by Malugani and Robert[48] and Wada *et al.*[49], who reported maximum room temperature ionic conductivities on the order of 10^{-3} S cm^{-1} for the LiI-Li_2S-P_2S_5 and B_2S_3-Li_2S-LiI glass systems – approximately 1000 times higher than the values obtained for oxide compositions. The generally higher Li^+ conductivity measured for the sulphide analogues of oxide electrolyte compositions was attributed to the greater polarizability of sulphur atoms compared to oxygen atoms[50–52]. Despite the success of sulphide solid electrolytes, the commercialization

of lithium-ion batteries in 1991 caused the focus of battery research to shift towards liquid electrolyte cells, which displayed much better performance overall and were significantly easier to manufacture due to the relative ease of achieving good liquid-solid interfacial contact[4,53,54]. Research priorities have since been undergoing a reversal; this has accelerated over the last decade because the performance limits of lithium-ion cells with organic liquid electrolytes and graphite anodes have essentially been reached[1].

1.3.2 Solid Electrolytes

1.3.2.1 Key Benefits over Liquid Electrolytes

The renewed interest in all-solid-state cells has been motivated by the desire to increase the specific energy and energy density of rechargeable batteries based on the expectation that certain solid electrolyte materials will display greater electrochemical stability in contact with lithium metal anodes and high voltage (>5 V) cathodes than the current organic liquid electrolytes[55–57]. Furthermore, it was widely anticipated that solid electrolytes would provide a more effective barrier to the growth of lithium metal dendrites during cell cycling[20,58]. Another property of many solid electrolytes is a Li^+ transference number (the ratio of the current of Li^+ to the sum of currents of other charge carriers) close to unity, whereas typical liquid electrolytes have values in the range 0.2 – 0.5[56]. For a given electrolyte conductivity, a higher power density is attained the closer the transference number is to unity because the concentration gradients developed at high cycling rates are shallower, resulting in a smaller polarization of the cell voltage[59].

1.3.2.2 Solid Electrolyte Materials

Solid electrolyte materials can be categorized broadly into the classes of ceramic/inorganic (including glasses), polymer and composite (which are usually combinations of ceramics and polymers). Prior to the commercialization of Li-ion cells, ceramic electrolytes had received the most attention and solid polymer electrolytes were emerging as a means to improve and maintain solid-solid contact and reduce interfacial resistance by virtue of their mechanical

compliance[60]. Composite electrolytes have garnered attention more recently in an effort to increase the ionic conductivity and stability of polymer electrolytes[61]. In general, ceramic electrolytes are more brittle than polymer electrolytes but display higher ionic conductivities, wider electrochemical windows and greater stability at high and low temperatures[62]. This investigation will focus on ceramic electrolytes, since the electrochemical windows of polymer electrolytes are currently too narrow to offer significant performance improvements on organic liquid electrolytes[4,63]. Ceramic electrolytes are commonly grouped by chemistry, with oxides and sulphides being the two main classes of materials. A wide variety of compositions, crystallographic structures and processing routes have been investigated. Table 1.2 provides examples of prominent ceramic solid electrolyte materials across a variety of subcategories that show good performance in at least one respect. The principal figures of merit for ceramic solid electrolytes are their ionic conductivity and electrochemical stability with anode and cathode materials. The processing route is also of interest from a manufacturing standpoint. Much of the current research on solid electrolytes is concerned with the influence of chemical composition and processing on structure and performance since an understanding of these relationships will help to guide further performance improvements.

Although the materials under investigation today are mostly different from those reported prior to the commercialization of Li-ion cells in the early 1990s, the overall picture is similar: sulphides have higher ionic conductivities than oxides, but oxides tend to have wider electrochemical stability windows. Indeed, the ionic conductivities of certain sulphide materials, including $Li_7P_3S_{11}$ and $Li_{10}GeP_2S_{12}$, are now on the order of the commercial organic liquid electrolytes (~10^{-2} S cm^{-1})[64]. Thus, the main factor limiting solid electrolyte performance in full cells is no longer the ionic conductivity; instead it is the limited compatibility of most solid electrolytes with the electrodes. Good oxidative and reductive stability has not been achieved simultaneously by any of the electrolyte materials studied to date[65]. For example, the NASICON compounds LATP and LAGP are stable to potentials

Table 1.2 Prominent ceramic solid electrolyte materials that have attracted significant research interest in recent years. [a)]LISICON stands for 'lithium superionic conductor'; [b)]NASICON stands for 'Na (sodium) superionic conductor', a structure type first investigated as an Na^+ conductor which also conducts Li^+[66,67].

Category	Example composition	RT Ionic conductivity (S cm^{-1})	Electrochemical stability	Typical processing route
Oxides				
Perovskite-type ABO_3 (A and B are cations). Cubic structure (*P*4/*mmm* or $Pm\bar{3}m$).	$Li_{3x}La_{2/3-x}TiO_3$ (LLTO)	Bulk: 1×10^{-3} Grain boundary: 7.5×10^{-5} Total: 7×10^{-5}[68]	Stable above 1.8 V *vs* Li^+/Li due to reduction of Ti^{4+} at lower potentials[69]. Predicted oxidation potential = 3.71 V *vs* Li^+/Li[70].	Powders calcined at 800 ˚C and 1150 ˚C, ground, pressed, then sintered at 1350 ˚C[68].
Antiperovskite-type Li_3OA (A = halide). Typically cubic structure ($Pm\bar{3}m$).	$Li_2(OH)_{0.9}F_{0.1}Cl$	3.5×10^{-5}[71]	Li_2OHCl, Li_2OHBr and $Li_2OHCl_{0.9}Br_{0.1}$ found to be stable in contact with Li metal at RT[72]. Calculated stability window for $Li_2(OH)_{0.9}F_{0.1}Cl$ and Li_2OHCl is 0.82-3.15 V *vs* Li^+/Li[73].	Pellets synthesized by reacting starting powders at 350 ˚C for 30 mins[71].
NASICON[b)]-type $LiM_2(PO_4)_3$ (M = cation)	$Li_{1+x}Al_xTi_{2-x}(PO_4)_3$ (LATP)	~5×10^{-3}[74]	Calculated stability window is 2.17-4.21 V *vs* Li^+/Li[70]	Powders reacted at temperatures up to 950 ˚C.[74,75]
	$Li_{1+x}Al_xGe_{2-x}(PO_4)_3$ (LAGP)	~2×10^{-4}[76]	Calculated stability window is 2.70-4.27 V *vs* Li^+/Li[70]	Powders annealed at 1450 ˚C, quenched, pressed, then annealed at 800 ˚C[76].
Garnet-type $Li_xLa_3M_2O_{12}$ (M = Ta, Nb, Zr). Cubic structure ($Ia\bar{3}d$ or $I\bar{4}3d$)[62,77].	$Li_{6.87}La_{2.97}Zr_{1.60}Ta_{0.56}O_{12-d}$ (LLZTO)	1.35×10^{-3}[78]	Calculated stability window is 0.05-2.91 V *vs* Li^+/Li for $Li_7La_3Zr_2O_{12}$[70]	Powders milled, calcined at 900 ˚C and 1100 ˚C, then spark plasma sintered at 1000 ˚C, 50 MPa[78].
Sulphides				
Glass ceramics	$Li_2S - P_2S_5$	1.7×10^{-2} for $Li_7P_3S_{11}$[79]	Calculated stability window is 2.28-2.31 V *vs* Li^+/Li[70]	Precursors heated at 700 °C, quenched, then ground. Followed by pressing and heat treatments at ~300 °C[79].
Thio-LISICON	$Li_{10}GeP_2S_{12}$ (LGPS) (tetragonal structure $P4_2/nmc$)	1.2×10^{-2} at 27 ˚C[80]	Calculated stability window is 1.71-2.14 V *vs* Li^+/Li[70]	Powders reacted in an evacuated quartz tube at 550 ˚C[80].
Argyrodites Li_6PS_5X (X = Cl, Br, I)[81] Cubic structure ($F\bar{4}3m$)[82,83]	Li_6PS_5Cl	4.96×10^{-3} at 26.2 °C[84]	Calculated stability window is 1.71-2.01 V *vs* Li^+/Li[70]	Powders mixed and annealed at 550 °C for 10 h[84].
Other				
Oxynitrides	$Li_{2.9}PO_{3.3}N_{0.46}$ (LiPON) (glassy structure)	3.3×10^{-6} at 25 °C[85]	Stable with Li metal and up to 5.5 V *vs* Li^+/Li (observed)[85]. Calculated stability window is 0.68-2.63 V *vs* Li^+/Li[70].	~1 µm thick films deposited by RF magnetron sputtering at room temperature using reactive N gas and Li_3PO_4 target[85].

above 4 V *vs* Li^+/Li and can therefore be paired with medium-voltage cathodes, but experiments have shown that the Ti^{4+} or Ge^{4+} cations are reduced when these electrolytes are combined with a lithium metal anode[86,87].

Even though none of the electrolyte materials in Table 1.2 are predicted to be thermodynamically stable in contact with lithium (only antiperovskites, garnets and LiPON are close), in some cases the experimental evidence appears to refute these predictions. For example, LiPON has shown outstanding stability over prolonged cycling in Li/LiPON/LCO cells, as will be discussed later. This behaviour is explained by the fact that reaction between the electrolyte and electrodes can be kinetically inhibited if the reaction products form passivating interphase layers[88]. To be passivating, these layers must have a low electronic conductivity; if the ionic conductivity is high, as is the case for LiPON, the effect on the cell performance will be minimal. While a solid electrolyte material that is thermodynamically stable in contact with both a lithium metal anode and a high voltage cathode may not exist, kinetic stabilization could facilitate stable operation of an all-solid-state cell.

1.3.3 Challenges Hindering the Commercialization of Solid-State Cells

Until relatively recently, the focus of solid electrolyte research was achieving the highest possible ionic conductivity[57]. The superiority of solid electrolytes over liquid electrolytes in terms of electrochemical stability and imperviousness to lithium filament growth was seemingly taken for granted. However, it is phenomena at the electrode-electrolyte interfaces caused by electrochemical and mechanical instability of the solid electrolyte that are now seen as the greatest barriers to achieving all-solid-state cells competitive with the best lithium-ion cells[57,65,88,89].

As alluded to previously, impedance growth and capacity fading during cycling can occur if SEI layers form at the cathode-electrolyte and anode-electrolyte interfaces due to oxidation and reduction of the electrolyte, respectively. This is a particular problem if the layers have a low ionic conductivity and/or are not passivating[65]. Contact loss is another major contribution

to impedance growth and a particular problem for solid-solid interfaces. It is primarily caused by the differential volume changes of the materials either side of the interface during cycling[90–92]. For example, intercalation cathodes such as $LiCoO_2$ and $LiNi_xMn_yCo_{(1-x-y)}O_2$ have been found to undergo volume changes of 2-4 %[93,94], while electrolyte volume changes are generally insignificant. The resulting contact loss limits the transfer of Li^+, leading to an increase in impedance and a decrease in the attainable capacity. Furthermore, achieving adequate interfacial contact during cell construction is also challenging, and composite cathodes consisting of both active and electrolyte material have been developed to try to increase the area of the cathode-electrolyte interface[89]. Consequently, the processing is significantly more complex than for a lithium-ion cell with a liquid electrolyte, in which extensive interfacial contact is achieved by infiltration of the cathode with liquid electrolyte.

The above interfacial issues typically result in performance degradation over several cycles. However, a more catastrophic problem which causes sudden and premature cell failure during cycling is short circuiting by lithium dendrites (more properly referred to as lithium filaments in solid electrolytes). Short circuiting has been observed for almost all solid electrolyte materials used in conjunction with a lithium metal anode and cycled at practical current densities (several mA cm^{-2})[58]. This demonstrates that most solid electrolytes are not as resistant to lithium metal penetration as initially anticipated.

The mechanisms of lithium filament formation and growth in an all-solid-state cell are not fully understood. Porz *et al.*[95] proposed a mechanism dependent on electrolyte surface flaws, which fill with lithium metal at the start of electrodeposition on the anode current collector. Once a flaw is full, and if its aspect ratio and the ionic current density are sufficiently high, the stress at its tip will exceed the fracture stress of the electrolyte material, causing it to propagate. The situation is illustrated schematically in Figure 1.4[95]. Therefore, for a particular electrolyte material, population of surface flaws, and test conditions, there is a critical current density at which lithium dendrites propagate through the electrolyte and cause a short circuit.

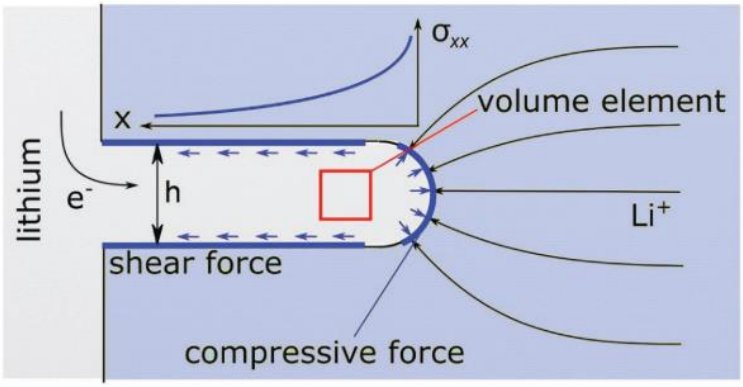


Figure 1.4 Schematic diagram illustrating the mechanism of lithium filament growth through solid electrolytes proposed by Porz *et al.*[95] The blue arrows at the rounded end of the lithium metal filament indicate the compressive stress exerted on the solid electrolyte by the accumulation of lithium metal, while the arrows along the sides indicate shear stresses. The plot of compressive stress along the length of the filament shows the significant stress concentration at the tip of the filament. Realistically, a much higher flaw aspect ratio would be required to concentrate enough stress to propagate the flaw through the electrolyte: the authors measured a thickness, *h*, of ~300 nm for dendrites which propagated in their experiments. Reproduced with permission from *Adv. Energy Mater.* **7**, 1–12 (2017)[95]. Copyright 2017 John Wiley and Sons.

Raj and Wolfenstine[96] proposed that defects within the bulk of the solid electrolyte, such as grain boundaries, can also act as sites for dendrite formation. Through a model based on classical nucleation theory, they showed that the electrochemical potential of lithium is locally raised at grain boundaries near the electrolyte-anode interface. Equation 1.10 provides the condition for the prevention of dendrite nucleation in their model, where j is the ionic current density, ρ_B, δ_B, and γ are the ionic resistivity, width, and specific energy of the grain boundary, respectively, α is the ratio of the distance of the grain boundary from the anode to the grain size, e is the electronic charge, Ω_{Li} is the atomic volume of lithium, r_c is the critical radius for nucleation and σ_F is the failure stress of the electrolyte.

$$j\rho_B\delta_B(1-\alpha)|e| \leq \frac{2\gamma\Omega_{Li}}{r_c} + \sigma_F\Omega_{Li} \qquad \textbf{Equation 1.10}$$

If the current density and ionic resistivity are sufficiently high and the distance from the anode, the grain boundary energy, and the failure stress of the electrolyte are sufficiently small, the electrochemical potential of lithium at the grain boundaries will rise above the reference potential, resulting in the nucleation of lithium metal. However, the authors did not propose a mechanism for the supply of electrons to a growing lithium metal precipitate within an electronic insulator.

Han *et al.*[97] reported that the electronic conductivity of many solid electrolytes is high enough to enable the reduction of Li^+ to metallic lithium within the electrolyte bulk. The authors supported their theory by highlighting the fact that $Li_7La_3Zr_2O_{12}$ (LLZO), $75Li_2S$-$25P_2S_5$ and LiPON have electronic conductivities of ~10^{-7} S cm^{-1}, ~10^{-8} S cm^{-1} and 10^{-14} S cm^{-1}, and critical current densities of 0.05–0.9 mA cm^{-2}, 0.4–1 mA cm^{-2} and >10 mA cm^{-2}, respectively[97–100]. This suggests that resistance to filament formation is inversely correlated with electronic conductivity in these materials. With the exception of LiPON, the critical current densities of these prominent oxide and sulphide electrolyte materials fall well short of a suggested current density target for fast charging applications (10 mA cm^{-2})[54]. Notwithstanding its very low electronic conductivity, the main reason for the outstanding resistance of LiPON to short circuiting may be the fact that it is an amorphous material largely free of defects, meaning that the mechanisms for internal lithium precipitation proposed by Raj and Wolfenstine[96] and Han *et al.*[97] may not operate. Despite the significant interest in amorphous electrolytes in the 1980s, with the main exception of LiPON this class of electrolyte structure has received little attention in recent years. This is somewhat surprising given that LiPON displays the best resistance to lithium filament propagation out of all the solid electrolytes investigated to date and is one of the few inorganic solid electrolytes to have been commercialized, albeit on a small scale.

The challenges hindering the commercialization of all-solid-state cells largely pertain to the structural and chemical properties of solid electrolytes and their interfaces with the

Table 1.3 Key challenges hindering the commercialization of all-solid-state cells, categorized into chemical and processing challenges. 'SE' stands for 'solid electrolyte'.

Chemical	Processing
Current SE materials are not thermodynamically stable in contact with lithium metal and typical commercial (>4 V) cathodes simultaneously.	It is difficult to achieve adequate solid-solid interfacial contact and maintain this during cycling.
Most SE materials under investigation contain surface and internal defects which lead to short-circuiting.	
Certain promising SE compositions have high electronic conductivity, which may increase the propensity for lithium filament formation and/or the self-discharge of a full cell.	High temperature, long duration processing is often required to achieve adequate SE density[101]. This increases costs, reduces productivity and leads to loss of volatile elements such as lithium.
	Lithium metal and many SEs – particularly sulphides[65] – are very air or moisture sensitive and require tightly-controlled processing environments to avoid the formation of high impedance surface reaction layers. This increases processing complexity and cost.

electrodes[88,89]. Since 'structure' (crystallographic, microstructure and cell-level structure) is determined by the chemical composition and processing route, the challenges can be grouped into the categories of 'chemical' and 'processing', as shown in Table 1.3.

To address these challenges, a better understanding of the relationships between the chemistry and processing and the resulting electrochemical performance of all-solid-state cells will be required. This work focused on overcoming the processing challenges using an alternative to the conventional powder processing techniques commonly used for ceramic electrolyte and electrode materials: physical vapour deposition (PVD). The next section starts with an overview of PVD techniques in the context of battery materials and proceeds to focus

on RF sputtering – the technique predominantly used in this work. This technique is of particular interest owing to its suitability for high-throughput production and it is used widely in the semiconductors industry[102].

1.4 Thin-Film Solid-State Batteries

1.4.1 Background

The principal components of a solid-state cell (anode, solid electrolyte, cathode and current collectors) can be processed into films less than 10 µm thick using a variety of PVD techniques including sputter deposition, pulsed laser deposition (PLD) and vacuum evaporation[46,103–105]. Vacuum evaporation and PLD both involve the evaporation or sublimation of material from a target (source) and subsequent condensation on a substrate, but PLD is better suited to high melting point ceramics and often replicates the stoichiometry of the target more closely[106]. By contrast, sputter deposition involves the bombardment of a target material by an ionized gas such as argon. This sputters away atoms which condense on a substrate and form a film. DC (direct current) sputtering is used to deposit electronically conductive components such as the metallic current collectors, while RF (radio frequency) sputtering is used to deposit components with higher electronic resistivities such as the cathode and electrolyte. A more detailed description of RF sputtering is provided in Section 2.2.1.

The use of thin film deposition techniques in solid-state battery research is not new, as revealed in the historical perspective in Section 1.3.1. From the late 1960s to the early 1990s there were two key motivations for using thin film deposition techniques to fabricate solid electrolytes and full cells: 1) to minimize the contribution to cell resistance of the generally low ionic conductivity solid electrolytes available at the time[39] and 2) to provide power sources, referred to as “microbatteries”[107] or more lucidly as “all-thin-film cells”, to support an anticipated revolution in miniaturized electronic devices. To some extent these motivations apply to the research on thin-film battery materials today, although various other benefits of

thin-film processing have since been discovered. These are best appreciated by reviewing the most successful ceramic solid electrolyte, LiPON, and the development of the archetypal Li/LiPON/LCO all-thin-film cell.

1.4.2 LiPON and the Li/LiPON/LCO All-Thin-Film Cell

The development of LiPON (lithium phosphorus oxynitride) electrolytes and all-thin-film cells based on LiPON mostly occurred during the 1990s at Oak Ridge National Laboratory in the US. At this time interest in amorphous – particularly glassy – electrolyte materials among the solid electrolyte research community was strong. Glasses in the Li-P-O-N system were first reported by Marchand[108] in 1983, although these glasses were produced by traditional methods and apparently without electrochemical applications in mind. In 1992, Bates *et al.*[109] reported an amorphous electrolyte thin film produced by the reactive RF magnetron sputtering of Li_3PO_4 in a pure nitrogen atmosphere. The chemical composition was $Li_{3.3}PO_{3.9}N_{0.17}$, and it was found to have an ionic conductivity of 2×10^{-6} S cm^{-1} at room temperature. In 1993, the same group reported the fabrication of an all-thin-film cell with a 1 μm thick amorphous V_2O_5 cathode (up to 3.8 V *vs* Li^+/Li), a 1 μm thick LiPON electrolyte and a 5 μm thick lithium metal anode, deposited by DC magnetron sputtering of V in O_2-Ar, RF magnetron sputtering and thermal evaporation, respectively[110]. Unlike the sputter-deposited amorphous Li_2O-SiO_2-P_2O_5 electrolytes also studied by this group, LiPON was found to be stable in contact with lithium as well as the cathode material. The LiPON synthesized in this study had a higher nitrogen content, with an overall composition of $Li_{2.9}PO_{3.3}N_{0.46}$, resulting in an increased Li^+ conductivity of 3.3×10^{-6} S cm^{-1}.

A later study reported the fabrication of all-thin-film Li/LiPON/LCO cells[111], the design of which is shown by schematic drawings in Figure 1.5. The cathode films were fabricated by RF magnetron sputtering an $LiCoO_2$ target in a 3:1 Ar:O_2 gas atmosphere followed by post-deposition annealing of the films in air at 700 °C for 2 hours. Annealing was required to achieve the crystalline $R\bar{3}m$ layered structure of the commercial LCO cathodes predominant

in lithium-ion cells at the time. The average composition of as-deposited films was found to be $Li_{1.15}CoO_{2.16}$, while the average specific capacity of films annealed at 700 °C was ~64 μAh cm^{-2} μm^{-1}, which is very close to the theoretical value when $0.5Li^+$ is extracted (69 μAh cm^{-2} μm^{-1}). Several cells were cycled over 40,000 times at 25 °C to ~96% depth of discharge with total capacity losses of less than 5%[85]. Furthermore, certain cells[111] could deliver 85% of the capacity measured on discharging from 4.2 to 3.0 V at 1 μA cm^{-2} when the current density was increased by a factor of 1000 to 1 mA cm^{-2}. This outstanding performance can largely be attributed to the stability of the LiPON electrolyte during cycling. Although an electrochemical stability window of 0.68 to 2.63 V *vs* Li^+/Li[70] was recently calculated for LiPON, which would render it unstable in contact with both lithium metal and LCO, the empirical stability range measured by linear sweep voltammetry and electrochemical impedance spectroscopy was 0 to 5.5 V *vs* Li^+/Li at room temperature[85]. Aside from electrochemical stability, the authors noted that LiPON must have a high mechanical stability, enabling it to block lithium filament growth over prolonged cycling and resist cracking as the cathode volume changed.

While the development of all-thin-film cells has continued since the Li/LiPON/LCO cell was first reported, remarkably little progress on improving performance has been made and LiPON remains the preeminent inorganic solid electrolyte owing to its unparalleled stability in lithium metal cells[112–114]. Recent studies have indicated that the stability of LiPON is due in part to the content of nitrogen, which forms stable, ionically-conductive decomposition products at the interfaces with the anode and cathode. These interphase layers are poorly characterized, although calculations and experiments indicate that Li_3N, Li_2O and possibly Li_3P form at the interface with lithium[114,115], while P_3N_5 and $Li_4P_2O_7$, amongst other compounds, form at the interface with the cathode[70,114,116]. The mechanical stability of LiPON likely stems from its near-pristine glassy structure. Strong support for this theory was provided by the recent study of Westover *et al.*[117], in which lithium filaments were found to grow along an artificial LiPON/LiPON interface but nowhere else during lithium plating on copper current collectors through a LiPON electrolyte. Another recent investigation[118] studied

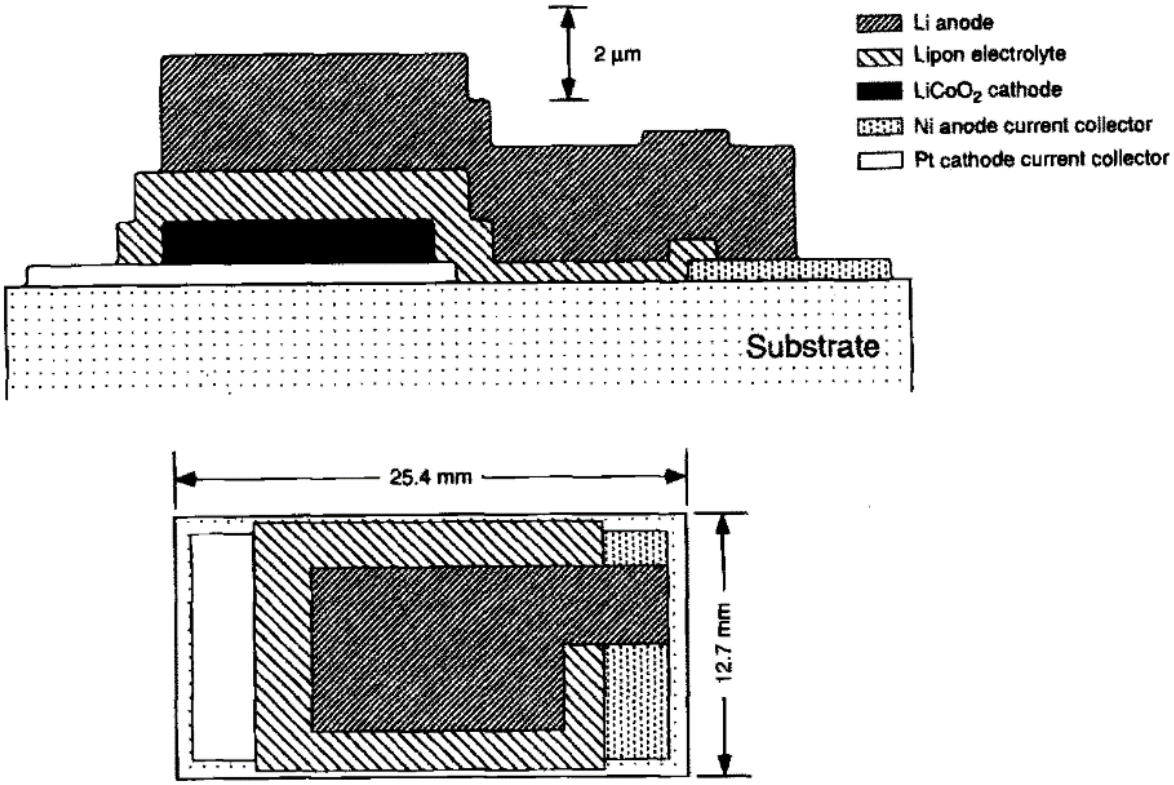


Figure 1.5 Schematic cross-sectional and plan view drawings of the all-thin-film Li/LiPON/LCO cell reported by Wang *et al.*[111] Reproduced with permission from *J. Electrochem. Soc.* **143**, 3203–3213 (1996)[111]. Copyright 1996 The Electrochemical Society, Inc.

the fracture toughness of LiPON using nanoindentation and concluded that LiPON demonstrates nanoscale plasticity by motion of the phosphate tetrahedra in its glassy structure, making it more resistant to cracking than brittle, crystalline ceramic electrolyte materials such as LLZO, LLTO and LATP.

The formation of the glassy structure in LiPON is a result of the bridging of phosphate tetrahedra by nitrogen atoms[113] and the nature of the thin-film processing route, since sputter deposition from ceramic targets onto unheated substrates provides a kinetic hindrance to crystallization, producing amorphous or nanocrystalline films[110]. Although LiPON has dominated research on thin-film battery materials since its exceptional performance was first reported[112,118], understanding the processing-structure-properties relationships pertaining to

the pre-eminent Li/LiPON/LCO cell will enable further performance enhancements to be realized across a variety of compositions.

1.4.3 Benefits over Powder Processing

The processing-structure-properties relationships for thin film processing are considerably different from those of the powder processing routes used for the majority of solid-state cell component fabrication, not least because of the different properties exhibited by a given material in bulk and thin film forms[119]. A range of thermodynamic and kinetic factors which have little influence on structural development in bulk materials can strongly influence the properties of thin films owing to the large surface area to volume ratios[106]. Although chemical composition has a strong bearing on the structural development of films, reports of prior experiments, including those on LiPON and LCO, reveal some general characteristics of films deposited by RF magnetron sputtering and how these influence the structural properties and performance of all-thin-film cells.

The advantages of RF magnetron sputter deposition over the powder processing routes typically used for solid-state cell fabrication are summarized as follows.

- Reduced microstructural flaw concentrations (cracks, porosity, etc.) in the bulk and at surfaces and interfaces. If appropriate processing conditions are used, highly conformal films close to 100% density can be achieved. RF magnetron sputtering is well-suited to the deposition of amorphous films which are completely free of crystallographic defects.
- Greater control over composition. There are several deposition parameters that can be adjusted to achieve fine control over the film composition, such as the molar ratio of compounds in a composite target or the composition and pressure of the process gas.
- Attainment of high-performance metastable phases. Metastable phases such as glasses and non-equilibrium crystal structures can be achieved owing to the

inherently rapid cooling rates of films during and after deposition, which provides kinetic stabilization. Certain metastable materials, such as LiPON, possess desirable characteristics.

- Formation of high-quality interfaces. Structural rearrangements at the atomic scale during deposition are inherent to sputter deposition. These create well-bonded, conformal interfaces. Optimal solid-solid contact minimizes the cell resistance and helps to reduce contact loss due to volume changes during cycling.
- Attainment of desirable structural properties without applied heating. Powder processing techniques often require the application of temperatures above 1000 °C to achieve densification[101], whereas fully dense films can be achieved by sputter deposition without any applied heating. Further, a great number of metastable phases, many of which are expected to have desirable properties, can be formed without annealing (either during or after deposition). In cases where annealing is required to achieve a fully crystalline film, the temperatures needed are relatively low (generally below 700 °C[101]), reducing energy requirements and helping to avoid the loss of volatile elements such as lithium.
- Increased energy density of electrodes and full cells. Inactive material added to ease powder processing, such as binders and sintering aids, are not required when sputter deposition is used. Furthermore, fabrication of all-thin-film cells allows the total mass and volume of inactive components such as the solid electrolyte, current collectors and encapsulation layers to be minimized.
- Ease of processing. Certain materials, such as the sulphide electrolytes, are highly air-sensitive. In many cases a complete thin-film cell can be built in a single deposition chamber without breaking the vacuum, avoiding any exposure to the external environment. Further, the fabrication of an entire cell in a single piece of equipment is much simpler than the fabrication of “bulk” solid-state cells, which involves numerous processing steps and pieces of equipment.

Thus there is the potential to overcome, at least to some extent, all the processing challenges identified in Table 1.3 using thin-film deposition techniques.

1.4.4 Current Research Directions

The development of all-thin-film cells since the discovery of LiPON electrolytes has parallels with the development of lithium-ion cells, which were commercialized shortly before the Li/LiPON/LCO cell was first reported: minor modifications to increase performance have been proposed, but the original design remains the most widely produced. Several companies began manufacture of all-thin-film Li/LiPON/LCO cells, including Front Edge Technology[120], Cymbet[121], Infinite Power Solutions[122] and STMicroelectronics[123]. However, the demand for these cells may have been lower than anticipated[124], as plans for significant scaling up of production[125] did not materialize. It is possible that the advantages of all-thin-film cells over small conventional lithium-ion cells are currently insufficient. Efforts are underway to improve the energy density and area-specific capacities of all-thin-film cells in the belief that they may at some point become competitive with the lithium-ion cells used in small portable devices such as mobile phones[126–128]. Research has focused primarily on the implementation of new cell architectures, higher-energy cathode materials and higher-conductivity electrolytes, but it is not yet clear which approaches are the most promising.

1.4.4.1 Lithium-Free Cells

A modified version of the “traditional” Li/LiPON/LCO all-thin-film cell architecture was proposed by the research group that first reported this cell[129]. The modified cell is similar to the original cell, except the vacuum-deposited lithium metal layer is omitted, hence the terms “lithium-free” or “anodeless” cell. Instead, the anode is formed during each charging half cycle using only lithium supplied by the cathode. Cycling of Cu/LiPON/LCO cells between 3.0 and 4.2 V was demonstrated for over 1000 cycles at 1 mA cm^{-2} and over 500 cycles at 5 mA cm^{-2}. Furthermore, around 30% of the theoretical capacity was obtained at a discharge rate of 10 mA cm^{-2}, which is a current density target proposed to meet the requirements of fast

charging[54]. Although the cell potential versus capacity profiles were similar for “Li-free” and corresponding Li/LiPON/LCO cells, the “Li-free” cells were found to have poorer cycling stabilities, which is probably a result of the structural changes that take place in the “Li-free” cell as the anode forms between the LiPON and current collector layers on plating. Nevertheless, there are some significant processing advantages associated with the “Li-free” architecture. Dispensing with lithium metal deposition enables the cell to be exposed to air during fabrication, simplifying processing. Furthermore, some applications of all-thin-film cells may require attachment to circuit boards by soldering, which would expose the cells to temperatures of ~250 °C. The absence of lithium metal – which melts at 181 °C – would be a distinct advantage in such applications.

1.4.4.2 3D Thin-Film Battery

Another new all-thin-film cell architecture, which has attracted considerable interest over the past 15 years, is the so-called “3D” thin-film battery[130–133]. Cells are fabricated on substrates containing three-dimensional microscale patterns, for example arrays of micropillars, micropores or microtrenches[132]. Silicon is frequently chosen as the substrate since it is amenable to processing by etching. The motivation for research on 3D thin-film batteries is the desire to increase the “footprint” capacity (i.e., the cell capacity normalized by the projected area of the substrate) compared to a conventional planar all-thin-film cell without sacrificing the rate performance. In a planar cell, the capacity can be increased by depositing thicker electrode layers. However, this increases the cell resistance and could impair performance at high cycling rates. The alternative strategy – employed in 3D cells – is to increase the total cell volume laterally without increasing layer thickness. The expected dependences of capacity and charging time on geometric properties are shown in Figure 1.6[132].

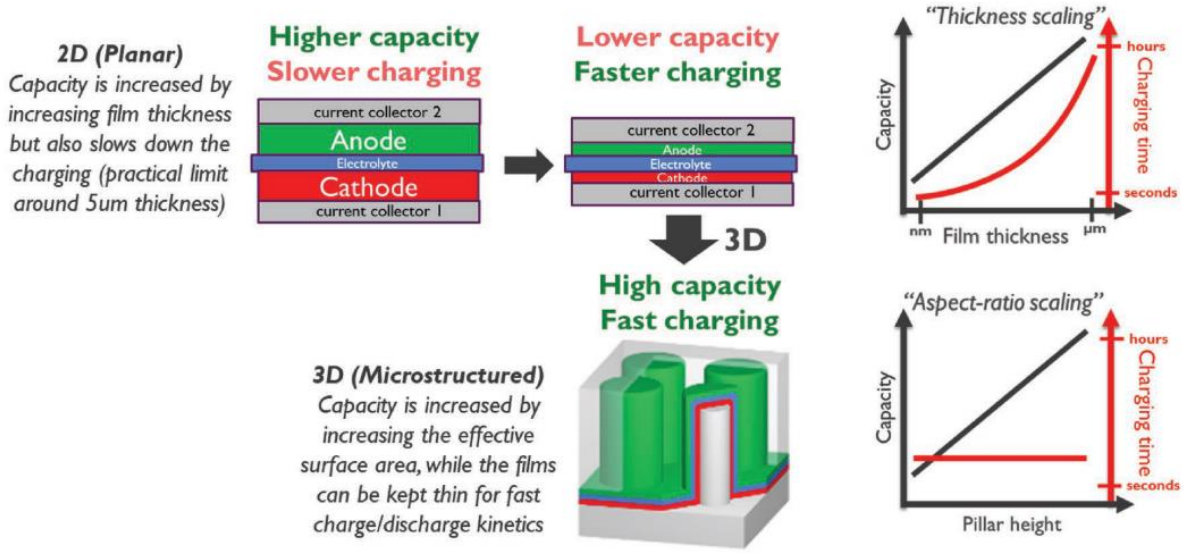


Figure 1.6 Schematic diagrams showing designs of planar (conventional) and "3D" all-thin-film cells with the corresponding relationships between the geometrical properties of the cells and the charge capacity and charging time. Reproduced with permission from *Adv. Mater. Interfaces* **6**, 1–17 (2019)[132]. Copyright 2019 John Wiley and Sons.

However, 3D all-thin-film cells have proven to be very challenging to fabricate[132]. RF magnetron sputtering, which is the most promising fabrication technique for planar thin-film cells, is not well-suited to deposition on highly textured substrates. This was apparent from the results of an investigation into the deposition of LiPON onto textured substrates by the group at Oak Ridge National Laboratory[131]. Although arrays of posts 70-100 μm in diameter and 500 μm high, spaced by 150 μm and composed of silver epoxy on stainless steel meshes were well-coated by sputter deposited LiPON, the deposition rate was found to be significantly lower than on flat substrates (1/8 of the rate at some locations). Moreover, the 3D features used in this investigation were rather large and well-spaced; to realize significant performance improvements over planar cells the density of these features would need to be increased. This would result in greater shadowing effects during deposition and an even lower deposition rate and film uniformity. So far, the only thin film deposition technique shown to achieve good film conformality on highly textured substrates is atomic layer deposition (ALD)[132]. However, the major drawback of ALD is its very low deposition rate; this

means that the maximum practical layer thickness is about 30 nm. For electrode layers of this thickness, it is very difficult to fabricate a 3D cell with an areal capacity exceeding that of a planar cell since an extremely large surface area would be required. This explains why a 3D cell that outperforms a planar all-thin-film cell has not yet been achieved.

It is not entirely clear why the “3D” design concept has received so much attention when an alternative strategy proposed by Dudney and Neudecker[112] in 1999 seems somewhat more practical from a processing perspective. The authors suggested that large area cells could be fabricated and subsequently rolled or folded to achieve the required energy density. Although this assumes that a suitable flexible substrate can be found, it is a promising research direction considering that many of the “3D” cell designs proposed so far are not very space efficient, with significant gaps between micropillars, for example. Folding or rolling up large area planar cells into an appropriate volume could increase both areal and volumetric capacities, yet this approach has received surprisingly little research attention. It is also far from clear that increasing the capacity of a planar cell by increasing the electrode thickness is not a viable approach, particularly for applications which require a long-duration, low current power source. Thus “3D” cell architectures may not prove to be a particularly fruitful research direction.

1.4.4.3 Improved Cathodes

Developing thin-film cathodes with higher energy densities is an important direction for future research. Moving away from the “traditional” LCO cathode would mirror the advances that have been made in commercial lithium-ion cells, which now feature a range of cathode materials as shown in Table 1.1. Indeed, there have been several attempts at fabricating these cathode materials as thin films and incorporating them into all-thin-film cells.

One of the most notable reports in this area came from the group at Oak Ridge National Laboratory[134]. The authors fabricated 1 μm thick $LiMn_{1.5}Ni_{0.5}O_4$ (LMNO) cathodes by RF magnetron sputter deposition onto Pt-coated alumina followed by annealing in air at 700 °C

for 1 hour. This resulted in the formation of the disordered spinel phase, which has a theoretical capacity of 147 mAh g^{-1} and a high operating voltage of ~4.7 V *vs* Li^+/Li. All-thin-film Li/LiPON/LMNO cells were then constructed by a similar procedure to that commonly used for Li/LiPON/LCO cells. The reversible capacity measured for the cathode on cycling the cells between 3.5 and 5.1 V *vs* Li^+/Li at 0.1 C was ~122 mAh g^{-1}, which is ~83% of the theoretical capacity. Even at a rate of 10 C, a reversible capacity of 90 mAh g^{-1} was measured. The cells showed remarkable performance during long-term cycling at 5 C, with 90.6% of the initial discharge capacity retained after 10,000 cycles (the cells were cycled at C/10 every 1000^{th} cycle, but no explanation for this was provided). Nevertheless, the cycle life of these cells should be more than adequate for most applications, meaning that the implementation of LMNO cathodes is a promising route to improving all-thin-film cell performance.

A recent investigation by Aribia *et al.*[135] studied the application of Li-rich NMC-811 cathodes in all-thin-film Li/LiPON/NMC cells. 600 nm thick cathode films were deposited on ITO-coated stainless steel by RF magnetron sputter deposition from a target with the composition $Li_{1.6}Ni_{0.8}Mn_{0.1}Co_{0.1}O_2$. This was followed by annealing at 600 °C for 1 hour in a flow of oxygen. The film composition, determined by a combination of several spectroscopic techniques, was found to be $Li_{1.95}Ni_{0.83}Mn_{0.08}Co_{0.09}O_x$; the content of O could not be determined reliably due to interference from the underlying ITO layer. Cycling of the all-thin-film cells was performed within a series of different voltage ranges. It was found that decreasing the lower voltage limit below 3.0 V *vs* Li^+/Li significantly increased the measured cathode capacity. Cycling at a rate of 0.1 C between 1.5 and 4.7 V *vs* Li^+/Li gave a first cycle discharge capacity of 350 mAh g^{-1}; this very high capacity was attributed to the participation of multiple electrons per NMC formula unit – a well-known phenomenon in lithium-rich NMC cathodes. However, the Coulombic efficiency was only 90.1 %. Cycling at 4 C between 1.5 and 4.3 V *vs* Li^+/Li gave an initial discharge capacity of 149 mAh g^{-1}. The capacity remained above 80% of this value for 904 cycles, and over 1000 cycles the Coulombic efficiency was

98.79%. Thus, like LMNO, NMC-811 is a promising cathode material for “next-generation” all-thin-film cells, albeit with a lower operating voltage.

1.4.4.4 Improved Electrolytes

A wide variety of Li^+-conducting thin-film electrolytes have been fabricated since the first all-thin-film cell based on lithium was reported in 1969[31,32]. Most of the materials under investigation in thin-film form today – other than LiPON – are those that have shown promise for application in “bulk” all-solid-state cells (Table 1.2)[136]. However, it is becoming apparent that this may not be the most fruitful strategy for thin-film electrolyte development, since in most cases the ionic conductivity measured for these materials in thin film form is at least an order of magnitude below the “bulk” value[101,128,137–139]. Besides, the cycling stability of LiPON is somewhat better than displayed by any of these materials, which is due in large part to its amorphous structure, as mentioned earlier. Therefore, a different strategy for electrolyte discovery, which takes advantage of the ease of glassy, amorphous and otherwise metastable film fabrication by PVD techniques such as RF magnetron sputtering, might be most appropriate. The paucity of publications in this area since the link was made between the stability of LiPON and its structural properties is somewhat surprising. Nonetheless, a few interesting studies have been reported.

Garbayo *et al.*[140] took an approach which could be described as a hybrid of the “old” and alternative strategies discussed above. The authors reported the fabrication by PLD of amorphous thin film electrolytes based on the garnet composition $Li_{6.19}Al_{0.28}La_3Zr_{1.75}Ta_{0.25}O_{12}$ (Al and Ta doped LLZO). The material was chosen based on the fact that “bulk” LLZO demonstrates a relatively high ionic conductivity (up to 10^{-3} S cm^{-1}) and reasonable stability against lithium metal (particularly when compared to other prominent oxide electrolytes such as LLTO, LATP and LAGP – see Table 1.2), while the amorphous structure may provide resistance to lithium filament growth. The highest ionic conductivity (6.35×10^{-3} S cm^{-1} at 400 °C) was measured in 300 nm thick films deposited from a garnet target with the

aforementioned composition onto Si_3N_4-coated silicon substrates held at a temperature of 300 °C. Based on XRD, Raman and transmission electron microscopy analysis, it was claimed that films deposited at this temperature contained a network of cubic garnet units with optimal alignment of bonding tetrahedra and octahedra. Different amorphous arrangements were found (referred to as polyamorphism) when the deposition temperature was changed, and the partial crystallization of the $La_2Zr_2O_7$ phase at higher temperatures had a deleterious effect on the ionic conductivity. While the authors demonstrate a novel approach to thin-film electrolyte development, the focus of the work appears to have been on investigating polyamorphism rather than demonstrating a viable thin-film electrolyte. A room temperature Li^+ conductivity of ~2×10^{-8} S cm^{-1} was determined by extrapolation from the values measured at high temperature (it is not clear why a measurement at room temperature was not reported). This is two orders of magnitude lower than the value for LiPON. Furthermore, the cycling stability was not demonstrated. Overall, this work does not make a convincing case for synthesizing amorphous versions of the crystalline materials that show good performance in bulk cells, at least in the case of garnets.

The lithium-rich antiperovskites (LiRAPs) are a class of solid electrolytes which were first reported in 2012 after the discoveries of high Li^+ conductivity (~10^{-3} S cm^{-1}) in Li_3OCl by Reckeweg *et al.*[141] and Zhao and Daemen[142]. This class of solid electrolytes has attracted increasing attention in recent years, but the greatest success has been had in the synthesis of hydroxide halide compounds such as Li_2OHCl and Li_2OHBr due to the thermodynamically unstable nature of Li_3OCl, which has a tendency to break down into Li_2O and LiCl on cooling from the synthesis temperature to room temperature[143]. Nevertheless, the two reported attempts to synthesize Li_3OCl thin films by PLD, both by Lü *et al.*[126,144], are significant. In their first report[126], the authors synthesized an "Li_3OCl" deposition target using a similar procedure to that reported by Zhao and Daemen[142]. Films were deposited from this target onto $LaAlO_3$ or stainless steel substrates – which had been coated with gold or lithium – at a temperature of 175 °C. The room temperature ionic conductivity of the resulting films was found to be

8.9×10^{-6} S cm^{-1}, which is somewhat higher than measured for the deposition target material (5.8×10^{-7} S cm^{-1}) and similar to that of LiPON. In their second report[144], the authors used a pellet produced by pressing a stoichiometric mixture of Li_2O and LiCl precursor powders for the deposition target, which drastically simplified processing. It was hoped that the energy provided by the laser beam would cause these compounds to react together to form Li_3OCl. The films deposited from this target had an ionic conductivity of 2.0×10^{-4} S cm^{-1} at room temperature – over two orders of magnitude higher than measured for the previous films. The reason for this was not investigated, but the strong dependence of conductivity on Li^+ and Cl^- vacancy concentrations was mentioned, which could depend on the properties of the target. While the reported characterization was insufficient to prove that the intended Li_3OCl compound had been synthesized, these reports highlight the utility of thin-film deposition in synthesizing promising but thermodynamically unstable and air-sensitive materials.

A series of reports by Braga *et al.*[145–151] indicates that glasses based on LiRAP compositions are worth investigating as solid electrolyte materials. The authors primarily studied the composition $Li_{2.99}Ba_{0.005}ClO$ (lightly doped Li_3OCl), which they synthesized as glassy powders from LiCl and lithium and barium hydroxides. Controversially, given the hygroscopicity of Li_3OCl, water was added to aid synthesis and was later removed by drying and vacuum pumping. Some remarkable properties were reported including a room temperature Li^+ conductivity above 10^{-2} S cm^{-1} and electrochemical stability to higher than 8 V *vs* Li^+/Li[145], as well as unusual, potentially advantageous behaviour during cycling[146,147,149–151]. Hanghofer *et al.*[152] were critical of the reports on the synthesis of these glasses given the deliberate exposure to moisture and air during synthesis. In their own study[152], these authors found that exposing Li_3OCl to air caused it to break down into Li_2CO_3 and amorphous $LiCl \cdot xH_2O$, which could explain the high ionic conductivity values measured by Braga *et al*. Nevertheless, the various controversies associated with LiRAP compounds, especially the synthesis of Li_3OCl-type glasses, make these materials worthy of further investigation. RF magnetron sputtering, which has been used previously for the deposition of glassy electrolytes and features an

inherently moisture-free synthesis environment, could be used to determine whether the synthesis of glasses based on Li_3OCl is viable, and if it is, whether the properties are as remarkable as claimed by some researchers.

1.5 Summary and Aims of This Work

Notwithstanding the various benefits of applying thin-film deposition techniques to the fabrication of solid-state cells, all-thin-film cells do possess a number of limitations, chiefly their low areal capacities[136]. For low power applications this is not a significant issue, and the lack of optimized processing routes for large-scale manufacturing is a greater barrier to commercialization. As discussed above, research is being conducted on the fabrication of high voltage, high capacity cathode materials by RF magnetron sputtering, which will help to improve the areal capacities of all-thin-film cells. Nevertheless, the ultimate cause of limited areal capacity is the small cathode volume used in these cells. Cathodes must necessarily be kept fairly thin to avoid limiting the rate performance, since thin-film cathodes do not contain electronically-conducting additives and the cathode-electrolyte interfacial area is much smaller than in lithium-ion cells containing liquid electrolytes. Furthermore, low deposition rates may make the fabrication of thicker cathodes unattractive. The extent to which cathode thickness can be increased without impacting the cell performance and viability of the processing route has not been explored adequately. Thus, the first aim of this work was to achieve good electrochemical cycling performance in relatively thick (several μm) sputter-deposited LCO cathodes using processing conditions optimized for large-scale manufacturing.

The accessible capacity of a cell is determined in large part by the polarization of the cell voltage due to the internal resistance, which is made up of contributions from the electrodes, the electrolyte and their interfaces. LiPON is the preeminent thin-film electrolyte, yet its ionic conductivity is relatively low (~10^{-6} S cm^{-1}) and it demonstrates kinetic – not thermodynamic – stability at its interfaces with lithium metal anodes and high voltage cathodes. Ideally, a

higher conductivity electrolyte which is thermodynamically stable against lithium metal and high voltage cathodes would be used. It is not certain that such a material exists, but it is likely that some improvement over LiPON is achievable since there are huge compositional and structural fields which have not been explored. The recently reported LiRAP class of electrolyte materials is interesting for several reasons. First, several reports suggest that Li_3OCl and certain closely related compositions possess outstanding properties including very high Li^+ conductivities and wide electrochemical stability windows. Second, there is uncertainty over whether "true" Li_3OCl can be synthesized, either in crystalline or glass form. These materials are clearly under-researched and attempting synthesis using RF magnetron sputtering could be used to establish their fundamental characteristics. Thus, the second aim of this thesis was to determine the feasibility of Li_3OCl synthesis by RF magnetron sputtering, employing a more rigorous approach to moisture exclusion and phase identification than reported in previous studies.

2 Experimental Techniques

2.1 Introduction

This chapter provides an overview of the experimental techniques used in this work for sample fabrication and characterization. Certain experimental parameters were material-specific, thus detailed experimental conditions are provided in the Experimental Methods sections of Chapter 3 and Chapter 4.

2.2 Fabrication Techniques

2.2.1 RF Magnetron Sputter Deposition

RF (radio frequency) magnetron sputter deposition is a physical vapour deposition (PVD) process: a thin film is grown by the transfer of atoms from a target material to a substrate *via* a plasma. In contrast to DC (direct current) magnetron sputtering, RF magnetron sputtering can be used to sputter electrically insulative targets as well as metallic ones by virtue of capacitive coupling between the radio frequency electric field generator and the gas discharge[43,106]. Uncompacted ceramic powder and solid metal targets were used in this work along with a variety of substrate materials including glass, silicon and a nickel superalloy. The powder targets were used for the deposition of cathode and electrolyte films (Chapter 3 and Chapter 4, respectively), while solid metal targets were used for depositing electrical contacts for in-plane and through-plane impedance measurements (see Section 2.5.1) as well as very thin coatings on samples for SEM and PFIB characterization (see Section 2.3.2) to prevent charge build-up. Details on material-specific sputtering conditions are given in the experimental sections of the relevant chapters.

The key components of an RF magnetron sputtering system are shown in Figure 2.1. Before starting a deposition process the target is attached to a circular magnetron source. A metallic shield connected to the chamber but electrically isolated from the target is placed around it.

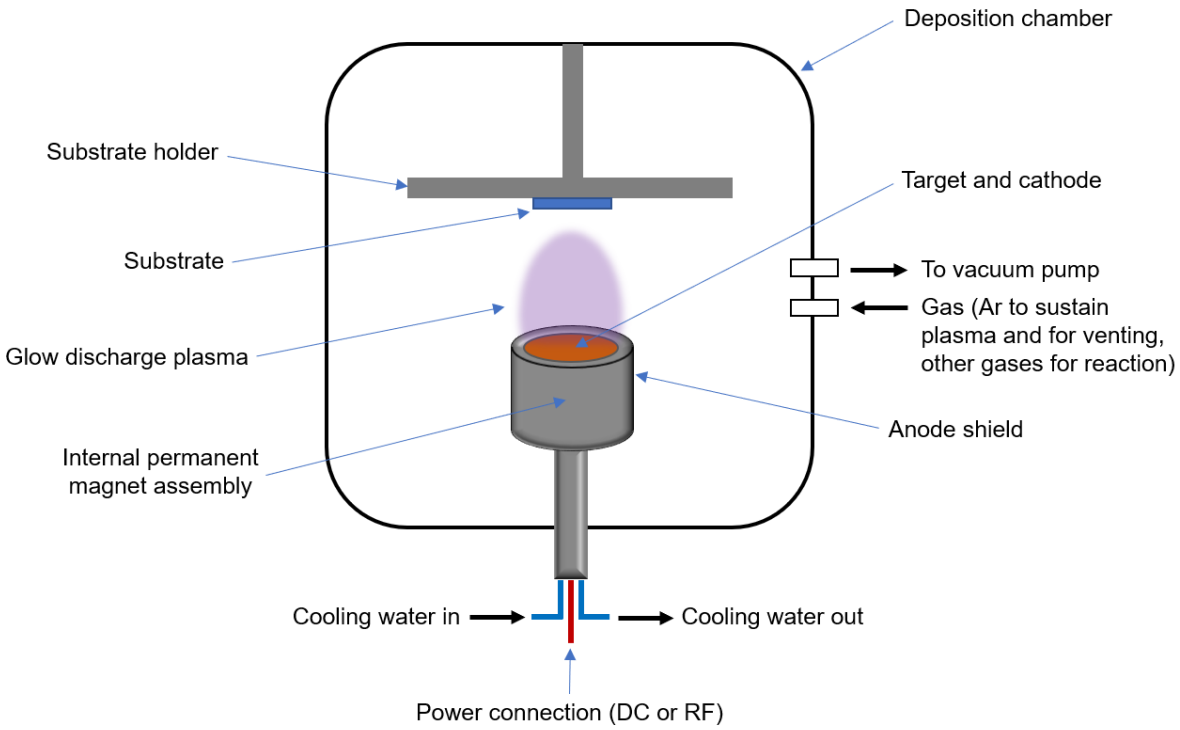


Figure 2.1 Schematic diagram of magnetron sputtering.

The substrates are attached to a holder positioned above the target at a separation of several centimetres (smaller separations increase the deposition rate but also have undesirable effects such as reduced film uniformity). Kapton or metal sheet masking may be applied to the substrates to confine film growth to particular areas. For example, masking was used in the deposition of the metal contacts used to measure the impedance of electrolyte films (Section 2.5.1). After loading the target and substrates, the deposition chamber is sealed and a roughing pump is used to achieve a medium vacuum (below 1 mbar). Activation of a turbomolecular pump brings the pressure below 10^{-6} mbar. The value of the chamber pressure immediately before introducing gas at the start of sputtering is known as the base pressure; the usual aim is to minimize this pressure in order to remove as much volatile contaminating material from the chamber as possible.

For plasma ignition, an easily ionized gas (argon in this work) is flowed into the chamber to achieve a relatively high pressure of $1\text{-}5\times10^{-2}$ mbar. Ionization begins when a radio

frequency (typically 13.56 MHz) alternating electric field is applied between the target and the chamber[106]. This creates a negative sheath potential on the target, as electrons arrive more quickly than positive ions in the fluctuating field[43]. Thus the target becomes the cathode of the system while the rest of the chamber becomes the anode and a plasma is formed. Ar^+ ions accelerate towards the cathode where they collide with atoms of the target material, a proportion of which are ionized and ejected into the plasma. Electrons are released in this process and are drawn to the shield surrounding the target, ionizing more argon atoms and releasing more electrons on the way, thereby sustaining the process. The magnetic field lines from the array of permanent magnets in the magnetron source arc across the target from the perimeter to the centre, trapping electrons and increasing the rate of sputtering. To transfer maximum power from the RF generator to the load (the gas discharge), the impedance of the load must be matched as closely as possible to that of the source. This is facilitated by a matching network consisting of two variable capacitors between the source and the load[153].

After ignition, the operator usually reduces the flow of argon gas to achieve a chamber pressure between 10^{-3} and 10^{-2} mbar. This decreases the frequency of collisions between the sputtered atoms and the process gas ions, increasing the mean free path and hence the deposition rate[106]. To maximize the deposition rate, the optimum balance between sputtering rate (increases as pressure increases) and mean free path of the sputtered atoms (decreases as pressure increases) must be achieved. However, the choice of process pressure and RF power also affects the crystallography and microstructure of the deposited films, which may be of greater concern than the deposition rate.

A shield or shutter is usually placed between the target and substrates during plasma ignition and for some amount of time after sputtering has commenced. This step of the process is known as ‘pre-deposition sputtering’ and its primary purpose is to clean contaminants from the target surface. Deposition commences after this shield is moved to expose the substrates

to the plasma. A thin film is built up on a substrate by the formation of nuclei of the depositing species, which grow and coalesce as more material arrives from the vapour phase[106]. Three basic growth modes are observed in thin-film deposition processes:

1. Island growth
2. Layer growth
3. Stranski-Krastanov (S-K) or layer-plus-island growth (a combination of the first two growth modes).

Island growth occurs if the clusters of atoms on the substrate grow in three dimensions to form islands, and is common for metallic films deposited on oxide substrates[106]. This growth mode is energetically favoured when the surface energy of the substrate is low relative to that of the depositing material and the island-substrate interfacial energy. In other words, the atoms in the islands are more strongly bound to each other than to the substrate. By contrast, the growth of clusters in layer growth is predominantly two dimensional, which results in the formation of sheets. Layer growth occurs when the film-substrate interfacial energy and the film surface energy are low relative to the substrate surface energy.

The S-K growth mode is commonly seen in metallic films deposited on metallic substrates and metallic films deposited on semiconductor substrates[106]. S-K growth commences in a similar manner to layer growth, but after several monolayers have formed there is a transition to island growth. Unlike layer growth, which is sustained by a monotonically decreasing binding energy, the formation of layers becomes energetically unfavourable as the film thickness increases. This is often due to a lattice mismatch between the growing film and the substrate, resulting in an increasing strain energy per unit area that becomes large relative to the film surface energy. Thus, nuclei tend to form after 5-6 monolayers have been deposited.

A diverse array of microstructures can develop in as-deposited films depending on the nature of the target and substrate materials and the set of conditions used for the deposition[106].

Nevertheless, polycrystalline thin films frequently form with a columnar microstructure, which has the appearance of an equiaxed grain structure at the film surface. Columnar growth is favoured by the low mobility of the species that adsorb on the substrate during deposition and by shadowing from previously deposited material. It can occur in both crystalline and amorphous deposits. Nevertheless, films can display a vast array of structures ranging from fully columnar to fully equiaxed and can be virtually featureless in the case of some amorphous films.

The substrate temperature (relative to the melting temperature of the deposited material) strongly influences the film microstructure[106]. At low substrate temperatures, the formation of nanocrystalline or amorphous films is promoted. While columnar structures are often observed at relatively low temperatures, recrystallization can occur at higher temperatures; this often results in the formation of equiaxed grain structures above a homologous temperature of ~0.5. A similar effect is seen when columnar films are heated in post-deposition annealing processes, although the application of substrate heating to encourage recrystallization may obviate the need for post-deposition annealing and simplify processing. This was tried for LCO films in Chapter 3.

Prior to the start of film deposition, the process gas composition may be changed by introducing flows of gases which react with the sputtered material and alter the film composition and structure. This is commonly termed 'reactive sputtering'[106]. For example, nitrogen or oxygen can be used to encourage the growth of nitride or oxide films. In the deposition of LiPON from an Li_3PO_4 target, the argon gas flow is often completely replaced by nitrogen to maximize the nitridation of the Li_3PO_4[110,154–157].

2.2.2 Post-Deposition Annealing

The usual purpose of post-deposition annealing is to increase the crystallinity of as-deposited ceramic films, which tend to have amorphous or nanocrystalline structures if the substrate is unheated during deposition owing to the rapid rate of cooling encountered by the adsorbed

atoms[106]. This was the purpose of the annealing in Chapter 3 and Chapter 4 of this work. Regardless of the furnace type and atmosphere, the basic principle is to heat the sample to the minimum temperature required to achieve a large volume fraction of the desired crystallographic phase within a practical timescale. Determination of the appropriate conditions usually involves trying several different annealing temperatures and durations until the desired crystallographic properties – as characterized by XRD – are achieved. This simple strategy is sometimes complicated by other processes which occur at elevated temperatures, or during transition between temperatures. For example, some substrate materials such as silicon and most metals and alloys oxidize at an appreciable rate above ~200 °C, which can lead to film cracking and delamination. Furthermore, the expansion coefficients of the film and substrate materials are often dissimilar, which can lead to the accumulation of stresses in the films during heating or cooling. Since most films subjected to annealing are brittle ceramics, stress is most often relieved by crack propagation. These problems are compounded for multilayer samples: not only are the optimum annealing conditions likely to be different for each layer, reaction between the layers as well as the undesirable substrate interactions detailed above can conspire to make the processing of these samples very difficult indeed.

Muffle furnaces were used for annealing thin film samples in this work. These furnaces operate rather like electric kilns and can reach temperatures over 1000 °C. They offer a controlled heating rate, but cooling is either slow (if the sample is left in the well-insulated furnace) or rapid (if the sample is removed from the furnace straight after annealing). The heating and cooling rates can affect the structural properties of a sample. In cases where the phase of interest is stable from the annealing temperature down to room temperature, the rates of heating and cooling are less of a concern and should be chosen to minimize the processing time while avoiding cracking due to thermal shock. Slow, uncontrolled cooling at the natural rate for the furnace is often used in these cases. If the desired phase is stable only at elevated temperatures it may be necessary to accelerate the cooling by removing the

sample from the furnace before the lower phase transition temperature is reached. Owing to the small volumes and high aspect ratios of thin films, the rate of cooling in air or inert gas is usually sufficient to achieve the kinetic stabilization of high-temperature phases at room temperature.

2.2.3 Fabrication of Airtight Cells for Galvanostatic Cycling and Impedance Measurements

2.2.3.1 Coin Cell Fabrication

Coin cells are used to encapsulate the key components of an electrochemical cell: cathode, electrolyte and anode. They were used in Chapter 3 to test the electrochemical performance of thin-film LCO cathodes in full cells with an organic liquid electrolyte and lithium metal anode. To construct a coin cell, the electrodes and electrolyte are placed into stainless steel coin cell cases along with several other mechanical components, as shown in Figure 2.2. The coin cell cases used in this work were of the 2032 type, meaning the outer diameter of the cell was 20 mm and its height when sealed was 3.2 mm.

The function of the spring and stainless steel spacer is to maintain internal pressure and good contact between all cell components once the cell has been sealed. A polymer gasket (not shown) is fitted to the coin cell lid before cell assembly to prevent contact between the two sides of the cell, which would create a short circuit and possibly destroy the cell. The assembly procedure is carried out within a glovebox to avoid air exposure and to create an inert environment within the coin cell.

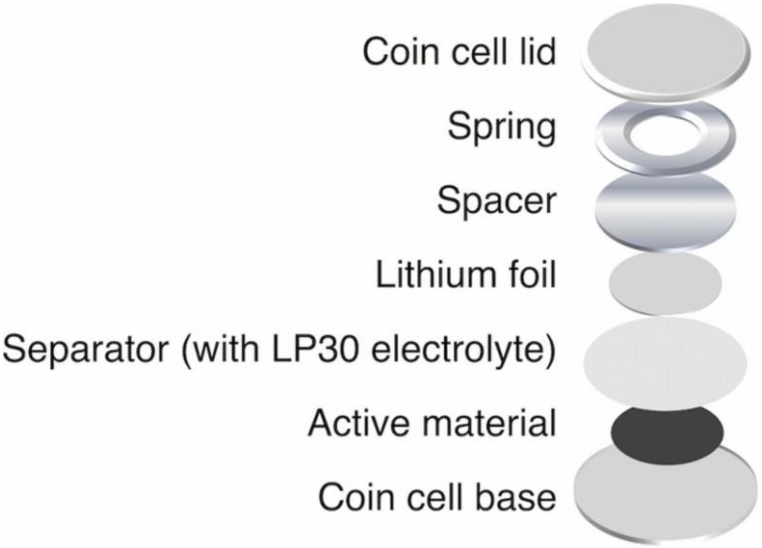


Figure 2.2 Diagram showing the components of a coin cell and the order in which they are stacked. Reproduced from Birkl *et al.*[158] under CC BY-NC-ND terms.

Once the components have been placed into position, the cell is pressed together and sealed using a coin cell press with a special die assembly that crimps the cell during pressing, creating a hermetic seal. The cell can then be removed from the glovebox and transported to the electrochemical testing station, being careful to avoid contact with conductors which could short the cell.

2.2.3.2 Pouch Cell Fabrication

Pouch cells offer far more freedom than coin cells regarding the component geometries and the way in which the electrodes are connected to the cell contacts. This is particularly important for solid-state cells, since solid electrolytes are fabricated in a wide variety of form factors. In Chapter 4, samples for through-plane impedance testing (see Section 2.5.1) were sealed in pouches to protect them from air exposure during testing outside of the glovebox. To assemble a pouch cell, the cell components are placed in a heat-sealable pouch made from sheets of laminated aluminium. Current collectors – usually copper or aluminium foils – are connected to the cell electrodes and folded over the outer edges of the pouch to provide external electrical contacts. Figure 2.3 shows the typical arrangement used in this work. Lengths of hot melt adhesive tape are then placed behind and in front of the copper strips at

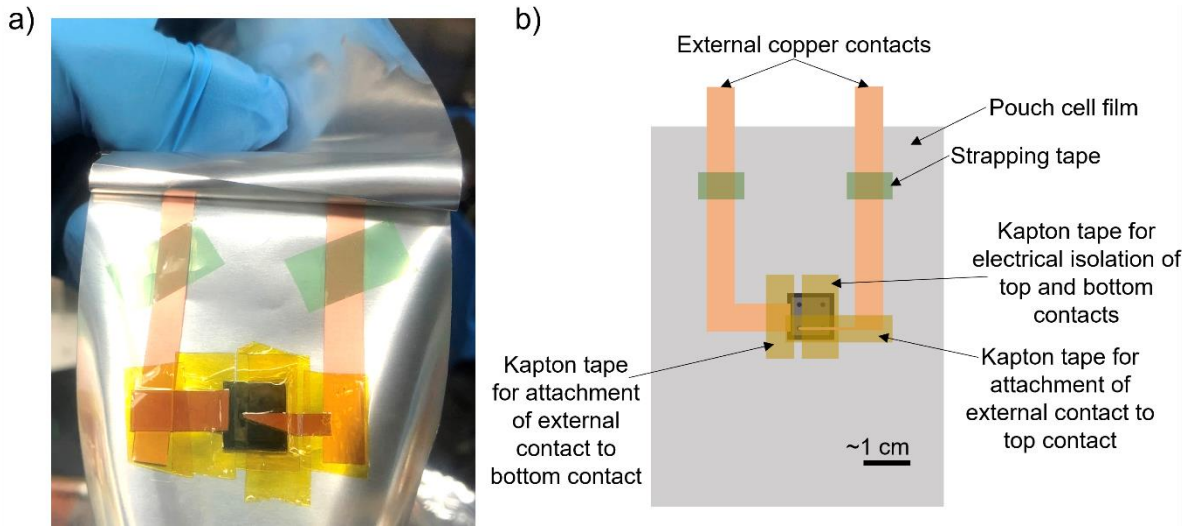


Figure 2.3 a) Photograph and b) schematic diagram (approximately to scale) of the typical arrangement of copper electrical contacts and sample (centre) within a heat sealable pouch used for through-plane impedance testing in Chapter 4. The sample shown here has impedance contacts with the “small circle” design (see Section 2.5.1).

the top of the pouch to ensure the creation of a complete seal during heat sealing. Finally, the sides of the pouch are sealed using a vacuum heat sealer located inside the glovebox.

2.3 Structural Characterization

2.3.1 X-Ray Diffraction

X-ray diffraction (XRD) is a powerful yet practically simple characterization technique for determining the crystallography of samples. The laboratory-based diffractometers used in this work contained a copper K alpha X-ray source with wavelength λ = 1.5406 Å. In almost all commercial diffractometers, the source, sample holder and X-ray detector are precisely positioned in a circular geometry with the source and detector on the circumference and the sample at the centre on the diffractometer axis. In this work, the correct sample alignment was achieved by levelling the sample surface with the top of the sample holder. To mount thin film samples, plasticine was placed beneath the substrate and a glass microscope slide was used to press the sample down, deforming the plasticine until the sample surface was level with the top of the holder.

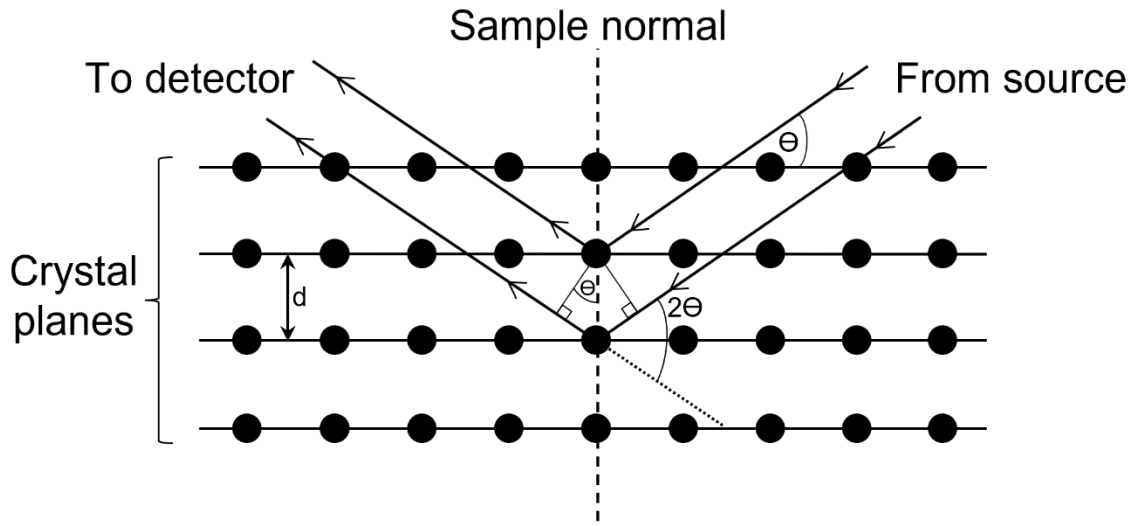


Figure 2.4 Schematic diagram of an X-ray diffraction experiment performed on a cubic monocrystalline sample. The angle Θ and interplanar spacing *d* related by Bragg's law are indicated. The angle between the incident and diffracted beams (2Θ) is used in plots of diffracted intensity against diffraction angle (diffraction patterns).

There are two common mechanisms used to change the angle between the X-ray beam and sample surface: "theta-two-theta" (Θ-2Θ) in which the X-ray source stays at a fixed position and the sample and detector are moved, and "theta-theta" (Θ-Θ) in which the sample stays at a fixed position and the source and detector move around the diffractometer circle. Diffractometers employing each of these mechanisms were used in this work. The diffracted intensity is plotted in real time as a function of the diffraction angle, 2Θ, by software running on a computer connected to the detector of the diffractometer.

For 2Θ values at which planes parallel to the sample surface satisfy Bragg's law (equation 2.1), constructive interference between parallel X-rays occurs and a peak appears in the diffraction pattern.

$$2d \sin\theta = n\lambda \qquad \textbf{Equation 2.1}$$

In words, constructive interference occurs for angles at which the difference in path length between X-rays scattered off parallel planes ($2d \sin\theta$, by inspection of Figure 2.4) is equal to a whole number of wavelengths, meaning that the waves are in phase.

The most basic information garnered from an X-ray diffraction pattern is whether a sample is crystalline (well-defined peaks are present) and if it is, what crystal systems the constituent phases belong to. Phase identification, peak indexing and lattice parameter determination are often performed in specialist software packages by comparing the experimental diffraction pattern to powder patterns of candidate phases generated from crystallographic information files (CIFs), particularly for complex crystal structures and multiphase materials. In this work, CrystalDiffract software (CrystalMaker Software Ltd) was used for this purpose with CIFs obtained from the Inorganic Crystal Structure Database (ICSD).

More complex structural information can be determined from other properties of the diffraction patterns such as the peak widths (crystallite size and strains) and peak heights (atomic positions). However, in samples with preferred crystallographic orientation – which includes most crystalline thin films – the peak height ratios differ from those of the powder pattern. Therefore, in this work, only phase identification and lattice parameter determination were performed. Further information on X-ray diffraction experiments can be found in standard textbooks[159].

2.3.2 Scanning Electron Microscopy and Focused Ion Beam Milling

While XRD experiments give information about a sample at the level of its atoms and grains, scanning electron microscopy (SEM) enables study of its microstructure and morphology. In this work, SEM was used to study the surface and cross-sectional morphology of sputter-deposited films and to measure film thickness and impedance contact dimensions (see Section 2.5.1). SEM offers several benefits over optical microscopy, including:

- Significantly higher resolution (smallest observable feature can be ~1 nm compared to ~200 nm for optical microscopy)[160,161]
- Higher depth of field, allowing clearer imaging of surface topography
- The ability to use a range of detectors to access different information about the sample, including chemical composition.

Although optical microscopy is a useful tool in certain applications, the requirement in this work to study the morphology, topography and chemical composition of thin films and their interfaces at the submicron scale necessitated the use of SEM.

In an SEM instrument, an electron beam is generated by a thermionic or field emission source. Only instruments with field emission sources were used in this work, since these sources are much brighter and give fewer distortions, leading to better image resolution. The electron beam is focused and scanned across the sample in a raster pattern using electromagnetic lenses and coils. The beam penetrates the sample and interacts with its atoms over a characteristic volume beneath the surface. This is known as the interaction volume and tends to have a teardrop shape in low average atomic mass samples – which includes most battery materials – owing to the reduced stopping power of lighter elements. The interaction volume is illustrated schematically in Figure 2.5[162–165].

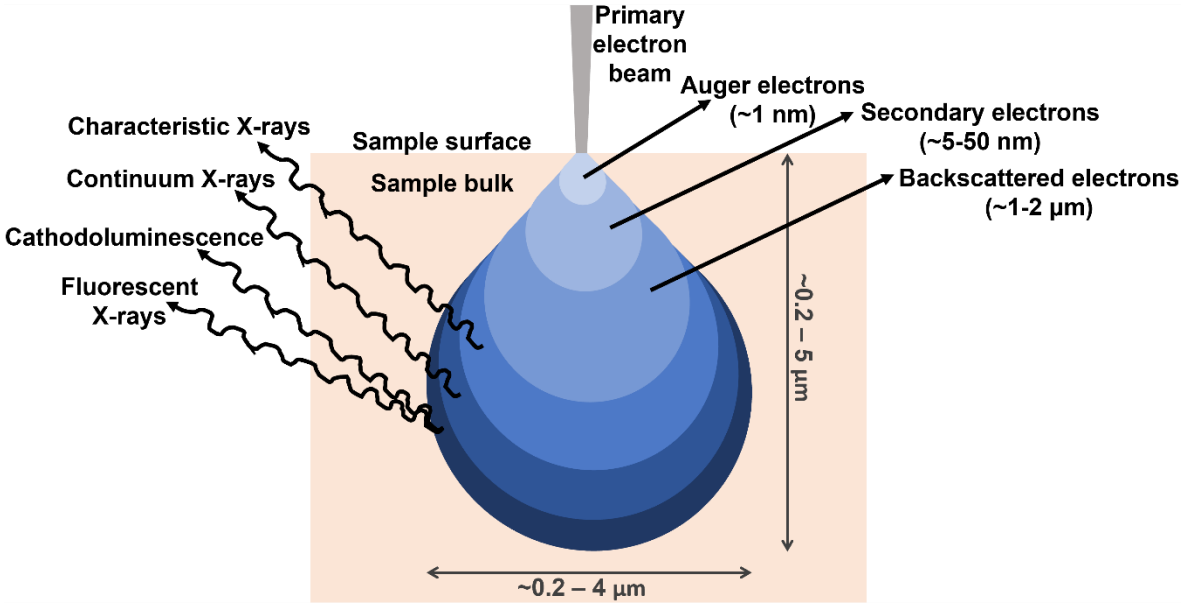


Figure 2.5 Schematic diagram of the interaction volume of the incident (primary) electron beam within a sample, showing the signals generated and the regions from which they arise. Approximate depths of origin for the electron signals are given in brackets. Drawn with reference to other diagrams[162–165].

Elastic and inelastic interactions between the electrons and sample atoms generate a variety of signals, as shown in Figure 2.5. A different detector is required for each signal type. The nature of these signals determines how strongly they are attenuated and thus the greatest depth from which they are detected. Secondary electrons are ejected in inelastic collisions between the incident beam and sample electrons. Only electrons near the surface can escape, so image contrast is determined primarily by the surface topography; tilted surfaces allow more secondary electrons to escape and appear bright, while surfaces at lower tilt angles appear darker. The backscattered electron signal is also commonly used for imaging; this signal arises from the elastic scattering of incident beam electrons, which exit the sample. Backscattered electrons travel from a much deeper sampling region, so provide little information about the sample surface. Instead, the intensity is modulated by factors that influence elastic scattering such as the average local atomic number (“Z contrast”) and crystallographic properties such as grain orientation. The choice of signal to measure is thus

determined by the property of interest. Since the primary use of SEM in this work was the characterization of film morphology, only the secondary electron signal was used for imaging.

Unlike the resolution of an optical microscope, which is limited by wavelength of visible light, the resolution of SEM is limited by the size of the interaction volume. Since secondary electrons originate from a small sampling volume near the sample surface, the resolution obtained is higher than that from backscattered electrons. Nevertheless, the resolution attained with both signals can be improved by reducing the size of the interaction volume. For a given specimen, this can be achieved by lowering the probe current, which decreases the probe diameter. Reducing the probe current also decreases the signal-to-noise ratio, which can affect image clarity as well as the intensity of the X-ray signal used for energy dispersive X-ray spectroscopy (EDX). Nevertheless, a low probe current and accelerating voltage are generally necessary for battery materials (electrode and solid electrolyte) for two key reasons:

1) These materials contain light elements and are thus susceptible to beam damage
2) Most of these materials – particularly solid electrolytes – are poor electronic conductors and are thus susceptible to charging in the electron beam, which causes image distortion.

Therefore, an accelerating voltage of 3-10 kV and a probe current of 0.1-1 nA were used in this work, with the precise values chosen based on the observed charging and degradation characteristics of the sample under investigation. Further precautions were taken to reduce sample charging by maximizing the conduction of electrons to ground. Owing to the air sensitivity of the samples studied in this investigation, most samples were mounted on holders within a glovebox using adhesive copper tape. Furthermore, the use of standard SEM gold and platinum coaters to deposit thin (~10 nm) conducting layers on the samples was only appropriate for less air-sensitive samples; the most air-sensitive samples were coated using an RF magnetron sputtering system housed in a glovebox (see Section 4.2.2).

While the imaging of sample surfaces was straightforward, cross-sectional imaging posed challenges. Many of the films in this work were deposited on ceramic or glass substrates, which could be fractured neatly by scoring the reverse side with a diamond scribe and snapping into two pieces. However, films on metallic substrates had to be cut using a guillotine, and the resulting plastic deformation of the substrates made it difficult to avoid damage to the films. The fractured or cut samples were mounted in notched pin stubs or on regular holders using metal clips prior to metal coating (where required to avoid charging) and imaging.

For certain aspects of the characterization, very clean cross-sections with minimal damage were required. A Plasma Focused Ion Beam (PFIB) instrument was used to produce cross-sections in these cases. The PFIB instrument used in this work contained both an SEM column with a field emission source and a focused ion column with a xenon ion (Xe^+) source in the same chamber. For each sample requiring sectioning, a platinum strap layer was deposited within the instrument at the site selected for cross-sectioning to protect the underlying film. A trench from the top surface to the substrate was then milled parallel to the strap using the ion beam, exposing the cross-section of the film which was imaged using the SEM column and secondary electron detector. Since the FIB column was at a 52° angle to the SEM column, samples had to be tilted to this angle for milling and imaging of the cross-section. The instrument software could be used to correct the images so that they appeared to have been taken with the electron beam perpendicular to the plane of the cross-section. This was particularly important when measuring the film thickness from micrographs.

2.4 Chemical Characterization

2.4.1 Energy Dispersive X-Ray Spectroscopy

Energy dispersive X-ray spectroscopy (EDX) is a chemical analysis technique performed in an SEM with an X-ray detector fitted. The technique can be used to determine the elements present in the region imaged by the SEM, making use of the characteristic X-rays emitted

from atoms within the interaction volume (Figure 2.5). These X-rays are generated when electrons from the incident beam eject electrons from the inner shells of sample atoms; the subsequent replacement of these electrons by outer shell electrons releases energy in the form of X-rays, which are classified according to the corresponding energy transition, as shown in Figure 2.6 a)[166]. For example, if an electron from the K shell is ejected and replaced by an electron from the L shell, the resulting X-ray is referred to as K_α; if it is replaced by an M shell electron it is referred to as K_β. The K_α, K_β etc. energies are different for each element, allowing the elements present to be determined by comparing the spectral peak positions (Figure 2.6 b)) with the known energy values for all elements in the periodic table.

EDX is most often used for qualitative and semi-quantitative analysis; for example, the construction of intensity plots showing the variation in elemental concentrations over an area imaged by the SEM or a line which crosses interfaces or microstructural features. Quantification can also be performed, with elemental concentrations reported in atomic or weight percent; however, the accuracy of these measurements is affected by a number of instrumental and sample-related factors. Battery materials present a particular challenge in this regard since they often contain light elements which produce low intensity, low energy X-ray signals. Lithium, for example, cannot in general be detected using this technique, since its characteristic X-rays are mostly absorbed by components such as the window before they reach the detector. Even the detection of heavier elements can be compromised by the low accelerating voltages typically used to study battery materials (a minimum accelerating voltage of 5 kV was used for the EDX performed in this work), as some higher energy transitions will not be excited.

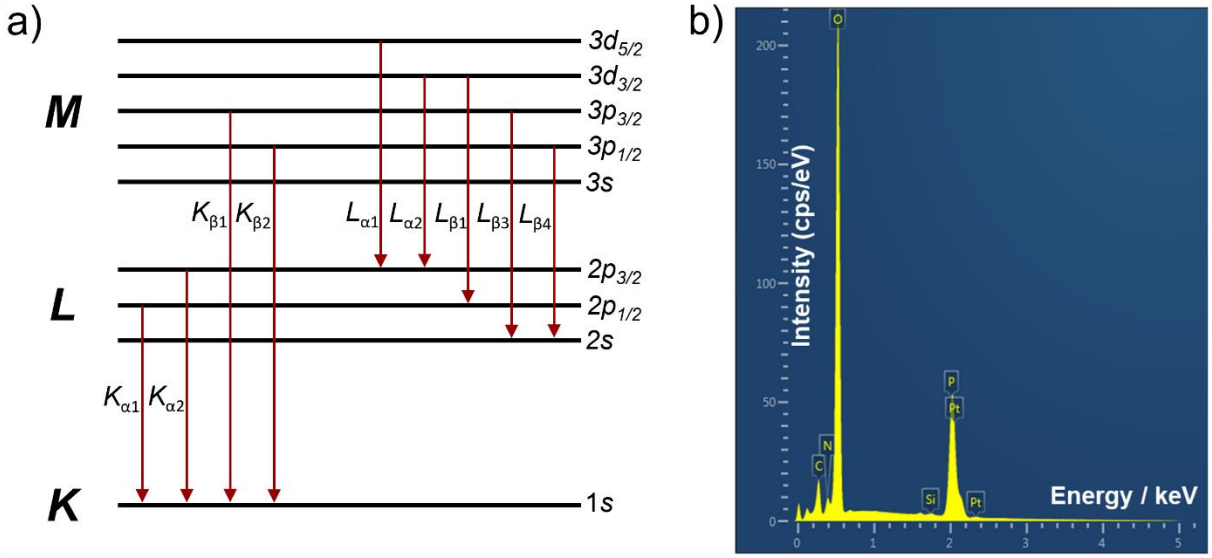


Figure 2.6 a) Schematic energy level diagram (drawn with reference to another diagram[166]) of an atom in a sample under examination by SEM, illustrating possible electron energy transitions (red arrows) which give rise to the emission of characteristic X-rays after core shell (*K* and *L*) ionization by primary electrons; b) example of an EDX spectrum (from a LiPON film sample on a glass substrate).

One challenge particular to the characterization of thin films had to be addressed in this work. This was the fact that, in general, the interaction volume of the incident electron beam was somewhat deeper than the film thickness, so a significant contribution from the substrate was seen in EDX spectra. If the substrate contains elements which are also present in the film, such as oxygen, this precludes quantification of the film composition and can make interpretation of elemental surface mapping difficult. The challenge was surmounted to a large extent by performing measurements on cross-sectional surfaces where possible, since in this geometry the film material extends to a much greater depth below the surface – certainly deeper than the interaction volume. Uncertainties due to the lateral spread of the interaction volume into neighbouring layers still exist in this geometry – particularly for the thinnest films – but these were expected to be somewhat lower than the uncertainties in the original measurement geometry because of the ‘teardrop’ shape of the interaction volume.

2.4.2 X-Ray Photoelectron Spectroscopy

X-ray photoelectron spectroscopy (XPS) is a highly surface-sensitive technique performed under ultra-high vacuum (UHV) in a dedicated instrument, and was performed in this work with a monochromatic Al K-alpha source (1486.6 eV) and energy analyser[167]. It is used to analyse the chemical compositions of surfaces and interfaces, although the attachment of an Ar-ion gun, as was present on the system used in this work[168], allows compositional depth profiling by progressive etching of the surface and reanalysis. The energy resolution of the technique is very high, and unlike EDX, lithium and all heavier elements can be detected down to a level of about 0.1 at%[167]. However, a limitation is the relatively poor lateral resolution (on the order of 10 μm[169]), which is a consequence of the difficulty in focusing X-rays[170]. Therefore, unlike EDX, XPS cannot be used to produce high resolution compositional maps.

In an XPS instrument, an X-ray beam is directed at the region of interest on the sample. The X-ray photons transfer their energy to the electrons of the sample atoms, ejecting them from the sample as photoelectrons with kinetic energies, E_k, given by equation 2.2, where $h\nu$ is the energy of the X-ray photons, E_b is the binding energy of the photoelectron and ϕ is the work function of the spectrometer[171]. The surface sensitivity of the technique is due to the fact that photoelectrons can only escape from a shallow depth (~10 nm) without being absorbed[167]. When they reach the detector, the numbers of photoelectrons with each possible kinetic energy are counted by the energy analyser. Since the X-ray energy is fixed and the work function of the spectrometer is known, it is straightforward to plot a spectrum of intensity (in counts or counts per second) against the photoelectron binding energy, as shown in Figure 2.7.

$$E_k = h\nu - E_b - \phi \qquad \textbf{Equation 2.2}$$

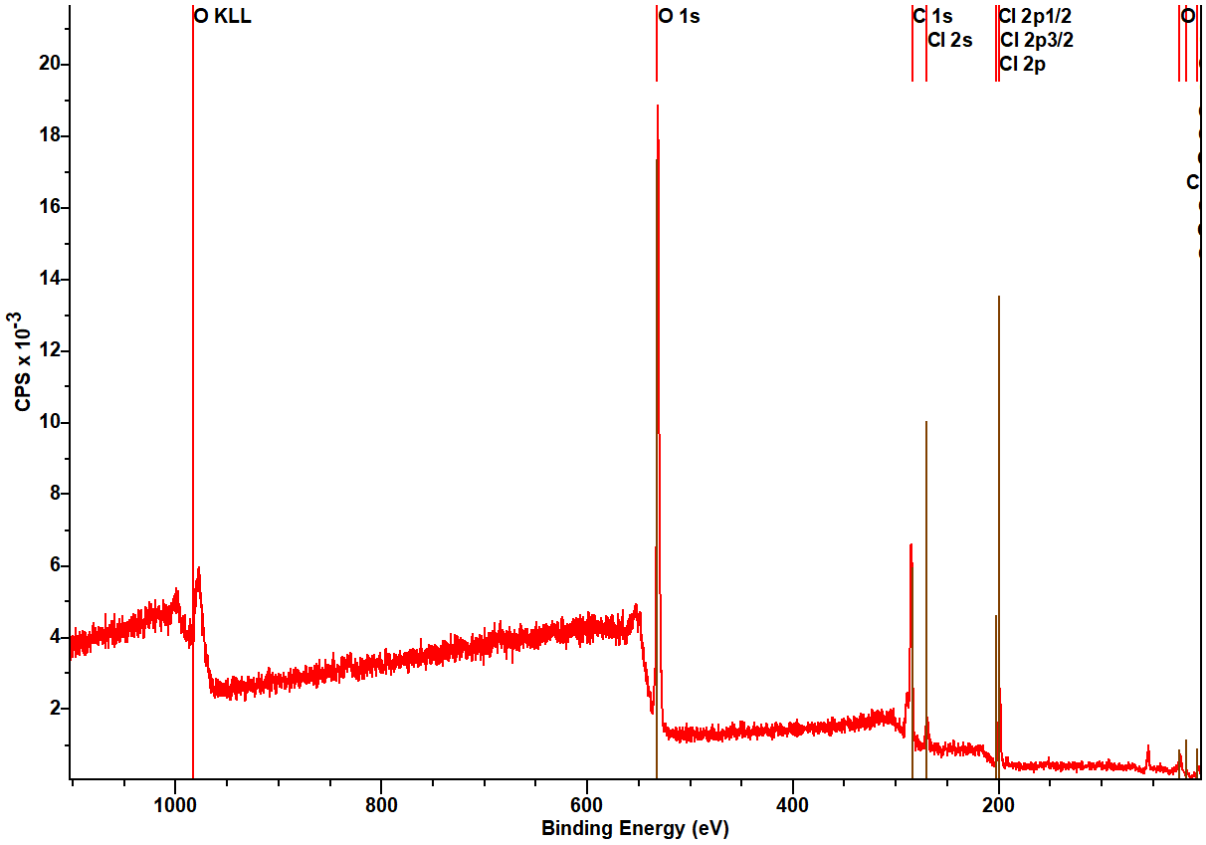


Figure 2.7 Example of an XPS spectrum (from a film sputter deposited from a 1:1 molar ratio Li_2O + LiCl target onto a nickel-coated glass substrate). Markers corresponding to some of the expected elemental peak positions are shown. The XPS data collection used to create this figure was performed by Dr Sudarshan Narayanan.

Each element has characteristic photoelectron binding energies which are modulated by the local chemical environment. Thus it is possible to determine both the chemical composition of the surface region and some details of the local bonding from an XPS spectrum. The intensities of the peaks can be converted into elemental concentrations without the need for standards, making XPS a useful tool for quantifying the chemical composition of near-surface regions[167]. The technique is well-suited to thin film analysis, since it is possible, with Ar-ion etching, to approach the central region of the film and determine a composition that is close to the overall composition. In this work, the principal motivation for performing XPS characterization was to verify the presence of lithium and investigate its local bonding environment in the electrolyte films fabricated in Chapter 4.

2.4.3 Fourier Transform Infrared Spectroscopy

Fourier transform infrared spectroscopy (FT-IR) measures the interaction of light with the bonds in a sample[172]. In an FT-IR spectrometer, mid infrared light is passed through a sample. An interferometer is used to change the combinations of wavelengths present in the incident light by scanning the position of one of the mirrors in the beamsplitter[173]. This results in the destructive interference of a different wavelength at each mirror position. Some frequencies of the light are absorbed by the material; these frequencies correspond to energies at which vibrations are excited in the bonds of the sample[174–176]. The transmitted light is measured by a detector and recorded as an interferogram showing the total energy of light at every position of the beamsplitter mirror[173]. A Fourier transform is used to convert the data into a spectrum showing the fraction of the original light intensity detected (transmittance) as a function of absolute wavenumber[174]. Alternatively, absorbance by the sample can be plotted, as shown in Figure 2.8 b). In both cases, the absorbed frequencies appear as peaks in the spectrum, providing a “fingerprint” that can be compared to known spectra for material identification[175,176]. Furthermore, the functional groups present in the sample can be determined directly, since each has unique vibrations which manifest as characteristic peaks in the IR spectrum[175]. The simultaneous measurement of all wavelengths greatly reduces the time taken to analyse a sample, which is an advantage of FT-IR over other types of IR spectroscopy[173].

FT-IR was used in this work to detect the presence of O-H bonding in the electrolyte films fabricated in Chapter 4. The spectrometer was configured for attenuated total reflection (ATR) measurements, which is the most common setup for FT-IR experiments[175,176]. In this setup, the sample to be analysed is pressed against a crystal (diamond was used in this work). The IR beam is then directed at the bottom surface of the crystal where it enters, undergoes a total internal reflection off the top surface (in contact with the sample) and travels to the detector. An evanescent wave forms on the sample side of the boundary and different amounts of energy from this wave are absorbed depending on the mix of

frequencies in the incident IR beam. This results in attenuation of the reflected beam detected by the spectrometer, as described previously. An illustration of this setup is shown in Figure 2.8 a)[173,177]. The penetration depth of the IR beam in the sample depends on the wavenumber, angle of incidence and difference in refractive index between the sample and the film, but is typically 0.1-5 μm[178]. Therefore, for thin film samples on the order of ~1 μm in thickness, the measured spectrum is likely to be representative of the sample bulk but may also contain contributions from the substrate. ATR was determined to be more appropriate than a transmission geometry for the measurements performed in this work, since the contributions from the substrate would likely have been higher in a transmission setup.

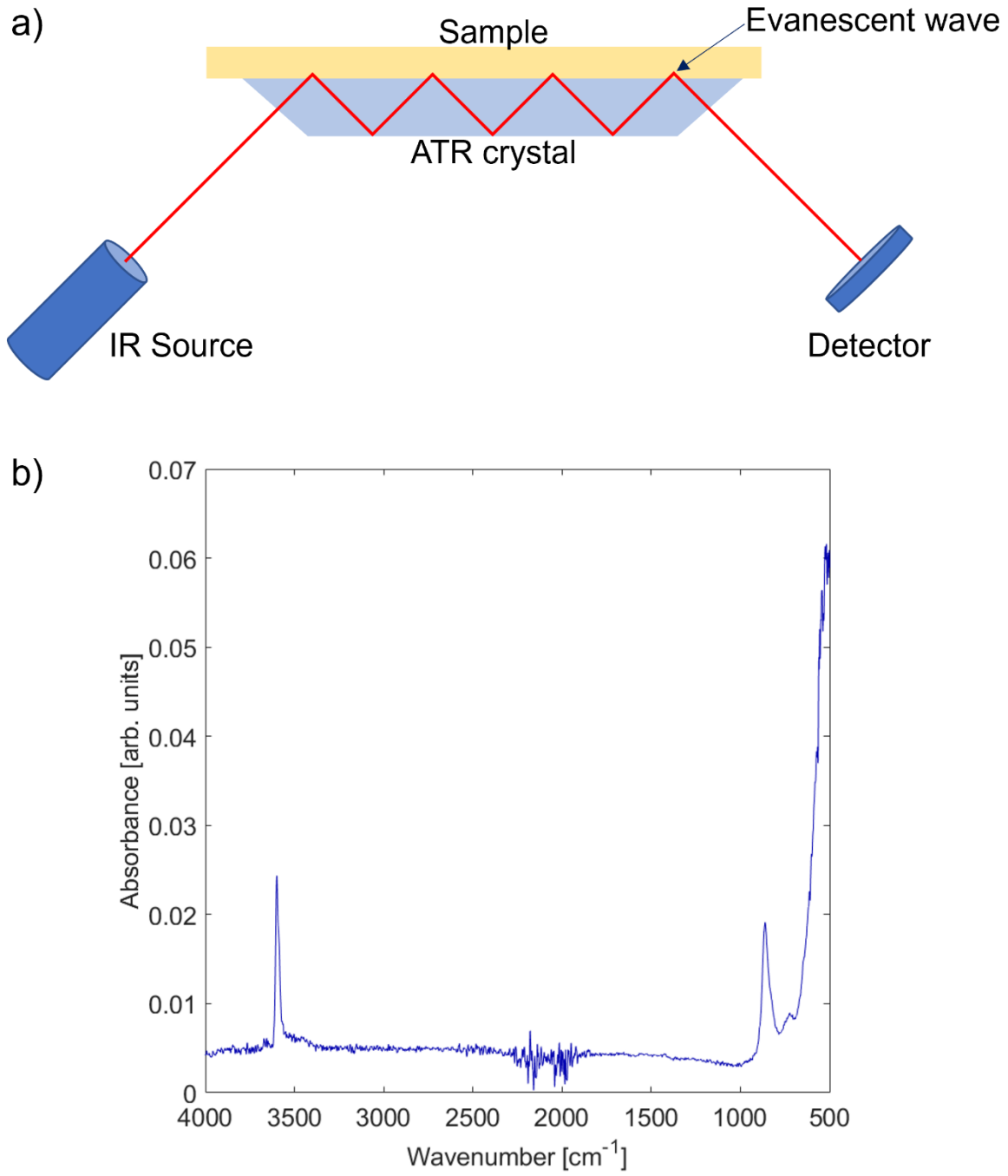


Figure 2.8 a) Schematic diagram (drawn with reference to other diagrams[173,177]) showing the attenuated total reflection (ATR) measurement technique commonly used in FT-IR experiments; b) example of an FT-IR spectrum (from a sample of Li_2OHCl powder) collected by Dr Hyeon Jeong Lee. The IR beam undergoes total internal reflection in the ATR crystal (e.g. diamond). An evanescent wave forms on the sample side of the boundary with the ATR crystal; absorption of energy from this wave by the sample attenuates the reflected beam and enables collection of an FT-IR spectrum[173].

2.4.4 Inductively Coupled Plasma Optical Emission Spectroscopy

Inductively coupled plasma optical emission spectroscopy (ICP-OES) is used for very accurate determination of the concentrations of elements present in an analyte solution. It was used in Chapter 3 to determine the Li/Co atomic ratio in thin-film LCO cathodes. Solid samples must be digested completely to form a solution; aqua regia was used as the digestant in this work. Subsequent dilution with 2% nitric acid (HNO_3) solution was used to increase the stability of the analyte. To perform the analysis, the analyte solution is fed into the instrument via plastic tubing and peristaltic pumps. It passes through a nebulizer to produce an aerosol, which is directed into an inductively coupled argon plasma[179]. The plasma is at a temperature of ~10,000 K, and the thermal energy is sufficient to atomize and ionize the atoms of the solution[180]. Electrons are moved to higher energy levels; on falling to their ground states, they emit photons at discrete energies[179]. The combination of photon wavelengths emitted is different for each element, so the operator chooses appropriate wavelengths for intensity measurement by the spectrometer according to the elements of interest.

To determine the elemental concentrations in the analyte solution, it is necessary to prepare a series of calibration solutions containing the elements of interest. Each solution must have a different concentration, and the range of concentrations should be chosen such that it covers the concentrations expected for the elements of interest in the analyte solution. Commercial multielement solutions are available specifically for this purpose and can be diluted to the required concentrations using an appropriate solvent such as 2% HNO_3. These solutions are then analysed sequentially, and plots of intensity against known concentration (calibration curves) are constructed for each wavelength of interest. The concentrations corresponding to the intensities measured from the analyte solutions are then read off these curves, enabling the concentrations of the elements in the analyte solution to be determined.

2.5 Electrochemical Characterization

2.5.1 Electrochemical Impedance Spectroscopy

Electrochemical impedance spectroscopy (EIS) is commonly used for determining the impedance, and hence ionic conductivity, of solid electrolytes. In this work, the impedances of thin-film solid electrolytes fabricated in Chapter 4 were measured in the through-plane configurations shown in Figure 2.9 a). “Blocking” electrical contacts of nickel or platinum were deposited using RF magnetron sputtering; in this context, “blocking” means that the contacts conduct electrons but not lithium ions. The two electrical contact designs are referred to as “overlapping strip” and “small circle” owing to their appearances. The “overlapping strip” design, which features mutually perpendicular top and bottom contact strips, was influenced by the work of Yu *et al.*[85]. Kapton shadow masks – shown in Figure 2.9 b) – were used to achieve the required electrical contact shapes. Similar stainless steel masks were also used for certain samples, as explained in Section 4.2.5. Samples with both electrical contact designs were produced by first depositing the bottom contact (this covered the entire substrate surface in the case of the “small circle” design), then the electrolyte layer, and finally the top contact layer. Kapton tape or hole-punched aluminium foil was used to mask a border around the sample surface prior to electrolyte film deposition so that the bottom contact would remain accessible.

The theory underpinning the EIS technique is the same for both the “overlapping strip” and “small circle” electrical contact designs and impedance measurements were performed in the same way. The only difference was the overlap area between the top and bottom contacts, calculation of which was required to determine the ionic conductivity from the measured impedance value. Both contact designs were intended to make the overlap area between top and bottom contacts (the current path area) as small as practically possible to minimize the probability of encountering a pinhole and creating a short circuit.

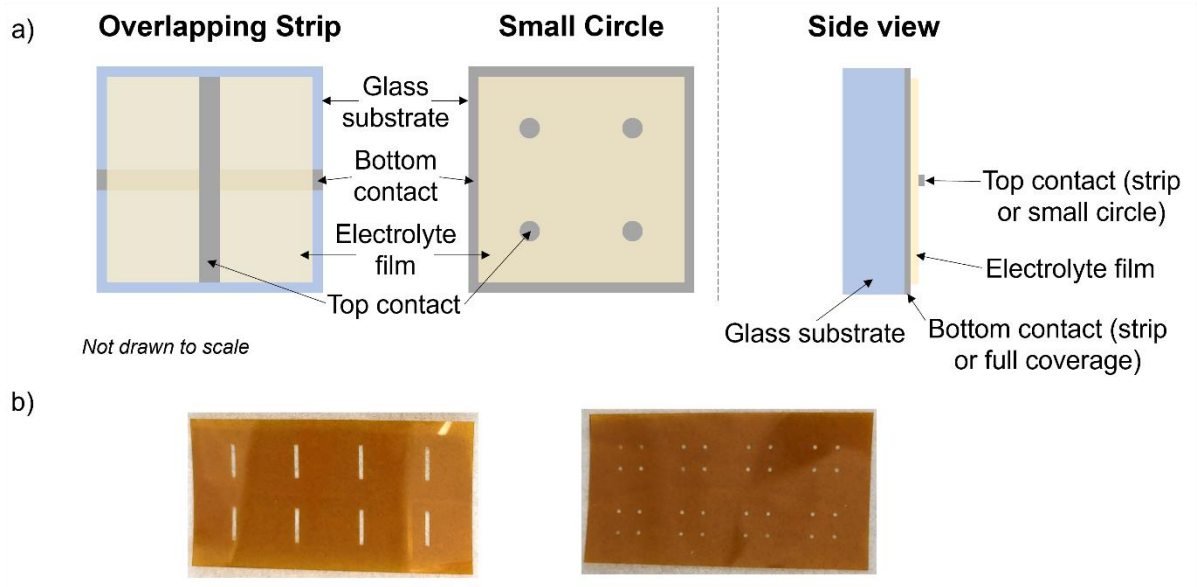


Figure 2.9 a) Plan and side view schematic diagrams of the two electrical contact designs used for measuring the through-plane impedance of thin-film electrolytes in Chapter 4; b) the Kapton shadow masks used to form the contact shapes during sputter deposition.

The basis of EIS is to view the physical system in terms of analogous AC (alternating current) circuit components, principally resistors and capacitors. When a voltage, *E*, alternating as a function of time, *t*, (equation 2.3) is applied to the system, an alternating current, *I*, response (equation 2.4) will be generated at the same frequency but a different phase[181]. For a low amplitude applied voltage, it is assumed that the behaviour of the system is linear, and thus the impedance, *Z*, is given by an expression analogous to Ohm's law for resistance in DC circuits (equation 2.5).

$$E(t) = E_0 \exp(j\omega t) \qquad \textbf{Equation 2.3}$$

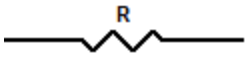
$$I(t) = I_0 \exp(j[\omega t - \varphi]) \qquad \textbf{Equation 2.4}$$

$$Z(\omega) = \frac{E(t)}{I(t)} = Z_0 \exp(j\varphi) = Z_0(\cos\varphi + j\sin\varphi) \qquad \textbf{Equation 2.5}$$

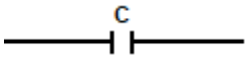
E_0, I_0 and Z_0 are the amplitudes of the voltage, current and impedance, respectively, *j* is the imaginary number $\sqrt{-1}$, ω is the angular frequency and φ is the phase shift. Owing to the

phase difference between input and output signals, it is convenient to write the expressions for voltage, current and impedance in complex form. The impedance can then be plotted in the complex plane. Conventionally, -Im(Z) is plotted against Re(Z), and the diagram is referred to as a Nyquist plot. The impedance at a given input frequency is plotted as a single point on this plot. It is the change in the impedance of the system with frequency that enables the properties of its elements to be determined, since different types of element have different frequency responses. Thus, EIS involves applying a sinusoidal voltage at a fixed amplitude using a potentiostat, sweeping from high to low frequency, measuring the current response and plotting the real and imaginary components of the impedance on a Nyquist plot.

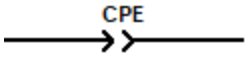
The relationships between the impedances of the fundamental equivalent circuit components – the resistor (R) and capacitor (C) – and angular frequency (ω) are given by equation 2.6 and equation 2.7, respectively[5,181]. Equation 2.8 provides the impedance of a constant phase element (CPE), which is used to model the non-ideal (leaky) nature of capacitive elements often seen in real systems.



$$Z_R = R = \frac{V_0}{I_0}$$ **Equation 2.6**



$$Z_C = \frac{-j}{\omega C}$$ **Equation 2.7**



$$Z_{CPE} = \frac{1}{T(j\omega)^P}$$ **Equation 2.8**

The impedance of a resistor does not depend on frequency and is thus equal to its DC resistance, R. Applying a sinusoidal potential to a capacitor (with capacitance, C) gives an output signal with a 90° phase shift, so the impedance is purely imaginary and thus multiplied

by *j*. The expression for the impedance of a CPE is analogous to that of a capacitor; however, two parameters – T and P – are used to describe the non-ideal capacitive behaviour of the CPE. For both capacitors and CPEs, the impedance decreases with increasing angular frequency.

An electrochemical system can be modelled using a combination of series and parallel configurations of the above fundamental AC circuit components. The equivalent circuit should closely mirror the physical setup; however, differences between the simulated and measured Nyquist plots often reveal non-ideal behaviour which requires modelling with alternative components. For example, constant phase elements are frequently used in place of capacitors. Further information on non-ideal behaviour is provided in Chapter 4. In this work, ZView software (Scribner Associates Inc.) was used for plotting the measured impedance data and for constructing and simulating equivalent circuit models.

Assuming that the electrolyte has a uniform ionic resistance and that all elements in the physical system display ideal behaviour, the measurement configurations shown schematically in Figure 2.9 a) can be modelled by the equivalent circuit in Figure 2.10[5]. In this circuit the resistor, R_i, represents the ionic resistance of the solid electrolyte, while C_{int} represents the capacitive nature of the two electrolyte-electrode interfaces. The capacitive behaviour arises from the fact that the electrolyte is a pure ionic conductor while the electrodes are pure electronic conductors, meaning that charges accumulate either side of each interface. The geometric capacitance, C_{geom}, is in parallel with the series combination of the ionic resistance and interfacial capacitance since the setup as a whole is rather like a parallel plate capacitor with the solid electrolyte as the dielectric medium. The result of simulating the impedance of this circuit over a wide frequency range is shown in the Nyquist plot in Figure 2.11.



Figure 2.10 Equivalent circuit model (the Debye equivalent circuit) used to represent the physical arrangements in Figure 2.9 a) when the sample behaviour is ideal.

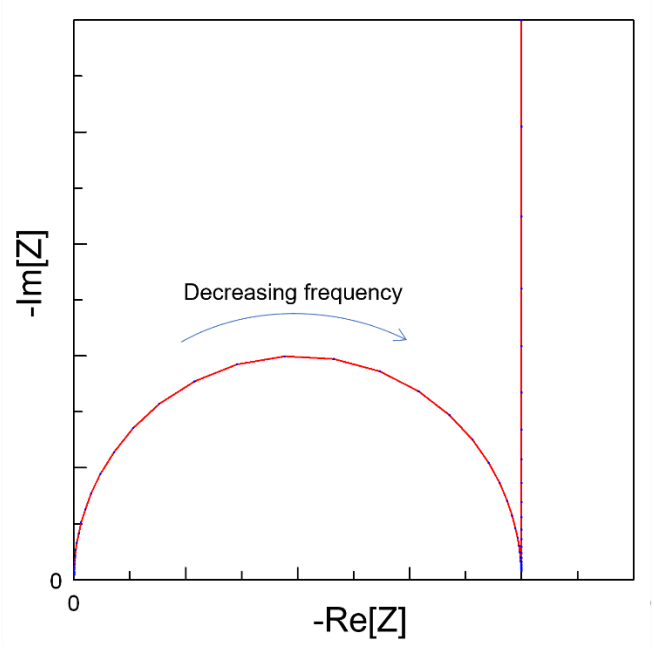


Figure 2.11 Nyquist plot showing the result of simulating the impedance of the circuit in Figure 2.10 over a wide frequency range.

This Nyquist plot shows a semicircle over the high to medium frequency range followed by a vertical tail at low frequencies. Its appearance can be understood as follows. At the very highest frequency both capacitors in the equivalent circuit have negligible impedances, so the geometric capacitor shorts the configuration giving a total impedance of approximately zero. As the frequency decreases the impedance of the geometric capacitor increases, but that of the interfacial capacitor remains negligible since the interfacial capacitance is usually much larger than the geometric capacitance (equation 2.7). The imaginary component of the impedance reaches a maximum when the impedance of the geometric capacitance and resistor are equal; it decreases again as the frequency continues to decrease, since most of

the current then flows through the branch of the circuit containing the resistor. Eventually the geometric capacitor becomes insulating and the second intersection of the semicircle with the real axis gives the value of the ionic resistance. The impedance of the interfacial capacitor is still negligible at this point, but as the frequency continues to decrease the impedance of this capacitor rises, tracing the tail shown on Figure 2.11. By changing the values of capacitance and resistance used in the simulation, the simulated plot can be fitted to the experimental one, although alternative components representing non-ideal behaviour may be required as mentioned previously. Furthermore, in some cases an additional semicircle may be present next to the first at a lower frequency. This semicircle typically corresponds to the properties of internal interfaces – which often have higher ionic resistances – such as grain boundaries. It is modelled in the equivalent circuit by adding an additional resistor-capacitor parallel unit in series with the bulk ionic resistance, R_i. Thus, the overall ionic resistance of the electrolyte is the sum of the bulk and interfacial resistances. Occasionally the highest frequency semicircle can be offset slightly from the origin along the real axis. This is due to a small electronic resistance arising from the electrical contacts or instrument cabling and can be accounted for by adding a resistor in series with the Debye equivalent circuit in Figure 2.10.

Once known, the ionic resistance of the electrolyte can be converted into an ionic conductivity, σ_i, value using equation 2.9.

$$\sigma_i = \frac{L}{RA} \qquad \textbf{Equation 2.9}$$

In this equation, L is the separation of the two electrodes, R is the ionic resistance of the electrolyte and A is the area of the current path (the area of overlap between the top and bottom contacts). The other quantity frequently calculated is the activation energy for ionic conduction; this is determined by performing impedance measurements at a series of temperatures, plotting $\ln(\sigma_i)$ against 1/T (an Arrhenius plot) and fitting a straight line to the data. The activation energy is determined from the gradient of the line.

2.5.2 Cyclic Voltammetry

In lithium battery research, cyclic voltammetry (CV) is often used to study electrochemical reactions as a function of cell voltage and time. In Chapter 3, CV was used to study the redox behaviour of the Waspaloy substrates used for thin-film LCO cathodes. To perform CV, the electrochemical cell under investigation is connected to a potentiostat programmed to increase the potential in small steps up to a pre-defined limit, then decrease it back to the lower limit using the same step size[182]. The current is measured and plotted as a function of potential (typically with respect to Li^+/Li) on a cyclic voltammogram. Several such cycles – or scans – may be performed in an experiment. The magnitude of the current reflects the rate at which electrochemical reactions are occurring within the cell; the current changes with applied potential and cycle number, revealing the potential and time dependencies of the processes. The rate at which the potential is scanned also influences the current values measured. In general, a low scan rate is required to ensure that processes with slow reaction kinetics are captured.

2.5.3 Galvanostatic Cycling

Galvanostatic cycling is a very common charge-discharge cycling technique performed on full lithium-ion and lithium-metal cells[183]. Special computer-controlled battery cycling systems are used for precise application of small constant currents and measurement of the voltage response (potential of the cathode with respect to Li^+/Li) over time. To set up the cycling experiment, the operator writes a simple program specifying the values of the key experimental parameters. These include the applied current, upper and lower voltage limits and number of cycles. The applied current is often calibrated using the predicted capacity of the cell (calculated using the cathode mass and theoretical specific capacity) and can be expressed in the form of the 'C-rate'. The C-rate is the reciprocal of the time in hours that should be required for one complete charge or discharge of the cell at the chosen current. The current – and hence C-rate – can be changed periodically during cycling to study the effect of the cycling rate on the cell performance. The upper and lower voltage limits are

typically chosen based on prior knowledge of the charging characteristics of the cathode material. They specify the cell voltages at which the polarity of the applied current is reversed to switch from charging to discharging and *vice versa*. Finally, the number of cycles is chosen according to whether the short-term or long-term cycling behaviour is of interest. If the capacity of the cell deteriorates rapidly during cycling, or the cell fails catastrophically, it may be necessary to terminate the experiment before the specified number of cycles is reached.

There are several ways in which the data collected in cycling experiments can be presented. Plots of voltage against time or specific capacity are common. These plots reveal the charge-discharge characteristics of the cell, for example the presence of plateaus at certain potentials, and allow the polarization of the electrode potentials due to degradation during cycling to be studied. The specific capacity at any point during cycling is defined as the amount of charge stored in the cell (the applied current multiplied by the time into the half cycle) divided by the mass of the cathode (or the entire cell in some cases)[5]. Another common representation of the cycling data is a plot of specific capacity for charge and discharge half cycles against cycle number. These plots allow the decline of the cell capacity over cycling to be studied. They are also used to show the effect of the applied current on the capacity and its rate of decline in experiments where the cycling rate is changed periodically.

In Chapter 3, galvanostatic cycling was used to evaluate the performance of LCO thin film cathodes. The effects of the voltage limits, cycle rate and cathode fabrication procedure on the cell performance were studied.

3 Improving the Processing and Performance of $LiCoO_2$ (LCO) Thin Film Cathodes

A significant proportion of the work reported in this chapter was first reported in the following published research article: Turrell, S. J., Zekoll, S., Liu, J., Grovenor, C. R. M. & Speller, S. C. Optimization of a potential manufacturing process for thin-film $LiCoO_2$ cathodes. *Thin Solid Films* **735**, 138888 (2021)[184].

3.1 Introduction

The discovery of the $LiCoO_2$ (LCO) cathode by Goodenough and co-workers[7] led to the commercialization of the lithium-ion secondary battery by Sony in 1991, initiating a portable electronics revolution and later the rise of electric vehicles[1,53]. LCO remains the dominant cathode material in commercial lithium-ion batteries owing to its array of favourable electrochemical properties, including a relatively high discharge voltage (~3.9 V *vs* Li^+/Li), flat discharge profile and high specific capacity (up to 137 mAh g^{-1} for a voltage window of ~3.0-4.2 V *vs* Li^+/Li)[185,186]. An exemplar first cycle charge-discharge voltage profile for an Li/(organic liquid electrolyte)/LCO cell is shown in Figure 3.1[187]. The development of cathode materials such as NMC-811 has led to moderate improvements in energy density, but a future step change will require the implementation of high-voltage cathodes such as LMNO (~4.7 V *vs* Li)[188]. Since organic liquid electrolytes are unstable at this voltage, successful implementation of these cathodes is likely to require pairing with solid electrolytes.

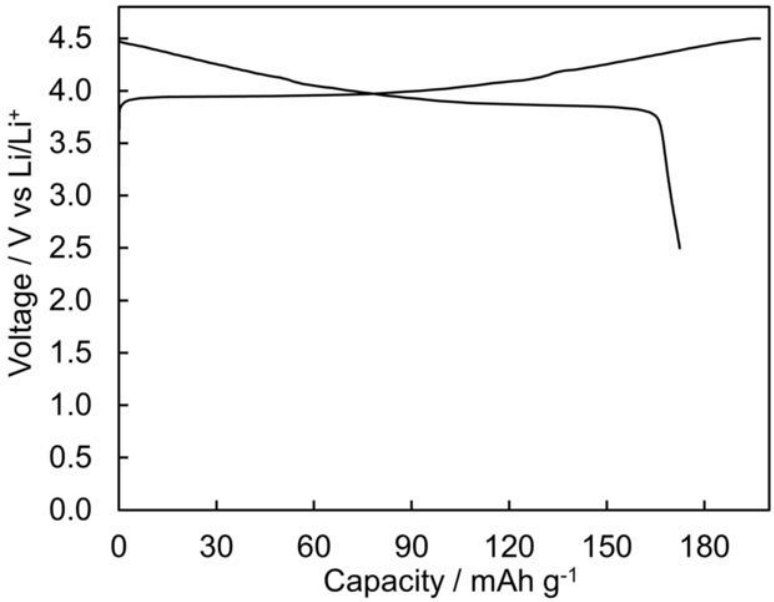


Figure 3.1 Exemplar first cycle charge-discharge voltage profile measured for an Li/(organic liquid electrolyte)/LCO cell cycled at 0.1 C. A wide voltage window of 2.5-4.5 V *vs* Li^+/Li was used, resulting in higher maximum charge and discharge capacities than typically observed for LCO. The excess (irreversible) capacity measured on the first charge is typically attributed to partial decomposition of the electrolyte. Reproduced with permission from *ChemistrySelect* **1**, 3992-3999 (2016)[187]. Copyright 2016 John Wiley and Sons.

Like commercial lithium-ion cells, most all-thin-film cells fabricated to date contain an LCO cathode. The most common thin-film cell configuration is Li/LiPON/LCO, in which the LCO cathode and LiPON electrolyte are usually deposited by RF magnetron sputtering and the lithium metal anode is deposited by vacuum evaporation or grown electrochemically from lithium in the cathode. This cell design was developed by a group at Oak Ridge National Laboratory and first reported by Wang *et al.*[111] in 1996. It has since been commercialized by several companies on a small scale, as discussed in Section 1.4.4. One of the key challenges associated with the development of thin-film battery technology relates to processing: how to obtain better electrochemical performance while making the fabrication route more amenable to large-scale manufacturing.

To make a thin-film deposition process suitable for large-scale manufacturing, its throughput must be maximized and the utilization of resources such as materials and energy must be

minimized[189,190]. Thus, deposition conditions which achieve the optimum balance between throughput and resource utilization must be found. Two key parameters are the applied RF power and process gas pressure, which strongly influence the deposition rate in magnetron sputtering processes; generally the deposition rate increases with applied RF power[191] and there is a value of process pressure which maximizes the deposition rate for a given set of experimental conditions[43]. From the perspective of resource utilization, process gas consumption should be minimized and the efficiency of energy-intensive aspects of the processing such as post-deposition annealing should be maximized. Thus, it is these factors which will receive the greatest attention in this investigation. A survey of the literature on the fabrication of thin-film LCO cathodes by RF magnetron sputtering reveals that most studies report similar processing conditions: an RF power density of ~2-5 W cm^{-2}, a deposition pressure of at least 1×10^{-2} mbar, a mixed argon-oxygen process gas, an unheated ceramic substrate coated with precious metal (Au, Pt or Ag), and post-deposition annealing in air or an oxygen/argon-oxygen atmosphere at 600–700 °C for 1-2 hours[111,192–211]. This suggests there is great scope to explore alternative processing conditions that are better suited to large-scale manufacturing and may also result in superior structural and electrochemical properties.

Although several “next-generation” cathode materials such as LMNO are currently under investigation for application in thin-film cells, LCO is ideal for investigating processing-structure-properties relationships in thin films because many aspects of the structure-properties relationships are already well understood. It is generally acknowledged that the ‘HT-LCO’ (high-temperature LCO) crystallographic structure is optimum for LCO cathodes. This structure is referred to as ‘high-temperature LCO’ because it is thought to be the most stable structure of LCO above ~400 °C[212]. In this structure, which has the $R\bar{3}m$ (rhombohedral) space group, the lithium, cobalt and oxygen atoms are arranged into separate layers perpendicular to the c-axis[111,192,212], as shown schematically in Figure 3.2. Thus, it is alternatively referred to as the ‘layered structure’ of LCO. Polycrystalline sputter

deposited films often display a preferred crystallographic orientation[106], and in HT-LCO it is desirable for (104), (101) and (110) planes to align parallel with the film surface[192,203,212–217]. This causes the (003) planes, in which lithium ions reside, to intersect the surface, creating a low impedance interface with the electrolyte for Li^+ insertion and extraction during cell operation[212,217,218]. Preferential alignment of (003) planes parallel to the film surface should be avoided as no intragranular routes for Li^+ migration to and from the film surface exist in this orientation, increasing the length and tortuosity of Li^+ insertion/extraction pathways and hence the impedance of the cathode. These pathways are shown schematically for three different preferred orientations in Figure 3.2[211].

The primary aim of this work was to find an alternative set of deposition and post-deposition annealing conditions for the fabrication of LCO thin films that are more suitable for large-scale manufacturing, but do not sacrifice the structural and electrochemical properties required for effective cathode operation. Industrial manufacturing requires the minimization of resource use and maximization of throughput. Thus, finding conditions that increase the film deposition rate, reduce the use of process gases and allow low-temperature, short-duration annealing treatments is desirable. A secondary aim was to deposit thicker films than typically reported in the literature in order to increase the cathode capacity, which is one of the factors limiting the more widespread application of thin-film cells. Only a handful of reports feature RF magnetron sputter deposited LCO films with thicknesses greater than 2 μm[208,212,215,216,219,220], and most reported LCO films have thicknesses below 1 μm[202,221–228].

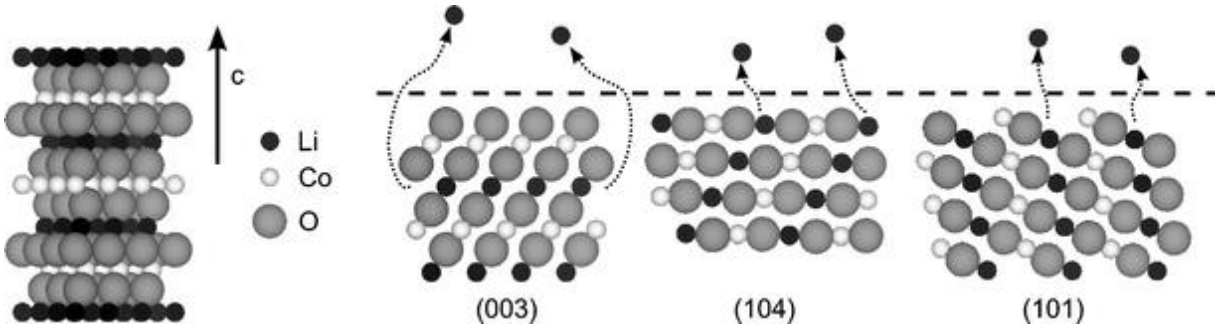


Figure 3.2 Crystal structure of HT-LCO and schematic diagrams showing possible Li^+ insertion/extraction pathways (dotted lines) for three preferred crystallographic orientations commonly seen in LCO thin films. The planes stated below each diagram are those parallel to the film surface (dashed line). Reproduced with permission from *J. Solid State Electrochem.* **17**, 2095-2099 (2013)[211]. Copyright 2013 Springer Nature.

3.2 Experimental Methods

3.2.1 Sputtering Target and Substrate Preparation

The $LiCoO_2$ powder target used for RF magnetron sputtering was produced by drying commercial $LiCoO_2$ powder (Sigma Aldrich, 99.8%) at 80 °C inside a chamber furnace (Carbolite CSF 1200) then lightly pressing it with a glass microscope slide into a copper disc containing a 2 mm deep, ~3” diameter circular depression.

The substrate materials used in the fabrication of samples for structural and chemical characterization were <100> oriented polished silicon wafers (various suppliers), glass cut from microscope slides and ~250 µm thick Waspaloy (58Ni-19Cr-14Co-Mo-Ti-Al-Fe [wt%]) foil (HAYNES® 282® alloy, Goodfellow Cambridge Ltd). Polished silicon wafers were chosen on the basis that they have been used frequently as substrate materials for LCO in prior reports. Glass was used in certain experiments owing to its smooth surface finish and propensity to fracture cleanly, forming clear cross-sectional surfaces which enabled accurate film thickness measurements to be made. Waspaloy was chosen for its electronic conductivity (essential for electrochemical characterization) as well as its oxidation resistance and stability at high temperatures. Although aluminium is conventionally used as the current

collector material for LCO cathodes[229] it melts at 660 °C[230], which is within the range of annealing temperatures used for LCO films in prior studies. Therefore, the use of Waspaloy should avoid disruption of the LCO film by substrate melting and oxidation during annealing.

The substrate materials were cut into 10*10 mm squares. To allow electrochemical testing of LCO films in coin cells, circular Waspaloy substrates of 15 mm diameter were produced by laser cutting (Scitech Precision Ltd, Rutherford Appleton Laboratory, UK). For galvanostatic cycling between 3.0 V and 4.3 V, and for the cyclic voltammetry experiments, the native oxide layer on the Waspaloy surface was left in-situ; however, for the subsequent galvanostatic cycling between 3.0 V and 4.2 V the oxide layer was removed by grinding on a series of silicon carbide papers, finishing on a 4000 grit paper. All substrates were cleaned by successive sonication in acetone, ethanol and isopropanol. The substrates were weighed before and after film deposition to allow calculation of film mass.

3.2.2 Thin Film Deposition and Post-Deposition Annealing

LCO films were deposited in a magnetron sputtering system (Ion Tech Ltd) with a circular magnetron source and a target-to-substrate distance of ~6.5 cm (target-to-substrate distances reported previously for the sputter deposition of LCO are mostly between 5 and 10 cm[111,202,212,213,215,221,222,231,232]). The base pressure immediately prior to sputtering was less than 10^{-6} mbar. Pure argon process gas (BOC Pureshield 99.998 %) was used in all depositions rather than the argon-oxygen mixtures typically used in the literature, since several reports indicate that the Ar:O_2 ratio has only a weak effect on film structure [2,17,23]. Targets were subjected to pre-deposition sputtering for at least 30 minutes prior to film deposition. Substrate heating by quartz lamp heaters positioned at the top of the deposition chamber was used in only one of the deposition experiments. The other key deposition conditions (process pressure, RF power density and deposition duration) were varied systematically and are reported for each experiment in Section 3.3.1.

Annealing treatments were performed in air within a chamber furnace (Carbolite CSF 1200). In most cases, the samples were placed on a bed of LCO powder within a covered alumina crucible to suppress the loss of volatile lithium by increasing the partial pressure of lithium in the vapour phase. In all cases, samples were allowed to cool within the furnace at its natural rate and were removed when cool enough to handle with gloves (below ~200 °C). The other key annealing conditions (heating rate, maximum temperature and holding time) were varied systematically along with the deposition conditions and are reported in Section 3.3.1.

3.2.3 Structural and Chemical Characterization

The crystallographic properties of the LCO films, substrates and target powder were characterized by X-ray diffraction (XRD) using a diffractometer with a θ-θ geometry (Malvern Panalytical Empyrean) and crystallographic information files for candidate structures[233–236]. For the first two sets of films (processed using the conditions in Table 3.1 and Table 3.2), surface profilometry (Veeco Dektak 6M) was used to measure the film thickness. Owing to the difficulty in performing reliable measurements on films with relatively rough (unpolished) substrates (i.e., the Waspaloy), SEM was used for all subsequent thickness measurements. Secondary electron imaging was performed with a Zeiss Merlin SEM. A Thermo Scientific Helios G4 PFIB CXe DualBeam PFIB was used to cross-section LCO films on Waspaloy substrates and perform secondary electron imaging of the glancing trench surfaces. EDX detectors (Oxford Instruments XMax 150mm^2 and Ultim Max 170, respectively) attached to these microscopes were used to perform elemental mapping and line profiling on the regions imaged. AZtec® software (Oxford Instruments Nanotechnology Tools Limited) was used to record and interpret the X-ray spectra measured in “TruMap” and “QuantLine” scans. The LCO films on silicon substrates that had undergone EDX mapping to determine O/Co ratios were then subjected to ICP-OES analysis in a PerkinElmer Optima 8000 instrument. Plotting of calibration curves and composition calculations were performed using Syngistix software (PerkinElmer Inc.).

3.2.4 Electrochemical Characterization

Optimized LCO films deposited on Waspaloy were tested electrochemically in coin cells with a lithium metal anode and 100 µL of liquid electrolyte (lithium hexafluorophosphate solution 746711, Merck) containing 1 M $LiPF_6$ in a 1:1 volume ratio of ethylene carbonate and dimethyl carbonate. The liquid electrolyte was absorbed by a glass fibre separator inserted between the lithium metal anode and LCO cathode. Prior to testing, the maximum attainable charge capacities were calculated from the film masses and the theoretical specific capacity of $LiCoO_2$ when $0.5Li^+$ is transferred (136.9 mAh g^{-1}). After assembly, each cell was left to rest for at least 24 hours before testing to allow the OCV to stabilize. The galvanostatic cycling experiments were performed using a MACCOR Series 4600A Automated Battery Test System. To achieve a particular cycling rate ("C-rate") the current required was determined from the maximum attainable cathode capacity values. A similar "LCO-free" coin cell was constructed with a bare Waspaloy disc on the positive side, and cyclic voltammetry was performed using a Biologic MPG-2 battery cycler to analyse the electrochemical activity of the Waspaloy. A nominal scan rate of 33 µV/s was used to perform five voltage scans between 3.0 V and 4.3 V *vs* the lithium counter electrode since this resulted in a forward or reverse scan time of approximately 10 hours, which is the same as the charge/discharge time selected for the initial galvanostatic cycling. All cells were held at 30 ˚C during testing.

3.3 Results and Discussion

3.3.1 Structural Characterization

3.3.1.1 LCO Powder

Prior to LCO film deposition, the powder used to produce the sputtering target was characterized by XRD. The resulting diffraction pattern is shown in Figure 3.3. The key observation from the powder pattern is that by far the most intense peak is (003), and the second most intense peak is (104). This will be of significance when inferring preferred crystallographic orientation from the diffraction patterns recorded for film samples.

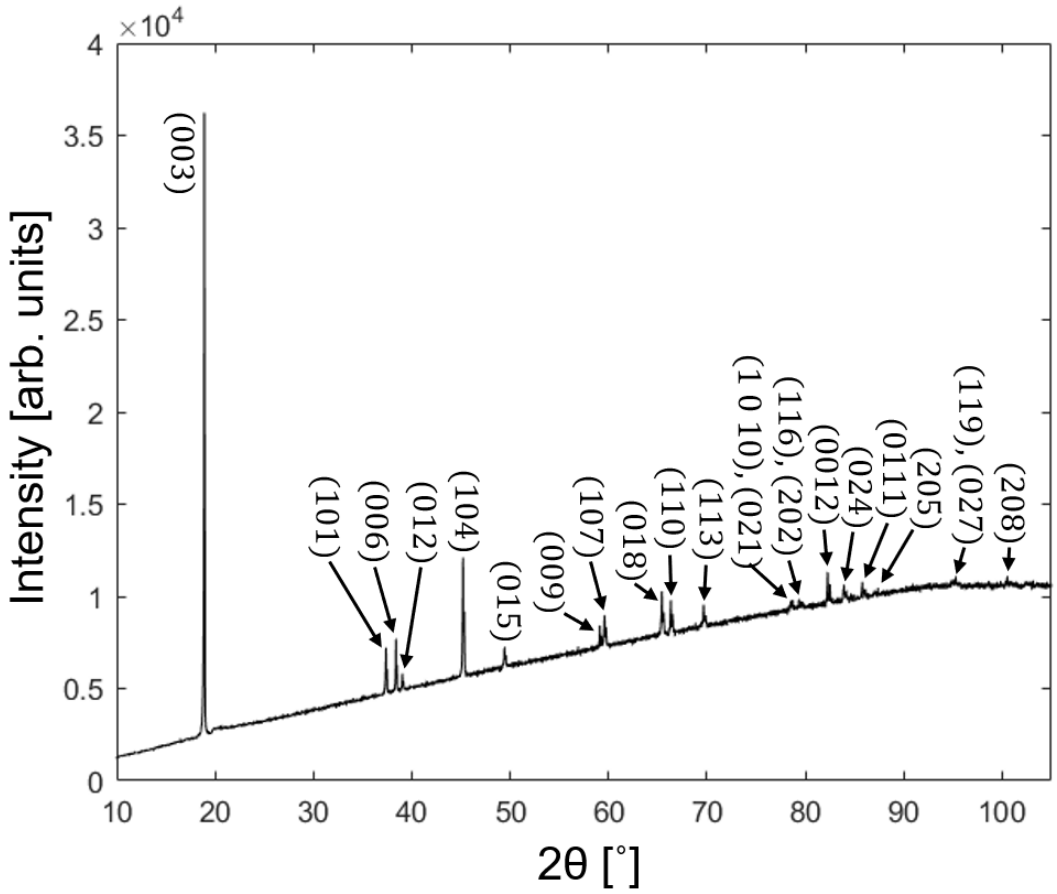


Figure 3.3 XRD pattern from a sample of the LCO powder used to produce the sputtering target.

3.3.1.2 Films Processed Using Typical Conditions from the Literature

It was decided that a logical starting point for this investigation was to verify that a set of commonly-used processing conditions from the literature result in the expected structural properties when used with the laboratory equipment available for this investigation. These reference processing conditions are listed in Table 3.1. It should be noted that the typical argon-oxygen process gas mixture was not used in this investigation since the facility to mix process gases was not available in the sputtering system at the time this work was performed.

Table 3.1 Conditions used to fabricate the first set of LCO films for structural characterization. These conditions will be used as a reference since they are based on prior reports.

Parameter	Value
Substrate	<100> silicon wafer
Process pressure	~1×10^{-2} mbar
RF power	100 W (2.2 W cm^{-2})
Deposition duration	6 hours
Annealing temperature	700 ˚C
Time at annealing temperature	1 hour
Heating rate	2 ˚C/min
Annealing atmosphere	Air (no LCO powder bed)

Measurements of the as-deposited film thickness by surface profilometry gave values in the range 1.3-1.5 μm, meaning that the average deposition rate was 220-250 nm h^{-1}. A wide range of film thicknesses is reported in the literature, but values on the order of 1 μm are common[111,192,212–214,219,226,232,237], making these films representative. The deposition rate depends strongly on the target-to-substrate distance of the sputtering system; in this investigation, the target-to-substrate distance was fixed so that the effects of the other deposition parameters on the deposition rate could be studied. Typical XRD patterns and SEM micrographs from as-deposited and annealed films are shown in Figure 3.4 a) and b), respectively.

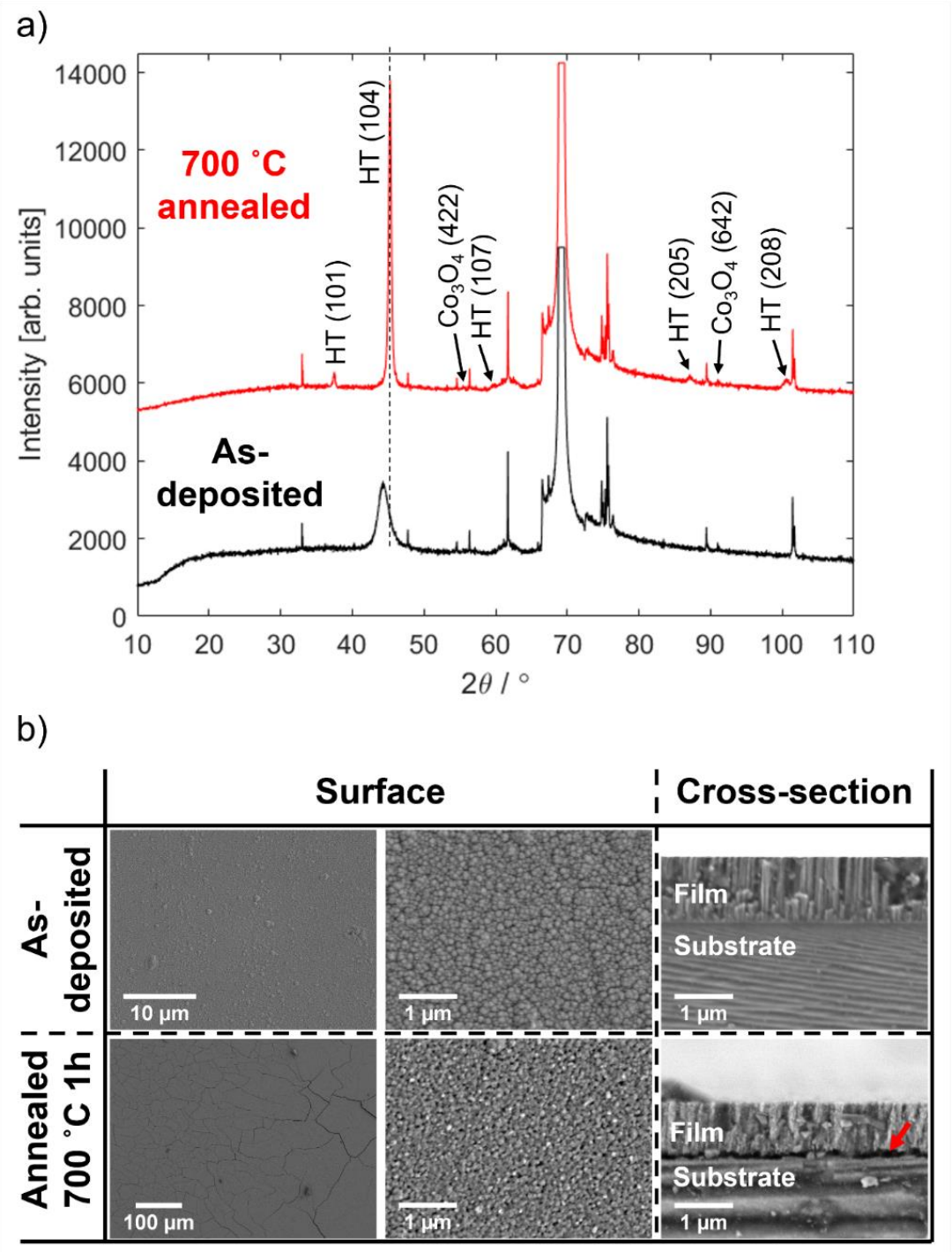


Figure 3.4 a) XRD patterns from as-deposited and annealed films processed using the conditions in Table 3.1; b) corresponding surface and cross-sectional SEM micrographs (captured by Dr Stefanie Zekoll). Peaks labelled 'HT' in the XRD patterns correspond to HT-LCO; unlabelled peaks are from the substrate or the sample holder. The red arrow on the cross-sectional micrograph from the annealed sample points to the delamination of the LCO film from the silicon substrate.

The XRD patterns in Figure 3.4 a) show that an initially nanocrystalline film undergoes extensive crystallization into the HT-LCO structure on annealing, as expected. The most intense peak in the pattern from the annealed film is (104), and the (003) peak – which is the most intense peak in the powder pattern – is absent, suggesting extensive alignment of (104) planes with the film surface. This challenges the belief sometimes expressed in the literature that a mixed argon-oxygen process gas is required to develop the desired LCO phase and crystallographic texture[192,238]. A couple of very low intensity peaks corresponding to a Co_3O_4 impurity phase are present, which may be a result of omitting oxygen from the process gas. This phase is electrochemically inactive, and steps are often taken to avoid its formation[127,196,223,239]. However, based on the intensity of Co_3O_4 peaks relative to HT-LCO peaks, its volume fraction is likely to be negligible. The single, broad peak in the as-deposited pattern cannot be identified conclusively; it is at a slightly lower angle (44.3°) than expected for the HT-LCO (104) peak (45.2°)[235,240], and it is also near the positions expected for the Co_3O_4 (400) peak (44.8°)[233] and peaks from the cubic polymorphs of LCO[234,236]. A similar peak has been seen in XRD patterns reported previously for as-deposited LCO films[196,241,242], and it has been assigned to the (104) reflection of nanocrystalline HT-LCO. If this assignation is valid here, the discrepancy in peak position suggests the presence of a uniform tensile strain perpendicular to the film surface which disappears on annealing.

The surface view SEM micrographs in Figure 3.4 b) show that the as-deposited and annealed films have a “particulate” appearance; the cross-sectional micrographs reveal that this is due to a columnar microstructure, which may reflect the preferred film orientation. While the crystallographic structure of the LCO improves on annealing, the microstructural properties of the film deteriorate: extensive cracking appears across the film surface and partial delamination of the film from the substrate can be seen in the cross-sectional view, as indicated by the red arrow. These changes can be attributed to differential thermal expansion between the film and substrate and may have been avoided in previous reports by the

deposition of a metallic electrical contact such as Au or Pt between the substrate and the film.

3.3.1.3 Effect of *In Situ* Substrate Heating

The next step was to determine whether a well-crystallized HT-LCO film could be achieved without post-deposition annealing by using *in situ* substrate heating during sputter deposition. This may avoid film cracking and simplify the processing route. Thus, the processing conditions used for this deposition (Table 3.2) were similar to those used previously, except that constant substrate heating was applied throughout the process.

Table 3.2 Conditions used to fabricate the set of "hot-sputtered" LCO films.

Parameter	Value
Substrate	<100> silicon wafer
Process pressure	~2×10^{-2} mbar
RF power	100 W (2.2 W cm^{-2})
Temperature at top of chamber*	168 °C
Deposition duration	6 hours

*The temperature at the top of the deposition chamber (above the substrate heaters) was measured since the facility to measure the substrate temperature directly was not available on this sputtering system.

The thickness range measured by surface profilometry for these films (1.5-1.6 μm) was similar to that measured for the previous set and corresponds to an average deposition rate of 250-270 nm h^{-1}. A typical XRD pattern is shown in Figure 3.5. For comparison, the pattern from the film deposited on an unheated substrate is also plotted.

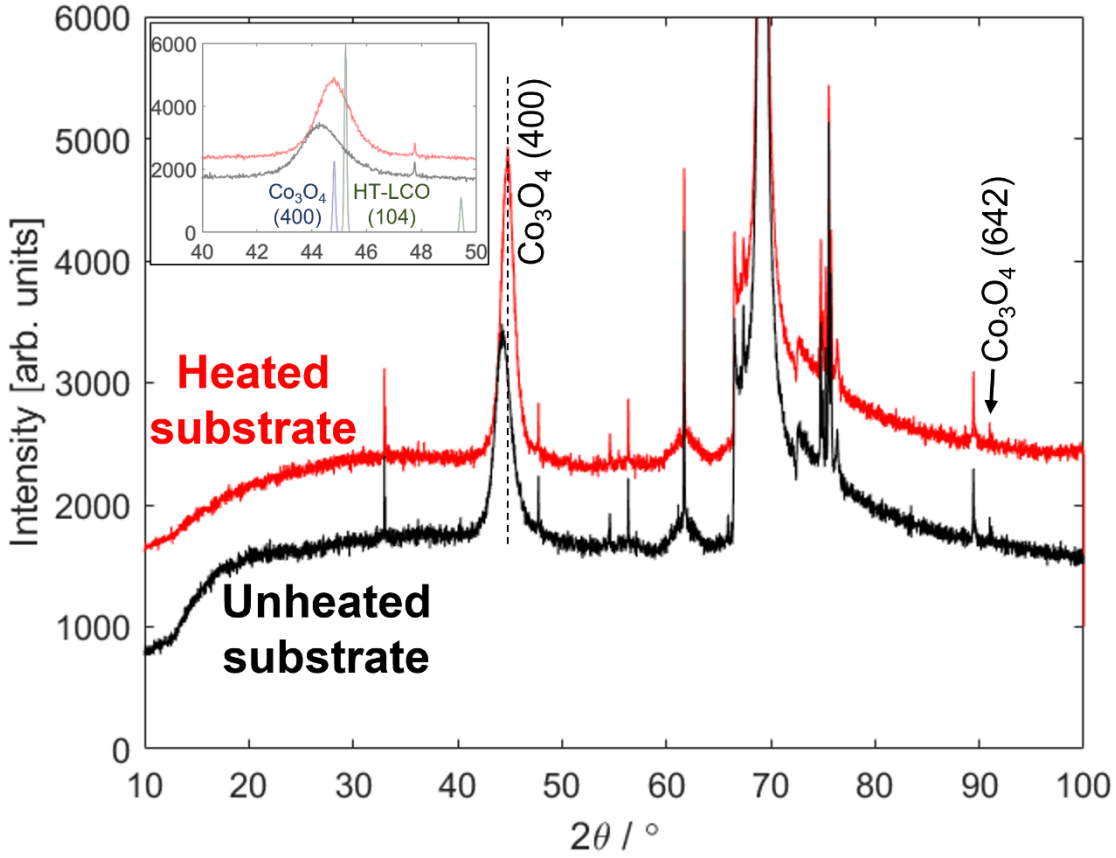


Figure 3.5 XRD patterns from LCO films deposited on heated and unheated substrates. The conditions used to deposit the film on the heated substrate are given in Table 3.2; the pattern from the film deposited on the unheated substrate is reproduced from Figure 3.4 a) for comparison. The inset shows a view of the peaks present in the 2θ = 40-50° range along with simulated powder patterns[233,240] for Co_3O_4 and HT-LCO. Unlabelled peaks are from the substrate or the sample holder.

The differences between the two XRD patterns in Figure 3.5 are small; in both patterns only one film peak of significant intensity near 2Θ = 44.5° is visible. This peak is more intense relative to the substrate peaks in the "heated substrate" pattern, signifying a higher degree of crystallinity in the film. However, its 2Θ value is ~0.45° higher than that of the peak in the "unheated substrate" pattern, as shown clearly in the inset, and matches exactly the position expected for Co_3O_4 (400). It is reasonable to assume that the level of strain in the film deposited on the heated substrate was lower than that in the film deposited on the unheated substrate owing to the greater adatom mobility on heated substrates[106]. Therefore, while the

peak near 2Θ = 44.5° in the “unheated substrate” pattern can be attributed to HT-LCO (104) on the basis that the film is uniformly strained as discussed earlier, this justification is unlikely to be valid for the film deposited on the heated substrate. A small Co_3O_4 (642) peak is present in both patterns, suggesting that a volume of Co_3O_4 exists in both films. The fact that this peak appears in an identical position in both patterns adds to the evidence that the strained phase in the film deposited on the unheated substrate is HT-LCO rather than Co_3O_4 and that the primary crystalline phase in the film deposited on the heated substrate is Co_3O_4.

Despite the relatively low substrate temperature achieved in this experiment, a combination of volatilization and reduced adsorption of lithium on the heated substrates is likely to be the reason for the preferential formation of Co_3O_4. Indeed, in the first report on LCO film deposition a substrate temperature of 300 °C was used[209], which resulted in a lithium to cobalt ratio of ~0.4 in the as-deposited films – a significant lithium deficiency. Owing to the apparently lower degree of lithium loss caused by post-deposition annealing for 1 hour, all subsequent films in the present work were deposited on unheated substrates.

3.3.1.4 Effects of Substrate Material, RF Power and Annealing Atmosphere

The results presented so far show that the films processed using the reference conditions in Table 3.1 have desirable phase compositions and crystallographic properties. However, uncoated silicon substrates do not demonstrate sufficient stability during annealing at 700 °C and an electronically conducting substrate will be required for integration of the LCO into an electrochemical cell. In the next experiment, Waspaloy – an oxidation resistant nickel superalloy widely used in gas turbine engines[243] – was investigated as a substrate material to improve thermal stability without increasing processing complexity by obviating the need for metallic layer deposition. While the oxidation resistance of this material depends on the integrity of its surface oxide scale[244], the choice of Waspaloy was influenced by the success of Filippin *et al.*[205] in using a self-passivating Ni-Al-Cr alloy film as a current collector for thin-film LCO cathodes. As well as changing the substrate material, the RF power was doubled,

which should roughly double the deposition rate. In anticipation of this, the deposition duration was reduced to 2.5 hours. While this would be an attractive outcome for manufacturing, the effect on film structure must be investigated. The remaining changes concern the annealing process: to limit lithium loss during annealing, samples were placed on a bed of LCO powder in an enclosed crucible, thereby increasing the partial pressure of lithium in the annealing atmosphere and suppressing its loss from the film. A wide range of annealing temperatures between 300 and 800 °C were used to investigate the effect of annealing temperature on structural development, and the heating rate was increased to 10 °C/min to reduce the time required for the process. The full set of conditions used for this deposition experiment are shown in Table 3.3.

Table 3.3 Conditions used to fabricate the initial set of LCO films on Waspaloy substrates. The RF power was double the reference value in Table 3.1.

Parameter	Value
Substrate	Waspaloy foil
Process pressure	~2×10^{-2} mbar
RF power	200 W (4.4 W cm^{-2})
Deposition duration	2.5 hours
Annealing temperature	300 to 800 ˚C in 50 °C intervals
Time at annealing temperature	1 hour
Heating rate	10 ˚C/min
Annealing atmosphere	Enclosed crucible with LCO powder bed

The as-deposited film thickness measured using SEM was 1.2-1.3 µm, meaning the average deposition rate was 480-520 nm h^{-1}. As expected, this is roughly twice that achieved using the literature conditions. Typical XRD patterns from these films are shown in Figure 3.6 for all annealing temperatures.

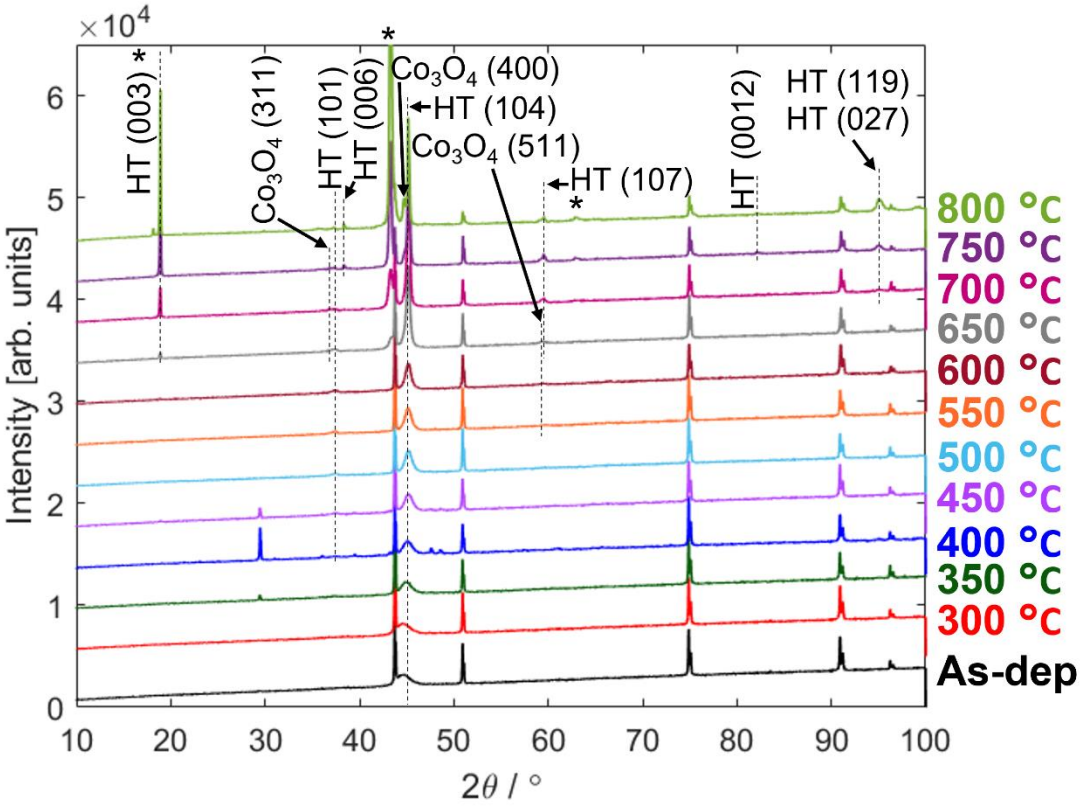


Figure 3.6 XRD patterns from LCO films deposited on Waspaloy substrates and annealed at temperatures between 300 °C and 800 °C. The full set of processing conditions is given in Table 3.3. Peaks labelled with an asterisk (*) appear at higher annealing temperatures and correspond to oxides that form on the surface of the Waspaloy. Unlabelled peaks are from the substrate or the sample holder.

Figure 3.6 shows that the main film peak near 45° appears in the position expected for HT-LCO (104) at 400 °C; below this temperature it is present at lower 2Θ values, as was seen previously for as-deposited films produced using the conditions in Tables 3.1 and 3.2. The HT-LCO (101) peak also appears at 400 °C, and both film peaks grow in intensity with increasing annealing temperature, reflecting the increasing crystallization of the HT-LCO phase. Significant changes occur on annealing above 650 °C: the HT-LCO (003) and (006) peaks appear, signifying the development of an unfavourable crystallographic orientation for Li^+ insertion and extraction. Small HT-LCO (119) and (027) peaks also appear, but crucially the emergence of Co_3O_4 (311) and (400) peaks is symptomatic of lithium loss at the highest annealing temperatures. On balance, 600 °C seems to be the optimum annealing

temperature for this set of processing conditions. Although a very minor Co_3O_4 (511) peak is present in the 600 °C pattern, this temperature achieves a balance between a high (104) peak intensity and the avoidance of extensive parallel alignment of the (003) planes with the film surface. While the films annealed between 400 °C and 600 °C are less crystalline, their performance as cathodes may be adequate for certain applications.

3.3.1.5 Effect of Process Pressure

The significant modulation of the deposition rate by the process pressure was described in Section 2.2.1. However, process pressure is also expected to affect LCO film structure and chemistry. Several literature reports suggest that reducing the process pressure increases the volume fraction of Co_3O_4 in sputter-deposited LCO films as well as the concentration of lithium in excess of its stoichiometric value[192,201,202,205,208]. While an excess of lithium may be considered beneficial as it could compensate for lithium lost during annealing, the presence of Co_3O_4 is undesirable. The conditions in Table 3.4 were used to deposit a series of films at a pressure approximately one order of magnitude below the reference value in Table 3.1. For this experiment, the RF power was set to the value in Table 3.1 to exclude effects from an increased power density.

Table 3.4 Conditions used to investigate the effect of a significant reduction in process pressure on the structure of LCO films compared to those deposited using the reference conditions in Table 3.1.

Parameter	Value
Substrate	Waspaloy foil
Process pressure	~1×10^{-3} mbar
RF power	100 W (2.2 W cm^{-2})
Deposition duration	4 hours
Annealing temperature	500 and 700 ˚C
Time at annealing temperature	1 hour
Heating rate	10 ˚C/min
Annealing atmosphere	Enclosed crucible with LCO powder bed

The as-deposited film thickness measured using SEM was 0.51-0.57 µm, meaning the average deposition rate was 130-140 nm h^{-1}. This is ~50-60% of the deposition rate achieved using the conditions in Table 3.1, suggesting the pressure reduction tried here is too large to be of benefit to large-scale manufacturing. Despite this, films were annealed at 500 °C and 700 °C and the crystallographic properties were investigated, as shown by the XRD patterns in Figure 3.7.

In addition to a significant reduction in the deposition rate, Figure 3.7 shows that reducing the process pressure by this amount has a detrimental effect on the film structure: the HT-LCO (104) peak is absent in all patterns and the only HT-LCO peaks are of very low intensity and do not correspond to the desired orientations. The two Co_3O_4 peaks present after annealing at 700 °C have higher intensities than the single HT-LCO peak. Therefore, it is clear that reducing the process pressure by one order of magnitude has only deleterious consequences for film processing and structure. This appears to support the observation in some literature reports that the Co_3O_4 to HT-LCO volume ratio increases as the process pressure decreases.

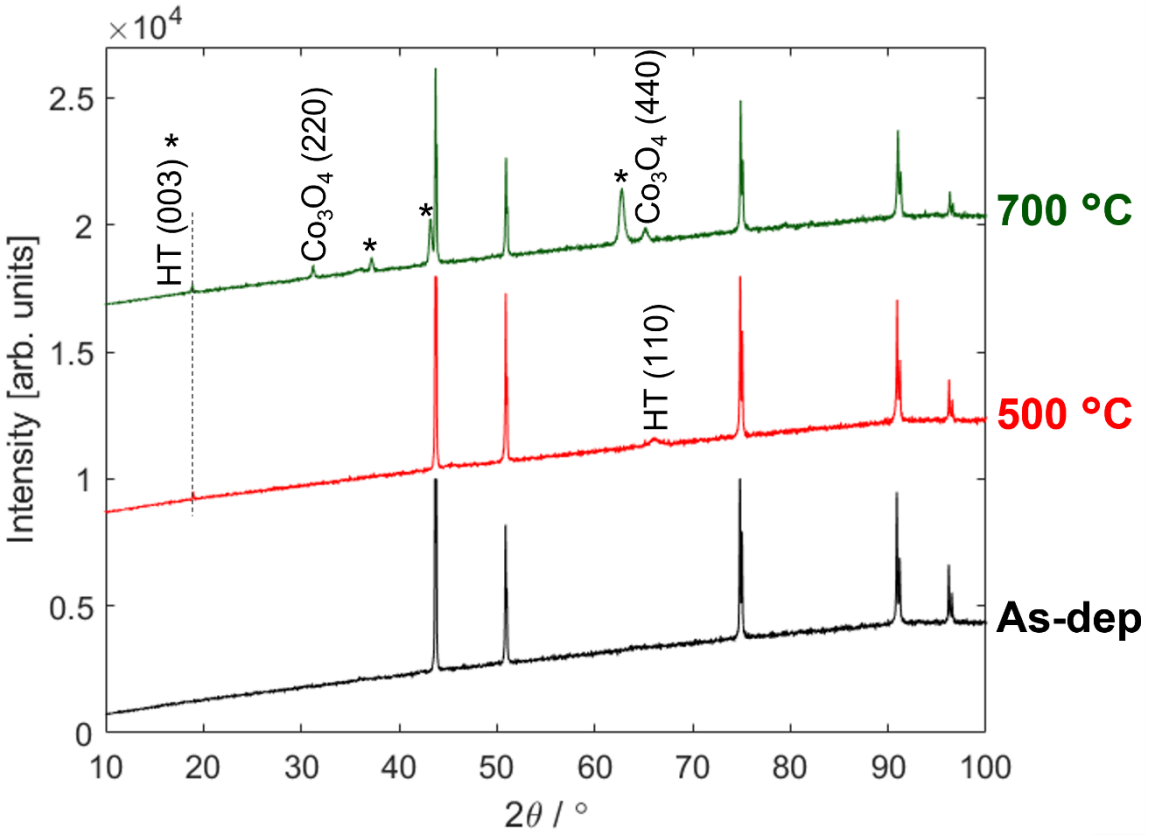


Figure 3.7 XRD patterns from LCO films deposited on Waspaloy substrates at a low process pressure. The full set of processing conditions is given in Table 3.4. Peaks labelled with an asterisk (*) correspond to oxides that form on the surface of the Waspaloy during annealing at 700 °C. Unlabelled peaks are from the substrate or the sample holder.

To identify a more appropriate process pressure, a “pressure-rate calibration” experiment was performed whereby a series of LCO films was deposited at different process pressures and the corresponding deposition rates were determined. The conditions used are shown in Table 3.5.

SEM was used to measure the film thicknesses, which were converted into deposition rates and plotted against process pressure along with a “high pressure” data point from one of the films deposited using the reference conditions in Table 3.1, as shown in Figure 3.8. The error bars represent the standard measurement errors determined from 6-9 measurements of film thickness; the trend was for the measurement error to decrease with increasing film thickness, as expected.

Table 3.5 Deposition conditions used to produce a series of LCO films in an experiment to investigate the relationship between the process pressure and deposition rate. The reference value of RF power from Table 3.1 was used for all depositions.

Parameter	Value
Substrate	Glass from microscope slides*
Process pressures	1.0×10^{-4} mbar, 1.0×10^{-3}, 2.5×10^{-3} mbar and 5.0×10^{-3} mbar
RF power	100 W (2.2 W cm^{-2})
Deposition duration	0.5 hours for each film

*Glass – rather than Waspaloy – was used owing to its smoother surface, allowing more accurate measurements of film thickness.

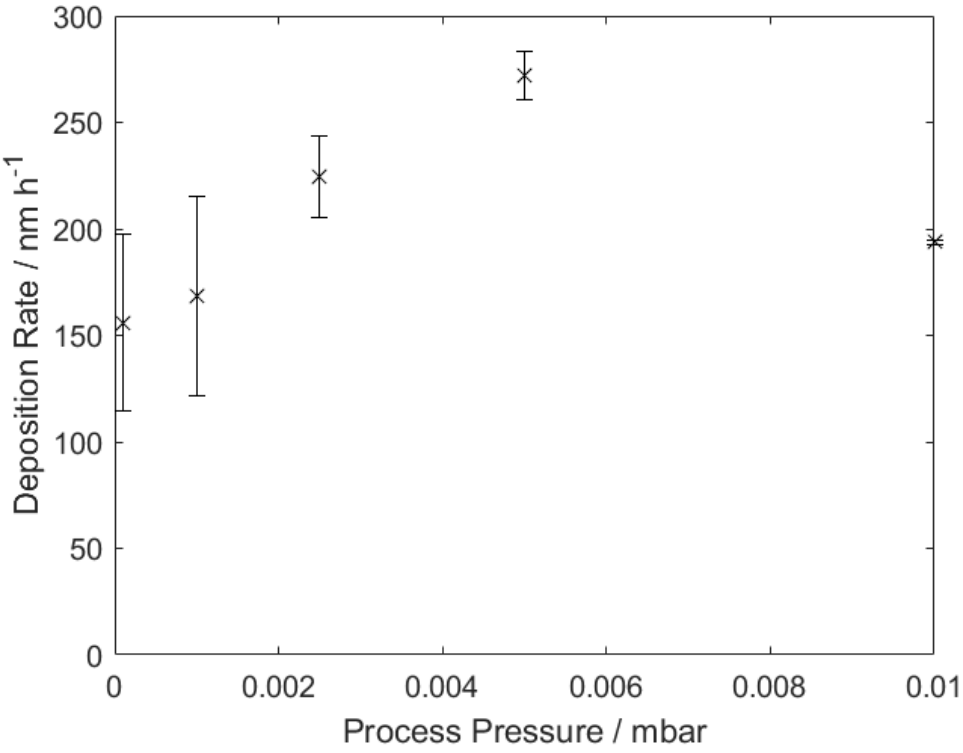


Figure 3.8 Plot of deposition rate against process pressure for a series of as-deposited films produced using the conditions in Table 3.5 and Table 3.1. Error bars were calculated from the standard errors in the film thickness measurements made using SEM.

Notwithstanding the large error bars on the deposition rate values for the films deposited at low pressure, the trend shown by the data points reflects the one expected from theory. The deposition rate reaches a maximum near a pressure of 5×10^{-3} mbar. From a throughput perspective, this would be the optimum pressure. However, the effect on film structural properties must be investigated before this pressure is deemed to be optimum.

3.3.1.6 Further Refinement of Processing Conditions

After finding that the deposition rate reaches a maximum at a process pressure of ~5×10^{-3} mbar, deposition at this pressure and similar conditions to those in Table 3.3 was performed. The full set of conditions is given in Table 3.6. Compared to the reference conditions in Table 3.1, the key differences are a higher RF power and lower process pressure. On the basis of the earlier experiments reported here, these changes are expected to result in a significant increase in deposition rate.

The as-deposited film thickness measured using SEM was 1.1-1.3 μm, meaning the average deposition rate was 440-520 nm h^{-1}. This is very similar to that achieved using the deposition conditions in Table 3.3, which indicates that the rate-enhancing effects of increased power density and reduced process pressure were not additive in this case. The XRD patterns from this series of films are shown in Figure 3.9.

Table 3.6 Processing conditions used to study the effect on LCO film structure of using a low process pressure and high RF power relative to the reference values in Table 3.1.

Parameter	Value
Substrate	Waspaloy foil
Process pressure	5×10^{-3} mbar
RF power	200 W (4.4 W cm^{-2})
Deposition duration	2.5 hours
Annealing temperature	300 to 700 ˚C in 100 °C intervals
Time at annealing temperature	1 hour
Heating rate	10 ˚C/min
Annealing atmosphere	Enclosed crucible with LCO powder bed

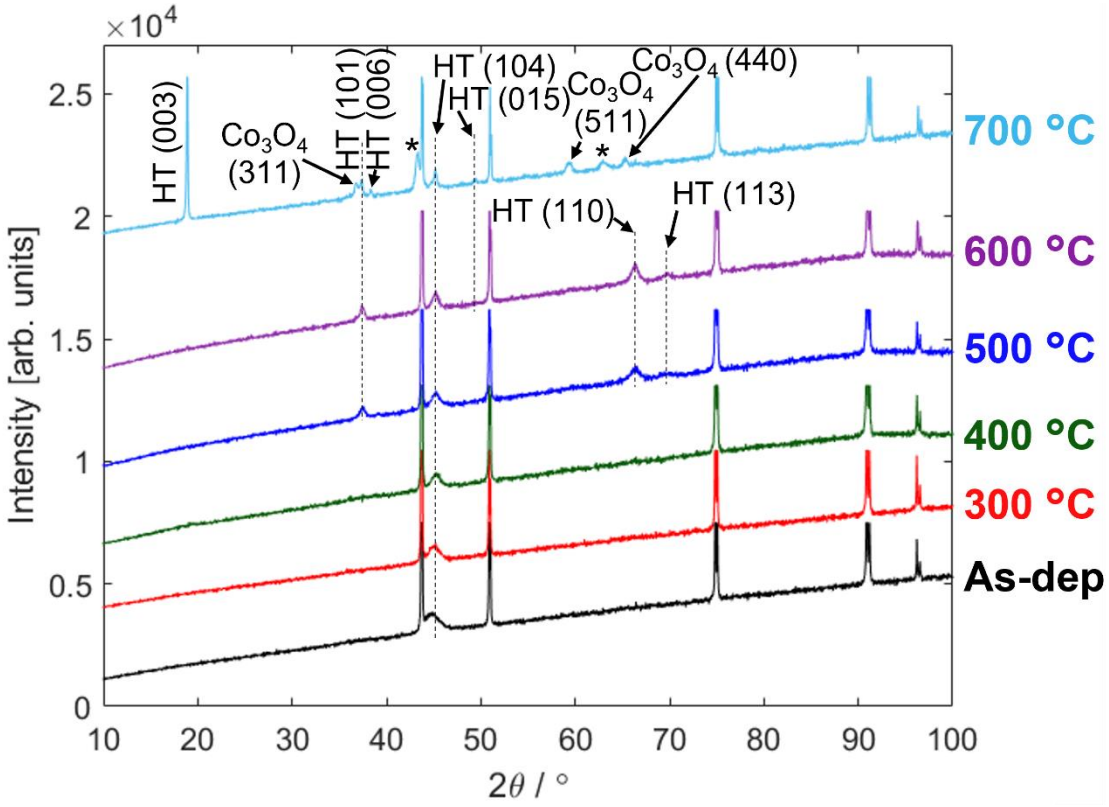


Figure 3.9 XRD patterns from LCO films deposited on Waspaloy substrates and annealed at a series of temperatures between 300 °C and 700 °C. The full set of processing conditions is given in Table 3.6. Peaks labelled with an asterisk (*) appear on annealing at 700 °C and correspond to oxides that form on the surface of the Waspaloy. Unlabelled peaks are from the substrate or the sample holder.

The XRD patterns in Figure 3.9 appear similar to those from the set of films deposited at a higher process pressure in Figure 3.6. Again, 600 °C seems to be the optimum annealing temperature since parallel alignment of HT-LCO (003) planes with the film surface occurs on annealing at 700 °C and several Co_3O_4 peaks appear. Although the intensity of the favoured HT-LCO (104) peak relative to the substrate peaks is lower than in Figure 3.6, a peak corresponding to HT-LCO (110) is present. This peak is absent in Figure 3.6 and shows that a significant fraction of LCO grains align in an alternative favourable orientation for lithium insertion and extraction. Furthermore, the Co_3O_4 (511) peak seen in the 600 °C annealed pattern in Figure 3.6 is not present in the corresponding pattern in Figure 3.9, and no other Co_3O_4 peaks are present.

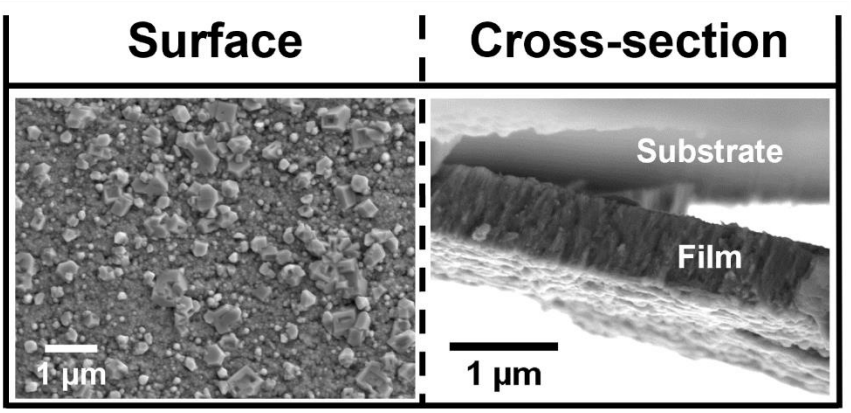


Figure 3.10 Surface and cross-sectional micrographs of the LCO film processed using the conditions in Table 3.6 and annealed at 600 °C. The film has partially detached from the substrate in the cross-sectional view due to plastic deformation of the Waspaloy during sectioning.

Figure 3.10 shows surface and cross-sectional SEM micrographs of the film annealed at 600 °C. The surface view micrograph shows a distribution of highly facetted crystallites on top of the columnar structure that formed during film growth, indicating that the film partially recrystallized during annealing at 600 °C. The cross-sectional image confirms that the columnar structure, which may be associated with the dominant HT-LCO (104)//surface orientation, was mostly retained. Inspection of the surface view micrograph reveals that some of the crystallites have hexagonal faces, consistent with the Wulff (equilibrium) shape[245] determined for LCO[246] by minimizing the total surface energy. In some cases these faces are parallel to the film surface, which may reflect incipient alignment into the (003) // surface orientation seen in Figure 3.9 for films annealed at 700 °C. However, hexagonal faces are not visible on most of the crystallites, meaning that the Wulff shape did not develop fully in these cases or that the crystallites assumed alternative orientations, for example with (101), (104) or (110) aligned parallel to the film surface.

The films investigated so far have had similar thicknesses to the majority of LCO films reported in the literature. To increase cathode capacity, it is necessary to increase film thickness. Furthermore, the literature suggests that alignment of (104) and (101) planes with

the surface should be favoured in thicker films, since this minimizes volume strain energy[212,247]. For the next deposition, the objective was to increase film thickness while maintaining crystallinity and limiting the increase in deposition duration. To achieve this, the power density was raised to increase the deposition rate further. However, owing to the greater film volume, the annealing duration was increased to allow more time for crystallization. The set of conditions used is shown in Table 3.7.

Table 3.7 Processing conditions used to study the effect on LCO film structure of increasing the deposition duration, RF power and annealing duration compared to the previous values in Table 3.6.

Parameter	Value
Substrate	Waspaloy foil
Process pressure	5×10^{-3} mbar
RF power	250 W (5.5 W cm^{-2})
Deposition duration	4 hours
Annealing temperature	300 to 700 ˚C in 100 °C intervals
Time at annealing temperature	3 hours
Heating rate	10 ˚C/min
Annealing atmosphere	Enclosed crucible with LCO powder bed

Film thicknesses measured by SEM were in the range 2.5-2.8 μm, which is over double the thickness measured for films deposited using the previous set of conditions (Table 3.6), despite the only 60% increase in deposition duration. This is attributable to the increase in average deposition rate by ~40% to 630-700 nm h^{-1}. However, the increase in RF power was only 25%. This disproportionate increase in deposition rate may be attributable to the influence of the optimized process pressure, since this effect was expected, but not seen, in the previous deposition. It is not clear why this should occur, unless the effects of changing RF power and process pressure are interrelated. The XRD patterns from this series of films are shown in Figure 3.11.

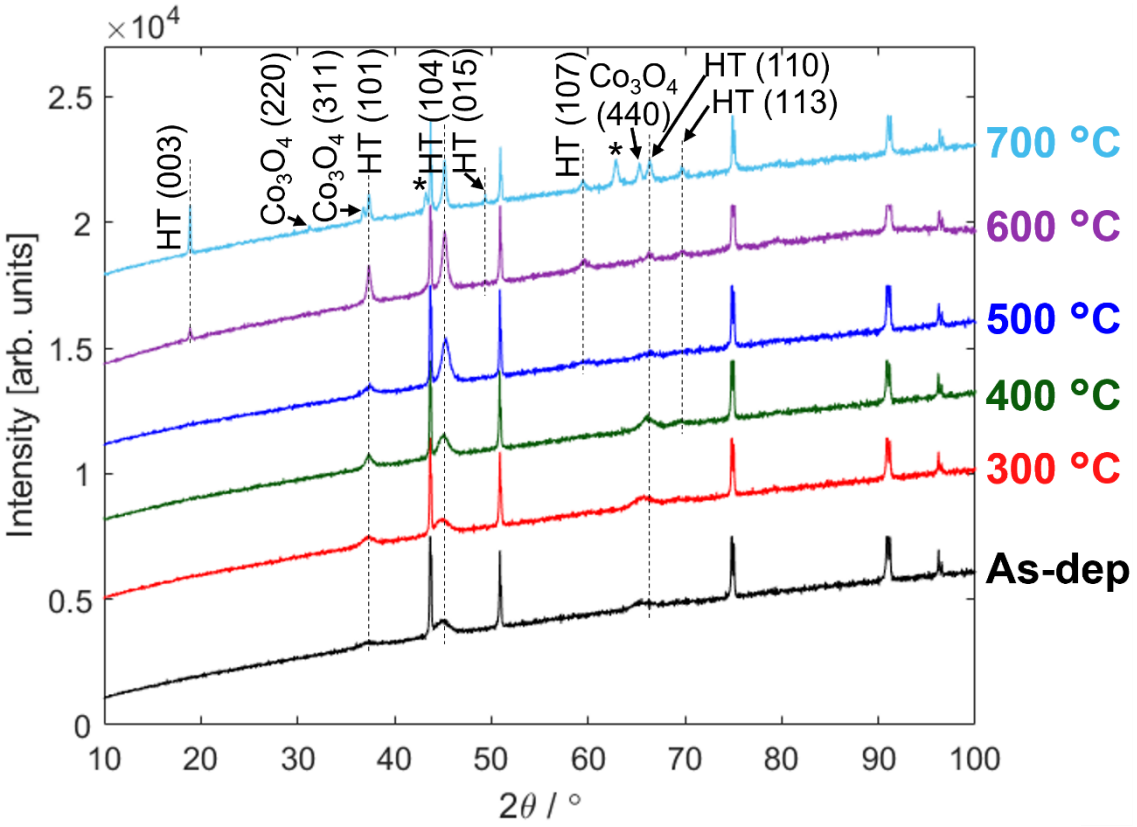


Figure 3.11 XRD patterns from LCO films deposited on Waspaloy substrates and annealed at a series of temperatures between 300 °C and 700 °C. The processing conditions are given in Table 3.7. Peaks labelled with an asterisk (*) appear on annealing at 700 °C and correspond to oxides that form on the surface of the Waspaloy. Unlabelled peaks are from the substrate or the sample holder.

The XRD patterns in Figure 3.11 have a similar appearance to those from the thinner films deposited at a lower RF power and annealed for a shorter time (Figure 3.9), although most of the HT-LCO peaks have a higher intensity relative to the substrate peaks in Figure 3.11. Part of the reason for this is the increase in film thickness, since a greater number of crystallographic planes contribute to the diffracted intensity. Nevertheless, an increase in crystallization as a result of the longer annealing time may also be partly responsible. Furthermore, the (104) and (101) relative peak intensities are more than double their values in Figure 3.9, which may reflect increased alignment of these planes with the film surface as predicted for thicker films.

The achievement of significantly increasing film thickness while also improving structural properties bodes well for cathode performance. However, it has come at the cost of an increased processing time. Therefore, it was worth investigating whether an annealing time of intermediate length (2 hours) could achieve similar structural properties. A further set of films was deposited using the conditions in Table 3.8. Since 600 °C tends to be the optimal annealing temperature regardless of the processing conditions, this was the only annealing temperature used for these films.

Table 3.8 Processing conditions used to study the effect on LCO film structure of using a shorter annealing time than used for the previous set of films (Table 3.7).

Parameter	Value
Substrate	Waspaloy foil (<100> silicon wafer for chemical characterization)
Process pressure	5×10^{-3} mbar (Ar flow rate = 50 sccm*)
RF power	250 W (5.5 W cm^{-2})
Deposition duration	4 hours
Annealing temperature	600 °C
Time at annealing temperature	2 hours
Heating rate	10 ˚C/min
Annealing atmosphere	Enclosed crucible with LCO powder bed

*Standard cubic centimetres per minute

For consistency, the thickness measurements were performed on an as-deposited film using SEM, and the range of thicknesses was found to be 2.5-3.2 μm. The film thickness can be stated as (2.8±0.1) μm (mean and standard error of the five measurements), which is slightly greater than the value of (2.62±0.05) μm determined from the five measurements performed on the film from the previous deposition. The primary reason for this discrepancy is likely to have been a slight difference in substrate positioning with respect to the target in the two deposition experiments, resulting in a small difference in the local deposition rate. The XRD pattern from the film annealed at 600 °C for 2 hours is shown in Figure 3.12, along with the

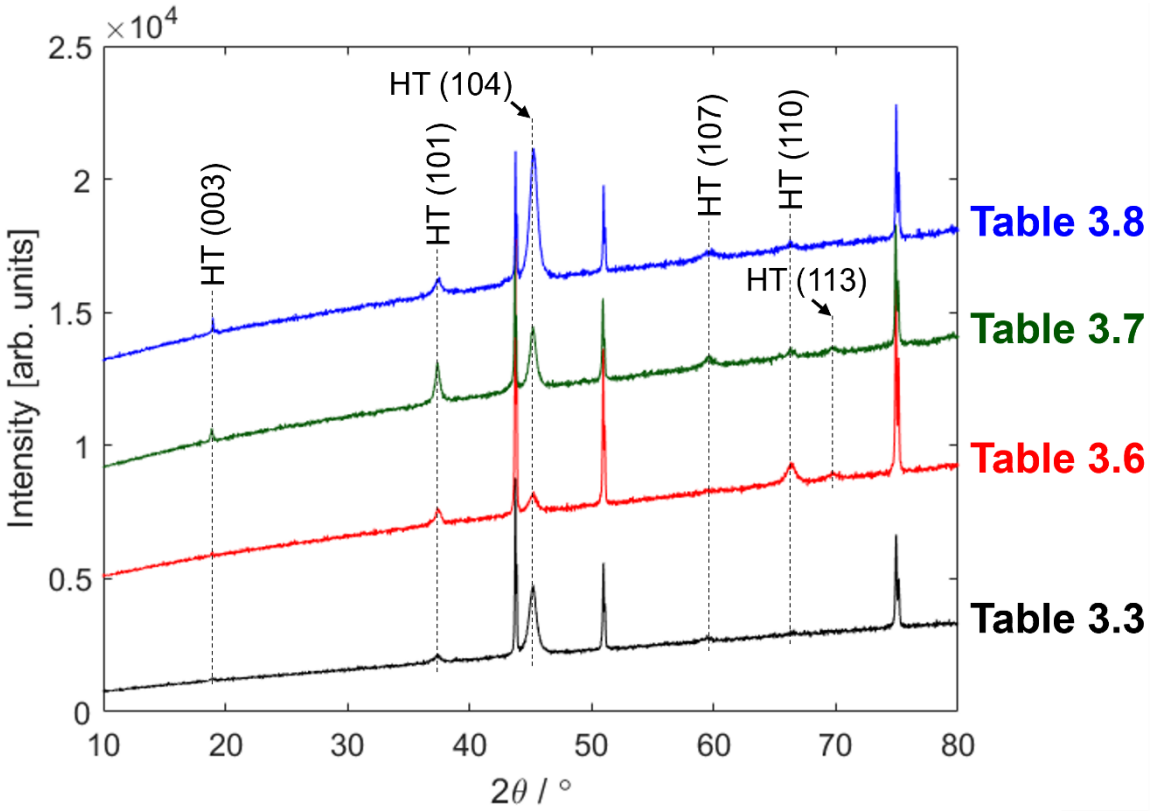


Figure 3.12 XRD patterns from LCO films deposited on Waspaloy substrates and annealed at 600 °C using the processing conditions in Table 3.3, 3.6, 3.7 and 3.8. Unlabelled peaks are from the substrate or the sample holder.

XRD patterns from all other 600 °C annealed LCO films fabricated in this investigation to allow direct comparison of the crystallographic structures.

Interestingly, reducing the annealing time from 3 hours (Table 3.7) to 2 hours (Table 3.8) increases the intensity of the HT-LCO (104) peak relative to the substrate peaks to the highest level seen in any of the patterns in Figure 3.12. There is a slight reduction in the relative intensity of the HT-LCO (101) peak, and a small (003) peak is present, but overall it is clear that the processing conditions in Table 3.8 result in the best crystallographic properties out of all the conditions tried with Waspaloy substrates.

Surface and cross-sectional view SEM micrographs of as-deposited and annealed films processed using the conditions in Table 3.8 are shown in Figure 3.13. The as-deposited film

has a similar columnar structure to that of the film deposited using the reference conditions (Figure 3.4 b)). However, the film surface in Figure 3.13 is somewhat rougher, which may be attributable to the relative unevenness of the Waspaloy substrate. This is not necessarily a problem for cathode applications; if the contact with the electrolyte is good, it may actually improve cycling performance by increasing the area of the cathode-electrolyte interface. Significant coarsening of the structure occurs on annealing, but the columnar morphology is maintained. The surface grains appear somewhat smoother than those of the films processed using the conditions in Table 3.6 and annealed at 600 °C (Figure 3.10), suggesting they are the grains that were present in the as-deposited film. Thus, the films do not appear to have undergone partial recrystallization. This is likely the reason for the preservation of the strong HT-LCO (104) // surface orientation during annealing at 600 °C; the XRD patterns in Figure 3.12 suggest that this alignment was significantly weaker in the films processed using the conditions in Table 3.6.

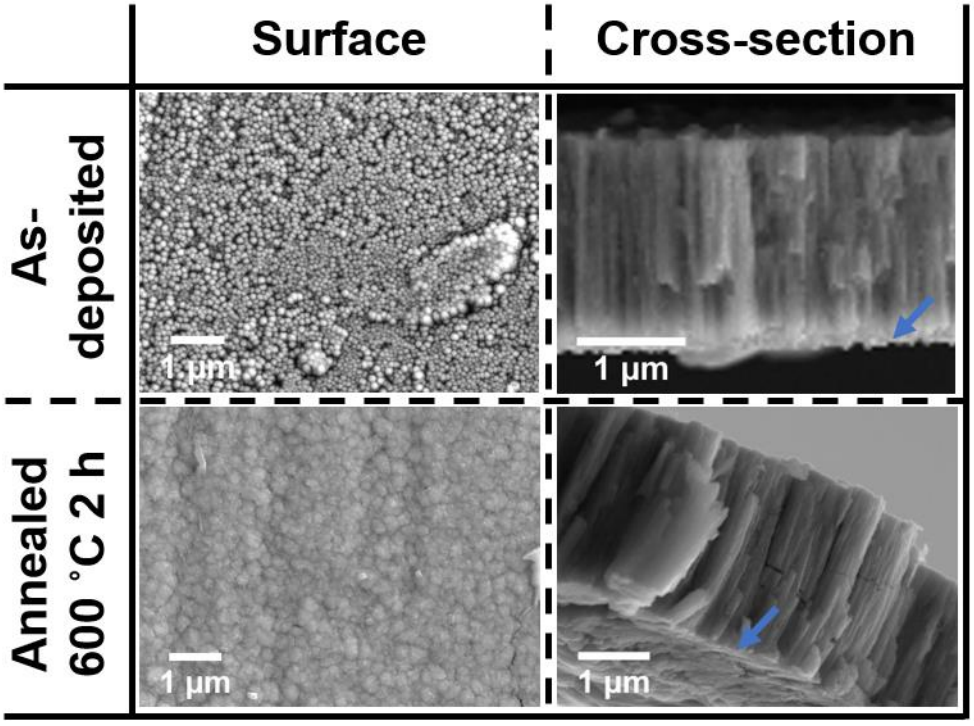


Figure 3.13 Surface and cross-sectional micrographs of the LCO films processed using the conditions in Table 3.8. The cross-sectional views show partial detachment of the films from their substrates due to plastic deformation of the Waspaloy during sectioning. The blue arrows point to the film surfaces.

Overall, the structural characterization presented here shows that it is possible to omit oxygen from the process gas and still achieve the desired HT-LCO phase purity and strong (104) // surface orientation. Furthermore, these properties are largely retained in films deposited on Waspaloy substrates when the annealing temperature is lowered, the film thickness and deposition rate are increased and the process gas usage is reduced relative to the reference conditions in Table 3.1. In other words, it is possible to achieve desirable structural properties even when the processing conditions are altered considerably to make them more appropriate for large-scale production and applications demanding higher cathode capacity.

3.3.2 Chemical Composition

After optimizing the film structure, the chemical compositions of as-deposited and annealed films on silicon substrates processed using the “optimized” conditions in Table 3.8 were determined using a combination of EDX (O/Co ratio) and ICP-OES (Li/Co ratio). Silicon substrates were used since Waspaloy contains cobalt and is unstable in the aqua regia solution used to digest the films. EDX data were obtained by performing elemental mapping at two locations on the surface of each sample. A repeat ICP-OES analysis was performed on the as-deposited sample to validate the experimental methodology. The compositions of the films are given in Table 3.9; ranges are provided for the O/Co and Li/Co ratios where repeat measurements were performed. As a single ICP-OES analysis was performed on the annealed sample, the Li/Co ratio is provided to one significant figure. These compositions are approximate due to the low quantitative accuracy of EDX (minimum uncertainty for “standardless” analysis ~2%)[248,249] compared to ICP-OES (minimum uncertainty ~0.2%)[250].

Table 3.9 Approximate compositions of as-deposited and annealed LCO films on silicon substrates, processed using the conditions in Table 3.8. The Li/Co and O/Co atomic ratios were determined by ICP-OES and EDX analysis, respectively. Ranges are provided in cases where a repeat measurement was performed.

Sample	Overall Composition
As-deposited	$Li_{(0.57\text{-}0.60)}CoO_{(1.89\text{-}1.90)}$
Annealed	$Li_{0.8}CoO_{(1.73\text{-}1.75)}$

As has been reported previously[209,242], the as-deposited film was deficient in lithium. It also had a slight oxygen deficiency, which may have been a consequence of the lack of oxygen in the process gas. The lithium deficiency may explain why the single broad film peak in the XRD patterns from as-deposited films is present at a lower angle than expected for HT-LCO (104), since the rhombohedral LCO unit cell is known to expand as lithium is removed[251]. Ménétrier *et al.*[252] prepared samples of Li_xCoO_2 with values of x in the range $0.5 \leq x \leq 1.0$ and studied them using XRD. Their measured lattice parameters for $Li_{0.60}CoO_2$ (similar to the as-deposited composition in Table 3.9) show that the 2θ position of the (104) peak (45.0°) is ~0.2° below that for a fully lithiated film and matches the value measured for the as-deposited film in Figure 3.11. Therefore, this provides evidence that the as-deposited films fabricated using the conditions in Table 3.8 (and Table 3.7) contain nanocrystalline HT-LCO.

Interestingly the lithium content of the film increased on annealing, demonstrating the benefit of adding LCO powder to the annealing environment. Although the oxygen deficiency increases on annealing, it was evidently insufficient to destabilize the HT-LCO structure. The fact that HT-LCO appears to be the stable phase of LCO in both annealed and as-deposited films is the critical finding: as long as the layered structure remains stable during electrochemical cycling, the lithium deficiencies should be eliminated by the lithium transferred from the anode.

3.3.3 Electrochemical Characterization

The optimized processing conditions in Table 3.8 were used to produce a series of as-deposited and annealed LCO films on circular Waspaloy substrates. These were incorporated into coin cells as cathodes along with an organic liquid electrolyte and lithium anode. Various experiments were performed to investigate the electrochemical properties of the LCO film and Waspaloy substrate.

3.3.3.1 Galvanostatic Cycling Between 3.0 V and 4.3 V *vs* (Li^+/Li)

Galvanostatic cycling between 3.0 and 4.3 V *vs* (Li^+/Li) was performed for 50 cycles at a rate of 0.1 C to investigate the medium-term cycling performance of the LCO cathode films. 4.3 V was chosen as the upper voltage limit since this is generally recognized as the highest potential that can be reached before significant structural degradation of the $LiCoO_2$ occurs[253–255]; using this value should therefore maximize the accessible capacity. The results from the best-performing cells are shown in Figure 3.14 and Table 3.10.

The cycling curves recorded from the annealed cathode in Figure 3.14 b) have roughly the appearance expected for LCO thin films, approaching a plateau at ~3.9 V. This tendency is seen to a lesser extent in the cycling curves from the as-deposited films in Figure 3.14 a), which is to be expected considering they were nanocrystalline and possibly contained some amorphous material[111]. Differential capacity plots were constructed from the cycling data and are shown in Figure 3.15. Both plots show peaks on charge and discharge near 3.9 V, although they appear at a slightly lower potential in the plot for the as-deposited cathode and are broader, supporting the observations from the cycling curves in Figure 3.14. In both plots, the separation between the pairs of charge and discharge peaks increases with cycle number, reflecting the increasing polarization by the growing internal resistance of the cell. However, this occurs to a much greater degree in the plot from the annealed film.

A key observation from the cycling curves and plots of capacity versus cycle number for both as-deposited and annealed films is that the early cycling behaviour is erratic, with large

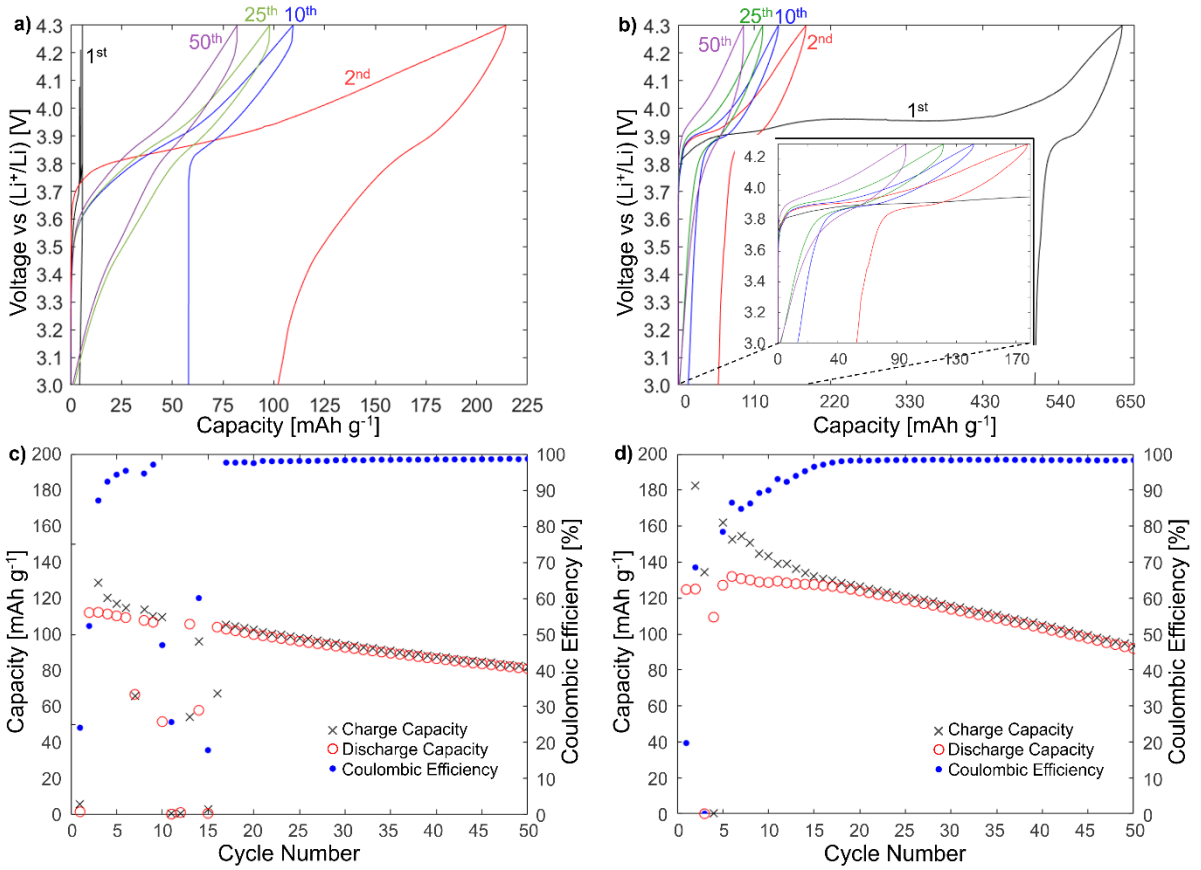


Figure 3.14 Galvanostatic cycling performance of cells with as-deposited and annealed LCO cathode films fabricated using the conditions in Table 3.8 and cycled between 3.0 and 4.3 V *vs* (Li^+/Li) at 0.1 C for 50 cycles. Charge-discharge curves recorded at several different stages of the cycling experiment are shown for a) as-deposited and b) annealed LCO cathodes. Plots showing the charge and discharge capacities and the Coulombic efficiency over the course of the cycling experiment are shown for c) as-deposited and d) annealed LCO cathodes. The anomalously large first cycle charge capacity has been removed from d) to allow for the use of a more appropriate scale.

fluctuations in the values of charge and discharge capacity. The as-deposited cathodes display this behaviour for 17 cycles, while it only took 6 cycles for the capacity fluctuations of the annealed cathode to disappear. The first cycle specific charge capacity of the annealed cathode was anomalously large at 634 mAh g^{-1}, which is almost 5 times the theoretical value of 137 mAh g^{-1} when $0.5Li^+$ is transferred. This value was not plotted in Figure 3.14 d) so that a more appropriate scale could be used for the rest of the data. While the first cycle charge capacity of the as-deposited cathode was close to zero, the second cycle charge capacity

Table 3.10 Key performance figures for the LCO cathode films.

	As-deposited	Annealed
Film mass (with standard error)[a]	(2.2±0.2) mg	(2.3±0.1) mg
Film thickness (with standard error)[b]	(3.00±0.04) μm	(2.77±0.02) μm
Current to achieve 0.1 C cycling rate	30 μA	31 μA
Maximum discharge capacity	247 μAh (3rd cycle)	304 μAh (6th cycle)
Maximum areal discharge capacity[c]	140 μAh cm^{-2}	172 μAh cm^{-2}
Maximum specific discharge capacities (% of theoretical for 0.5Li extracted)[d]	112 mAh g^{-1} (82%) 47 μAh $cm^{-2}\mu m^{-1}$ (67%)	132 mAh g^{-1} (96%) 62 μAh $cm^{-2}\mu m^{-1}$ (90%)
50th cycle specific discharge capacities[d]	81 mAh g^{-1} 34 μAh $cm^{-2}\mu m^{-1}$	92 mAh g^{-1} 43 μAh $cm^{-2}\mu m^{-1}$
Percentage of maximum discharge capacity remaining in the 50th cycle	72%	70%
Average discharge capacity decrease from maximum per cycle	0.59%	0.69%

[a]Mass measurements were made prior to annealing since the Waspaloy substrate underwent a mass gain during annealing that could not be determined reliably.
[b]The thickness is the mean value of at least five measurements made on other LCO films fabricated in the same deposition process.
[c]The area of the cathode was assumed to be equal to the area of the Waspaloy substrate.
[d]LCO film thickness and mass measurements were used to normalize the absolute capacity values.

was unusually large (214 mAh g^{-1}). For both cathodes, most of this excess capacity was not released on discharging, leading to Coulombic efficiencies of 52% (2nd cycle) and 20% (1st cycle) for the as-deposited and annealed cathodes, respectively. Although the charge and discharge capacities of subsequent cycles were somewhat lower, the increase in Coulombic efficiency with cycle number was rather slow for both films, only stably rising above 95% in the 17th and 14th cycles of the as-deposited and annealed cathodes, respectively. Excess charge capacities in the early stages of cycling are to be expected when a lithium metal

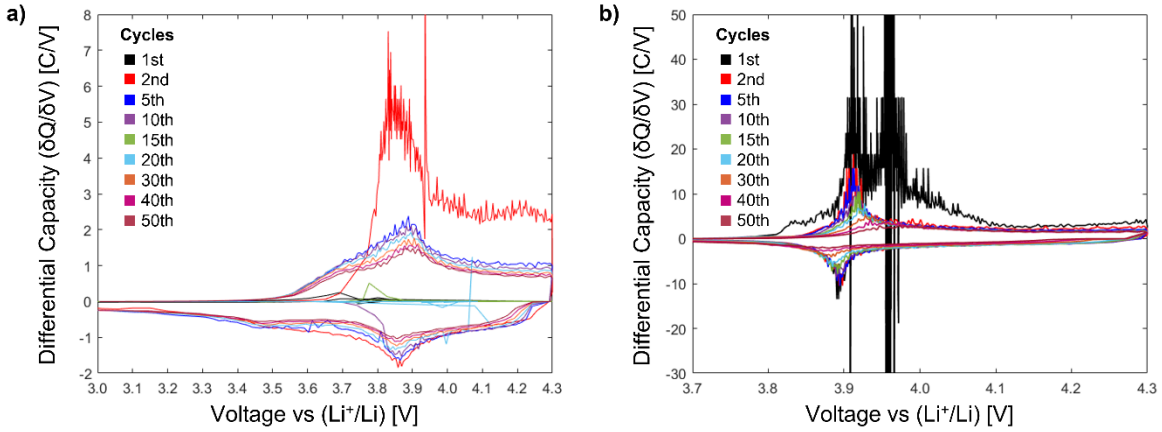


Figure 3.15 Differential capacity (δQ/δV) plots for a) the as-deposited and b) the annealed LCO cathode.

anode is used in conjunction with an organic liquid electrolyte, since charge is consumed in the reduction of the electrolyte to form the passivating SEI layer. However, this cannot fully account for the behaviour seen here, since first cycle Coulombic efficiencies reported previously for LCO films cycled under similar conditions (but over a voltage range of 3.0 to 4.2 V *vs* (Li^+/Li)) are often over 80%[193,196,201,204,215,231]. It is likely that a large proportion of the excess capacity seen on charging in this work can be attributed to the oxidation of the Waspaloy substrate if the passivating oxide layer had not fully formed prior to LCO film deposition. This may also explain the erratic cycling behaviour and why the increase in Coulombic efficiency took longer for the as-deposited film, as some degree of oxidation would occur during annealing.

The maximum specific discharge capacity of the annealed cathode (Table 3.10) was high on both a mass and a volumetric basis; the latter was only slightly lower than the highest published value for LCO films of 67 μAh cm^{-2}μm^{-1}, reported by Tintignac *et al.*[202] for a bias sputtered and annealed film cycled at a rate of 0.2 C over 3.0 to 4.2 V *vs* (Li^+/Li). Moreover, the maximum areal discharge capacity achieved here was significantly higher than the value of 33.5 μAh cm^{-2} reported by Tintignac *et al*. for their 0.5 μm thick cathode due to the much greater cathode thickness reported here (~2.8 μm). This value is also higher than achieved in most previous reports[192,193,196,201,202,206,221,231,242] (most of these used a voltage range of 3.0 to

4.2 V *vs* (Li^+/Li), but one used an upper cutoff of 4.25 V[192] and another used 4.3 V[206]) owing to the fact that the majority of LCO films reported previously were thinner than 1 μm. In a later report, Tintignac *et al.*[215] fabricated a 3.6 μm thick LCO cathode, achieving an areal capacity of ~200 μAh cm^{-2} on discharging at rate of 0.1 C from 4.2 to 3.0 V *vs* (Li^+/Li). Although this areal discharge capacity value is slightly higher than that reported here, the specific capacity was lower: ~56 μAh $cm^{-2}\mu m^{-1}$ compared to the value of 62 μAh $cm^{-2}\mu m^{-1}$ reported here. This suggests that cathodes fabricated using the processing conditions reported in this work may outperform the 3.6 μm thick cathode reported by Tintignac *et al.* if the deposition time is increased to achieve the same cathode thickness.

The retention of 70% of the maximum discharge capacity after 50 cycles compares favourably to most other reports in which an organic liquid electrolyte has been used[192,193,196,197,208,241], which is particularly significant considering the films studied here are somewhat thicker than in most of the reports, and capacity fading has been found to be more rapid in thicker films[111]. Discrepancies between the values of capacity normalized by mass and by film volume as a fraction of the theoretical specific capacities can be attributed to the fact that the films would not have been fully dense. The density likely increases on annealing, which is why the maximum specific discharge capacity (by volume) of the annealed film is somewhat higher as a fraction of the theoretical value than that of the as-deposited film.

Considering that the HT-LCO phase in the as-deposited cathode was nanocrystalline and the film may have contained some amorphous material, its electrochemical performance was remarkably good. The maximum specific discharge capacity (by mass) was 82% of the theoretical value for the extraction of $0.5Li^+$. Furthermore, the discharge capacity retained over 50 cycles was 2% higher than that retained by the annealed cathode, and the rate of capacity loss seen in Figure 3.14 c) decreased with cycle number, whereas it increased with cycle number for the annealed film, as seen in Figure 3.14 d). Very few previous studies on thin-film LCO cathodes have performed galvanostatic cycling on as-deposited films that were

not subjected to substrate heating or potential biasing during deposition. In those that have, the as-deposited films have either demonstrated a significantly lower maximum discharge capacity (~1% of the theoretical value[208]) or a higher rate of capacity loss during cycling (average of ~1.3% per cycle over 25 cycles[196]) than reported here. The results of this work raise the prospect that adequate cathode performance is achievable without post-deposition annealing for some applications when appropriate deposition conditions are used, which would greatly simplify processing and reduce manufacturing costs.

The erratic behaviour at the beginning of cycling for both as-deposited and annealed LCO films is undesirable in practical applications and must be investigated further. A study of the differential capacity plots in Figure 3.15 provides more information about the processes occurring in the early stages of cycling. In the plot from the annealed film in Figure 3.15 b), an additional peak is seen in the first cycle at a potential between 3.9 V and 4.0 V. This peak is absent in subsequent cycles and could reflect the oxidation of the Waspaloy, which occurs rapidly in the first cycle and somewhat more slowly in subsequent cycles due to surface passivation. The second cycle in the plot from the as-deposited film also contains an additional peak, but this occurs at a higher potential (~4.2 V). Nevertheless, this peak is shallow and part of a broader region of intensity than seen in the first cycle of the plot for the annealed film, which could reflect the lower degree of passivation in the as-deposited sample prior to starting the experiment. Interestingly, in the plot from the as-deposited film, the main peak in the second cycle is at a lower potential (~3.85 V) than the main peaks in subsequent cycles (~3.89 V). This may be a result of the polarization that occurs after the oxide growth in the second cycle. In both plots there is a significant drop in peak intensity in subsequent cycles, which highlights the fact that most of the passivation of the Waspaloy substrate occurs right at the beginning of cycling. Nevertheless, it takes several cycles for the Coulombic efficiency to rise above 95%, signalling that passivation continues through the early stages of cycling.

3.3.3.2 Characterization of the Waspaloy/LCO Interface

To isolate the behaviour of the Waspaloy substrate from that of the LCO cathode, cyclic voltammetry was performed in the 3.0 to 4.3 V *vs* (Li^+/Li) potential range on a bare Waspaloy substrate which had been subjected to the annealing conditions in Table 3.8 and assembled into a coin cell with lithium metal on the negative side and the same liquid electrolyte as used previously. The results are shown in the CV plot in Figure 3.16. After cell assembly, the OCV was ~0 V; however, the cell was allowed to rest for 13 days before performing CV, by which time the OCV had risen to 2.57 V. This was therefore the starting voltage for the first forward scan. This increase in OCV suggests that the Waspaloy and electrolyte reacted to some degree during the rest period to form a product with a potential of ~2.6 V *vs* (Li^+/Li).

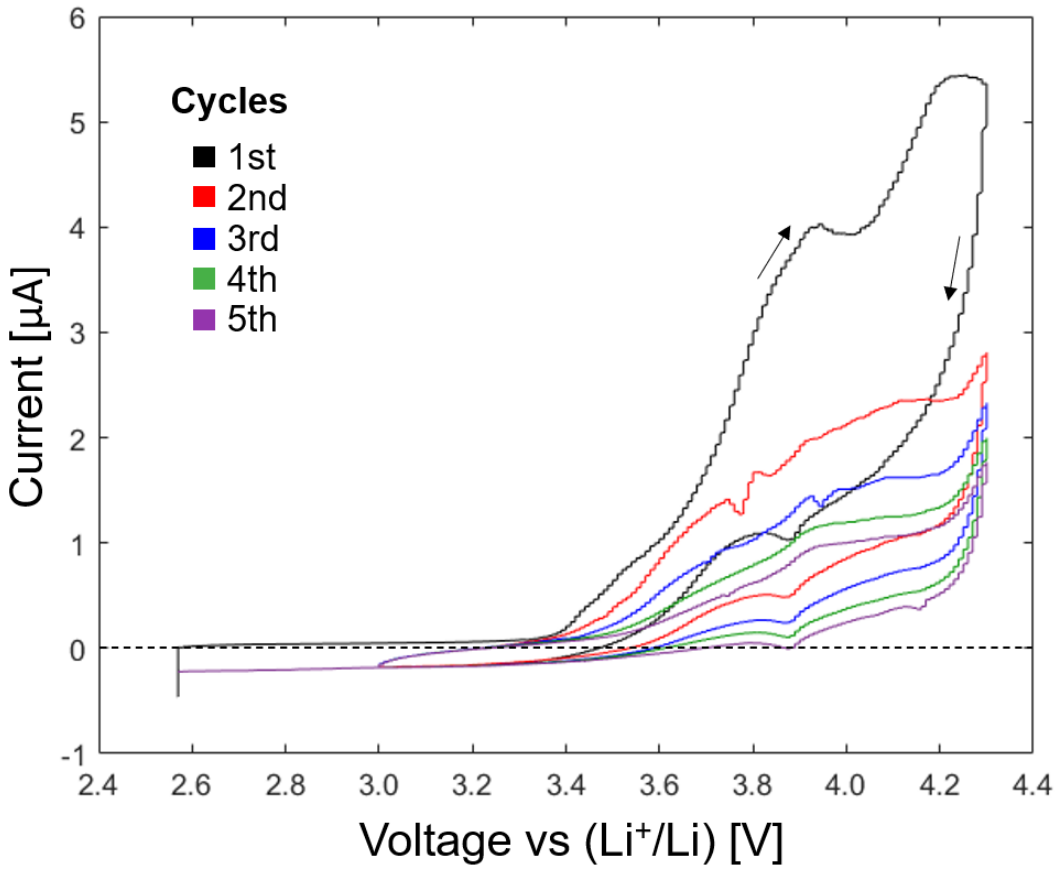


Figure 3.16 CV plots for bare Waspaloy annealed using the conditions in Table 3.8 and tested between 3.0 V and 4.3 V *vs* (Li^+/Li) for 5 scans at a nominal rate of 0.033 mV s^{-1}.

As expected from the analysis of the differential capacity plots in Figure 3.15, the greatest oxidation currents were measured during the first scan, and the values measured during the second scan are significantly lower. In subsequent scans the current drops further, but by somewhat smaller amounts, reflecting the ongoing passivation of the Waspaloy surface during the early stages of cycling. Below ~3.5 V the current becomes negative, signalling the onset of reduction, but the maximum reduction current is 0.18 μA, which is only 3.4% of the maximum oxidation current. The fact that reduction does not start until the voltage has dropped from 4.3 V to ~3.5 V in the first scan shows that the system is initially far from equilibrium at the scan rate used. This deviation from equilibrium could explain the erratic and sometimes negligible discharge capacities measured for both cathodes in the early stages of cycling (Figure 3.14), since oxidation of the Waspaloy may occur simultaneously with reduction of the LCO. In subsequent scans, the potential at which reduction begins increases, showing that passivation brings the system closer to equilibrium. Equilibrium, and hence passivation, may have been reached more quickly in the galvanostatic cycling shown in Figure 3.14 owing to the fact that the potential did not change at a constant rate and for most of the cycling it was in the 3.8 to 4.2 V range. As shown by Figure 3.16, the oxidation rate of the Waspaloy is relatively high over this potential range.

Two peaks in the oxidation current are visible in the first forward scan in Figure 3.16, the first at 3.94 V and the second between 4.24 and 4.26 V, which reaches the maximum current of 5.44 μA. Interestingly, these two peaks correspond to the positions of the additional peaks in the differential capacity plots from the annealed film (first cycle) and as-deposited film (second cycle), respectively. This provides further evidence that the additional peaks, and hence the excess first/second cycle charge capacities, were associated with Waspaloy oxidation. In subsequent scans, the peak current is always seen at the highest potential (4.3 V), suggesting that a reduction in the upper potential limit would help to limit the ongoing oxidation of the Waspaloy substrate responsible for the low Coulombic efficiency in the early stages of cycling.

The changes in chemical composition in the region of the Waspaloy/LCO interface during cycling were studied by measuring EDX composition profiles along the surfaces of trenches milled by PFIB in an uncycled annealed sample and the annealed sample that was cycled in the experiment reported earlier (Figure 3.14). The results are shown in Figure 3.17. The cycled film in Figure 3.17 b) is a little thicker than the uncycled film in a), but this is attributed to variations in local deposition rate with sample position in the deposition chamber rather than an effect of cycling. Both films have a similar composition across the majority of their thickness, displaying an O/Co ratio of ~2, as expected for $LiCoO_2$. The SEM images show that the LCO film remains well adhered to the Waspaloy substrate during cycling, which is essential for a reliable, high-performance cathode. Prior to cycling, small peaks in the Ti and Al concentrations are present in the composition profiles at the Waspaloy/LCO interface, which suggests that the native oxide layer – or that formed during annealing – mainly consisted of Ti and Al oxides. It is difficult to determine whether any elemental diffusion between the LCO and Waspaloy layers occurred since the EDX scans were performed while the samples were at 52° tilt about the axis parallel to the interface and trench surface, which had the effect of decreasing the spatial resolution. However, it is clear that no long-range interdiffusion occurred.

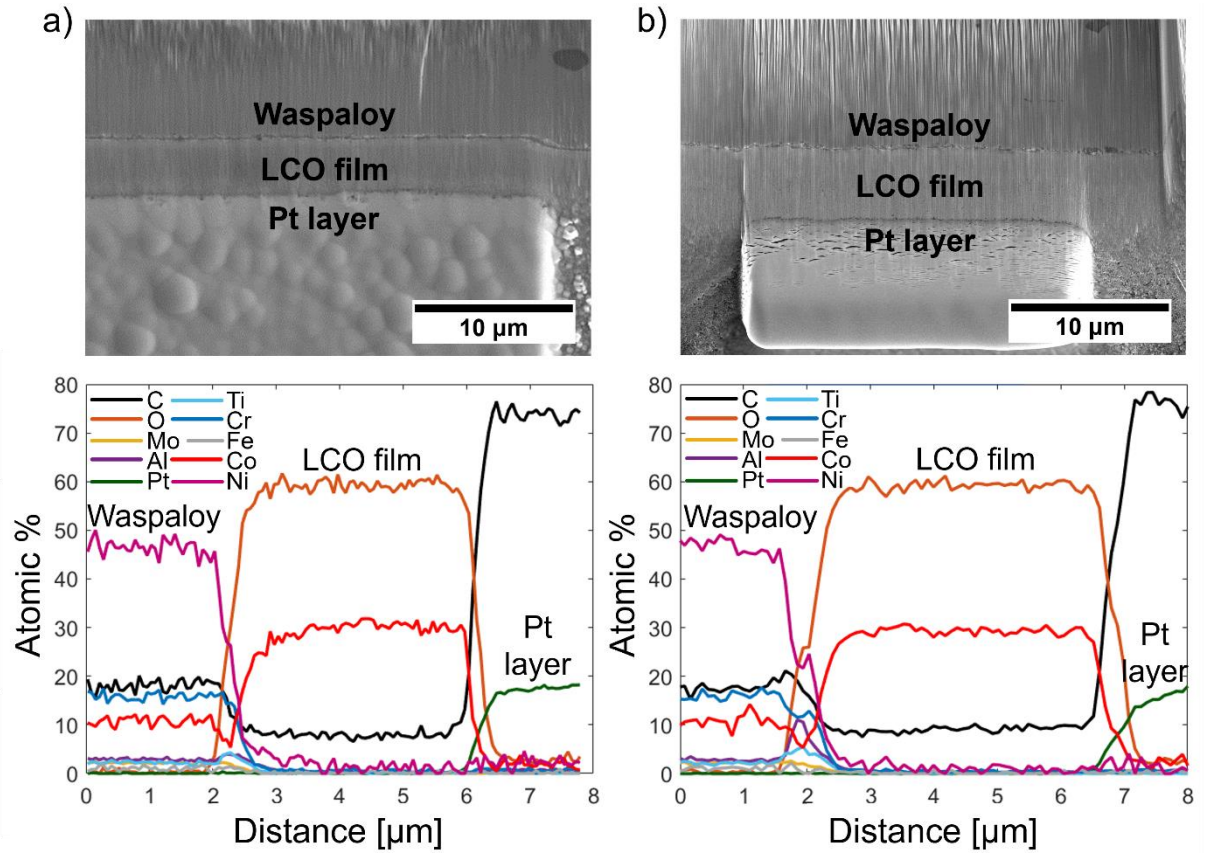


Figure 3.17 Secondary electron micrographs of the glancing trench surfaces produced by PFIB sectioning and composition profiles measured perpendicular to the sample interfaces using EDX for (a) an uncycled LCO thin film fabricated using the conditions in Table 3.8 and (b) the LCO film cycled at 0.1 C for 50 cycles. The Pt layer ("strap") was deposited within the PFIB to protect the LCO surface during milling by the xenon ion beam. As EDX is unable to detect lithium, the atomic concentrations plotted do not account for the concentration of lithium present. The PFIB sectioning, SEM imaging and EDX data collection used to create this figure were performed by Dr Junliang Liu.

After cycling, the peak in Al concentration at the Waspaloy/LCO interface is significantly higher and is accompanied by new peaks in Cr and Ni concentrations, implying that the oxides of these elements formed at the interface during cycling. The Ti peak is also slightly higher. These observations support the interpretation of the galvanostatic cycling and CV data discussed earlier.

3.3.3.3 Structural Changes in the LCO Films During Cycling

While the decline in excess charge capacity and accompanying increase in Coulombic efficiency during the early stages of cycling can be attributed to oxidation and passivation of the Waspaloy substrate, the decline in discharge capacity over the cycling experiments is likely a result of structural changes occurring within the LCO cathode film. To investigate the structural changes, XRD was performed on the as-deposited and annealed films cycled earlier and the diffraction patterns were compared to those from the uncycled films. The results are shown in Figure 3.18.

There was little discernible change in the crystallographic structure of the as-deposited film during cycling, which may be a consequence of the nanocrystalline character of this film. The annealed film exhibited much clearer crystallographic changes: some of the HT-LCO phase predominant in the uncycled film transformed to Co_3O_4 during cycling. Since Co_3O_4 is electrochemically inactive, it is clear why this transformation would lead to capacity loss. This may explain why the rate of capacity fading of the annealed film was slightly higher than that of the as-deposited film, although other structural changes could have occurred in the as-deposited film that were not revealed by XRD such as cobalt dissolution into the electrolyte. Co_3O_4 formation[256,257] and cobalt dissolution[253,254] have been reported in several previous studies as consequences of overcharging LCO cathodes, so the observation of Co_3O_4 formation in this work suggests that reducing the upper voltage limit may improve cycling stability. In both sets of patterns in Figure 3.18, little evidence of oxide growth on the Waspaloy substrate can be seen, but this is likely due to the thinness of the oxide layer, its low degree of crystallinity, and attenuation of the X-ray beam by the LCO film.

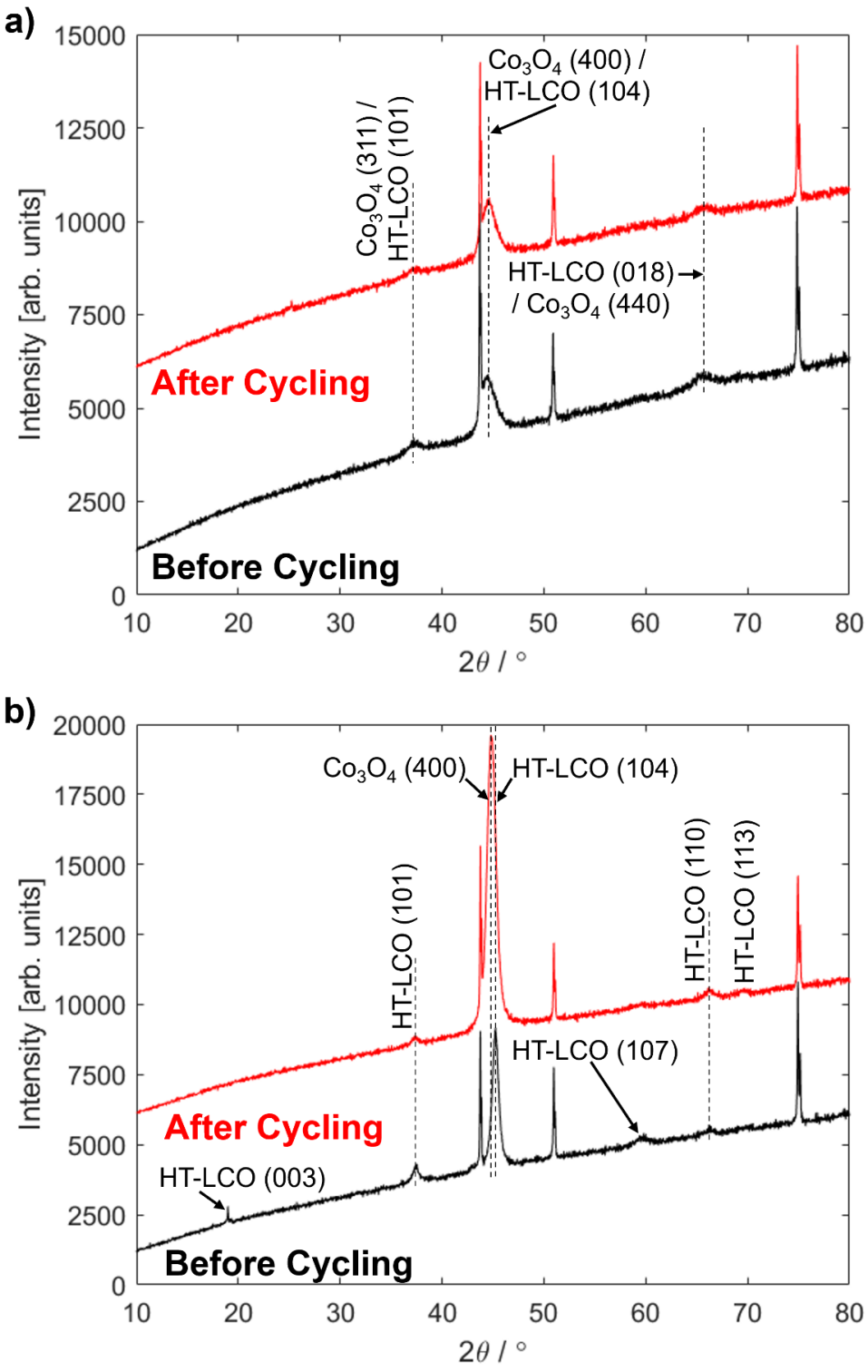


Figure 3.18 XRD patterns from a) as-deposited and b) annealed LCO films recorded after the galvanostatic cycling shown in Figure 3.14. Patterns from uncycled samples are also plotted for comparison. Unlabelled peaks are from the substrate or the sample holder.

3.3.3.4 Improving Cycling Stability and Measuring Rate Performance

The results discussed so far have revealed two separate processes that have a negative effect on the cycling performance: oxidation of the Waspaloy substrate and structural degradation of the LCO cathode. The CV plots in Figure 3.16 suggest that reducing the upper voltage limit used in galvanostatic cycling from 4.3 V to 4.2 V would help to reduce the rate at which the Waspaloy oxidizes, but since little time is spent at the higher voltages during galvanostatic cycling the effect may be small. Nevertheless, reducing the upper voltage limit should help to limit the structural degradation of the LCO cathode. Removing the native oxide layer from the Waspaloy substrate prior to LCO deposition may lead to steadier, more controlled oxidation during annealing and the subsequent cycling. Thus, for the next set of cycling experiments – which aimed to study the effect of cycling rate on capacity – the upper voltage limit was reduced to 4.2 V and the native oxide layer was removed by grinding prior to LCO deposition. Galvanostatic cycling was performed at a series of different cycling rates, with the required currents calculated using the measured LCO film mass of (2.1 ± 0.2) mg and the theoretical specific capacity when $0.5Li^+$ is transferred. The initial 10 cycles were performed at 0.1 C (29 μA), followed by 5 cycles at 0.5 C, 5 cycles at 1 C, 5 cycles at 2 C, 5 cycles at 5 C, and a final 5 cycles at 0.1 C. The results of this cycling experiment are shown in Figure 3.19, and corresponding differential capacity plots are shown in Figure 3.20 for selected cycles. Only an annealed film was tested since the as-deposited film used in the previous galvanostatic cycling experiment did not show clear structural degradation during cycling, so any ameliorating effect from reducing the upper voltage limit would not have been clear.

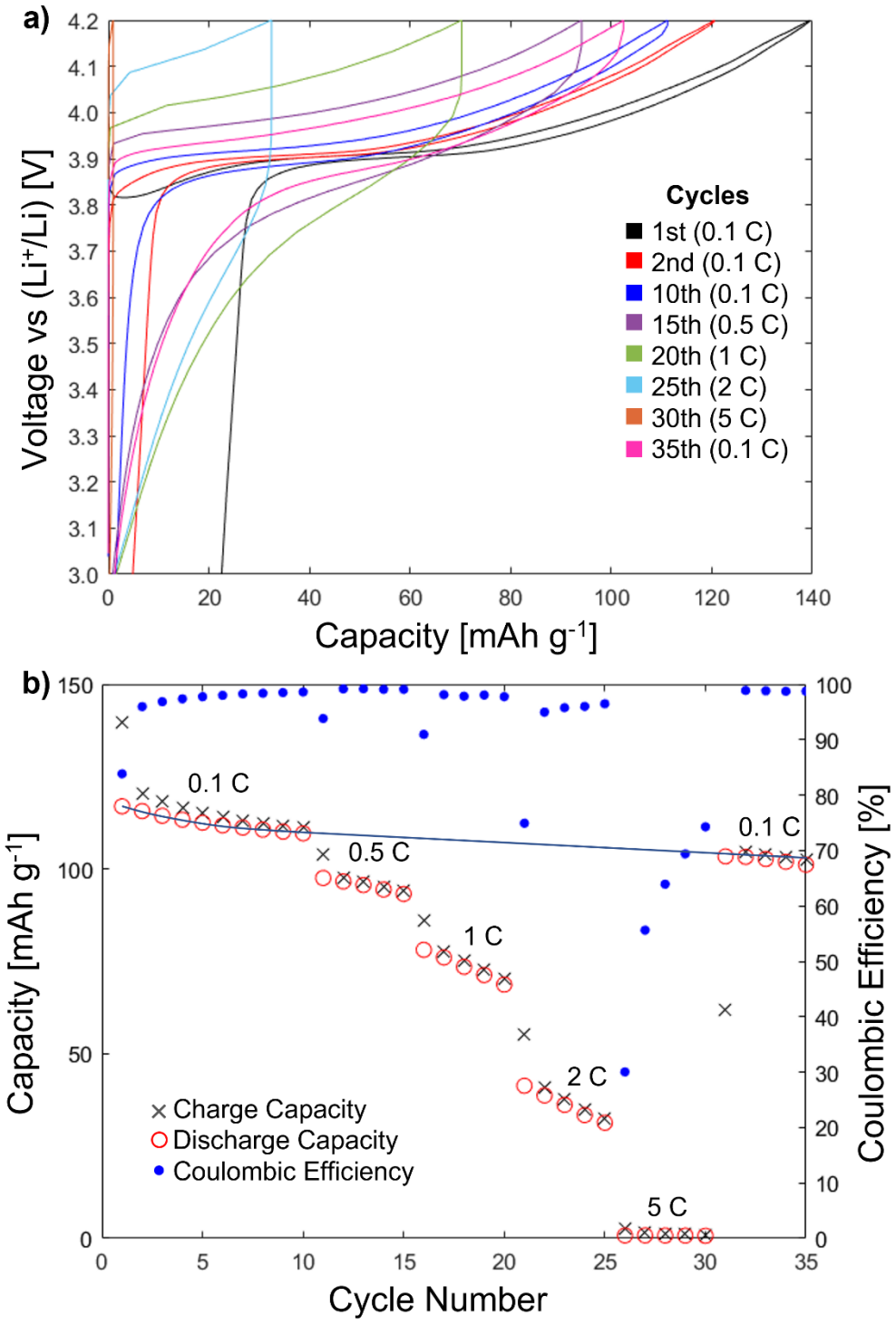


Figure 3.19 Galvanostatic cycling performance of a cell with an annealed LCO thin-film cathode fabricated using the conditions in Table 3.8 and cycled between 3.0 and 4.2 V *vs* (Li^+/Li) at a series of different currents corresponding to C-rates of 0.1, 0.5, 1, 2 and 5 C. The native oxide layer was removed from the Waspaloy discs prior to LCO deposition. Charge-discharge curves recorded at several different stages of the cycling experiment are shown in a), while the plot in b) shows the charge and discharge capacities and the Coulombic efficiency over the course of the cycling experiment. The blue curve highlights the trend set by the first 10 cycles at 0.1 C and extrapolates it to the 35th cycle.

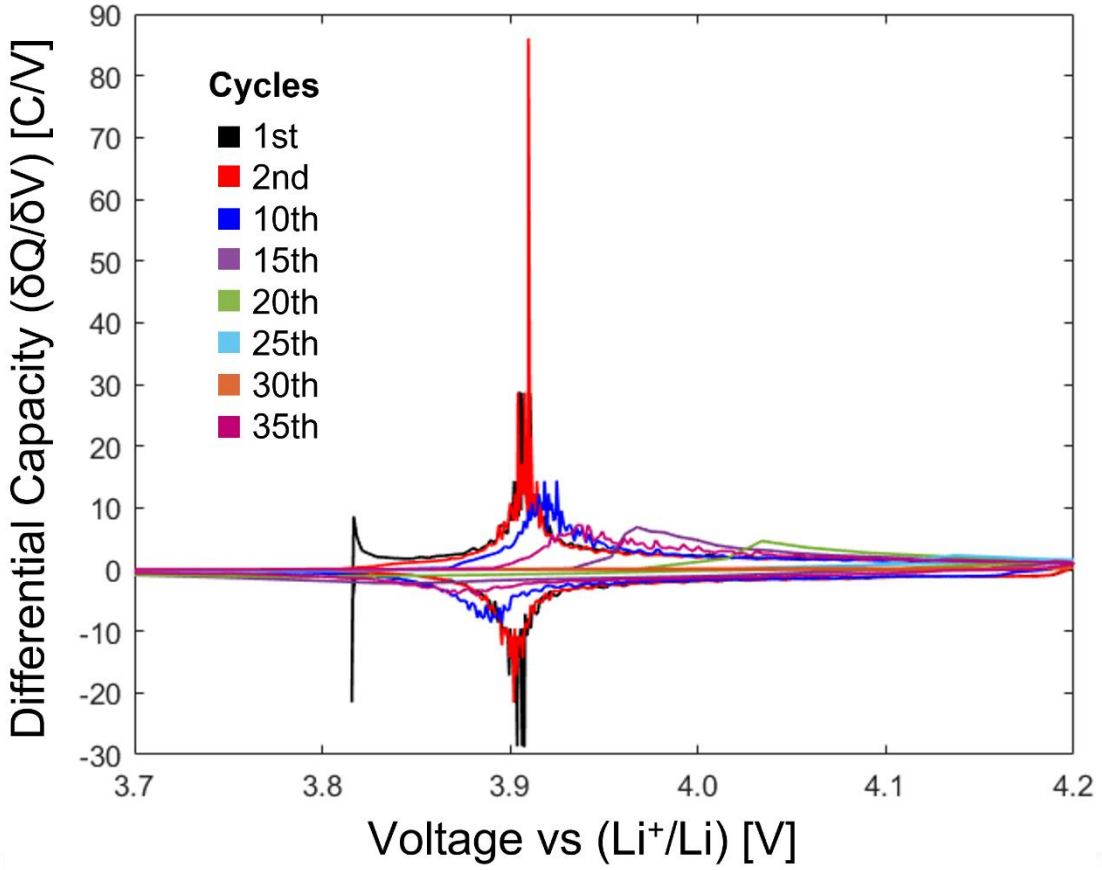


Figure 3.20 Differential capacity (δQ/δV) plots for selected cycles from Figure 3.19.

The absence of an additional oxidation peak in the first cycle on the differential capacity plot in Figure 3.20 indicates that the rapid oxidation of Waspaloy between 3.9 V and 4.0 V seen in Figure 3.15 b) did not occur here, which must have been due to removing the native oxide layer. As a result, the excess charge capacity of the first cycle at 0.1 C (Figure 3.19) is much smaller than seen for the annealed film in the previous galvanostatic cycling experiment (Figure 3.14), and the Coulombic efficiency reaches 96% in the second cycle. Furthermore, the capacity values follow the overall trend closely and do not display the erratic fluctuations seen previously. The maximum specific discharge capacity, which occurred in the 6th cycle in the previous experiment, is seen in the first cycle, and has a value of 117 mAh g^{-1}. While this value is approximately 89% of that measured in the previous experiment, most of this lost capacity should be attributable to the reduced upper voltage limit used here, as extrapolation of the cycling curve in Figure 3.19 a) to 4.3 V suggests.

As expected, the charge and discharge capacities decrease markedly with each increase in cycling rate and the rate of capacity fading within each cycling segment increases. Despite this, reasonable performance was still obtained at a rate of 0.5 C; the discharge capacity of the 11th cycle was 98 mAh g^{-1} (83% of the maximum value) and the average rate of capacity decrease from this value over the 5 cycles was 0.88%, which is not significantly higher than that seen over the first 10 cycles at 0.1 C (0.63%). Even at a rate of 1 C, the discharge capacity achieved in the 16th cycle was 78 mAh g^{-1}, which is 2/3 of the maximum discharge capacity, but the average capacity decrease per cycle over the 5 cycles increased to 2.4%. At a rate of 2 C, the discharge capacity measured in the 21st cycle was 41 mAh g^{-1} with an average capacity decrease per cycle of 4.9% over the 5 cycles, but at 5 C almost no charge could be transferred, and the discharge capacity was <1 mAh g^{-1} for each of the 5 cycles. Interestingly, on decreasing the cycling rate back to 0.1 C for the final 5 cycles, the capacity values increased to a level that was not far below that of the trendline extrapolated from the first segment of cycling at 0.1 C, suggesting that little permanent structural degradation due to the segments of high-rate cycling occurred in the cathode. Resilience against permanent structural degradation in thin film LCO cathodes during short periods of high-rate cycling has been reported previously, albeit for much thinner films (~400 nm)[204]. The differential capacity plot in Figure 3.20 appears to confirm the structural stability of the LCO films studied here; the increasing separation between oxidation and reduction peak pairs with increasing cycling rate suggests that most of the capacity loss at high cycling rates was due to polarization by the internal resistance of the cell rather than structural degradation. Nevertheless, the greater separation of the peaks in the final cycle at 0.1 C compared to that seen in the 10th cycle at 0.1 C indicates that a small amount of permanent structural degradation did occur, resulting in an increase in the internal resistance.

Across the entire experiment the average discharge capacity decrease per cycle from the maximum value was only 0.39%, which is just under 2/3 of the value calculated for the first 35 cycles of the similar cathode in the previous galvanostatic cycling experiment (0.61%).

This rate of capacity loss is lower than most previous reports for similar cells. Tintignac *et al.*[202] claimed to have achieved (to their knowledge) the best capacity retention for an LCO film cycled in the 3.0 to 4.2 V range in a liquid electrolyte cell. They reported an average discharge capacity decrease per cycle (over 50 cycles) from the maximum value of 0.2%. Crucially, their constant cycling rate of 0.2 C was somewhat lower than the average cycling rate used in this work, and the authors used much thinner (500 nm) LCO films. Therefore, it appears that the reduction of the upper voltage limit from 4.3 V to 4.2 V greatly reduced the structural degradation of the LCO cathode in this work, and the intrinsic cycling stability of these cathodes is one of the highest reported for cycling in liquid electrolyte cells.

Two additional cells were prepared and tested together with the cell reported above to assess the repeatability of the cycling behaviour. The results from the testing of these cells, along with the cell reported above ("Cell 3") are plotted together in the figure in Appendix A. The initial and final discharge capacities of Cell 2 are 112 mAh g^{-1} and 96 mAh g^{-1}, respectively, which are 96% and 95% of the corresponding values for Cell 3. Thus, the capacities and rates of capacity fade are very similar for Cell 2 and Cell 3, although the rate performance of Cell 2 at 0.5–2 C is somewhat worse. The initial and final discharge capacities of Cell 1 are 105 mAh g^{-1} and 83 mAh g^{-1}, respectively, which are 90% and 82% of the corresponding values for Cell 3. A possible explanation for the lower capacities and capacity retention of Cell 1 compared to the other two cells is that its cathode film may have undergone a greater degree of exfoliation during annealing or cell construction; this was not accounted for when calculating the current required for cycling and the specific capacity values. Therefore, the actual specific capacity and C-rate values for Cell 1 may have been slightly higher than stated. Developing a technique to determine the actual cathode mass more accurately should reduce the variability in the cycling results of similar cells.

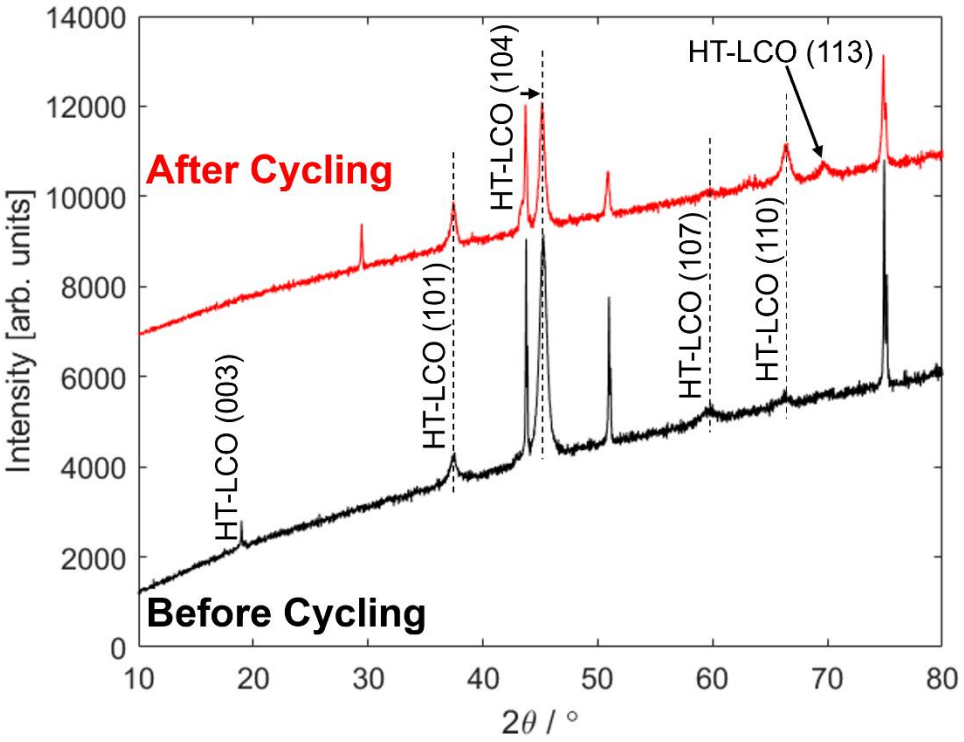


Figure 3.21 XRD patterns from the LCO cathode subjected to galvanostatic cycling between 3.0 V and 4.2 V for 35 cycles at a series of different rates (Figure 3.19). The pattern from an uncycled sample is also plotted for comparison. Unlabelled peaks are from the substrate or the sample holder.

To investigate the structural stability further, XRD was performed on the cathode cycled in the present experiment (corresponding to the cycling results in Figure 3.19). The measured diffraction pattern is plotted alongside the pattern from an uncycled sample in Figure 3.21. Comparing the diffraction patterns in Figure 3.21 indicates that no phase transformation occurred during the rate test cycling experiment, with the only differences between the patterns being minor changes in the intensities of the HT-LCO peaks relative to those of the substrate. This contrasts with the results of the structural characterization performed after the previous galvanostatic cycling experiment in Figure 3.18 b), which showed partial transformation from the HT-LCO phase to the delithiated, electrochemically inactive Co_3O_4 phase. These results confirm that reducing the upper potential limit from 4.3 V to 4.2 V increased the structural stability of the LCO cathode film during galvanostatic cycling,

resulting in less permanent capacity loss per cycle. However, reducing the upper potential limit did come at the cost of a lower maximum discharge capacity.

3.4 Conclusions

Thin LCO cathode films were fabricated by RF magnetron sputtering and post-deposition annealing using a set of processing conditions better-suited to large-scale manufacturing than those reported by the majority of previous studies. Early in the investigation, it was found that a lightly compacted LCO powder target could be used in place of a sintered target and that oxygen could be removed from the process gas with no deleterious effects on the structural properties of the resulting films. These measures would simplify the manufacturing process and reduce costs. The deposition conditions were refined iteratively to increase the deposition rate, since this is desirable for manufacturing productivity. Overall, the process pressure was reduced from the reference value of ~1×10^{-2} mbar to 5×10^{-3} mbar and the RF power density was increased from 2.2 W cm^{-2} to 5.5 W cm^{-2}, which increased the deposition rate by a factor of 3-4 and reduced the use of process gas. Despite assertions in the literature that a relatively high process pressure (~10^{-2} mbar) is required to achieve good structural properties, the (104), (101) and (110) planes of the HT-LCO phase exhibited a high degree of parallel alignment with the film surface, which is favourable for Li^+ insertion and extraction. A very small amount of unfavourable (003) // surface alignment was also observed, but this did not appear to have a significant impact on the electrochemical properties. Furthermore, the volume fraction of electrochemically inactive secondary phases such as Co_3O_4 was so low as to be undetectable by XRD.

The post-deposition annealing conditions were also optimized to achieve the best balance between film structure and manufacturability. Unlike in most literature reports, LCO powder was added to the annealing atmosphere and this was found to *increase* the concentration of lithium in the films, in stark contrast to the lithium loss that is often observed during annealing. This helped to stabilize the desired HT-LCO phase and avoid the formation of

Co_3O_4. Although the best structural properties resulted from annealing at 600 °C, adequate structural properties were also achieved at significantly lower annealing temperatures than typically used for LCO films. Furthermore, galvanostatic cycling experiments revealed that even an as-deposited film – which contained nanocrystalline HT-LCO – demonstrated a reasonable level of performance: its maximum specific discharge capacity was 85% of that displayed by the annealed film and its rate of capacity fading during cycling was slightly lower. In some applications these properties may be sufficient, and the benefits of drastically simplifying the manufacturing process may outweigh the reduction in electrochemical performance.

The maximum specific discharge capacities of the annealed film cycled between 3.0 and 4.3 V at 0.1 C (132 mAh g^{-1} and 62 µAh $cm^{-2}µm^{-1}$) were close to the theoretical maxima when $0.5Li^+$ is extracted (136.9 mAh g^{-1} and 69.1 µAh $cm^{-2}µm^{-1}$) and only slightly lower than the highest published value for a thin film LCO cathode (67 µAh $cm^{-2}µm^{-1}$)[202]. Furthermore, the maximum areal discharge capacity (172 µAh cm^{-2}) was higher than most values reported previously owing to the fact that few studies have investigated LCO films thicker than reported in this work. It is striking that despite the relative thickness of the cathode films reported here and the consequently higher rate of structural degradation that might be expected, 70% of the maximum discharge capacity was retained after 50 cycles between 3.0 V and 4.3 V at 0.1 C, which is comparable with previous reports on cycling in organic liquid electrolytes. Moreover, when cycled between 3.0 and 4.2 V, the rate of capacity loss over 35 cycles was lower than almost all previous reports[202], despite the inclusion of segments of high-rate cycling (up to 5 C). These cathodes delivered reasonable discharge capacities up to a rate of 1 C and short bursts of current could be provided at 2 C without any significant structural degradation.

A major limitation to the performance of the cathodes tested in the first galvanostatic cycling experiment was the oxidation and gradual passivation of the Waspaloy substrate, which led

to excessive charge capacities in the early stages of cycling and erratic fluctuations in the discharge capacity. As a result, it took 14 cycles for the Coulombic efficiency to rise above 95%. This issue was almost fully overcome by removing the incomplete native oxide layer from the Waspaloy prior to LCO deposition and reducing the upper voltage limit from 4.3 V to 4.2 V. The reduction in the upper voltage limit also reduced the structural degradation of the LCO film itself during the second cycling experiment, even though it was subjected to segments of high-rate cycling (up to 5 C). While this came at the cost of a lower maximum discharge capacity (89% of the specific value by mass achieved in the initial experiment), the rate of capacity fading per cycle was reduced to just under 2/3 of the value seen in the initial experiment. Thus, the choice of voltage limit in practical applications will depend on the required balance between power density and cycle life.

Although this work has shown that Waspaloy sheet is a suitable substrate and current collector for LCO thin films, metallized ceramic substrates may be more appropriate for the envisaged application of thin-film cells in microscale devices. Indeed, many prior investigations on thin LCO cathodes have used silicon wafers coated with precious metals such as Pt and Au. It is expected that a metallic film with a similar composition to Waspaloy should exhibit similar behaviour to that seen in this investigation for the polished Waspaloy substrates, and replacing the precious metal films with a nickel-based alloy should lead to significant cost reductions. Whichever substrate is chosen, these thin-film cathodes must be tested in all-solid-state thin-film cells to verify that their performance is sufficient in this cell format.

Although this investigation was concerned with optimizing processing conditions for large-scale manufacturing, when designing an actual manufacturing process, the “optimized” set of conditions reported here must be refined further for the specific production line equipment used. Nevertheless, this work has demonstrated the principle that processing conditions can be optimized for manufacturing without sacrificing electrochemical performance. Some of the

discoveries made here, such as the viability of removing oxygen from the process gas and using lower annealing temperatures as well as the benefit of adding LCO powder to the annealing atmosphere, should be relevant regardless of the processing equipment used. When designing a deposition system, the effect of target-to-substrate distance should also be considered to achieve the best balance between deposition rate and film properties. Although next-generation cathode materials such as LMNO are starting to arouse interest in the thin-film battery field, the principles demonstrated here are also applicable to the processing of these materials. Indeed, consideration of the manufacturing route is essential for any materials proposed for application in thin-film batteries.

4 Fabrication of Lithium-Rich Antiperovskite Chloride Electrolytes by RF Magnetron Sputtering

A significant proportion of the work reported in this chapter was first reported in the following published research article: Turrell, S. J., Lee, H. J., Siniscalchi, M., Narayanan, S., Pasta, M., Speller, S. C. & Grovenor, C. R. M. Fabrication of thin solid electrolytes containing a small volume of an Li_3OCl-type antiperovskite phase by RF magnetron sputtering. *Materials Advances* **3**, 8995–9008 (2022)[258].

4.1 Introduction and Aims of This Work

Lithium-rich antiperovskites (LiRAPs) are a class of solid electrolyte that has attracted increasing attention since high values of Li^+ conductivity – 2.5×10^{-3} S cm^{-1} at 443 K and 8.5×10^{-4} S cm^{-1} at room temperature – were reported for lithium oxychloride (Li_3OCl) by Reckeweg *et al.*[141] and Zhao and Daemen[142], respectively, in 2012. Since then, numerous computational and several experimental studies on Li_3OCl and lithium hydroxide chloride (Li_2OHCl) have been reported. Aside from high ionic conductivity, other envisaged benefits of LiRAPs include low densities, cost, toxicity[145] and electronic conductivities[142,259] as well as good stability against lithium metal, particularly in the case of oxyhalides such as Li_3OCl which contain no cations reducible by lithium[260]. While Li_3OCl and Li_2OHCl are the archetypal LiRAP compounds, compositions containing other halogens such as Br and F have also been studied[143]. In most of these compounds, a cubic structure is predicted to be stable, as shown in Figure 4.1 a) for Li_3OCl. Li_2OHCl is an exception, as it has an orthorhombic structure below ~35 °C (Figure 4.1 b)) but is cubic at higher temperatures[72,259,261,262].

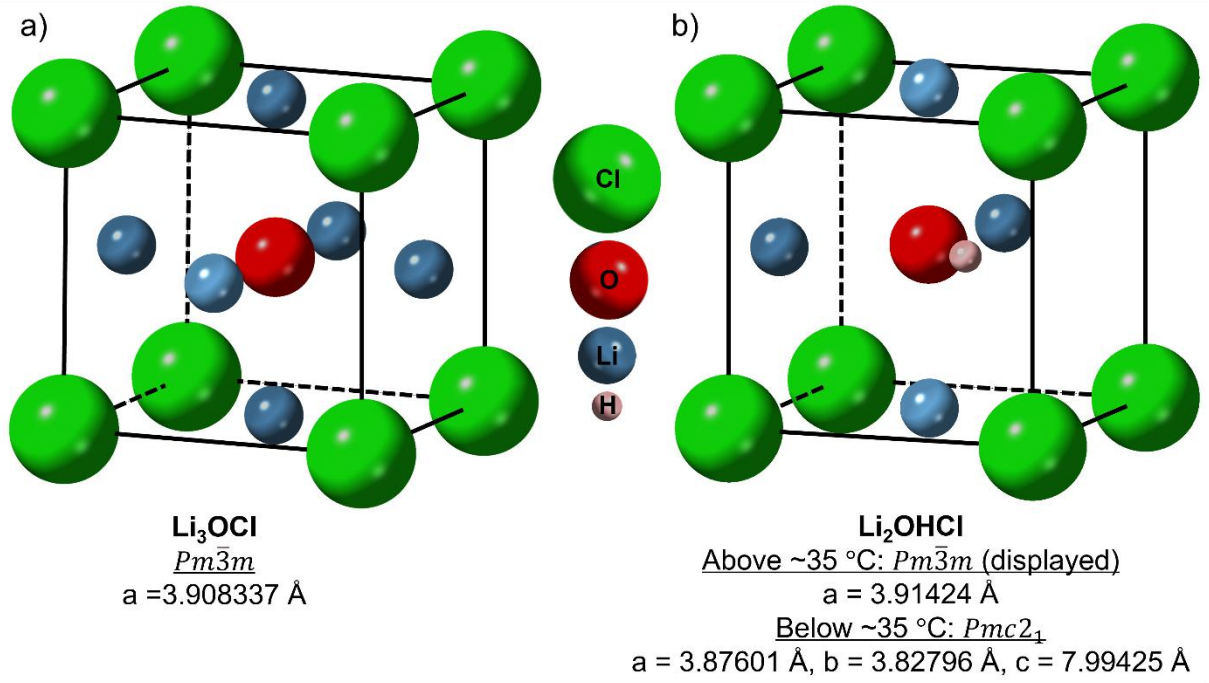


Figure 4.1 Crystallographic structures of a) Li_3OCl[263,264] and b) Li_2OHCl[72,259,261,262,265]. In Li_2OHCl, OH^- resides at the site that is occupied by O^{2-} in Li_3OCl, and only two thirds of the cation sites are occupied by Li^+; the remainder are vacant[143,259]. Li_2OHCl, The structures were visualized using CrystalMaker®: CrystalMaker Software Ltd, Oxford, England (www.crystalmaker.com).

Several recent articles[71,143,152,262] have been critical of studies claiming to have fabricated Li_3OCl, even suggesting that this compound may not be synthesizable[143]. At the heart of this controversy are two attributes of Li_3OCl which make its synthesis challenging: 1) it is predicted to be thermodynamically unstable at room temperature, with a driving force for decomposition by equation 4.1[73,266–271], and 2) it is extremely hygroscopic, meaning that any Li_3OCl formed is likely to react to form Li_2OHCl *via* equation 4.2[73,269,272] unless moisture and other sources of OH are eliminated from the synthesis environment. Although the thermodynamic instability of Li_3OCl has been known since the *ab initio* study by Zhang *et al.*[266] was published in 2013, subsequent synthesis attempts may have been performed in anticipation that sluggish decomposition kinetics at room temperature can "freeze" the compound in a metastable state[273]. However, this justification for continued synthesis attempts is rarely stated in published reports.

$$Li_3OCl \rightarrow Li_2O + LiCl \qquad \textbf{Equation 4.1}$$

$$Li_3OCl + H_2O \rightarrow Li_2OHCl + LiOH \qquad \textbf{Equation 4.2}$$

To compound these synthesis challenges, Li_3OCl and Li_2OHCl have very similar crystal structures and are indistinguishable in XRD patterns[152,262,273,274]. It is likely that many – if not all – previous studies claiming to have synthesized Li_3OCl inadvertently formed Li_2OHCl due to the use of inappropriate synthesis techniques, inadequate exclusion of H and OH from the synthesis and characterization environments and the use of characterization techniques unable to discriminate between Li_3OCl and Li_2OHCl[143,152]. Ideally, all syntheses of Li_3OCl would be performed with Li_2O and LiCl precursors, following the reaction in equation 4.3. However, studies have reported limited interdiffusion between the reactants, making solid-state synthesis difficult[142,275]. Melt processing has also been tried, but the reaction in equation 4.4 is usually targeted since the melting point of LiOH (462 °C) is much lower than that of Li_2O (1438 °C) and similar to that of LiCl (605 °C)[126,142,274,276,277].

$$Li_2O + LiCl \rightarrow Li_3OCl \qquad \textbf{Equation 4.3}$$

$$2LiOH + LiCl \rightarrow Li_3OCl + H_2O \qquad \textbf{Equation 4.4}$$

The clear issue with attempting the reaction in equation 4.4 is that the water produced as a by-product can react with the Li_3OCl to form Li_2OHCl and LiOH, even if attempts are made to remove it as it forms.

A wide range of Li^+ conductivities has been reported for "Li_3OCl" (1.26×10^{-7} S cm^{-1} to 8.5×10^{-4} S cm^{-1})[126,142,144,274,277], which is evidence of the widely varying phase purities, microstructures and degrees of hydration achieved in the various studies. Surprisingly, the range of Li^+ conductivities reported for Li_2OHCl is even wider (6.83×10^{-9} S cm^{-1} to ~4×10^{-5} S cm^{-1})[72,259,261,262]. These observations demonstrate the poor understanding of the processing-

structure-properties relationships pertaining to these LiRAP compounds. Nevertheless, Li_2OHCl has recently been found to form a passivating SEI layer in contact with lithium metal, which should provide good stability during cell cycling[72]. Therefore, based on current understanding, LiRAP compounds may be well-suited to application as protective layers for lithium metal anodes or as electrolytes in all-thin-film cells; minimizing the LiRAP thickness will minimize its contribution to the overall cell impedance, which will be important if high ionic conductivities cannot be achieved. However, there have been very few reports on the fabrication of LiRAP films using PVD techniques[126,144], and none of these used RF magnetron sputtering – the best-suited of all PVD techniques to large-scale manufacturing[43,278,279].

The primary aim of this work was to investigate the application of RF magnetron sputtering to the synthesis of Li_3OCl. Aside from the relevance of thin-film processing to the envisaged applications of LiRAPs, RF magnetron sputtering has several advantages over the standard ceramic processing routes used in previous studies. First, deposition is performed under vacuum, so the moisture content of the synthesis environment is negligible. Second, sputtering involves the atom-by-atom transfer of material from the target to the substrate, mixing the precursor elements and overcoming the diffusion limitations experienced previously[43,280]. Although the synthesis of Li_3OCl by pulsed laser deposition (PLD) was reported by one research group[126,144], no evidence for the absence of O-H bonding in the resulting films was provided. In this work, characterization techniques that distinguish between Li_3OCl and Li_2OHCl will be performed to determine whether Li_3OCl has been synthesized successfully. The second aim of this work was to produce a set of Li_2OHCl films by RF magnetron sputtering and post-deposition annealing. When characterizing a metastable, hygroscopic compound such as Li_3OCl, it is highly beneficial to have a sample of the likely decomposition product (Li_2OHCl in this case) in a similar format to determine whether any decomposition has occurred. Even if the Li_2OHCl phase is not synthesized successfully, the presence of O-H bonding in the film samples will enable the effectiveness of

the characterization techniques used to detect O-H bonding to be verified. A secondary objective was to develop a basic understanding of the processing-structure-properties relationships pertaining to thin films deposited from Li_2OHCl targets, since Li_2OHCl has also attracted significant interest as a solid electrolyte material[71–73,152,259,261,262,265,269,272,281–286] yet there have been no prior reports on the fabrication of Li_2OHCl thin films by RF magnetron sputtering.

4.2 Experimental Methods

4.2.1 Preparation of Substrates and Sputtering Targets

Soda-lime glass, silicon (various suppliers), stainless steel (Fe-18Cr-8Ni [wt%], 304 stainless steel, Goodfellow Cambridge Ltd.) and Waspaloy ((58Ni-19Cr-14Co-Mo-Ti-Al-Fe [wt%], HAYNES® 282® alloy, Goodfellow Cambridge Ltd.) were used as substrates for electrolyte film deposition. Glass and silicon were chosen owing to their smooth surface finishes, allowing highly conformal electrolyte and metal films to be deposited onto them. Furthermore, the fact that glass does not give rise to peaks in XRD patterns aided the study of film structures by avoiding peak overlap. Stainless steel and Waspaloy were chosen based on their oxidation resistance, which will be necessary if the electrolyte films require annealing, and for their electronic conductivity; it could be simpler to use bulk metallic substrates rather than metal-coated ceramic substrates for through-plane impedance measurements.

The glass, silicon and alloy substrates were cut from microscope slides, undoped <100> oriented polished wafers and 250 μm sheets, respectively, into approximately 10 mm × 10 mm square pieces. The alloy substrates were ground and polished, finishing with a 3 μm grade diamond suspension to achieve a surface free of visible scratches. All substrates were cleaned by sonication in distilled water and isopropanol prior to film deposition. Ni and Pt layers were sputter deposited on some of the glass substrates prior to electrolyte film deposition; the main purpose of this was to produce samples for through-plane EIS measurements (see Section 2.5.1).

The design of the Li_2O + LiCl sputtering target was similar to that used by Lü *et al.*[144] for the fabrication of "Li_3OCl" by PLD, except that in the present investigation the powder was not pressed into a pellet. All stages of target preparation were performed inside an argon-filled glovebox (MBraun) with O_2 and H_2O concentrations below 0.1 ppm to avoid hydration of the reactants. To produce each target, 1.502 g of Li_2O (99.5 % purity, Sigma Aldrich) and 2.141 g of LiCl (≥99.0 % purity, Sigma Aldrich) powders (1:1 molar ratio) were mixed by grinding with an agate pestle and mortar for approximately 10 minutes. The powder mixture and the substrates and utensils required for preparing the target were dried in the heated antechamber of the glovebox under vacuum (~1 mbar) at 80 °C for at least 2 hours to remove any residual moisture, except where indicated in Section 4.3.1. The powder was then poured into a 2" diameter circular copper holder (1 or 2 mm deep depending on the experiment – see Section 4.3.1) and lightly pressed and levelled using a glass microscope slide. A photograph and a schematic diagram of the ~2 mm deep holder are shown in Figure 4.2.

The Li_2OHCl sputtering target was prepared from Li_2OHCl powder. To obtain the powder, 1.935 g of LiOH (≥99.0 %, Sigma-Aldrich) and 3.426 g of LiCl (≥99.0 % purity, Sigma Aldrich) were ground and heated at a rate of 5 °C min^{-1} to 350 °C in a muffle furnace (KSL-1100X, MTI Corporation) located within a glovebox (MBraun) with O_2 and H_2O concentrations below 0.5 ppm. This temperature was held for 30 minutes to enable complete reaction between the precursors in the molten state. After this, the liquid Li_2OHCl was removed from the furnace and allowed to cool to room temperature. The resulting solid mass was ground with a mortar and pestle to produce Li_2OHCl powder, which was poured into a 2" copper powder target holder and lightly pressed and levelled using a glass microscope slide. The successful synthesis of Li_2OHCl was verified by performing XRD and comparing to published structures[259,265], followed by FT-IR to confirm the presence of O-H bonding.

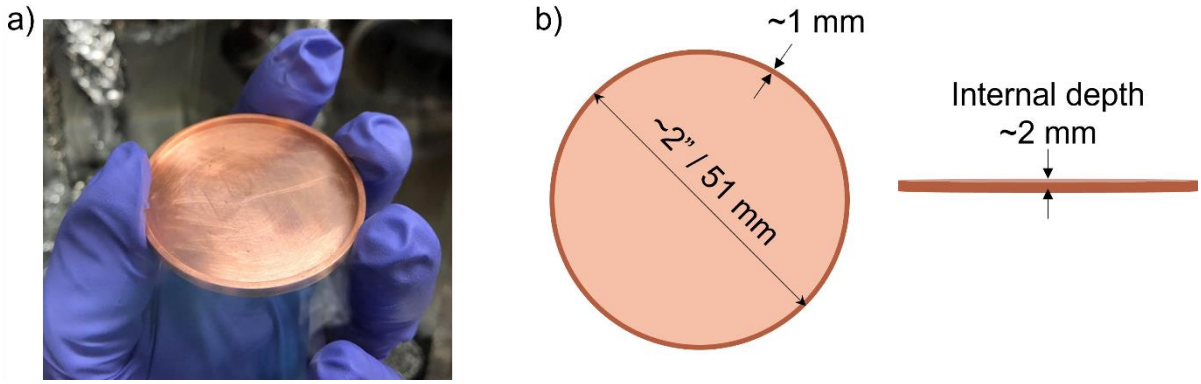


Figure 4.2 a) Photograph and b) schematic diagram of the ~2 mm deep, 2" diameter powder sputter target holder.

4.2.2 Thin Film Deposition and Post-Deposition Annealing

A PVD system (MB EVAP, MBraun) installed within a glovebox (MBraun) with O_2 and H_2O concentrations below 0.1 ppm was used for the RF magnetron sputter deposition of metal and antiperovskite thin films. This system contained a circular magnetron source (Gencoa Ltd) tilted towards the substrate holder from the vertical by ~30°, as shown in the photograph of the deposition chamber and annotated schematic in Figure 4.3. The target-to-substrate distance was ~12 cm, and substrate heating was not employed. The chamber was pumped down to achieve a base pressure below 5×10^{-5} mbar or 1×10^{-6} mbar for metal and antiperovskite deposition, respectively.

Owing to the lack of previous reports on sputter deposition from Li_2O + LiCl and Li_2OHCl targets, the deposition process had to be developed from scratch. The first part of the results section (Section 4.3.1) reports on the development of this process, and detailed sputter deposition conditions are listed there. Once a set of "optimized" conditions had been reached, films for structural, chemical and electrical characterization were deposited. For these deposition runs, pre-deposition sputtering of the Li_2O + LiCl targets was performed for approximately 30 minutes. However, this step was omitted for deposition from the Li_2OHCl target due to uncertainty over the length of time the target would remain stable during sputtering. In all deposition processes, BOC Pureshield argon (99.998 % purity) was used as

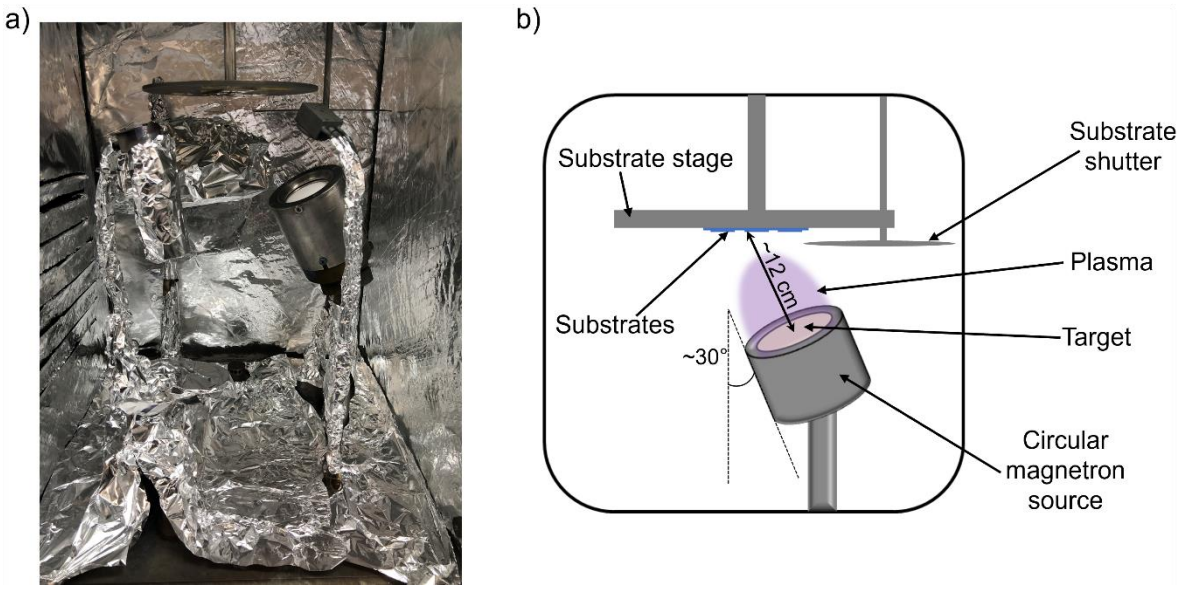


Figure 4.3 a) Photograph and b) schematic diagram of the MBraun MB EVAP PVD chamber used for the deposition experiments reported in this investigation. The photograph was taken immediately prior to an electrolyte layer deposition with the substrates and target loaded, while the schematic diagram shows an active deposition process.

a process gas. BOC N2.6 Zero Grade oxygen (99.6 %) purity was also used in depositions from Li_2O + LiCl targets.

Post-deposition annealing was performed on certain samples (as detailed in Section 4.3.2) using an alumina crucible and the same muffle furnace as that used for Li_2OHCl synthesis. This required the transfer of samples from the glovebox containing the PVD system to the glovebox containing the furnace; samples were stored in sealed glass vials to protect them during transfer, which typically took less than 5 minutes. A controlled heating rate of 5 °C/min was used for the annealing. After annealing, the samples were allowed to cool within the furnace at its natural rate to limit thermal stresses and consequent film cracking and delamination. After processing, all samples were stored inside a glovebox (MBraun) with O_2 and H_2O concentrations below 0.1 ppm awaiting characterization.

4.2.3 Structural Characterization

The crystallographic properties of the films and sputtering targets were characterized using a compact X-ray diffractometer (Rigaku Miniflex with a Θ-2Θ geometry) located inside a nitrogen-filled glovebox (MBraun) with O_2 and H_2O concentrations below 1 ppm. Sample transfer from other gloveboxes was performed using sealed vials, as described in Section 4.2.2. Crystallographic information files[259,263–265,287,288] for candidate structures were used for indexing the recorded diffraction patterns. Samples for SEM characterization were sputter-coated (using the in-glovebox PVD system) with ~30 nm of Pt prior to examination to reduce charging. A Thermo Scientific Helios G4 PFIB CXe DualBeam PFIB was used for cross-sectioning and secondary electron imaging of films deposited from the Li_2O + LiCl targets. A Zeiss Merlin SEM was used for secondary electron imaging of the films deposited from the Li_2OHCl target. Samples were transferred from the glovebox to these instruments using an airtight specimen transfer holder (Gatan ILoad).

4.2.4 Chemical Characterization

EDX measurements were performed on the cross-sections of certain films deposited from Li_2O + LiCl targets using an Oxford Instruments Ultim Max 170 X-ray detector attached to the PFIB instrument. AZtec® software (Oxford Instruments Nanotechnology Tools Limited) was used to record and interpret the X-ray spectra measured in “QuantLine” line scans. The presence of lithium was verified by performing XPS in a PHI VersaProbe III instrument; an airtight specimen transfer holder was used to transfer samples from the glovebox. Prior to measuring spectra, argon ion beam etching was carried out at 4 kV for 40 minutes to remove surface impurities. Energy calibration of the spectra was performed in CasaXPS software (Casa Software Ltd) using the adventitious carbon peak at 284.8 eV. FT-IR was performed on films deposited from both target types in a Thermo Scientific Nicolet iS10 instrument with a single reflection diamond ATR module located inside a nitrogen-filled glovebox (MBraun) with O_2 and H_2O concentrations below 0.1 ppm. Sample transfer from other gloveboxes was

performed using sealed vials, as described in Section 4.2.2. The film side of each sample was placed facing the laser beam.

4.2.5 Ionic Conductivity Measurements

EIS was used to measure the through-plane impedance of glass substrate/metal contact/electrolyte/metal contact layered samples fabricated in the way described in Section 2.5.1, where the electrolyte layer was a film deposited from an Li_2O + LiCl or Li_2OHCl target. For samples with the “small circle” contact design, four circular top contacts with a diameter of ~1 mm and spaced several millimetres apart were typically deposited on each sample. This allowed four impedance measurements to be made per sample, maximizing the chance of performing a successful measurement. Each metal strip used to create the overlapping strip design had a width of ~1 mm. The Kapton masks were laser cut by Laser Micromachining Limited. Some samples were produced before the Kapton masks had been obtained; in these cases the “small circle” design was used, and contacts were deposited using a stainless steel mask drilled in house.

Prior to performing impedance measurements, the samples were transferred to a glovebox (MBraun, O_2 and H_2O concentrations below 0.1 ppm) containing a pouch cell sealer using sealed vials, as described in Section 4.2.2. The samples were placed in pouches, as described in Section 2.2.3.2. Copper foil external contacts were used, which were connected to the sample contacts using Kapton tape. The pouches were evacuated for approximately 40 seconds prior to sealing the final side to ensure an inert environment and to improve the contact between components.

The pouches containing the impedance samples were placed in turn in a temperature-controlled climatic chamber and connected to an impedance analyser (ITS and MTZ-35, respectively, BioLogic Science Instruments) for measurements of impedance at temperatures between 25 °C and 100 °C using a voltage amplitude of 10 mV and a frequency range of 35 MHz to 0.1 Hz (10 measurements per decade, 20 cycles per

measurement). The programmed heating rate was 1 °C/min, and each temperature was held for 15-20 minutes prior to performing the impedance measurement to stabilize the system.

4.3 Results and Discussion

4.3.1 Stabilization of the Li_2O + LiCl Sputtering Target

Due to the absence of prior reports on the use of RF magnetron sputtering for the deposition of LiRAP films, a set of suitable processing conditions had to be developed from scratch. First, the sputtering conditions were investigated. For the first deposition from an Li_2O + LiCl powder target (in a 1 mm deep holder) a set of conditions (Table 4.1) was chosen based on a limited knowledge of the target properties. The pressure selected was found to be optimum for LCO deposition in Chapter 3, while a low power density was chosen since the thermal properties of the target were unknown.

Table 4.1 Initial set of conditions used to sputter an Li_2O + LiCl powder target.

Parameter	Value
Process gas	Ar
Process gas flow rate	70 sccm
Process pressure	5×10^{-3} mbar
RF power	30 W (1.5 W cm^{-2})

Prior to performing this deposition, it was expected that the processing conditions would need to be optimized according to their effect on the structural properties of the films. However, it was not anticipated that extensive optimization for target stability would be required. The need to find an alternative set of processing conditions is demonstrated by the appearance of the target after sputtering for ~3¾ hours using the conditions in Table 4.1, as shown in Figure 4.4.

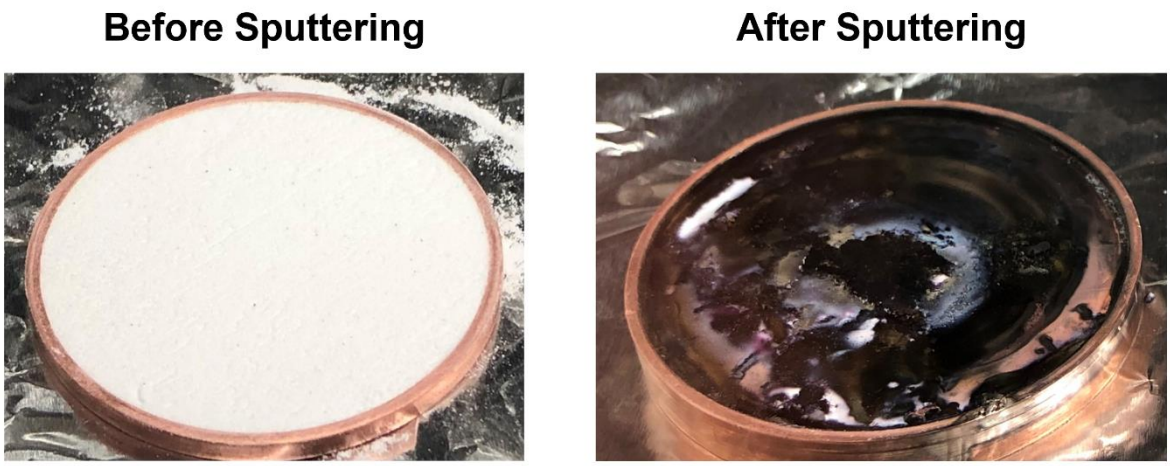


Figure 4.4 Photographs of an Li_2O + LiCl powder target before sputtering (left) and after sputtering for ~3¾ hours using the conditions in Table 4.1 (right).

Figure 4.4 shows that a significant transformation occurred within the target during sputtering. Aside from the white-to-black colour change, which was likely caused by the effect of structural changes on the scattering of light, it appears that the powder partially melted and revealed large regions of the copper holder surface. This transformation may have occurred due to reaction between the components of the target (Li_2O and LiCl), reaction with impurities (such as residual moisture) or the copper holder, or sintering/melting of one or both of the target components. Regardless of the precise mechanism, the cause was likely to have been excessive heating of the target due to its low thermal conductivity. Target instability must be avoided to create a stable, repeatable deposition process, maximize film uniformity and avoid contamination of the films by sputtering from the powder holder. Both process pressure and power density affect the flux of ions colliding with the target and thus the degree of target heating[106]. The aim of the next experiment was to investigate the relative importance of these two parameters in controlling target heating; the process pressure was reduced but the RF power increased to avoid a significant decrease in deposition rate. The full set of sputtering conditions is given in Table 4.2.

Table 4.2 Second set of conditions used to sputter an Li_2O + LiCl powder target (lower pressure and higher RF power compared to the values in Table 4.1).

Parameter	Value
Process gas	Ar
Process gas flow rate	12 sccm
Process pressure	2×10^{-3} mbar
RF power	45 W (2.2 W cm^{-2})

This time the deposition process ran for ~6.5 hours. A second deposition was performed using the same conditions except that the Li_2O + LiCl powder mixture was dried under vacuum prior to preparing the target and the deposition duration was only ~5 hours due to a fault with the deposition equipment. Photographs of the targets after performing these experiments are shown in Figure 4.5.

The cracking and lack of material flow seen for the targets in Figure 4.5 indicates that much less liquid phase was produced during sputtering than when the conditions in Table 4.1 were used (Figure 4.4) and the principal process causing morphological change was sintering. Sintering occurs at a lower temperature than melting, so this result suggests that lowering the process pressure was critical to increasing target stability while the effect of RF power was less important. Further, there is little difference in appearance between the targets shown in Figure 4.5 a) and b), indicating that residual moisture did not have a significant effect on target stability. Nevertheless, drying of the precursor powder was carried out prior to target preparation in all subsequent experiments as described in Section 4.2.1 to avoid introducing O-H bonding into the films.

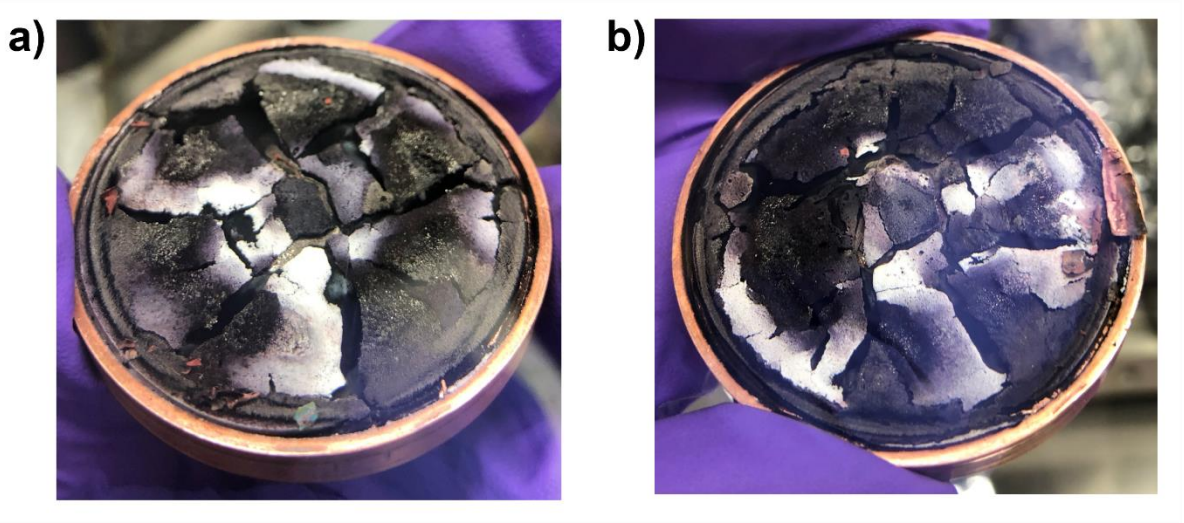


Figure 4.5 Photographs of Li_2O + LiCl powder targets after sputtering from a) undried powder for ~6.5 hours and b) dried powder for ~5 hours using the conditions in Table 4.2.

Having established that sintering occurs when the sputtering conditions in Table 4.2 are used, the next experiments were designed to ascertain whether this happens because of reaction between the precursor compounds or due to the properties of one of them. Thus, two sputtering targets were prepared: one consisting only of LiCl powder and the other only of Li_2O powder. These targets were sputtered in separate experiments, each for approximately 1 hour, using the conditions in Table 4.2. However, a 1:1 (by flow rate) Ar:O_2 process gas was used for the sputtering of Li_2O to compensate for any oxygen loss that might occur during sputtering in case these films were required in another investigation. Photographs of the targets after sputtering are shown in Figure 4.6.

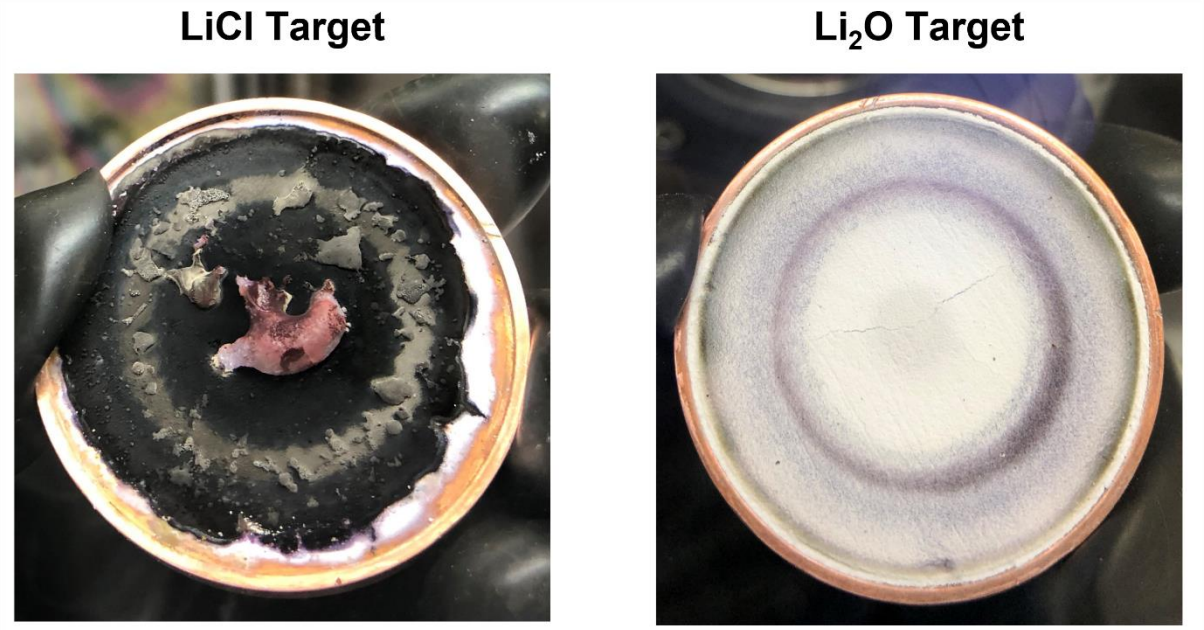


Figure 4.6 Photographs of LiCl and Li_2O powder targets after sputtering each for 1 hour using the conditions in Table 4.2 (except that a 1:1 (by flow rate) Ar:O_2 process gas mixture was used to sputter the Li_2O target).

Even though the deposition duration was only ~1 hour, it is clear from Figure 4.6 that the LiCl target became unstable in this time, undergoing what appears to have been sintering and partial melting. The Li_2O target, by contrast, changed little from its original appearance as a lightly pressed white powder. It is therefore reasonable to conclude that the instability of the mixed Li_2O + LiCl powder target was due to the behaviour of LiCl at the temperatures reached early in the deposition experiments rather than the occurrence of any chemical reactions. The behaviour of the LiCl can be explained by the fact that its melting temperature is 605 °C, whereas that of Li_2O is 1438 °C[275]. Temperatures above 605 °C are likely reached only at the very top of the target, but even in lower regions the homologous temperature of the LiCl must be high enough for sintering to occur. Therefore, to limit the partial melting and sintering of the LiCl constituent, the deposition conditions had to be modified further.

For the next experiment, the RF power was approximately halved. Further, a 2 mm deep powder holder was used rather than the 1 mm deep holder used up to this point. Although

this would be expected to decrease the conduction of heat away from the target, the additional target volume may help to reduce the through-target cracking seen previously and thus the contamination of the films by copper from the holder. The full set of deposition conditions is given in Table 4.3.

Table 4.3 Third set of conditions used to sputter an Li_2O + LiCl powder target (lower RF power compared to the value in Table 4.2).

Parameter	Value
Process gas	Ar
Process gas flow rate	12 sccm
Process pressure	2×10^{-3} mbar
RF power	22 W (1.1 W cm^{-2})

Figure 4.7 shows the appearance of the target after sputtering for ~6.5 hours using the conditions in Table 4.3. The photographs show that halving the RF power and doubling the depth of the powder holder limited target cracking and shape change. These changes also increased the uniformity of sintering during sputtering to the extent that it was possible to lift the target from the holder in one piece after the experiment. Unlike the top surface of the target, the bottom surface had not darkened, suggesting a difference in chemical composition. Further, a distribution of small, silvery globules of metal – presumably lithium – was present on the bottom surface. These globules were difficult to photograph, but one example visible in Figure 4.7 is indicated by a red arrow. The reason for the formation of lithium metal during sputtering is not clear, however it could be related to a change in the chemical composition due to the different sputter yields of the target elements.

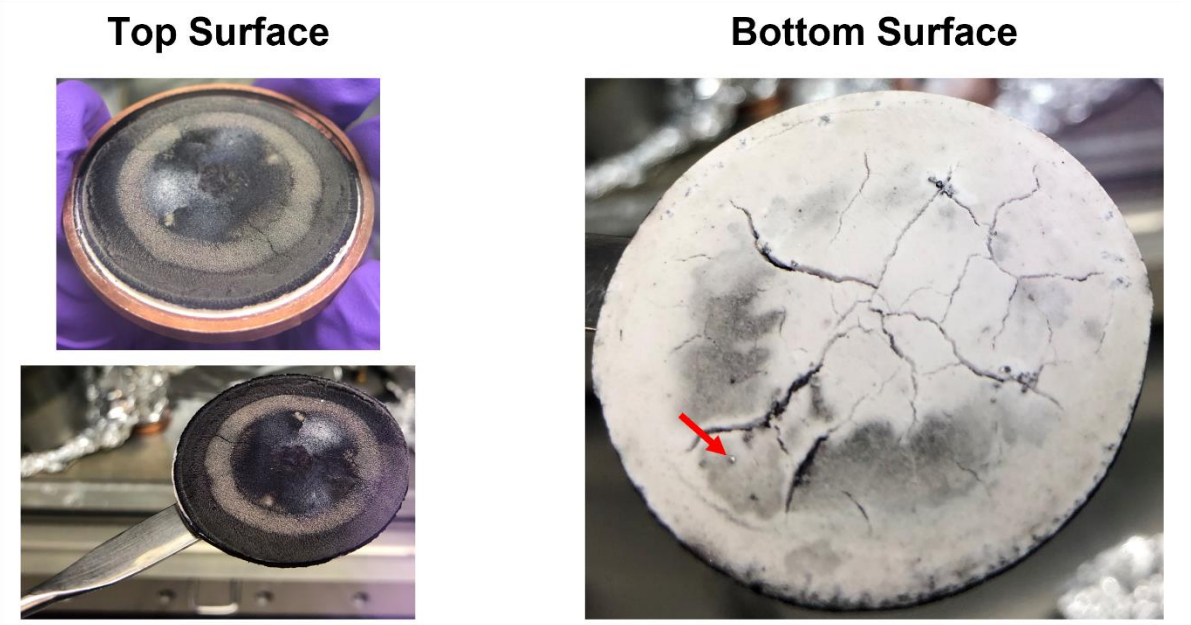


Figure 4.7 Photographs of the top and bottom surfaces of an Li_2O + LiCl powder target after sputtering for ~6.5 hours using the conditions in Table 4.3. The red arrow points to one of the globules of metallic lithium that formed on the bottom surface of the target during sputtering.

Oxygen was added to the process gas in the next deposition (to a level of 50% by flow rate) to try to increase the sputter yield of lithium, since the difference in atomic mass between lithium and oxygen is somewhat smaller than between lithium and argon, which should lead to greater kinetic energy transfer to the lithium ions[289]. This may also reduce the conversion of excess kinetic energy to thermal energy within the target, stabilizing it further. An additional small reduction in the RF power was made to try to eliminate the cracking seen in Figure 4.7. The full set of deposition conditions is given in Table 4.4.

Figure 4.8 shows the appearance of the target after sputtering for ~6.5 hours using the conditions in Table 4.4. The photographs in Figure 4.8 show that the small reduction in RF power and addition of oxygen to the process gas led to a further increase in target stability, with most of the cracking seen in Figure 4.7 now absent. Although changing the process gas composition did not prevent the formation of lithium on the bottom surface, the target stability was deemed to be sufficient. Thus, the conditions in Table 4.4 were used to deposit films for structural, chemical and electrical characterization in the next stage of the investigation.

Table 4.4 Fourth set of conditions used to sputter an Li_2O + LiCl powder target (minor reduction in RF power and change in process gas composition compared to the conditions in Table 4.3).

Parameter	Value
Process gas	Ar + O_2 (1:1 by flow rate)
Process gas flow rate	8 sccm for each of Ar and O_2
Process pressure	1×10^{-3} to 2×10^{-3} mbar*
RF power	20 W (1.0 W cm^{-2})

*The Ar and O_2 flow rates were each kept constant at 8 sccm for every deposition performed using the conditions in this table. The resulting process pressure was typically 1×10^{-3} mbar, but a value of 2×10^{-3} mbar was measured in some experiments.

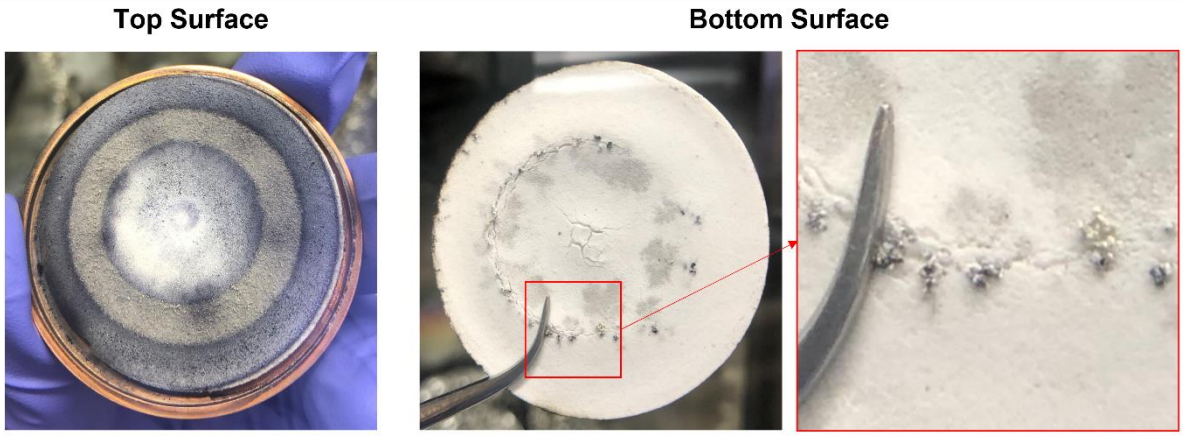


Figure 4.8 Photographs of the top and bottom surfaces of an Li_2O + LiCl powder target after sputtering for ~6.5 hours using the conditions in Table 4.4. An enlarged view of a region of suspected lithium metal formation on the bottom surface of the target (enclosed by the red box) is shown.

Prior to investigating the film properties, the target sputtered using the conditions in Table 4.4 was investigated by XRD to study its phase stability. Samples of powder taken from the top and bottom surfaces of the target after sputtering, as well as a sample from the precursor mixture used to prepare the target, were examined. The diffraction patterns are shown in Figure 4.9.

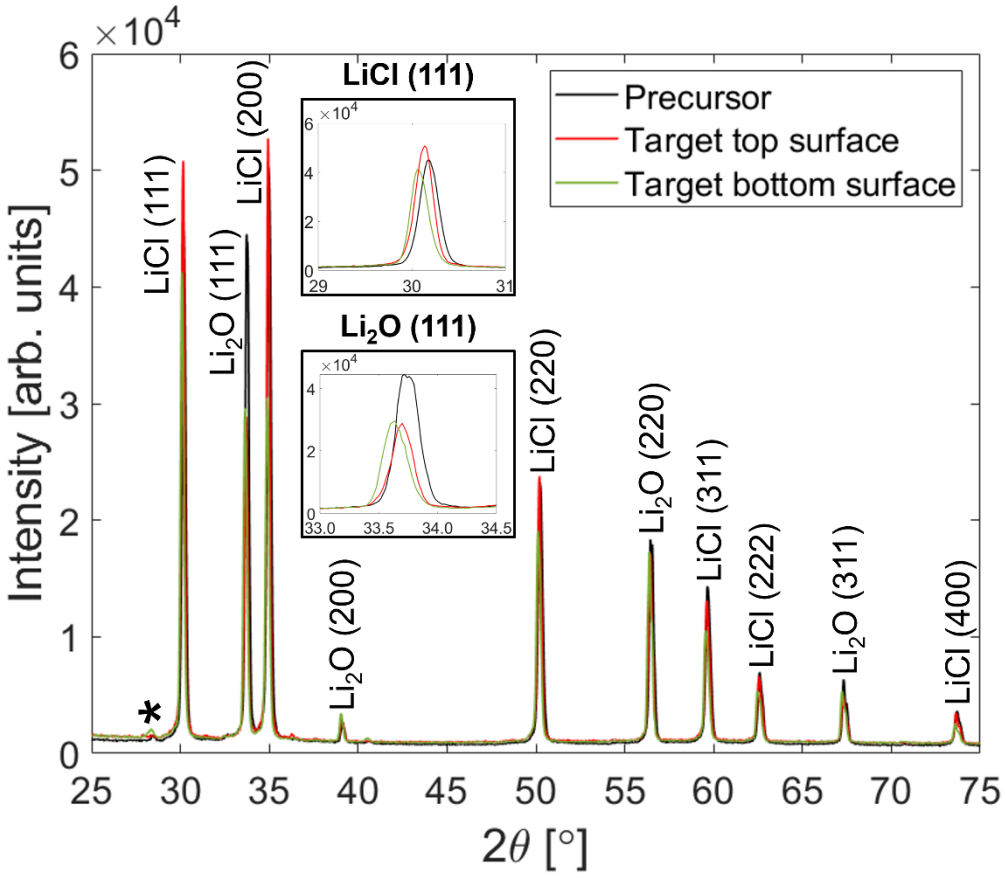


Figure 4.9 XRD patterns measured from powder samples taken from the top and bottom surfaces of the target sputtered for ~6.5 hours using the conditions in Table 4.4, as well as from the precursor mixture used to prepare the target. Views of the LiCl (111) and Li_2O (111) peaks in narrow 2θ ranges are shown in the insets. The peak marked * corresponds to an impurity phase thought to be KCl. The XRD data used to create this figure were collected by Dr Hyeon Jeong Lee.

Comparison of the diffraction pattern from the precursor with those from the target shows that no additional peaks appeared after sputtering and that the peaks present before sputtering did not shift position. This suggests that no new crystalline phases formed due to reaction between the precursors or with the copper holder. However, the peak intensities are different in the three patterns, which is probably due to a combination of differences in grain orientations and variations in chemical composition. The LiCl peaks are more intense in the pattern from the top surface of the target than in the pattern from the bottom surface, while the opposite is true for the Li_2O peaks, implying that LiCl migrated towards the target surface

during sputtering. This phenomenon may be attributable to partial melting of the LiCl, which would also explain the formation of lithium at the bottom of the target if partial electrolysis occurred in contact with the sputtering cathode. A further reduction in target heating would be required to avoid this. However, when pressure and power values lower than those in Table 4.4 were tried a plasma could not be sustained. Nevertheless, the target sputtered using the conditions in Table 4.4 demonstrated much greater stability than the target sputtered using the initial conditions in Table 4.1, facilitating a steady, repeatable deposition process.

4.3.2 Optimization of Films Deposited from Li_2O + LiCl Sputtering Targets

4.3.2.1 Crystallographic Properties

After optimizing the sputtering conditions for target stability, the focus changed to characterizing and optimizing the structural properties of the films deposited. A variety of substrates were used, and the effect of post-deposition annealing on structural properties was investigated. First, deposition onto two substrate materials commonly used in sputter deposition processes – glass and silicon – was studied. Deposition was performed for 12 hours using the conditions in Table 4.4. Since the melting temperature of Li_3OCl is unknown, annealing temperatures of 250 °C, 300 °C and 350 °C – which are close to the melting point of Li_2OHCl (~300 °C)[72] – were chosen. Each sample was held at its designated annealing temperature for 1 hour before cooling within the furnace at its natural rate. XRD patterns from these films are shown in Figure 4.10; the patterns in a) are from as-deposited films while those in b) are from annealed films.

The XRD patterns from as-deposited films on glass and silicon substrates in Figure 4.10 a) contain similar peaks, with three matching to positions expected for Li_3OCl (a = 3.91 Å) and a further three corresponding to LiCl. Despite the assignation to Li_3OCl, further evidence is required to confirm that Li_3OCl, rather than Li_2OHCl, was present since the XRD peak positions expected for these phases are almost identical. Nevertheless, these results show that some volume of an antiperovskite phase formed during the deposition process without

any applied substrate heating. All film peaks in Figure 4.10 a) are broad relative to the substrate/holder peaks, indicating that the films have a small grain size and may not be fully crystalline. Preferential alignment of the Li_3OCl (110) planes parallel to the film surface is suggested by the much higher intensity of the Li_3OCl (110) peak relative to the other Li_3OCl peaks in Figure 4.10 a) compared to the simulated powder pattern. The presence of LiCl peaks in both patterns in Figure 4.10 a) could be a sign of incomplete reaction between the precursor compounds. If this was the case then Li_2O must also have been present, but as an amorphous phase since it did not give rise to peaks in the XRD patterns. An alternative explanation is that the films contained an excess of LiCl. This is the more likely explanation considering that LiCl was found to migrate to the top of the target during sputtering, which would have increased the ratio of Cl to O in the flux of sputtered material. Furthermore, partial melting could have resulted in some evaporation of LiCl from the target, further enhancing its deposition rate relative to that of Li_2O. The Li_3OCl/LiCl peak intensity ratios appear to be similar in both patterns in Figure 4.10 a), suggesting that the relative volumes of crystalline Li_3OCl and LiCl were similar on both substrate types.

The films underwent significant changes during annealing, as seen in Figure 4.10 b), with three Li_2O peaks appearing and all peaks corresponding to Li_3OCl disappearing. Furthermore, the peaks that were present prior to annealing have become much narrower, reflecting an increased grain size. The structure appears to depend weakly on annealing temperature within the range used here, and the fact that both LiCl and Li_2O peaks are present in the patterns from the films on silicon substrates suggests that the antiperovskite phase underwent decomposition into Li_2O and LiCl – the precursors of Li_3OCl – during annealing at all temperatures. This is exactly the behaviour expected for Li_3OCl: although it is predicted to become thermodynamically stable above 500 K (227 °C)[269] (which is just below the lowest annealing temperature used here) the kinetic limitation preventing its decomposition at room temperature is removed during the slow heating and cooling ramps, allowing breakdown to occur. This is strong evidence that the antiperovskite phase present in

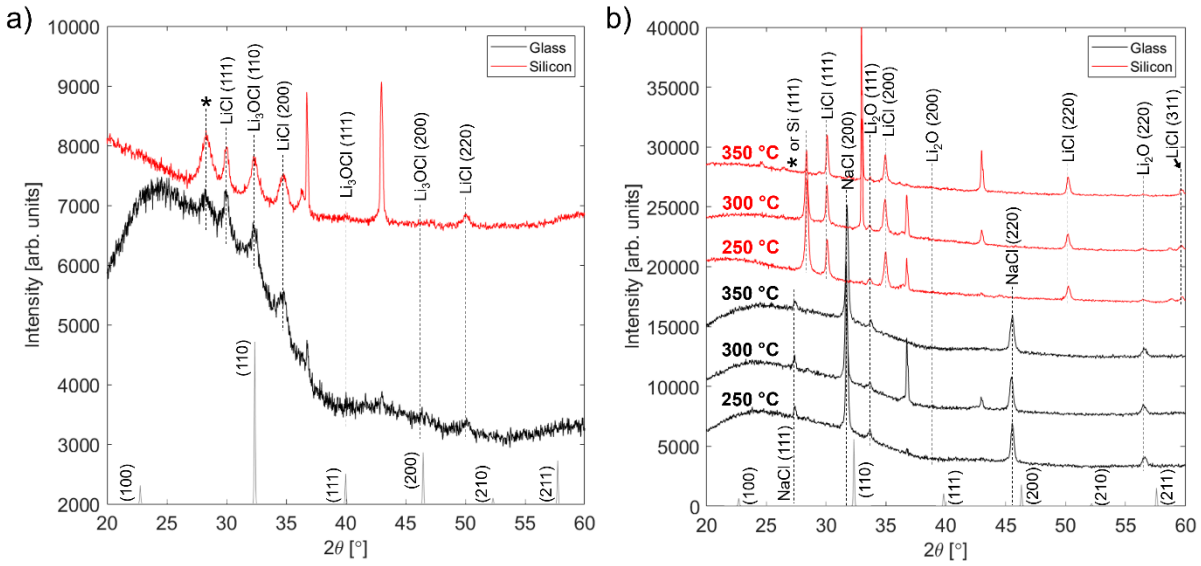


Figure 4.10 XRD patterns of films deposited from Li_2O + LiCl targets for 12 hours onto glass and silicon substrates using the conditions in Table 4.4. Patterns from as-deposited films are shown in a), while the patterns in b) are from films annealed at 250 °C, 300 °C or 350 °C for 1 hour. Peaks marked * correspond to impurity phases from the precursor mixture such as KCl. Unlabelled peaks are from the substrate or sample holder; the differing intensities of holder peaks are due to differences in the lateral positioning of samples within the holder. The simulated powder pattern for Li_3OCl[263,264] is shown at the bottom of each plot. The XRD data used to create this figure were collected by Dr Hyeon Jeong Lee.

the as-deposited films was indeed Li_3OCl rather than Li_2OHCl. During film deposition, the temperature of the growing film must have been sufficient to stabilize the Li_3OCl phase and cause partial crystallization. The immediate quenching of the plasma at the end of deposition and the thinness of the deposited films resulted in a cooling rate sufficiently rapid to retain a detectable volume of Li_3OCl at room temperature, held in a metastable state by vanishingly slow decomposition kinetics. Even if some Li_3OCl was re-formed during annealing above the stabilization temperature, the rate of cooling to room temperature was evidently low enough for complete decomposition to the precursor phases to reoccur.

Unlike the films on silicon substrates, those on glass substrates do not give rise to LiCl peaks in the XRD patterns measured after annealing. Instead, NaCl peaks appear. The most likely explanation for this is that Na^+ ions, possibly bound up in Na_2O, have enough mobility at the

annealing temperatures to diffuse from the glass into the film and react with the LiCl to form NaCl *via* the reaction in equation 4.5.

$$Na_2O + 2LiCl \rightarrow 2NaCl + Li_2O \qquad \textbf{Equation 4.5}$$

To investigate the onset of this reaction and the temperature range over which Li_3OCl begins to break down during heating from room temperature, films deposited on glass substrates and annealed at 100 °C or 200 °C were also studied. Their XRD patterns are shown in Figure 4.11 along with the patterns from as-deposited and 250 °C annealed films for comparison.

Figure 4.11 shows that the LiCl peaks present in the XRD pattern from the as-deposited film are absent after annealing at 100 °C. However, two new peaks labelled ‘A’ and ‘B’ appear at positions intermediate between those expected for LiCl (111) and NaCl (200), and LiCl (200) and Li_2O (111), respectively. These peaks disappear after annealing at 200 °C and are replaced by NaCl (200) and Li_2O (111) peaks. Therefore, the ‘A’ and ‘B’ peaks seem to correspond to intermediate structures formed while the reaction in equation 4.5 was underway. This implies that diffusion of Na_2O from the glass substrate to the film occurs at a low rate during annealing at 100 °C. Some decomposition of the Li_3OCl phase may have occurred during annealing at this temperature given the slight decrease in Li_3OCl (110) absolute peak intensity, but due to the lack of consistent reference peaks it is not possible to determine whether the relative peak intensity decreased, which is the most reliable indicator of decreasing phase fraction. Nevertheless, there is no trace of any Li_3OCl peaks in the patterns measured after annealing at 200 °C, showing that complete breakdown had occurred by the end of annealing at this temperature. The absolute intensities of the NaCl and Li_2O peaks are higher in the pattern from the film annealed at 250 °C than in that from the film annealed at 200 °C, which could reflect higher rates of reaction and crystallization at 250 °C. Figure 4.10 b) shows that annealing at temperatures above 250 °C made little difference to the crystallographic properties of the films. The fact that Na_2O does not

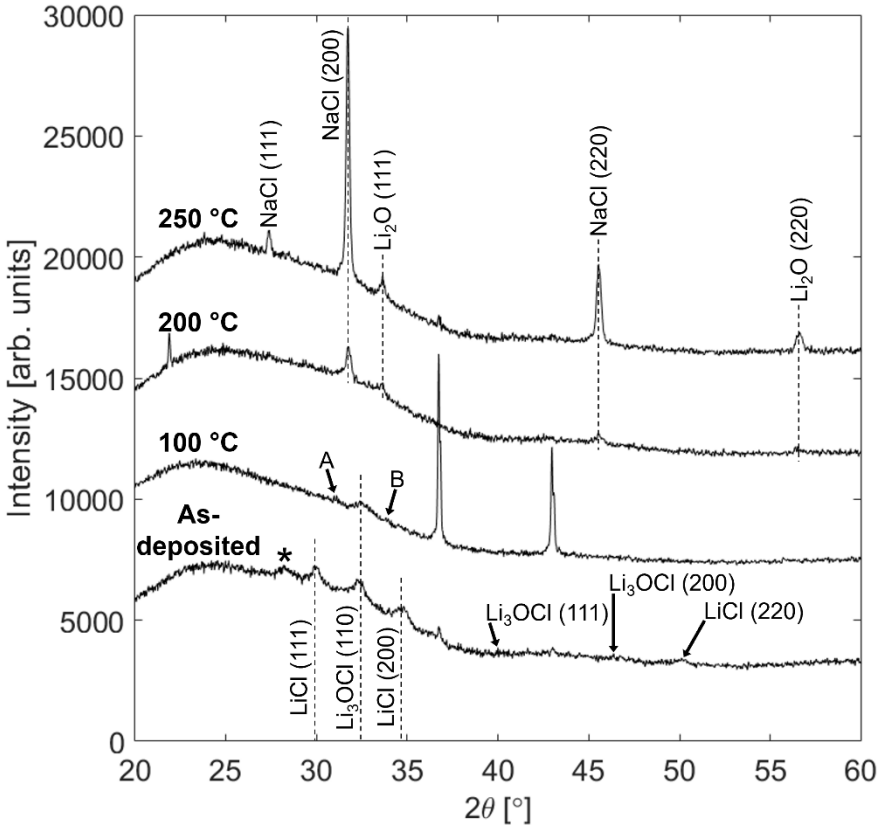


Figure 4.11 XRD patterns of films deposited from Li_2O + LiCl targets for 12 hours onto glass substrates using the conditions in Table 4.4 and annealed at 100 °C, 200 °C or 250 °C for 1 hour along with a pattern from an as-deposited film. Peaks labelled 'A' and 'B' are at positions intermediate between LiCl (111) and NaCl (200), and LiCl (200) and Li_2O (111), respectively. Peaks marked * correspond to impurity phases from the precursor mixture such as KCl. Unlabelled peaks are from the sample holder; the differing intensities of these peaks are due to differences in the lateral positioning of samples within the holder. The XRD data used to create this figure were collected by Dr Hyeon Jeong Lee.

crystallize to any detectable degree in the films suggests that its reaction with LiCl happens as soon as it enters the film; this may provide the downhill chemical potential gradient required for its diffusion into the film. Since the volume fraction of the Li_3OCl phase is maximized by avoiding post-deposition annealing, the choice of glass or silicon substrates should make little difference to the structural and chemical properties of films processed using optimal conditions.

Although the evidence so far suggests that a volume of Li_3OCl phase was obtained in films deposited on glass and silicon substrates, electronically conductive (but Li^+ blocking) substrates are required for through-plane impedance measurements. There are two strategies in this regard: use metal/alloy sheets or coat insulating substrates with a metallic layer. Both strategies were tried in this investigation. However, sputter deposition of nickel and platinum layers on silicon proved to be unfeasible without the use of an Al_2O_3 or Ti interlayer to improve adhesion, whereas adequate adhesion was achieved on glass substrates without the use of interlayers. Owing to the structural similarity of as-deposited films on glass and silicon substrates as well as the potential to simplify the processing, the decision was made not to proceed with the use of metal-coated silicon substrates. Films were deposited from Li_2O + LiCl targets onto Ni/Pt-coated glass, Waspaloy and stainless steel substrates using the conditions in Table 4.4. Waspaloy was determined to be a suitable conductive substrate owing to its nickel base (which should block Li^+) as well as its successful application as a current collector for LCO films in Chapter 3, while stainless steel was selected because of its widespread application as a Li^+ blocking electrode in previous studies[145,290–292]. Deposition on the metal-coated glass substrates was performed for 12 hours, as for the previous substrates. However, the duration was doubled for deposition on the alloy substrates since pinholes were discovered in LiPON films deposited on similar substrates (not reported in this work), which may have been due to the relatively high roughness of the alloy substrates. In this investigation the alloy substrates were polished prior to use, but thicker films were also targeted to reduce the risk of pinhole formation and hence short-circuiting during impedance measurements. Typical XRD patterns from films deposited on nickel-coated glass and alloy substrates are shown in Figure 4.12. The pattern measured from the film deposited on uncoated glass is also plotted for comparison.

The Li_3OCl (110) peak is present in all the XRD patterns in Figure 4.12. While it is not possible to calculate the volume fraction of Li_3OCl phase in each of the films, the ratios of integrated Li_3OCl to LiCl peak intensity in the patterns from the films on glass and alloy

substrates appear to be similar, indicating similar phase compositions in the three films. The lack of LiCl peaks in the pattern from the film on nickel-coated glass and its low Li_3OCl (110) peak intensity make comparison with this film difficult. Nevertheless, the Li_3OCl phase appears to form in all three of the films deposited on conductive substrates. Further characterization is required to determine which of the conductive substrates is the most suitable.

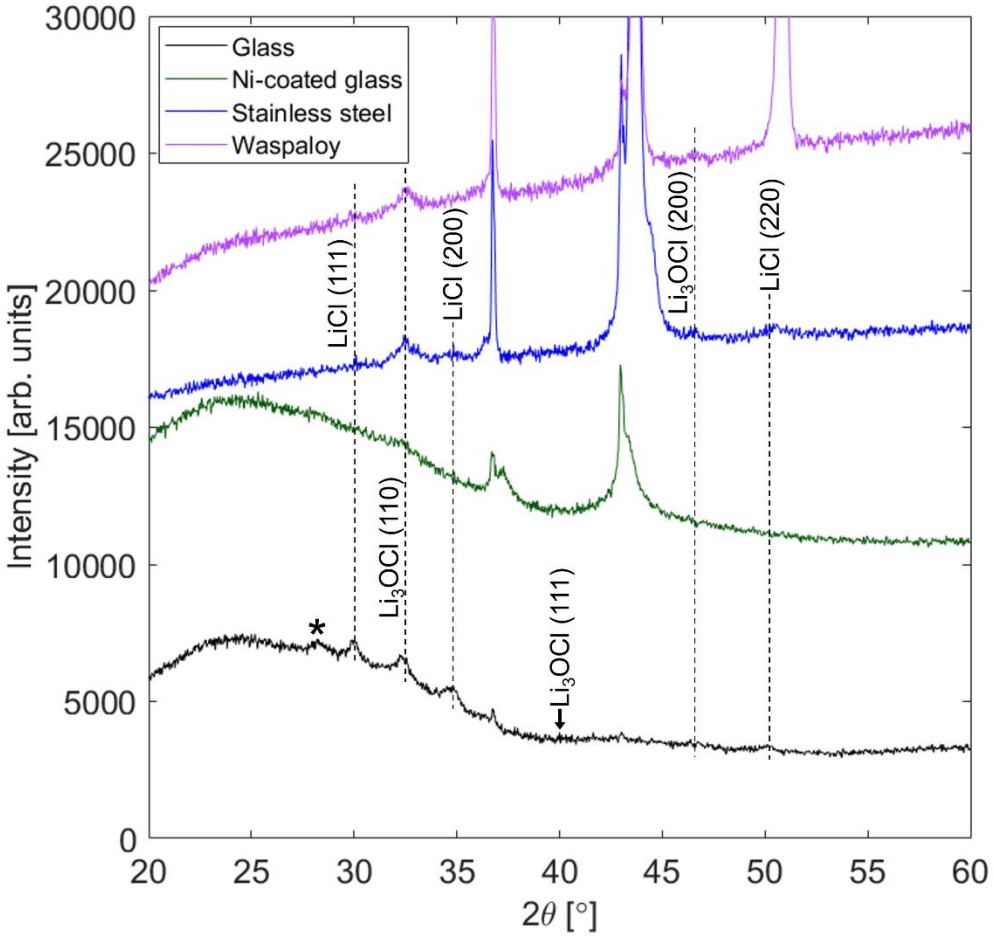


Figure 4.12 XRD patterns of films deposited from Li_2O + LiCl targets for 12 hours onto glass and nickel-coated glass substrates and for 24 hours onto stainless steel and Waspaloy substrates using the conditions in Table 4.4. Peaks marked * correspond to impurity phases from the precursor mixture such as KCl. Unlabelled peaks are from the substrate or sample holder; the differing intensities of holder peaks are due to differences in the lateral positioning of samples within the holder. The XRD data used to create this figure were collected by Dr Hyeon Jeong Lee.

4.3.2.2 Morphological Properties

The influence of the substrate material on the morphological properties of the films was studied using SEM. To enable reliable through-plane impedance testing, a smooth film with a low density of pinholes is desirable since this will create good electrical contact with the metallic electrodes and reduce the occurrence of short circuiting. Figure 4.13 shows SEM micrographs of films on glass, nickel-coated glass, stainless steel and Waspaloy substrates.

The surface view micrographs in Figure 4.13 show that the films on all substrate types have a “particulate” appearance. These particulate features have a typical size of several microns on the alloy substrates but are somewhat smaller (mostly below one micron) on the glass and nickel-coated glass. Thus, the films on stainless steel and Waspaloy are much rougher than those on glass and nickel-coated glass, which is shown clearly by the cross-sectional micrographs and represented quantitatively by the ranges and standard deviations of the film thickness measurements (Table 4.5). Aside from roughness, the thickness measurements show that despite doubling the deposition duration, the films on the alloy substrates were *thinner* (by ~8-15% on average) than the film on glass. Further, the film on nickel-coated glass was deposited for the same time as the film on uncoated glass, yet it was ~30% thinner on average. This indicates that the sticking coefficient is lower on metallic substrates than on uncoated glass for this film material.

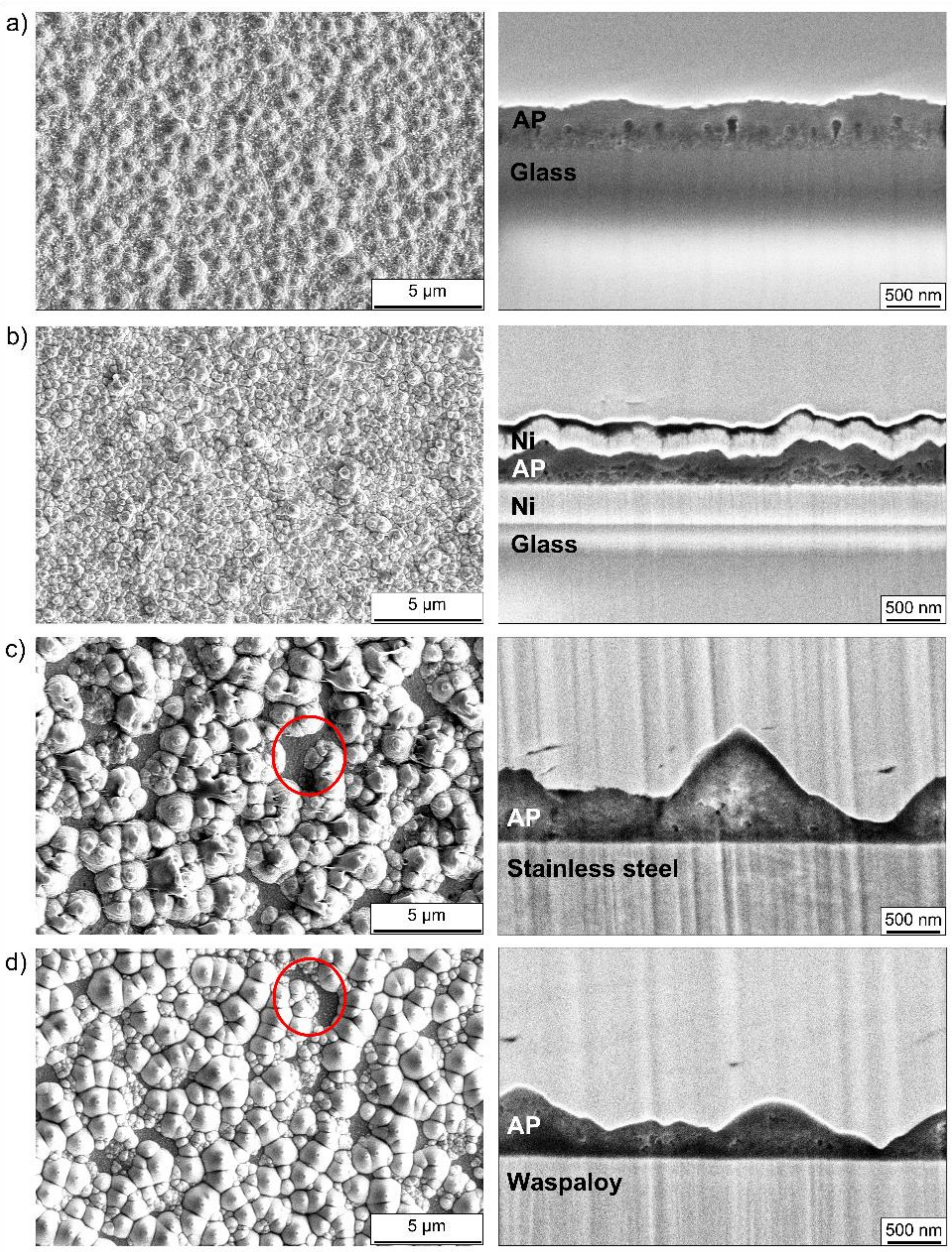


Figure 4.13 SEM micrographs of surfaces (left) and cross-sections made by PFIB sectioning (right) of films deposited from Li_2O + LiCl targets for 12 hours onto a) glass and b) nickel-coated glass substrates and for 24 hours onto c) stainless steel and d) Waspaloy substrates using the conditions in Table 4.4. The cross-sectional micrographs were taken at a 38° angle to the normal of the section plane, meaning that the scale bars are valid only for horizontal measurements. The films are labelled 'AP' since they contain an antiperovskite phase. The material above the films is Pt that was deposited within the PFIB to protect the underlying film during sectioning. The site of a nickel top contact was chosen for imaging the cross-section in b). Red circles on the surface view micrographs in c) and d) indicate holes in the films. The PFIB sectioning and SEM imaging used to create this figure were performed by Marco Siniscalchi.

Table 4.5 Thicknesses of films deposited from Li_2O + LiCl targets for 12 hours onto glass and nickel-coated glass substrates and for 24 hours onto stainless steel and Waspaloy substrates using the conditions in Table 4.4. At least eight measurements were made for each film on tilt-corrected cross-sectional SEM micrographs.

Substrate	Film thickness range [nm]	Mean [nm]	Standard deviation [nm]
Glass	640-800	730	58
Ni-coated glass	410-600	520	59
Stainless steel	160-1390	620	360
Waspaloy	90-1410	670	404

Evidence for poor adsorption of sputtered material on the alloy substrates during film deposition is provided by the surface view micrographs in Figure 4.13 c) and d). The coverage of the films on the alloy substrates is not complete and a high density of through-thickness holes is present, examples of which are indicated by red circles on the micrographs. The frequency of these holes across the films rendered them unreliable for through-thickness impedance measurements, since short-circuiting between the top and bottom electrical contacts is likely to occur at all contact locations no matter how small the contacts are made. As well as having a similar roughness to the film on uncoated glass, the film on nickel-coated glass appeared to show a similar substrate coverage, despite the apparently poorer sticking coefficient.

The morphology of an as-deposited ceramic film is expected to be dictated primarily by the film growth mode, and the particulate appearance seen in the micrographs in Figure 4.13 is characteristic of 'island-like' or Stranski-Krastanov (S-K or 'layer plus island') growth[106]. Island-like growth occurs if the energy of the substrate surface is low relative to that of the film surface and the film-substrate interface. S-K growth begins in a layer-by-layer fashion due to crystallographic lattice matching across the film-substrate interface and a consequently low interfacial energy. Several monolayers typically form before a transition to island growth occurs to reduce the strain energy within the growing film.

While a detailed study of the film growth modes was outside the scope of this investigation, it is useful to understand why the films on alloy substrates were significantly rougher than those on glass and nickel-coated glass. Interestingly, the cubic lattice parameters of 304 stainless steel and Waspaloy (both ~3.6 Å)[293,294] are only about 8% smaller than that of the Li_3OCl phase (~3.9 Å)[263,264]. The (110) planes of the Li_3OCl phase seem to align preferentially with the film surface (Figure 4.12), and the interatomic spacings within these planes are ~3.9 Å, ~5.5 Å and ~3.4 Å for Cl-Cl ∥ [001], Cl-Cl ∥ $[\bar{1}10]$ and Cl-O pairs, respectively. Low intensity Li_3OCl (111) and (200) peaks are also visible in Figure 4.12; these planes possess Cl-Li and Li-Li pairs, respectively, with an interatomic spacing of ~2.8 Å. The stainless steel and Waspaloy substrates do not exhibit strong preferred crystallographic orientations. Nevertheless, the interatomic spacings within the (111), (200), (220) and (311) planes are ~2.5 Å, ~2.5 Å / ~3.6 Å, ~2.5 Å / ~3.6 Å and ~5.1 Å, respectively. Thus, certain spacings within the (111), (200), (220) and (311) planes of the alloy substrates closely match those in the (110), (111) and (200) planes of Li_3OCl, so some degree of lattice matching between the Li_3OCl phase and the alloy substrates might be expected during film nucleation. This would increase the tendency for growth by the S-K mode. However, on the glass substrates no lattice matching can occur; this would be expected to promote island-like growth if the surface energy of the glass is low relative to that of the film material, but subsequent island coalescence could occur to reduce the film surface area. This would have the advantageous effect of smoothing the film surface. Thus, growth of the films on the alloy and glass substrates by the S-K and island-like growth modes, respectively, could explain the film morphologies seen in Figure 4.13. Since the lattice parameter of nickel (~3.5 Å)[295] is also close to that of Li_3OCl, growth by the S-K mode might also be expected on nickel-coated glass. However, the morphology of the film deposited on this substrate is similar to that of the film deposited on the uncoated glass, suggesting the growth modes were the same. A possible explanation is the fact that the nickel layer was nanocrystalline, evidenced by the lack of clear peaks corresponding to nickel in the XRD pattern in Figure 4.12, which may

have prevented sufficient lattice matching between the film and the substrate for growth to proceed by the S-K mode.

Although the films on glass and nickel-coated glass substrates are somewhat smoother than those on the alloy substrates, they are still relatively rough as is clearly seen when compared to the bottom nickel layer in the cross-sectional view of Figure 4.13 b). This roughness may be due in part to the gentle sputtering conditions that were required to stabilize the Li_2O + LiCl target, since the use of low pressure and RF power values limits two processes that promote the growth of smooth films: planarization (break-up of surface clusters) and re-sputtering of loosely bound ions[106]. Nevertheless, these films likely contain a lower density of holes than those deposited on alloy substrates and are more suitable for through-plane impedance measurements, hence only glass and metal-coated glass substrates were used in subsequent deposition processes.

4.3.2.3 Chemical Composition

EDX line scans were performed along the cross-sections of films on glass and nickel-coated glass substrates created in the PFIB. These were positioned centrally or towards the top surface of the films to minimize contributions from the glass substrate which, like the films, contains oxygen. This enabled the relative atomic fractions of the main elements in the films (excluding lithium) to be determined. The locations of typical line scans on the cross-sectional surfaces along with the associated X-ray spectra and tables of chemical composition are shown in Figure 4.14.

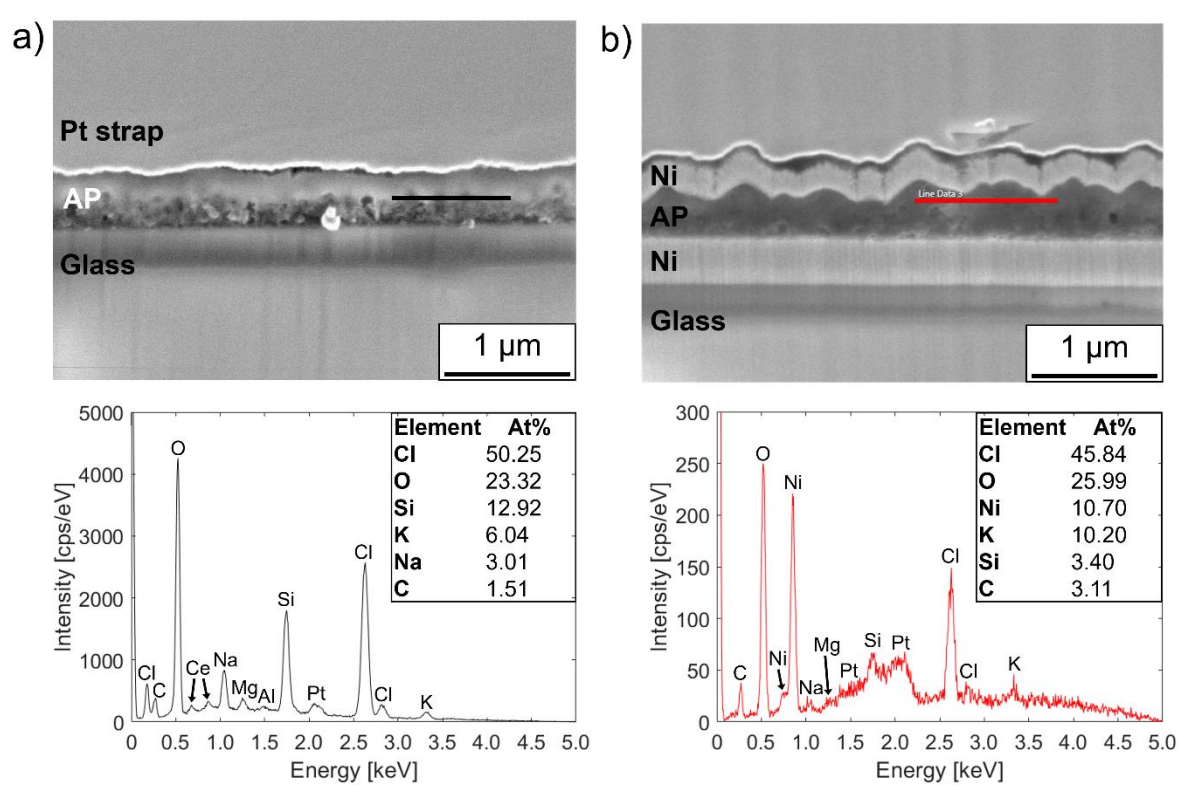


Figure 4.14 EDX spectra measured on the cross-sections of films (labelled 'AP)' deposited from Li_2O + LiCl targets for 12 hours onto a) uncoated glass and b) nickel-coated glass substrates using the conditions in Table 4.4. The black and red lines drawn on the SEM micrographs show the respective locations of the line scans. Although the elemental concentrations are given as atomic percentages, they do not account for the lithium content of the films and are thus valid only for calculations of relative atomic fraction. Elements present at concentrations below 1 at% have not been listed. The PFIB sectioning, SEM imaging and EDX data collection used to create this figure were performed by Marco Siniscalchi.

The Cl/O atomic ratios calculated from the compositional data in Figure 4.14 are ~2.2 for the film on the uncoated glass substrate and ~1.8 for the film on the nickel-coated glass. These values support the interpretation of the XRD patterns in Figure 4.9 and 4.10, which indicated the presence of an overall LiCl excess in the films due to LiCl rising to the top of the sputtering target during deposition. However, the quantitative accuracy of the compositional data calculated from the EDX spectra would have been compromised to some degree by the low energy of the incident electrons (~5 keV) used in these experiments compared to the

highest X-ray energy emitted by the elements of interest, which is ~2.6 keV (Cl Kα)[296]. To obtain adequate spectral line intensity, an electron energy at least double that of the highest X-ray transition of interest is usually recommended[297], but in this investigation, as is often the case when studying battery materials composed mostly of light elements, it was necessary to limit the accelerating voltage to 5 kV to avoid beam damage and sample charging. The validity of the data was also limited by the fact that, due to the geometry of the area milled in the PFIB, measurements were performed with the cross-sectional plane normal tilted by 38° to the SEM beam, which will have increased the penetration of the beam into the substrate. The X-ray signal detected from the substrate would have been enhanced as a result, making the concentrations of substrate elements (e.g. Si, K, Na) in the films appear higher than they actually were.

An EDX line scan was also performed along the cross-section of an annealed film (250 °C, 1 hour) on a glass substrate to investigate the chemical changes that occurred during annealing, previously inferred from the XRD patterns in Figure 4.10 b) and Figure 4.11. Figure 4.15 shows the location of the line scan, which started above the film surface and ended in the substrate on the cross-sectional surface of the film, along with the associated chemical composition profile. The line profile shows that the atomic concentration of sodium (not accounting for the presence of lithium) in the film after annealing was ~33%, while that in the glass substrate, like in the as-deposited film in Figure 4.14 a), was ~3%. This supports the interpretation of the XRD patterns in Figure 4.10 b) and Figure 4.11, demonstrating that sodium (probably in the form of Na_2O) migrates into the film from the glass substrate during annealing where it reacts with LiCl to form NaCl.

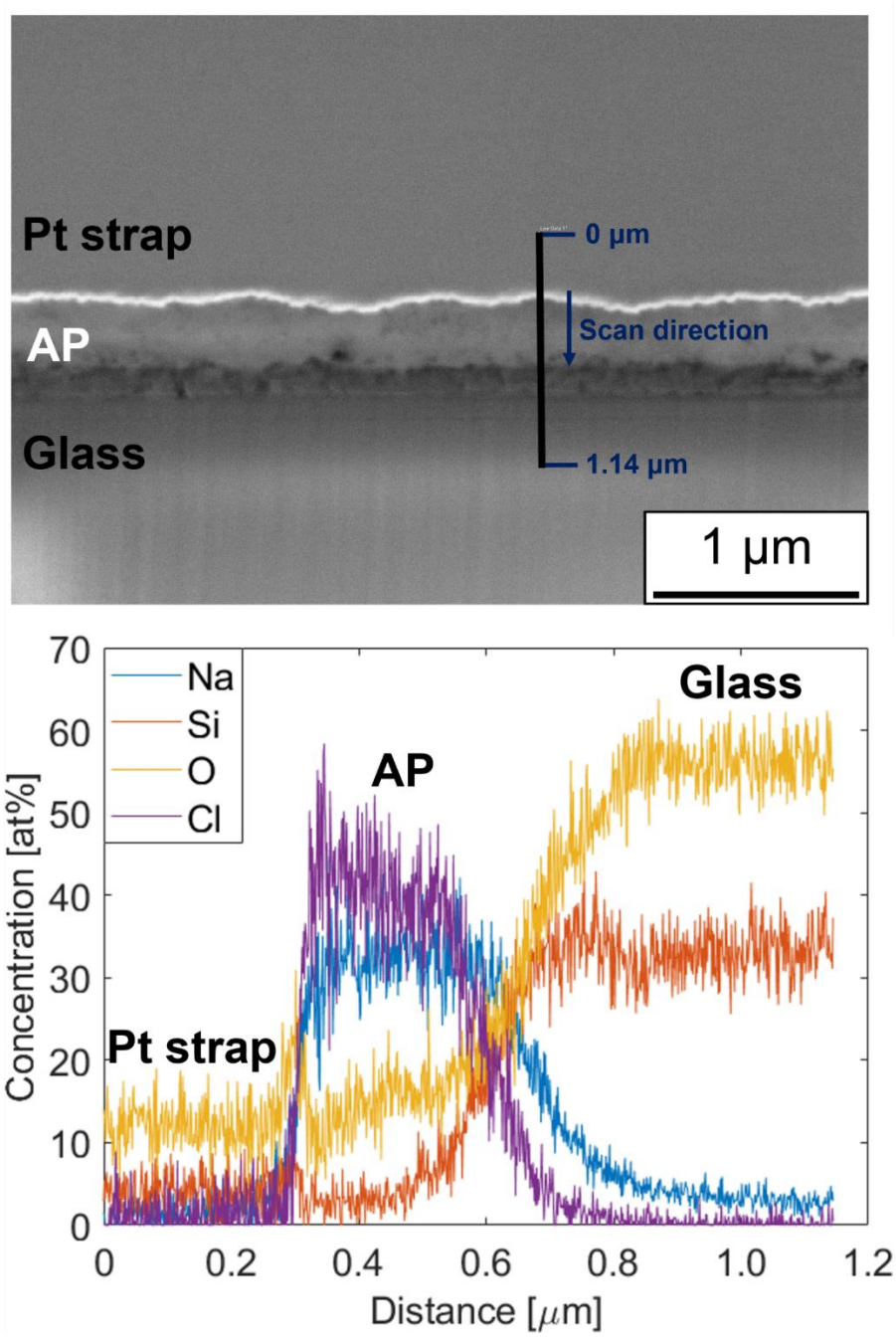


Figure 4.15 EDX line profile for sodium, silicon, oxygen and chlorine measured on the cross-section of a film (labelled 'AP') deposited from an Li_2O + LiCl target. The film had been deposited for 12 hours onto an uncoated glass substrate using the conditions in Table 4.4, then annealed at 250 °C for 1 hour. The black line on the SEM micrograph shows the location of the scan, which started above the film surface and ended in the substrate. Only the key elements of interest in the film and substrate have been plotted in the profile. Although the elemental concentrations are given as atomic percentages, they do not account for the lithium content of the film and are therefore only valid for determining relative concentrations. The PFIB sectioning, SEM imaging and EDX data collection used to create this figure were performed by Marco Siniscalchi.

XPS was performed on as-deposited films to verify that lithium was present in the bonding environments expected for Li_3OCl. A spectrum taken after etching the film surface using a 4 kV Ar-ion beam for 40 minutes to remove impurity layers is shown in Figure 4.16. The presence of strong peaks corresponding to oxygen and chlorine (from the film), along with low intensity sodium, calcium, magnesium, cerium and silicon peaks (from the substrate), supports the EDX results in Figure 4.14 a). The Li 1s peak spans the energy range expected for the bonding in Li_3OCl and could contain components from Li-O (54.04 eV) and Li-Cl (54.87 eV)[298]. Thus, the XPS results show that lithium is present in the films and is likely to be bonded to the expected elements.

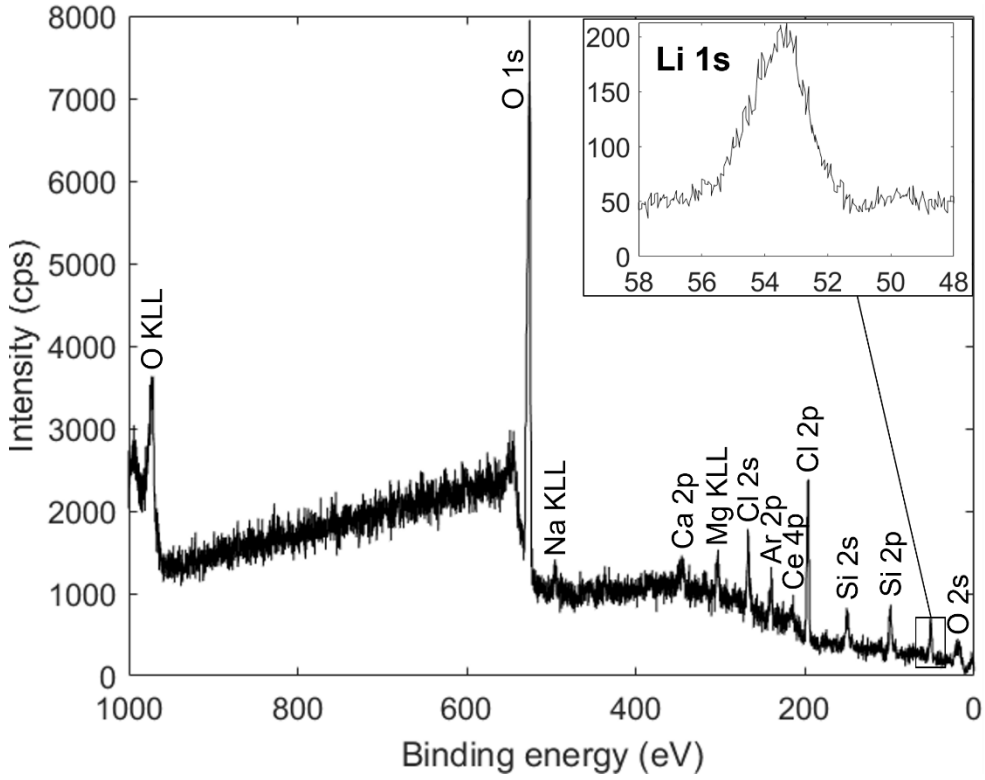


Figure 4.16 XPS spectrum of a film deposited from an Li_2O + LiCl target for 12 hours on a glass substrate using the conditions in Table 4.4, measured after etching the film surface using a 4 kV Ar-ion beam for 40 minutes to remove surface impurities and carbon-rich layers. The inset shows a high resolution plot of the Li 1s peak. Unlabelled peaks do not correspond to any probable film impurities and are thus attributed to contamination from the XPS chamber. The XPS data collection used to create this figure was performed by Dr Sudarshan Narayanan.

4.3.3 Deposition of Films from an Li_2OHCl Target

4.3.3.1 Stabilization of the Sputtering Target

In the next stage of the investigation, films were deposited from an Li_2OHCl powder target onto glass and nickel/platinum-coated glass substrates. The principal aim was to produce films containing the Li_2OHCl phase for comparison with the films deposited from Li_2O + LiCl targets, which are thought to contain the Li_3OCl phase. A secondary aim was to investigate the stability of the Li_2OHCl phase in these films, since there are no previous reports on the use of PVD techniques to fabricate thin films containing this phase. The melting temperature of Li_2OHCl (~300 °C) is roughly half that of LiCl (605 °C). Since the low melting temperature of LiCl was responsible for the initial instability of the Li_2O + LiCl target, the starting point for the deposition of films from the Li_2OHCl powder target was the relatively gentle set of sputtering conditions used for the Li_2O + LiCl target (Table 4.4). However, the plasma could not be stabilized using these conditions, and it was necessary to increase the RF power slightly and omit oxygen from the process gas to achieve a stable plasma. The values used for the key sputtering parameters are shown in Table 4.6.

Due to the insufficient quantity of Li_2OHCl powder available to fill the deeper powder target holder, the shallow (~1 mm deep) holder was used. While this should have improved the conduction of heat away from the powder, it was expected to result in decreased morphological stability during sputtering. Considering this risk, the pre-sputtering step was dispensed with to allow the thickest possible film to be deposited in the time that the target remained stable. However, this may have led to increased film contamination.

Table 4.6 Conditions used for deposition from the Li_2OHCl powder target based on those found to achieve stable sputtering from Li_2O + LiCl powder targets (Table 4.4).

Parameter	Value
Process gas	Ar
Process pressure	$1*10^{-3}$ mbar
RF power	22 W (1.1 W cm^{-2})

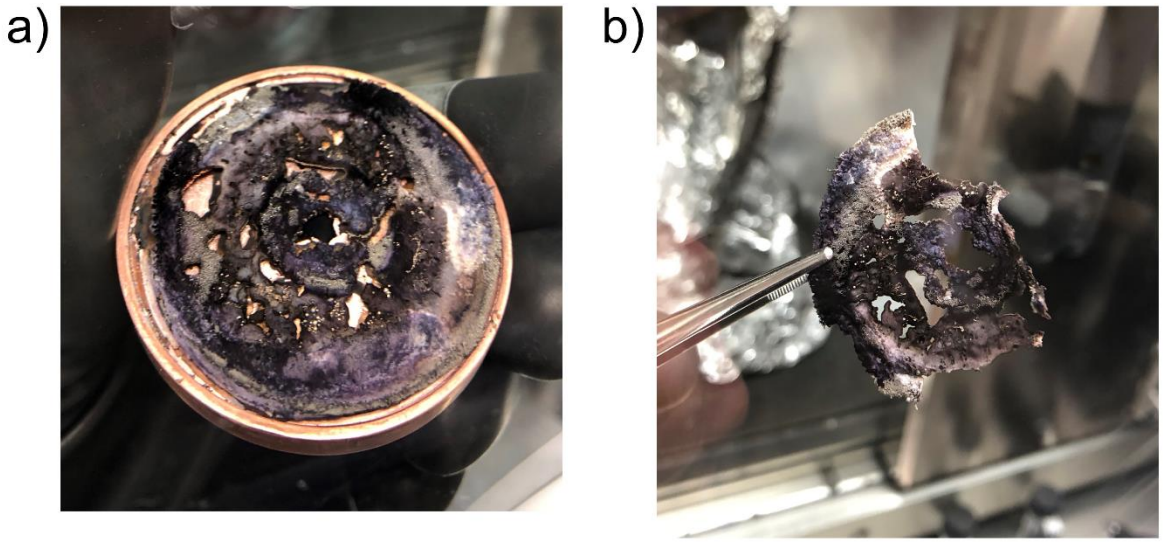


Figure 4.17 Appearance of the Li_2OHCl target after sputter deposition for 7 hours and 18 minutes using the conditions in Table 4.6: a) target in the copper holder and b) fragment of sintered/melted powder removed from the copper holder.

Figure 4.17 shows photographs of the Li_2OHCl target sputtered using the conditions in Table 4.6. The planned deposition duration was 12 hours, but the plasma became unstable and extinguished after 7 hours and 18 minutes, which may have occurred because of target instability. Indeed, the appearance of the target suggests that it was less stable during sputtering than the Li_2O + LiCl target deposited using the conditions in Table 4.4 (Figure 4.8) and may have undergone partial melting, revealing areas of the bottom of the copper holder. Since the plasma could not be stabilized when a lower RF power was used, there is little scope to make these processing conditions any gentler without making significant changes to the design of the sputtering system.

4.3.3.2 Structural Properties of the Films

Since adequate target stability was maintained for over 7 hours during deposition from the Li_2OHCl powder target using the sputtering conditions in Table 4.6, the structural properties of the resulting films were characterized. Several of the films were annealed at 250 °C for 1 hour; this temperature was chosen since it is just below the melting point of Li_2OHCl (~300 °C) and should result in a high rate of crystallization and grain growth. Typical XRD

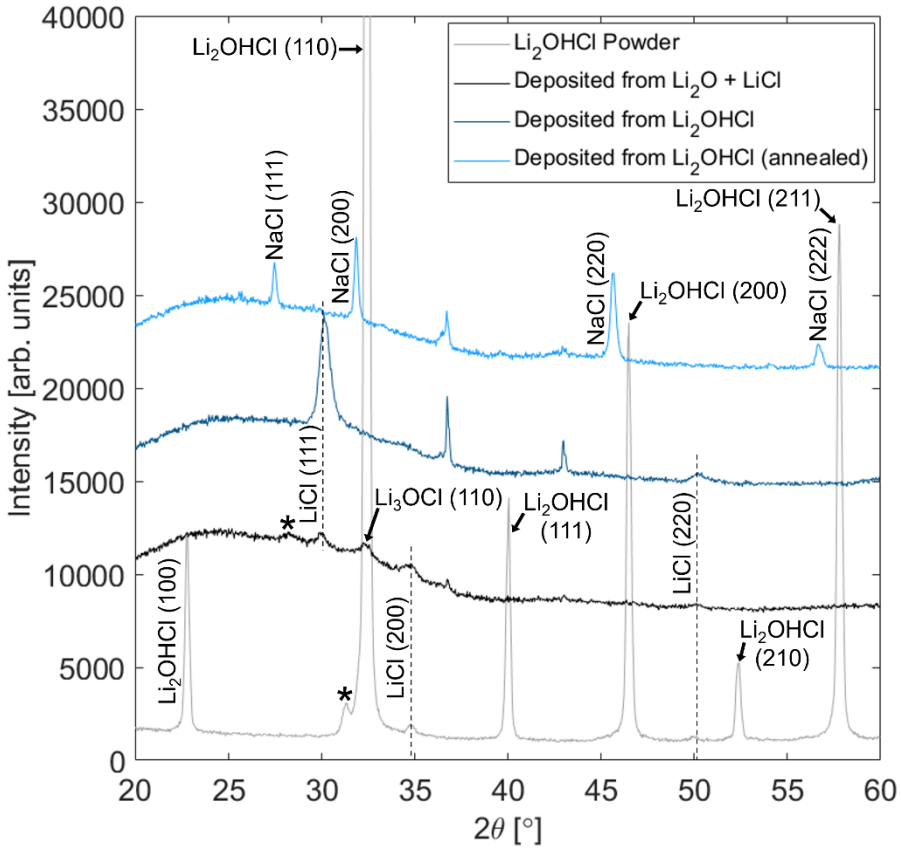


Figure 4.18 Typical XRD patterns of films deposited from an Li_2OHCl target for 7 hours and 18 minutes onto glass substrates using the conditions in Table 4.6 and annealed at 250 °C for 1 hour or left in the as-deposited condition. Patterns from the Li_2OHCl powder and a film deposited on glass from an Li_2O + LiCl target (shown previously in Figure 4.10 a), Figure 4.11 and Figure 4.12) are also plotted for comparison. Peaks marked * correspond to impurity phases from the precursor powder such as KCl. Unlabelled peaks are from the sample holder; the differing intensities of these peaks are due to differences in the lateral positioning of samples within the holder. The XRD data used to create this figure were collected by Dr Hyeon Jeong Lee.

patterns measured from as-deposited and annealed films on uncoated glass substrates are shown in Figure 4.18, along with patterns from the Li_2OHCl powder and a film deposited on glass from an Li_2O + LiCl target (shown previously in Figure 4.10 a), Figure 4.11 and Figure 4.12) for reference.

Unlike the films deposited from the Li_2O + LiCl target, those deposited from Li_2OHCl did not display any peaks corresponding to antiperovskite Li_2OHCl/Li_3OCl, either in the as-deposited

condition or after annealing. The only peaks present in the XRD pattern from the as-deposited film (other than those from the holder) correspond to LiCl. Annealing at 250 °C for 1 hour resulted in similar changes to those seen for the film deposited from an Li_2O + LiCl target (Figure 4.10 b) and Figure 4.11): the LiCl peaks disappeared and were replaced by NaCl peaks. However, the Li_2O (111) peak did not appear. The formation of NaCl indicates that, as seen previously, Na_2O from the glass reacted with LiCl in the films *via* equation 4.5. It is not clear why an antiperovskite phase formed in films deposited from Li_2O + LiCl targets but not in films deposited from Li_2OHCl, even after annealing, especially considering that Li_2OHCl is expected to be thermodynamically stable whereas Li_3OCl is not.

4.3.3.3 Detection of O-H Bonding

Despite the lack of a detectable volume fraction of antiperovskite phase in the films deposited from the Li_2OHCl target (Figure 4.18), FT-IR was performed on these films as well as on films deposited from Li_2O + LiCl and a sample of Li_2OHCl powder for reference. The primary objective was to determine whether any O-H bonding was present in the films deposited from Li_2O + LiCl. The measured IR spectra are shown in Figure 4.19.

Bands centred at ~3600 cm^{-1}, which correspond to O-H stretching vibrations, are present in the spectra measured from the Li_2OHCl powder and the film deposited from this powder. This confirms that O-H bonding was present in the film, even though crystalline phases containing O-H (Li_2OHCl, LiOH, $Li_4(OH)_3Cl$, etc.) were not seen in the corresponding XRD pattern in Figure 4.18. The fact that these results confirm the expected presence of O-H in films deposited from Li_2OHCl suggests that the FT-IR measurement procedure is valid for this type of sample. Therefore, the measurements made on the films deposited from Li_2O + LiCl targets should also be valid. The spectra from these films (both as-deposited and annealed) did not contain any bands over the wavenumber range corresponding to O-H stretching vibrations (3200-3600 cm^{-1}), meaning that the concentration of O-H bonding in these films was below the detection limit of the instrument and that the antiperovskite phase present was

likely Li_3OCl or an off-stoichiometric variant rather than a hydroxide chloride compound based on Li_2OHCl. Surprisingly, the film deposited from Li_2OHCl and annealed at 250 °C for 1 hour did not give rise to any bands corresponding to O-H stretching vibrations. The implication of this is that the film dehydrated – or lost LiOH – on annealing; this is further evidence that Li_2OHCl did not form successfully, since the results of prior experimental studies suggest it is thermodynamically stable at 250 °C[72,262,299,300].

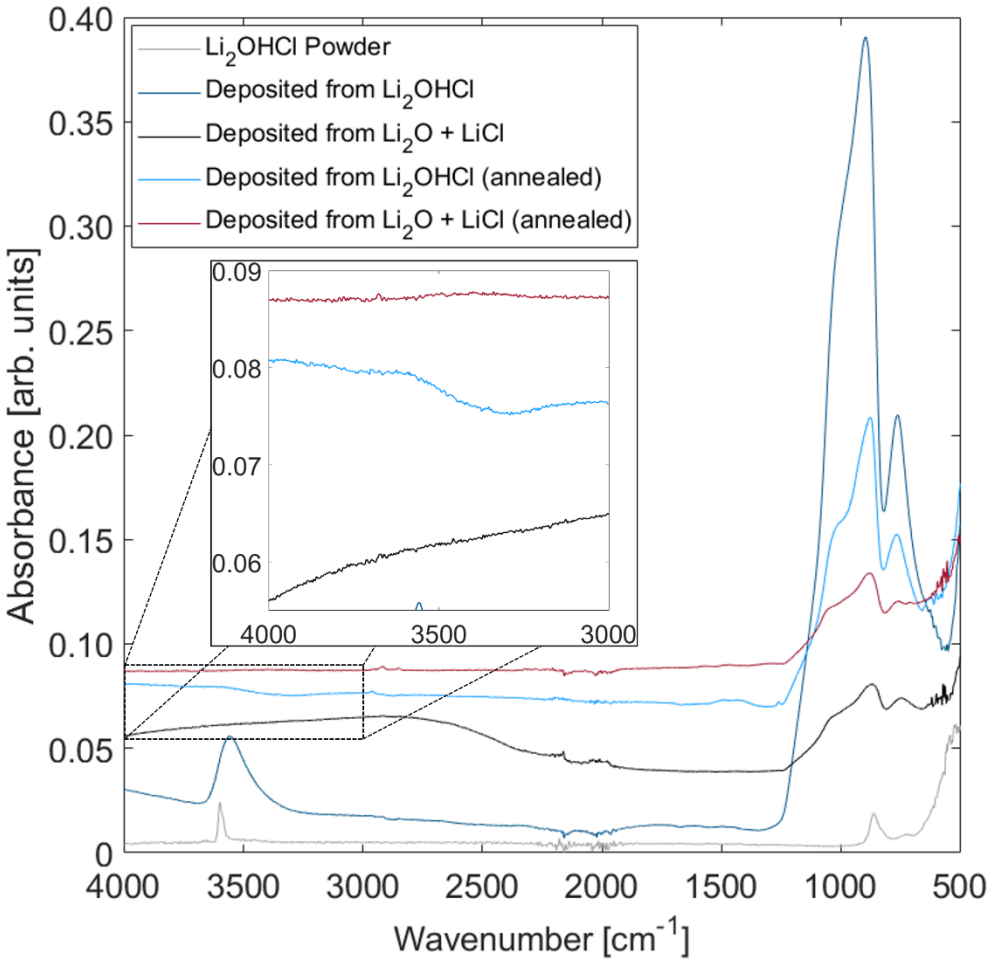


Figure 4.19 Typical FT-IR spectra measured from as-deposited and annealed (250 °C, 1 hour) films deposited from Li_2O + LiCl and Li_2OHCl targets onto glass substrates. A spectrum from a sample of Li_2OHCl powder, measured by Dr Hyeon Jeong Lee, is also shown for comparison. The enlarged IR spectral region covers the wavenumber range over which bands corresponding to O-H stretching vibrations are expected.

4.3.4 Characterization of Ionic Conductivity

So far the characterization performed on films deposited from Li_2OHCl suggests that crystalline Li_2OHCl is not present in as-deposited films and that an annealing temperature of 250 °C is too high. The decision was made to move on to the next stage of characterization and perform through-plane EIS experiments between 25 °C and 100 °C on films deposited from Li_2O + LiCl and Li_2OHCl targets. In addition to investigating the electrical properties, these experiments provided a convenient way to analyse phase changes over the range of measurement temperatures used. Figure 4.20 shows annotated photographs of typical samples used for these experiments accompanied by schematic diagrams labelled with approximate dimensions.

The failure rate of samples during EIS experiments was high: most either short-circuited due to the presence of pinholes (particularly those deposited from Li_2O + LiCl) or showed purely capacitive behaviour due to poor quality interfaces with the electrical contacts. The best results were achieved using nickel contacts with the “small circle” design on the film deposited from Li_2O + LiCl and platinum contacts with the “overlapping strip” design on the film deposited from Li_2OHCl (see Section 2.5.1 for further details on these electrical contact designs). Even the best-performing samples contained “soft” short circuits; these poor connections between the top and bottom electrical contacts resulted in electronic current flows small enough to allow both electronic and ionic impedance contributions to be measured from the Nyquist plots. The best results are shown in Figure 4.21 a) and b) alongside the equivalent circuit diagrams – c) to f) – used for modelling the systems and determining impedance values. The values for all equivalent circuit component properties required to model the Nyquist plots measured at each temperature are given in Appendix B. Although the maximum temperature setpoint was 100 °C, the highest test temperature reached for the film deposited from Li_2O + LiCl was 90 °C due to a fault with the temperature controller.

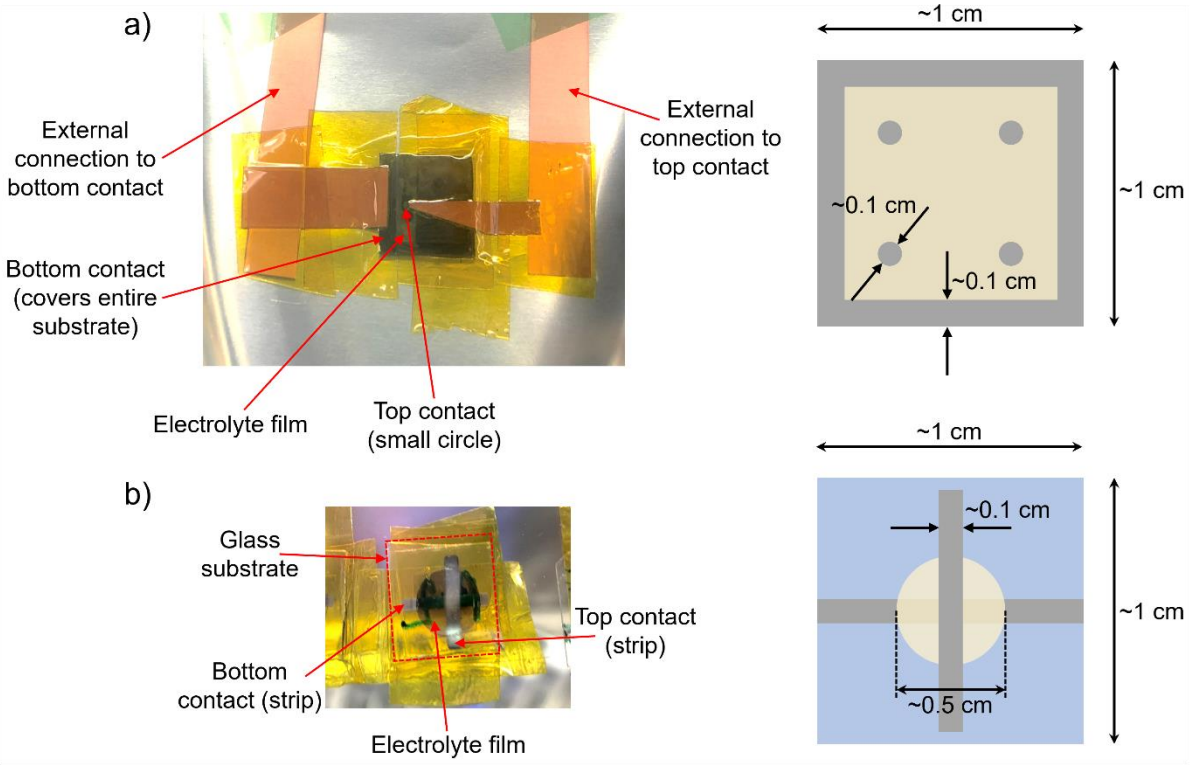


Figure 4.20 Annotated photographs and schematic diagrams of samples prepared for through-plane EIS measurements. A film deposited from an Li_2O + LiCl target with nickel electrical contacts in the "small circle" design (see Section 2.5.1) is shown connected within a heat sealable pouch in a), while a film deposited from an Li_2OHCl target with platinum electrical contacts in the "overlapping strip" design is shown immediately after top contact deposition in b). The glass substrate in b) has been outlined with a red dashed border for clarity. The schematic diagrams are based on those in Figure 2.9 a).

Evidence for the presence of soft short circuits in both samples is provided by the absence of low frequency tails in the Nyquist plots measured up to 60 °C (see Section 2.5.1), despite the use of blocking electrodes. The equivalent circuit models used for simulating the Nyquist plots in Figure 4.21 a) and b) in the 25-60 °C range (Figure 4.21 c) and d)) show that the "soft shorts" behave like shunt resistors bypassing the modified Debye circuit with resistance R_e. When the measurement frequency is low enough to prevent current flow through the geometric and interfacial capacitances, all current flows through the electronic resistance, and the high impedance intersection (actual or extrapolated) of the low frequency semicircle with the real axis is simply the value of the electronic resistance.

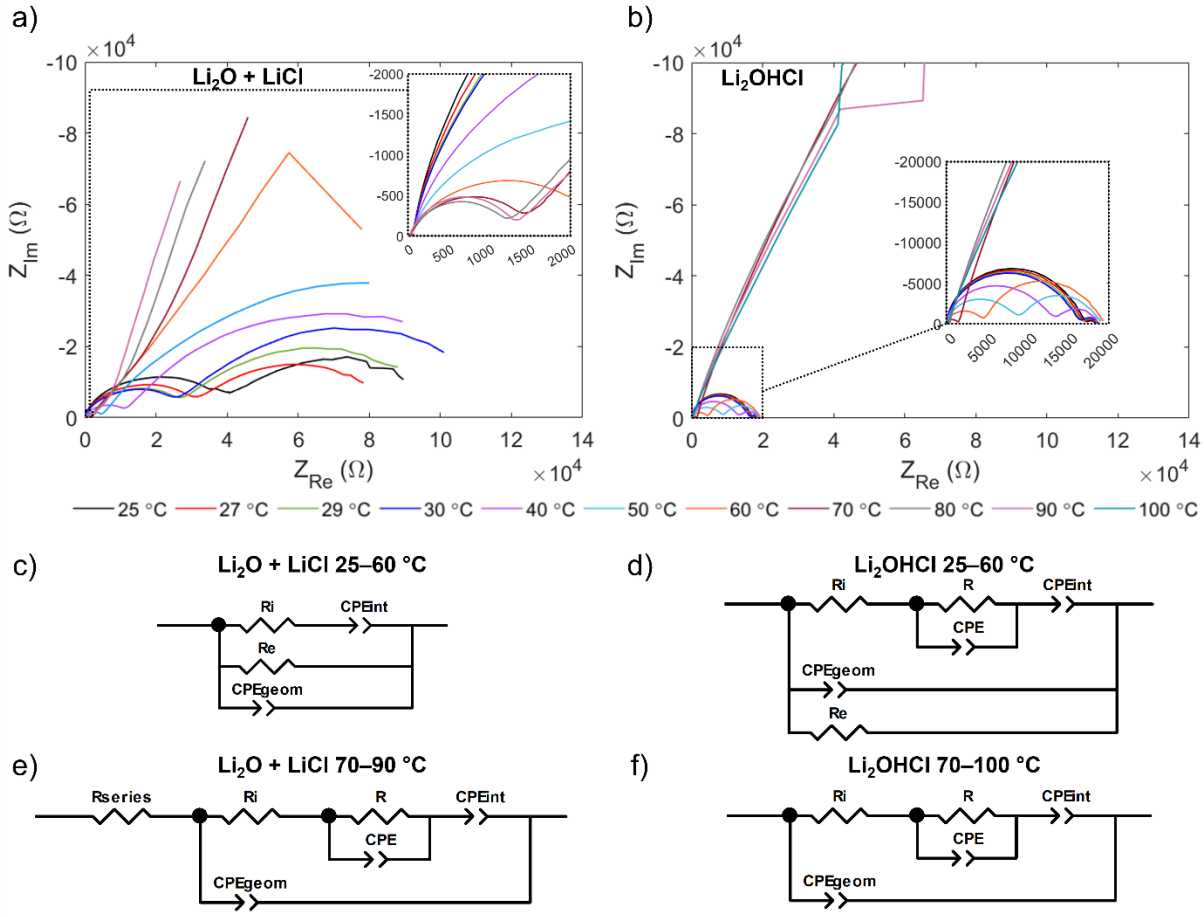


Figure 4.21 Results of through-plane impedance measurements performed at temperatures between 25 °C and 90/100 °C. Nyquist plots for the films deposited from Li_2O + LiCl and Li_2OHCl targets are shown in a) and b) respectively. Diagrams of the equivalent circuits used to simulate the experimental data are shown in c) and d) for the 25–60 °C range and in e) and f) for the 70–90/100 °C range. 'R_i' is the bulk ionic resistance, 'R_e' is the electronic resistance, 'R' is another ionic resistance component either within the electrolyte (e.g. grain boundary resistance) or external to it (e.g. reaction layer resistance), R_{series} is a series electronic resistance (e.g. the resistance of the electrical contacts), 'CPE_{int}' is the interfacial capacitance, 'CPE_{geom}' is the geometric capacitance and 'CPE' is the capacitance of the element associated with the resistance 'R'.

The Nyquist plots in the 25-60 °C temperature range in Figure 4.21 a) and b) show two semicircles; in both cases the semicircle at lower frequency grew in diameter as the temperature increased while the one at higher frequency became smaller. Enlargement of the lower frequency semicircle reflects the increase in electronic resistance, R_e, with temperature, which could be attributed to the formation of insulating oxidation layers on the

surfaces of the electrical contacts. The size of the higher frequency semicircle is expected to be dominated by the ionic contributions to impedance. Two ionic resistances – the bulk resistance R_i and a second resistance R (with an associated capacitive component CPE) – were used for simulating this semicircle for the film deposited from Li_2OHCl (Figure 4.21 d) and f)), whereas a good fit was initially achieved with just the bulk resistance in the case of the film deposited from Li_2O + LiCl (Figure 4.21 c)). The addition of R and CPE in the 70-90 °C range (Figure 4.21 e)) was required to model the electrolyte-electrode interfacial behaviour, while the addition of R_{series} accounted for the small offsets of the high frequency semicircle from the origin. Heating the samples to 70 °C and above caused the electronic shorts in both samples to disappear, as evidenced by the replacement of the low frequency semicircle with a tail characteristic of a current-blocking interface. This “healing” of the electronic shorts could have been a result of oxide layers at the electrolyte-electrode interfaces growing to a thickness at which electronic current flow through the pinholes in the electrolyte films was blocked completely. To reflect this, the electronic shunt resistance, R_e, was removed from the equivalent circuit diagrams used to fit the plots in the 70-90/100 °C range (Figure 4.21 e) and f)).

The semicircle controlled primarily by ionic conduction tends towards the real axis as the applied frequency decreases to the level at which all capacitances corresponding to ionic conduction in the electrolyte become blocking to electrical current. As in Figure 4.21 a) and b), the intersection point is not always reached due to interference from the low frequency response of the sample, but the point at which intersection would have occurred can be estimated by equivalent circuit modelling. Since the interfacial capacitance, CPE_{int}, is generally much larger than the other capacitances, it still has a negligible impedance at this frequency, so the impedance measured is usually the sum of the resistances corresponding to ionic conduction in the electrolyte. This is the case for both samples in the 70-90/100 °C temperature range (Z_{CPE} is also ~0 in Figure 4.21 c) since R and CPE are associated with the electrolyte-electrode interface). However, when an electronic shunt resistance, R_e, is present

(as for both samples in the 25–60 °C range), the impedance measured at the real axis intercept, R_{int}, corresponds to a series combination of ionic resistances in parallel with the electronic resistance. Thus, $\frac{1}{R_{int}} = \frac{1}{R_i} + \frac{1}{R_e}$ for the film deposited from Li_2O + LiCl and $\frac{1}{R_{int}} = \frac{1}{R_i+R} + \frac{1}{R_e}$ for the film deposited from Li_2OHCl. Measurement of R_e from the lowest frequency intercept, as described above, allowed the total ionic resistance of the electrolyte layer (R_i or R_i+R) to be determined at every measurement temperature for each of the samples. These resistance values were converted into ionic conductivity values using equation 2.9 and values of film thickness (Table 4.5 and Figure 4.23) and electrical contact overlap area measured by SEM (Appendix C).

The values of ionic conductivity measured at 25 °C and 50 °C for both samples are shown in Table 4.7. The uncertainties in these values were estimated by propagation of the uncertainties in the impedance and film thickness values; the uncertainties in contact area measurements were negligible by comparison. Since fitting of the equivalent circuit simulations to the Nyquist plots was performed manually by adjusting the values of the circuit components and judging the goodness of fit by eye (this resulted in the most accurate fitting), quantification of the uncertainties in the ionic impedance values was not straightforward. The difference in the impedance values obtained by manual and automatic fitting (using a tool in the software) for each Nyquist plot were taken as the uncertainties in the impedance measurements. In practice, these values are likely to be significant overestimates, since in many cases the results of automatic fitting were clearly poor.

Table 4.7 Li^+ conductivities of the films deposited from each sputtering target.

Sputtering target	**Li^+ conductivity of film at 25 °C [S cm^{-1}]**	**Li^+ conductivity of film at 50 °C [S cm^{-1}]**
Li_2O + LiCl	$(4.9\pm0.9)\times10^{-8}$	$(6\pm2)\times10^{-7}$
Li_2OHCl	$(1.2\pm0.7)\times10^{-8}$	$(1.7\pm0.5)\times10^{-7}$

The values of ionic conductivity measured for films deposited from the two targets have the same order of magnitude at each temperature, although the values measured for the film deposited from Li_2O + LiCl are a little higher. Very few, if any, reliable reports on the synthesis of Li_3OCl exist, so the magnitude of ionic conductivity expected is uncertain. However, there are several reports on the ionic conductivity of Li_2OHCl. The range of values measured previously at 25 °C is very wide (6.83×10^{-9} S cm^{-1} to ~4×10^{-5} S cm^{-1}), while at 50 °C it is a little narrower (~5.6×10^{-7} S cm^{-1} to ~1.1×10^{-5} S cm^{-1})[72,259,261,262]. The Li^+ conductivity values in Table 4.7 are at the lower ends of these ranges. Nevertheless, the results are consistent with the fact that the films deposited in this investigation had low antiperovskite phase purities, as revealed by the earlier XRD characterization. In fact, no antiperovskite phase was detected at all in the films deposited from the Li_2OHCl target.

To study the changes in activation energy with measurement temperature, Arrhenius plots were constructed from the Li^+ conductivity values calculated from the Nyquist plots in Figure 4.21. These are shown in Figure 4.22. The error bars represent the uncertainties in the values of $\ln\sigma$, which are simply the fractional errors in the ionic conductivity calculated using the uncertainty values discussed earlier. The uncertainties stated for the activation energy values are standard errors calculated from least squares linear fitting (the lines displayed on the plots are approximations) using the LINEST function in Excel.

The Arrhenius plot for the film deposited from Li_2O + LiCl in Figure 4.22 a) shows two linear regimes, while that for the film deposited from Li_2OHCl in b) shows three linear regimes. These regimes correspond to different crystallographic structures with different activation energies for Li^+ conduction. In previous published reports[72,259,261,300] Li_2OHCl has been found during heating to undergo a transformation from an orthorhombic structure stable at room temperature to a cubic structure stable above ~35 °C. Ionic conduction in the cubic structure has a lower activation energy than in the orthorhombic structure, hence the phase transformation shows up on the Arrhenius plot as change to a linear regime with a shallower

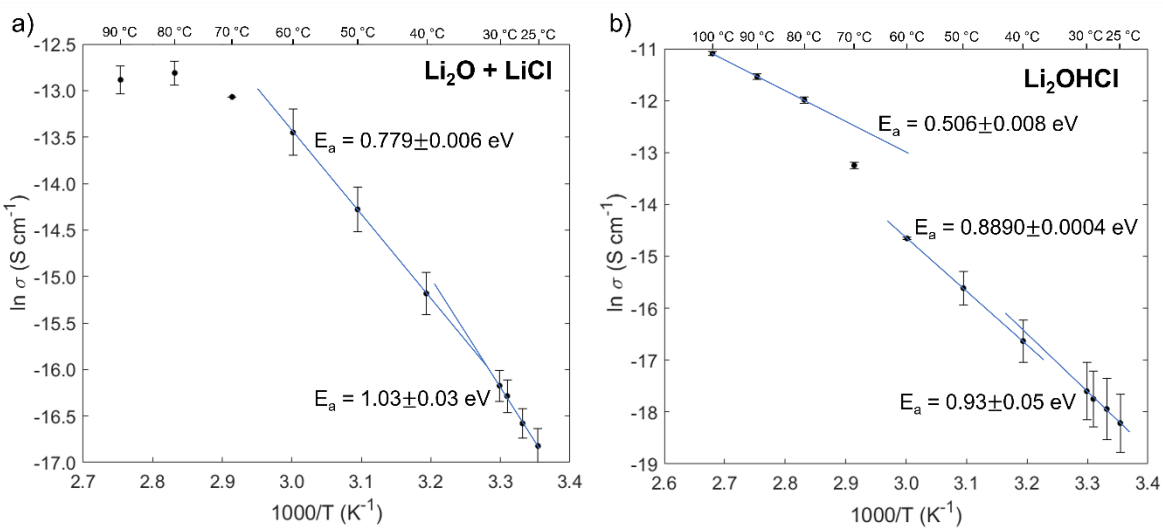


Figure 4.22 Arrhenius plots constructed from Li^+ conductivity values calculated from the through-plane impedance measurements performed at temperatures between 25 °C and 90/100 °C on films deposited from Li_2O + LiCl and Li_2OHCl targets (Figure 4.21). Activation energy (E_a) values and their standard errors calculated from the least squares linear fit lines (the lines shown are approximations) are displayed on the plots.

gradient on heating between 30 °C and 40 °C. Interestingly, both Arrhenius plots in Figure 4.22 show this characteristic change, even though such a phase transformation has not been predicted for Li_3OCl and no crystalline Li_2OHCl was detected by XRD characterization of the film deposited from the Li_2OHCl target. Although a transformation characteristic of Li_2OHCl appeared to occur in the film deposited from Li_2O + LiCl, the results of earlier structural and chemical characterization on similar films indicate that Li_2OHCl was not present. There is no reason why a phase transformation should not occur in Li_3OCl between 30 °C and 40 °C, especially if the composition is non-stoichiometric and the distortion from the cubic structure is small. Regarding the film deposited from Li_2OHCl, the fact that a transition to a linear regime with a slightly lower gradient occurred on heating between 30 °C and 40 °C may suggest that a very small volume fraction of crystalline Li_2OHCl was present in the films (below the detection limit of the X-ray diffractometer). However, when the standard error values are taken into account, the 25–30 °C and 40–60 °C activation energy regimes overlap,

meaning that it is not possible to make a valid conclusion that crystalline Li_2OHCl is present over these temperature ranges.

Unlike in previous Arrhenius plots reported for Li_2OHCl, there was a further reduction in activation energy when the measurement temperature reached 80 °C. This may reflect an abrupt increase in the volume fraction of cubic Li_2OHCl between 60 °C (where the previous linear regime ended) and 80 °C. The plot for the film deposited from Li_2O + LiCl in Figure 4.22 a) also shows a linear regime which ends at 60 °C; however, the data points for temperatures between 70 °C and 90 °C do not lie on a straight line, suggesting a more gradual structural or chemical change such as the incipient breakdown of the Li_3OCl phase or diffusion of sodium into the film from the glass substrate.

The activation energy values shown in Figure 4.22 are summarized in Table 4.8. Previous studies report activation energy values of ~0.8 eV for the orthorhombic phase of Li_2OHCl and 0.53–0.57 eV for the cubic phase[72,259,261,262]. The values measured here for the temperature ranges over which the orthorhombic and cubic structures of Li_2OHCl are stable are somewhat higher for both films up to ~70 °C. As mentioned previously, this can be attributed to the low volume fraction of antiperovskite phase present in each film. Nevertheless, in the high temperature regime (80–100 °C), the activation energy measured for the film deposited from Li_2OHCl was 0.506 ± 0.008 eV, which is slightly lower than the lowest value measured for cubic Li_2OHCl in previous studies. This supports the interpretation that the decrease in activation energy between 60 °C and 80 °C was due to an increase in the volume fraction of cubic Li_2OHCl.

Overall, the results of EIS measurements on films deposited from Li_2O + LiCl and Li_2OHCl targets support earlier findings that these films contained low volume fractions of LiRAP phases at room temperature. Thus, for both film types, the majority of the film volume was composed of poorly-conducting phases which limited the overall conductivity. It is possible that ionically conducting amorphous material based on Li_3OCl or Li_2OHCl was present and

Table 4.8 Activation energy values and their standard errors for Li^+ conductivity in films deposited from Li_2O + LiCl and Li_2OHCl targets, calculated from the Arrhenius plots in Figure 4.22 by least squares linear fitting using the LINEST function in Excel.

Temperature range [°C]	Activation energy [eV] (film from Li_2O + LiCl)	Activation energy [eV] (film from Li_2OHCl)
25–30	1.03±0.03	0.93±0.05
40–60	0.779±0.006	0.8898±0.0004
80–100	n/a	0.506±0.008

influenced the measured conductivity. The fact that the ionic conductivities measured here (Table 4.7) were much lower than reported by Braga *et al.*[145] (2.5×10^{-2} S cm^{-1} at 25 °C) for a glass electrolyte based on "Li_3ClO" suggests that the precautions taken in this work to avoid exposure of the films to moisture were effective (the conductivities of the glasses produced by Braga *et al.* may have been enhanced by inadvertent hydration – see Section 1.4.4.4). While increasing the temperature encouraged the growth of crystalline Li_2OHCl in the film deposited from the Li_2OHCl target, the crystalline Li_3OCl phase in the film deposited from Li_2O + LiCl became destabilized, as expected.

4.3.5 Additional Structural and Chemical Characterization

Structural and chemical characterization was performed on the film deposited from the Li_2OHCl target that had been subjected to EIS measurements in order to study any permanent structural and chemical changes that occurred during the temperature sweep. The film was also examined by SEM to study the morphology; Figure 4.23 shows surface and cross-sectional micrographs of the film.

Compared to the morphology of the films deposited from Li_2O + LiCl targets onto glass and nickel-coated glass substrates (Figure 4.13 a) and b)), the films deposited from an Li_2OHCl target onto glass were much smoother. This may reflect the formation of a low-energy interface with the glass substrate that favoured the growth of smooth layers rather than islands. The thickness determined from 8 locations along the film cross section was

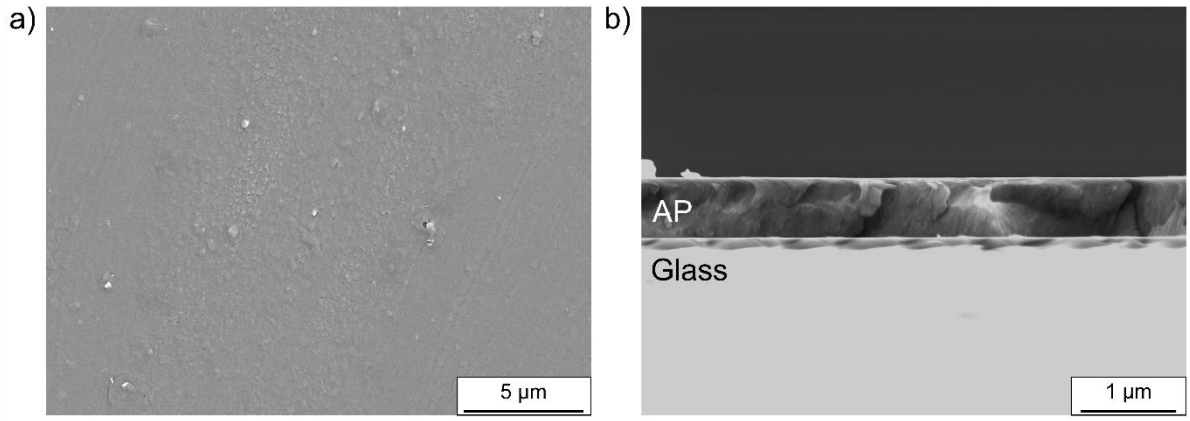


Figure 4.23 SEM micrographs of a film deposited from an Li_2OHCl target onto a glass substrate with platinum electrical contacts in an overlapping strip geometry (not present in the imaged region), taken after performing impedance measurements between 25 and 100 °C (Figure 4.21). The film surface is shown in a), while b) is a view of the cross-section produced by fracturing the sample. In the cross-sectional view, the image is slightly distorted due to charging by the electron beam.

(484±4) nm. This is 2/3 of the thickness measured for films deposited from Li_2O + LiCl onto glass substrates, as should be expected since the deposition duration was approximately 40% shorter.

The XRD pattern from this film in Figure 4.24 a) shows the presence of a small Li_2OHCl (110) peak, which is not present in the pattern from the as-deposited film. Other peaks corresponding to Li_2OHCl are also present, but unfortunately their positions also correspond to those expected for the platinum electrical contacts. Nevertheless, (110) is the most intense antiperovskite peak in the Li_2OHCl powder pattern and does not overlap with peaks expected from other phases so it is likely that a small volume of crystalline Li_2OHCl formed during the impedance measurements, supporting the interpretation of the Arrhenius plots in Figure 4.22. Owing to the difficulty in resolving the additional reflections from the orthorhombic Li_2OHCl structure in laboratory XRD systems, it is not possible to determine whether the peak corresponds to an orthorhombic or cubic phase. Moreover, the cubic to orthorhombic ratio of the Li_2OHCl powder cannot be determined, but this is not expected to have a bearing on its

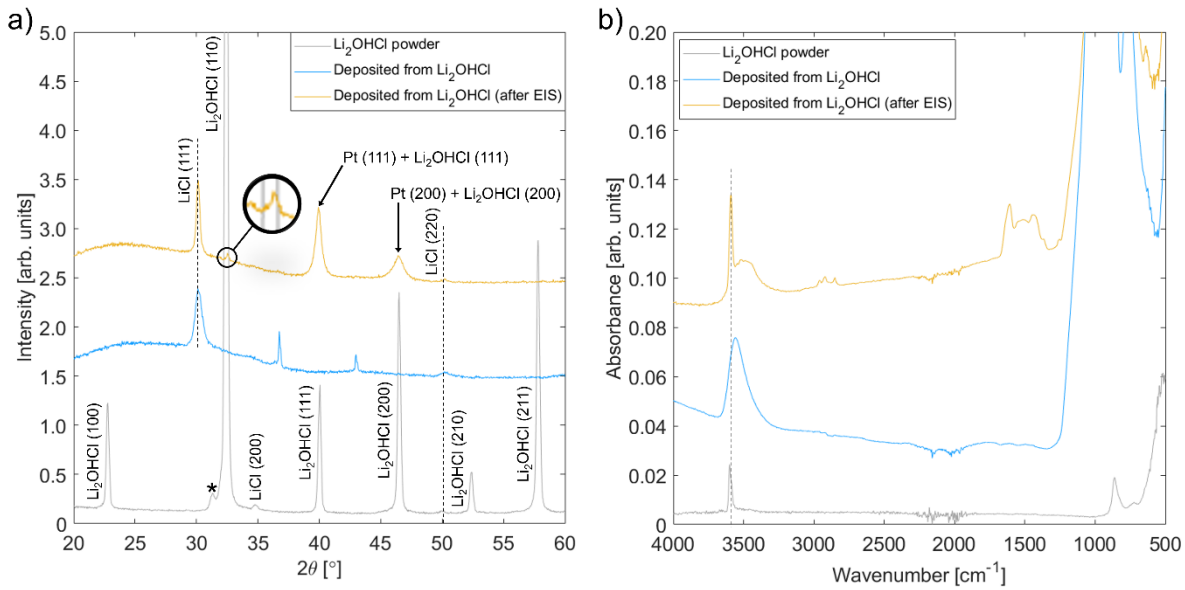


Figure 4.24 Structural and chemical characterization of a film deposited from an Li_2OHCl target onto a glass substrate with platinum electrical contacts in an overlapping strip geometry after performing impedance measurements between 25 °C and 100 °C (Figure 4.21). XRD patterns are shown in a), while b) shows corresponding FT-IR spectra. Data from an as-deposited film on glass and a sample of Li_2OHCl powder are also included for comparison. An enlarged view of the Li_2OHCl (110) XRD peak from the film subjected to EIS is shown in the large circle in a). Peaks marked * correspond to impurity phases from the precursor powder such as KCl. Unlabelled peaks on the XRD patterns are from the sample holder; the differing intensities of holder peaks are due to differences in lateral positioning of the samples within the holder. The XRD data shown in a), as well as the FT-IR spectrum from the Li_2OHCl powder in b), were collected by Dr Hyeon Jeong Lee.

performance as a sputtering target. LiCl (111) and (220) peaks are also present in the pattern recorded after performing EIS and have a similar intensity to those in the pattern from the as-deposited film, which is a further indication that any reaction to form Li_2OHCl proceeded only to a small extent during the EIS experiment.

The IR spectrum in Figure 4.24 b) for the film subjected to EIS measurements contains a band spanning the ~3300–3700 cm^{-1} wavenumber range, which corresponds to O-H stretching vibrations. This contrasts with the film that was annealed at 250 °C for 1 hour, which underwent dehydration and did not display any bands corresponding to O-H (Figure

4.19). Interestingly, the band appears to consist of two peaks: a sharp peak at ~3600 cm^{-1} merged with a broader, lower intensity peak centred at ~3500 cm^{-1}. These peaks are similar to those in the spectra from the Li_2OHCl powder and as-deposited film, respectively. Since the Li_2OHCl powder consisted of crystalline Li_2OHCl while the as-deposited film contained no detectable volume of this phase, it can be inferred that the sharper spectral peak corresponds to crystalline Li_2OHCl while the broader peak corresponds to amorphous phases containing O-H bonds, such as Li_2OHCl, LiOH or H_2O. Peak broadening with decreasing crystallinity has been observed previously in IR spectra[301,302]. Thus, the appearance of the spectrum from the film subjected to impedance measurements is consistent with the formation of a small volume of crystalline Li_2OHCl during heating to 100 °C, supporting the evidence from impedance measurements and XRD. These results suggest that an annealing temperature of 100 °C would be more appropriate than 250 °C for films deposited from Li_2OHCl targets, since crystallization of Li_2OHCl appears to occur at this temperature without any noticeable dehydration.

4.4 Conclusions

In this investigation, RF magnetron sputtering was applied to the synthesis of Li_3OCl and Li_2OHCl antiperovskite compounds for the first time. After developing a set of sputtering conditions that successfully stabilized the Li_2O + LiCl (1:1 molar ratio) powder sputtering target, a volume of a phase with properties corresponding to antiperovskite Li_3OCl was found to form in the films during deposition. Most, if not all, previous attempts to synthesize Li_3OCl have been unsuccessful due to inadvertent hydration of reactants and products during synthesis or characterization, poor interdiffusion between the precursor compounds and the inability to “lock in” the thermodynamically unstable product at room temperature. Furthermore, the characterization results typically reported are insufficient to conclude that Li_3OCl – rather than a hydrated compound such as Li_2OHCl – has been achieved. The success of the synthesis route used in this investigation was attributed to the atomic level

intermixing of the precursor compounds during sputtering and the rapid cooling from the deposition temperature facilitated by immediate quenching of the plasma and high rates of heat transfer from the thin films. Comprehensive measures were taken to remove moisture from the synthesis environment and prevent moisture ingress during synthesis and subsequent characterization. Furthermore, characterization designed to distinguish between Li_2OHCl and Li_3OCl compounds was performed, including the direct probing of O-H bonding using FT-IR and exploration of the effect of annealing on structural stability using XRD. Films deposited from the Li_2OHCl target contained O-H bonding, as expected, while no detectable level of O-H bonding was present in the films deposited from Li_2O + LiCl. Furthermore, heating to 100 °C was found to increase the antiperovskite phase fraction in the films deposited from Li_2OHCl, while the antiperovskite phase in the films deposited from Li_2O + LiCl began to decompose into the precursor compounds on heating. This was good evidence that the thermodynamically stable Li_2OHCl phase was present in the films deposited from Li_2OHCl powder, while the metastable Li_3OCl antiperovskite phase was present at room temperature in the films deposited from Li_2O + LiCl powder, held in this condition by vanishingly slow decomposition kinetics.

While the ionic conductivity values measured for films deposited from both Li_2O + LiCl and Li_2OHCl targets were low compared to those measured previously for Li_2OHCl, the films were not phase pure and secondary phases could have limited the Li^+ conductivity. Nevertheless, it was still possible to observe some of the underlying properties of the Li_3OCl and Li_2OHCl phases, including a decrease in activation energy between 30 °C and 40 °C. This behaviour was expected for Li_2OHCl and corresponds to the orthorhombic to cubic transition, but it had not been reported previously for Li_3OCl and implies that a structural transformation also occurs in this compound.

One reason for the low volume fraction of the Li_3OCl phase in the films deposited from Li_2O + LiCl targets may have been the excess LiCl content of these films. This was attributed to the

LiCl precursor partially melting and moving to the top of the target during sputtering, enhancing its rate of sputtering – and possibly evaporation – relative to that of Li_2O. Future investigations should look at ways to reduce the LiCl excess and mitigate the processes that cause it. Increasing the Li_2O:LiCl ratio in the target may help to reduce the Li_2O deficiency in the films, but strategies to prevent the partial melting of LiCl – such as enhanced target cooling – may be more effective. The ultimate solution – which would require re-designing the deposition system – could be “co-sputtering”. This would involve simultaneous sputtering from separate Li_2O and LiCl targets onto a single set of substrates, thereby avoiding the reduction in target homogeneity seen in this work and its effect on film composition. Another reason for the low volume fraction of the Li_3OCl phase could be that some of the Li_3OCl formed during deposition decomposed during cooling to room temperature. Increasing the cooling rate by using a substrate cooling system may increase the volume of Li_3OCl retained at room temperature. For films deposited from Li_2OHCl powder, increasing the volume fraction of the Li_2OHCl phase could be more straightforward and might be achieved by optimizing the post-deposition annealing process. The preliminary work performed here showed that 250 °C, despite being below the melting point of Li_2OHCl, is too high an annealing temperature, since it favours dehydration rather than growth of the Li_2OHCl phase. 100 °C appears to be suitable, but a higher rate of phase formation might be obtained at slightly higher temperatures.

While the morphology of films deposited from Li_2OHCl was smooth, the morphology of the films deposited from Li_2O + LiCl was found to be rough on a variety of substrate materials. The roughness was substantially decreased by using glass and metal-coated glass substrates. However, both sets of films contained a high density of pinholes and the interfaces with the current collectors were poor in some regions, causing most EIS measurements to fail. The volume fractions of antiperovskite phases in these films were low, and it is not known how increasing the volume fractions would affect the film morphologies and the propensity for pinhole formation. Therefore, steps to increase the volume fraction of

Li_3OCl and $L_{i2}OHCl$ should be attempted first, but if these do not lead to reduced pinhole formation it will be necessary to take other measures, such as applying a substrate bias to encourage planarization and re-sputtering of the films deposited from Li_2O + LiCl.

Despite these outstanding issues the overarching aims of this investigation, which were to demonstrate the feasibility of achieving the Li_3OCl and Li_2OHCl antiperovskite phases in thin films produced by RF magnetron sputtering and to develop an understanding of the processing-chemistry-structure-properties relationships, have largely been achieved. Based on this new understanding, specific suggestions for how to improve the properties of the films have been made. This work has shown that RF magnetron sputtering holds promise as a fabrication route for LiRAP thin films and may enable their use as thin-film solid electrolytes or as protective layers in all-solid-state lithium metal cells.

5 Conclusions and Further Work

All-thin-film batteries have been studied since the pioneering work of Sator in 1952 (Section 1.3.1). However, it was only after the discovery of LiPON electrolytes in the 1990s that interest really started to grow, since LiPON enabled the safe coupling of a revolutionary cathode material, LCO, with the ultimate anode material: lithium metal. To date, the Li/LiPON/LCO cell remains the most-studied all-thin-film cell and one of the few all-solid-state cells to have been commercialized.

The numerous benefits of thin-film processing over the powder processing routes commonly used to fabricate electrode and electrolyte materials for “bulk” solid-state cells were discussed in Section 1.4.3. Nevertheless, many of the challenges limiting the development of all-thin-film cells can be attributed to an insufficient knowledge of the processing-structure-properties relationships pertaining to electrode and electrolyte materials under investigation in thin-film form. This work studied these relationships for two materials fabricated by RF magnetron sputtering: LCO cathodes and lithium-rich antiperovskite chloride electrolytes.

The investigation on thin-film LCO cathodes in Chapter 3 sought to optimize the processing conditions for large-scale manufacturing and to increase areal capacity by increasing film thickness without sacrificing electrochemical performance. One of the first discoveries was that an oxygen gas flow is not required to achieve virtually phase-pure HT-LCO with a high degree of parallel alignment between the (104), (101) and (110) planes and the film surface, as desired for low impedance Li^+ transfer to the electrolyte. Further optimization of the processing conditions for manufacturability, which involved lowering the process pressure and increasing the RF power density used for sputtering as well as reducing the post-deposition annealing temperature, retained the desired structural properties. Even as-deposited films were found to contain the HT-LCO phase, albeit in nanocrystalline form. The cycling performance compared very favourably to previous reports; a maximum specific discharge capacity of 62 μAh $cm^{-2}μm^{-1}$ was reported for the annealed LCO film, which is just

below the highest reported value of 67 μAh $cm^{-2}μm^{-1}$. Moreover, the relatively thick films (~3 μm) provided one of the highest areal capacities ever reported for thin-film LCO cathodes: 172 μAh cm^{-2}. The increase in the deposition rate by a factor of 3-4 after optimizing the processing conditions makes the deposition of relatively thick films more viable from a manufacturing perspective. Furthermore, the cycling stability in the 3.0-4.2 V *vs* Li^+/Li range was very high, and structural degradation over 35 cycles at various cycling rates (including segments of up to 5 C) was negligible. Thus, the aims of this investigation were largely achieved, and the performance displayed by these LCO cathodes was superior in many respects to that reported in previous studies on thin-film LCO cathodes.

Future work must look at the cycling performance when combined with a LiPON electrolyte in an all-thin-film cell. Further, the use of ceramic substrates sputter-coated with an alloy of similar composition to the Waspaloy sheets used in this work should be investigated, since this strategy could prevent oxide layer formation and enable the use of more application-relevant base materials such as silicon. Although the processing will have to be optimized further for the deposition systems used in industry, the general principles demonstrated here should be applied to ensure that the requirements for low-cost, high-throughput manufacturing and optimal electrochemical performance are both met.

The investigation in Chapter 4 focused on harnessing the special properties of RF magnetron sputtering that could enable Li_3OCl – a very hygroscopic, thermodynamically unstable lithium-rich antiperovskite compound – to be “frozen” in a metastable state at room temperature. Additionally, it was noted that there are no reports on the synthesis of stable antiperovskite compounds such as Li_2OHCl by RF magnetron sputtering despite several previous reports of low ionic conductivities, which should be compensated for by minimizing the electrolyte thickness. This provided the opportunity to investigate the sputter deposition of Li_2OHCl for the first time. The aim of synthesizing Li_3OCl and Li_2OHCl in films deposited from Li_2O + LiCl and Li_2OHCl powder targets, respectively, was achieved and verified by a

series of experiments designed to discriminate between the Li_3OCl and Li_2OHCl phases. However, the antiperovskite phase purities of the films were low, resulting in ionic conductivity values on the order of 10^{-8} S cm^{-1} at 25 °C. The low ionic conductivity will not necessarily be a problem if the films are made sufficiently thin, but other attributes required for successful application in all-thin-film cells or as anode protective layers in bulk lithium metal cells must be verified.

An improved understanding of the processing-structure-properties relationships relevant to sputter-deposited Li_3OCl and Li_2OHCl thin films has revealed some promising directions for future research. The main objective should be to increase the volume fraction of the targeted antiperovskite phase in each film; obtaining the correct chemical composition will likely help to achieve this. Although the composition of films deposited from Li_2OHCl was not determined in this investigation, films deposited from Li_2O + LiCl targets were found to contain an excess of LiCl. Adding excess Li_2O powder to the target to try to correct this imbalance, or actively cooling the target during sputtering to avoid the formation of molten LiCl, which is thought to be responsible for the LiCl excess in the films, should be explored. Co-sputtering from separate Li_2O and LiCl targets will give the greatest degree of control over the film composition; however, this option would require a deposition system designed for simultaneous deposition from multiple targets. Aside from controlling the chemical composition, another measure that may increase the volume fraction of the Li_3OCl phase is the application of active substrate cooling at the end of the deposition process. This is based on the hypothesis that some of the Li_3OCl formed during deposition decomposes as the film cools to room temperature. The final problem that must be addressed in future studies is the short-circuiting through pinholes seen to occur in films deposited from both target compositions in this investigation. Improving film-substrate interactions is likely to be the solution, but it is not clear which substrate materials will minimize the interfacial energy. Various cathode films, starting with LCO, could be tried as alternatives to the metal-coated substrates used in this investigation. If pinholes are avoided in the antiperovskite films, these

substrates would allow the cycling performance of the electrolytes to be assessed in all-thin-film cells.

Thus, the investigations in this thesis studied the thin-film processing of two important battery materials, taking an approach rooted in materials science to provide new insights on challenges that are often approached from the standpoints of chemists and electrochemists. The results presented show the utility of RF magnetron sputtering in addressing some of the processing challenges facing the development of all-solid-state cells. On this basis, it seems likely that interest in thin-film deposition techniques among the solid-state battery research community will continue to grow. However, the focus of thin-film research may shift away from all-thin-film cells towards protective layers for lithium metal anodes and high voltage cathodes in bulk cells, since it is not clear that there is a strong demand for the miniature electronic devices originally envisaged as the main application for all-thin-film cells.

References

1. Goodenough, J. B. & Park, K. S. The Li-ion rechargeable battery: A perspective. *J. Am. Chem. Soc.* **135**, 1167–1176 (2013).
2. Alpen, U. v. Li3N: A promising Li ionic conductor. *J. Solid State Chem.* **29**, 379–392 (1979).
3. Blomgren, G. E. The Development and Future of Lithium Ion Batteries. *J. ofThe Electrochem. Soc.* **164**, A5019–A5025 (2017).
4. Ulvestad, A. A Brief Review of Current Lithium Ion Battery Technology and Potential Solid State Battery Technologies. *arXiv.org* (2018).
5. Huggins, R. A. *Advanced Batteries*. (Springer, 2009).
6. Nitta, N., Wu, F., Lee, J. T. & Yushin, G. Li-ion battery materials: present and future. *Mater. Today* **18**, 252–264 (2015).
7. Mizushima, K., Jones, P. C., Wiseman, P. J. & Goodenough, J. B. LixCoO2 (0<x⩽1): A new cathode material for batteries of high energy density. *Solid State Ionics* **3**–**4**, 171–174 (1981).
8. Thackeray, M. M., David, W. I. F., Bruce, P. G. & Goodenough, J. B. Lithium insertion into manganese spinels. *Mater. Res. Bull.* **18**, 461–472 (1983).
9. Hu, L.-H., Wu, F.-Y., Lin, C.-T., Khlobystov, A. N. & Li, L.-J. Graphene-modified LiFePO4 cathode for lithium ion battery beyond theoretical capacity. *Nat. Commun.* **4**, 1687 (2013).
10. Padhi, A. K., Nanjundaswamy, K. S. & Goodenough, J. B. Phospho-olivines as Positive-Electrode Materials for Rechargeable Lithium Batteries. *J. Electrochem. Soc.* **144**, 1188 (1997).
11. Id, C. S. *et al.* Improving the Electrochemical Performance of LiNi0.80Co0.15Al0.05O2 in Lithium Ion Batteries by LiAlO2 Surface Modification. *Appl. Sci.* **8**, 378 (2018).
12. Sutula, R. A. *FY 2000 Progress Report for the Advanced Technology Development Program*. (2000).
13. Ohzuku, T. & Makimura, Y. Layered Lithium Insertion Material of LiCo1/3Ni1/3Mn1/3 O2 for Lithium-Ion Batteries. *Chem. Lett.* **30**, 642–643 (2001).
14. Schmuch, R., Wagner, R., Hörpel, G., Placke, T. & Winter, M. Performance and cost of materials for lithium-based rechargeable automotive batteries. *Nat. Energy* **3**, 267–

278 (2018).

15. Kim, M.-H., Shin, H.-S., Shin, D. & Sun, Y.-K. Synthesis and electrochemical properties of Li[Ni0.8Co0.1Mn0.1]O2 and Li[Ni0.8Co0.2]O2 via co-precipitation. *J. Power Sources* **159**, 1328–1333 (2006).

16. Xiao, J. *et al.* Understanding and applying coulombic efficiency in lithium metal batteries. *Nat. Energy* **5**, 561–568 (2020).

17. Wu, B., Lochala, J., Taverne, T. & Xiao, J. The interplay between solid electrolyte interface (SEI) and dendritic lithium growth. *Nano Energy* **40**, 34–41 (2017).

18. Deng, D. Li-ion batteries: Basics, progress, and challenges. *Energy Sci. Eng.* **3**, 385–418 (2015).

19. Liu, J. *et al.* Pathways for practical high-energy long-cycling lithium metal batteries. *Nat. Energy* **4**, 180–186 (2019).

20. Luo, W., Yu, C. & Hu, L. Solid-State Electrolyte. *Encycl. Inorg. Bioinorg. Chem.* 1–9 (2019). doi:10.1002/9781119951438.eibc2666

21. Foley, R. T. Solid Electrolyte Galvanic Cells. *J. Electrochem. Soc.* **116**, 13C (1969).

22. Tubandt, C. & Lorenz, E. Molekularzustand und elektrisches Leitvermögen kristallisierter Salze. *Zeitschrift für Phys. Chemie* **87U**, 513–542 (1914).

23. Takahashi, T. Silver Ion Conducting Solid Electrolytes. in *Handbook of Solid State Batteries & Capacitors* (ed. Munshi, M. Z. A.) 79–109 (World Scientific Publishing Co. Pte. Ltd., 1995).

24. Hull, M. N. Recent progress in the development of solid electrolyte batteries. *Energy Convers.* **10**, 215–226 (1970).

25. Sator, A. Title Unknown. *Compt Rend. Acad. Sci.* **234**, 2283 (1952).

26. Rani, D. Silver solid state batteries. in *Handbook of Solid State Batteries & Capacitors* (ed. Munshi, M. Z. A.) 111–129 (World Scientific Publishing Co. Pte. Ltd., 1995).

27. Takahashi, T. & Yamamoto, O. The Ag/Ag3SI/I2 solid-electrolyte cell. *Electrochim. Acta* **11**, 779–789 (1966).

28. Owens, B. B. & Argue, G. R. High-Conductivity Solid Electrolytes: MAg 4 I 5. *Science (80-.).* **157**, 308–310 (1967).

29. Bradley, J. N. & Greene, P. D. Solids with high ionic conductivity in group 1 halide systems. *Trans. Faraday Soc.* **63**, 424 (1967).

30. Martins, D. T. A.-A. Compact Ion-source Based on Superionic Rubidium Silver Iodide

(RbAg4I5) Solid Electrolyte. (Universidade Nova de Lisboa, 2013).

31. Liang, C. C. & Bro, P. A High-Voltage, Solid-State Battery System. *J. Electrochem. Soc.* **116**, 1322 (1969).

32. Liang, C. C., Epstein, J. & Boyle, G. H. A High-Voltage, Solid-State Battery System. *J. Electrochem. Soc.* **116**, 1452 (1969).

33. Levasseur, A., Menetrier, M., Dormoy, R. & Meunier, G. Solid state microbatteries. *Mater. Sci. Eng. B* **3**, 5–12 (1989).

34. Greatbatch, W. *et al.* The Solid-State Lithium Battery: A New Improved Chemical Power Source for Implantable Cardiac Pacemakers. *IEEE Trans. Biomed. Eng.* **BME-18**, 317–324 (1971).

35. Burr, L. H. The lithium iodide powered cardiac pacemaker. Clinical experience with 250 implantations. *J. Thorac. Cardiovasc. Surg.* **73**, 421–423 (1977).

36. Ravaine, D. Ionic transport properties in glasses. *J. Non. Cryst. Solids* **73**, 287–303 (1985).

37. Ravaine, D. Glasses as solid electrolytes. *J. Non. Cryst. Solids* **38**–**39**, 353–358 (1980).

38. Tuller, H. L. & Barsoum, M. W. Glass solid electrolytes: Past, present and near future - the year 2004. *J. Non. Cryst. Solids* **73**, 331–350 (1985).

39. Glass, A. M., Nassau, K. & Negran, T. J. Ionic conductivity of quenched alkali niobate and tantalate glasses. *J. Appl. Phys.* **49**, 4808–4811 (1978).

40. Julien, C. & Balkanski, M. Thin-film growth and structure for solid-state batteries. *Appl. Surf. Sci.* **48**–**49**, 1–11 (1991).

41. Levasseur, A., Brethous, J. C., Reau, J. M., Hagenmuller, P. & Couzi, M. Synthesis and characterization of new solid electrolyte conductors of lithium ions. *Solid State Ionics* **1**, 177–186 (1980).

42. Levasseur, A., Kbala, M., Hagenmuller, P., Couturier, G. & Danto, Y. Elaboration and characterization of lithium conducting thin film glasses. *Solid State Ionics* **9**–**10**, 1439–1444 (1983).

43. Swann, S. Magnetron sputtering. *Phys. Technol.* **19**, 67–75 (1988).

44. Kbala, M., Makyta, M., Levasseur, A. & Hagenmuller, P. Characterization and electrical behavior of new lithium chalcoborate thin films. *Solid State Ionics* **15**, 163–169 (1985).

45. Miyauchi, K., Matsumoto, K., Kanehori, K. & Kudo, T. New amorphous thin films of lithium ion conductive solid electrolyte. *Solid State Ionics* **9**–**10**, 1469–1472 (1983).

46. Kanehori, K., Matsumoto, K., Miyauchi, K. & Kudo, T. Thin film solid electrolyte and its application to secondary lithium cell. *Solid State Ionics* **9**–**10**, 1445–1448 (1983).

47. Ohtsuka, H. & Yamaki, J. Electrical characteristics of Li2O_V2O5_SiO2 thin films. *Solid State Ionics* **35**, 201–206 (1989).

48. Malugani, J. P. & Robert, G. Preparation and electrical properties of the 0,37Li2S-0,18P2S5-0,45LiI glass. *Solid State Ionics* **1**, 519–523 (1980).

49. Wada, H., Menetrier, M., Levasseur, A. & Hagenmuller, P. Preparation and ionic conductivity of new B2S3-Li2S-LiI glasses. *Mater. Res. Bull.* **18**, 189–193 (1983).

50. Souquet, J., Robinel, E., Barrau, B. & Ribes, M. Glass formation and ionic conduction in the M2S□GeS2 (M = Li, Na, Ag) systems. *Solid State Ionics* **3**–**4**, 317–321 (1981).

51. Angell, C. Fast ion motion in glassy and amorphous materials. *Solid State Ionics* **9**–**10**, 3–16 (1983).

52. Mercier, R., Malugani, J.-P., Fahys, B. & Robert, G. Superionic conduction in Li 2 S - P 2 S 5 - LiI - glasses. *Solid State Ionics* **5**, 663–666 (1981).

53. Nishi, Y. Lithium ion secondary batteries; past 10 years and the future. *J. Power Sources* **100**, 101–106 (2001).

54. Albertus, P., Babinec, S., Litzelman, S. & Newman, A. Status and challenges in enabling the lithium metal electrode for high-energy and low-cost rechargeable batteries. *Nat. Energy* **3**, 16–21 (2018).

55. Fan, L., Wei, S., Li, S., Li, Q. & Lu, Y. Recent Progress of the Solid-State Electrolytes for High-Energy Metal-Based Batteries. *Adv. Energy Mater.* **8**, 1–31 (2018).

56. Bachman, J. C. *et al.* Inorganic Solid-State Electrolytes for Lithium Batteries: Mechanisms and Properties Governing Ion Conduction. *Chem. Rev.* **116**, 140–162 (2016).

57. Pasta, M. *et al.* 2020 roadmap on solid-state batteries. *J. Phys. Energy* **2**, 032008 (2020).

58. MacLaughlin, C. M. Innovations in Lithium Ion Battery Technologies: A Conversation with Will West, Nancy Dudney, and Andrew Westover. *ACS Energy Lett.* **4**, 786–788 (2019).

59. Diederichsen, K. M., McShane, E. J. & McCloskey, B. D. Promising Routes to a High

Li + Transference Number Electrolyte for Lithium Ion Batteries. *ACS Energy Lett.* **2**, 2563–2575 (2017).

60. Ratner, M. A. & Shriver, D. F. Ion transport in solvent-free polymers. *Chem. Rev.* **88**, 109–124 (1988).

61. Dirican, M., Yan, C., Zhu, P. & Zhang, X. Composite solid electrolytes for all-solid-state lithium batteries. *Mater. Sci. Eng. R Reports* **136**, 27–46 (2019).

62. Cao, S. *et al.* Modeling, preparation, and elemental doping of Li7La3Zr2O12 garnet-type solid electrolytes: A review. *J. Korean Ceram. Soc.* **56**, 111–129 (2019).

63. Yang, X. *et al.* Determining the limiting factor of the electrochemical stability window for PEO-based solid polymer electrolytes: main chain or terminal –OH group? *Energy Environ. Sci.* **13**, 1318–1325 (2020).

64. Sun, C., Liu, J., Gong, Y., Wilkinson, D. P. & Zhang, J. Recent advances in all-solid-state rechargeable lithium batteries. *Nano Energy* **33**, 363–386 (2017).

65. Dixit, M. *et al.* Current Status and Prospects of Solid-State Batteries as the Future of Energy Storage. in *Management and Applications of Energy Storage Devices* (IntechOpen, 2022). doi:10.5772/intechopen.98701

66. Takahashi, T., Kuwabara, K. & Shibata, M. Solid-state ionics - conductivities of Na+ ion conductors based on NASICON. *Solid State Ionics* **1**, 163–175 (1980).

67. Thangadurai, V., Shukla, A. K. & Gopalakrishnan, J. New lithium-ion conductors based on the NASICON structure. *J. Mater. Chem.* **9**, 739–741 (1999).

68. Inaguma, Y. *et al.* High ionic conductivity in lithium lanthanum titanate. *Solid State Commun.* **86**, 689–693 (1993).

69. Inada, R., Kimura, K., Kusakabe, K., Tojo, T. & Sakurai, Y. Synthesis and lithium-ion conductivity for perovskite-type Li3/8Sr7/16Ta3/4Zr1/4O3 solid electrolyte by powder-bed sintering. *Solid State Ionics* **261**, 95–99 (2014).

70. Zhu, Y., He, X. & Mo, Y. Origin of Outstanding Stability in the Lithium Solid Electrolyte Materials: Insights from Thermodynamic Analyses Based on First-Principles Calculations. *ACS Appl. Mater. Interfaces* **7**, 23685–23693 (2015).

71. Li, Y. *et al.* Fluorine-Doped Antiperovskite Electrolyte for All-Solid-State Lithium-Ion Batteries. *Angew. Chemie Int. Ed.* **55**, 9965–9968 (2016).

72. Lee, H. J. *et al.* Li-ion conductivity in Li 2 OHCl 1− x Br x solid electrolytes: grains, grain boundaries and interfaces. *J. Mater. Chem. A* **10**, 11574–11586 (2022).

73. Effat, M. B. *et al.* Stability, Elastic Properties, and the Li Transport Mechanism of the Protonated and Fluorinated Antiperovskite Lithium Conductors. *ACS Appl. Mater. Interfaces* **12**, 55011–55022 (2020).

74. Arbi, K., Rojo, J. M. & Sanz, J. Lithium mobility in titanium based Nasicon Li1+xTi2-xAlx(PO4)3 and LiTi2-x Zrx(PO4)3 materials followed by NMR and impedance spectroscopy. *J. Eur. Ceram. Soc.* **27**, 4215–4218 (2007).

75. Arbi, K., Mandal, S., Rojo, J. M. & Sanz, J. Dependence of ionic conductivity on composition of fast ionic conductors Li1+xTi2-xAlx(PO4)3, 0 ≤ x ≤ 0.7. A parallel NMR and electric impedance study. *Chem. Mater.* **14**, 1091–1097 (2002).

76. Cui, Y. *et al.* Ionic Conductivity and Stability of the Lithium Aluminum Germanium Phosphate. *ECS Trans.* **72**, 139–146 (2016).

77. Rettenwander, D. *et al.* Interface Instability of Fe-Stabilized Li7La3Zr2O12 versus Li Metal. *J. Phys. Chem. C* **122**, 3780–3785 (2018).

78. Baek, S.-W., Lee, J.-M., Kim, T. Y., Song, M.-S. & Park, Y. Garnet related lithium ion conductor processed by spark plasma sintering for all solid state batteries. *J. Power Sources* **249**, 197–206 (2014).

79. Seino, Y., Ota, T., Takada, K., Hayashi, A. & Tatsumisago, M. A sulphide lithium super ion conductor is superior to liquid ion conductors for use in rechargeable batteries. *Energy Environ. Sci.* **7**, 627–631 (2014).

80. Kamaya, N. *et al.* A lithium superionic conductor. *Nat. Mater.* **10**, 682–686 (2011).

81. Zhang, Z. *et al.* Synthesis and characterization of argyrodite solid electrolytes for all-solid-state Li-ion batteries. *J. Alloys Compd.* **747**, 227–235 (2018).

82. Deng, Z. Li6PS5Cl. *Materials Project* Available at: https://materialsproject.org/materials/mp-985592/. (Accessed: 7th June 2019)

83. Yu, C. *et al.* Revealing the relation between the structure, Li-ion conductivity and solid-state battery performance of the argyrodite Li6PS5Br solid electrolyte. *J. Mater. Chem. A* **5**, 21178–21188 (2017).

84. Yu, C. *et al.* Facile Synthesis toward the Optimal Structure-Conductivity Characteristics of the Argyrodite Li6PS5Cl Solid-State Electrolyte. *ACS Appl. Mater. Interfaces* **10**, 33296–33306 (2018).

85. Yu, X., Bates, J. B., Jellison, G. E. & Hart, F. X. A Stable Thin-Film Lithium Electrolyte: Lithium Phosphorus Oxynitride. *J. Electrochem. Soc.* **144**, 524–532 (1997).

86. Wang, L., Liu, D., Huang, T., Geng, Z. & Yu, A. Reducing interfacial resistance of a Li

1.5 Al 0.5 Ge 1.5 (PO 4) 3 solid electrolyte/electrode interface by polymer interlayer protection. *RSC Adv.* **10**, 10038–10045 (2020).

87. Liu, Y. *et al.* Stabilizing the Interface of NASICON Solid Electrolyte against Li Metal with Atomic Layer Deposition. *ACS Appl. Mater. Interfaces* **10**, 31240–31248 (2018).

88. Hartmann, P. *et al.* Degradation of NASICON-Type Materials in Contact with Lithium Metal: Formation of Mixed Conducting Interphases (MCI) on Solid Electrolytes. *J. Phys. Chem. C* **117**, 21064–21074 (2013).

89. Nanda, J., Wang, C. & Liu, P. Frontiers of solid-state batteries. *MRS Bull.* **43**, 740–745 (2018).

90. Han, F. *et al.* Interphase Engineering Enabled All-Ceramic Lithium Battery. *Joule* **2**, 497–508 (2018).

91. Wu, B. *et al.* Interfacial behaviours between lithium ion conductors and electrode materials in various battery systems. *J. Mater. Chem. A* **4**, 15266–15280 (2016).

92. Zhang, W. *et al.* (Electro)chemical expansion during cycling: monitoring the pressure changes in operating solid-state lithium batteries. *J. Mater. Chem. A* **5**, 9929–9936 (2017).

93. Ohzuku, T. & Ueda, A. Solid-State Redox Reactions of LiCoO2 (R3m) for 4 Volt Secondary Lithium Cells. *J. Electrochem. Soc.* **141**, 2972–2977 (1994).

94. Yabuuchi, N. & Ohzuku, T. Novel lithium insertion material of LiCo1/3Ni1/3Mn1/3O2 for advanced lithium-ion batteries. *J. Power Sources* **119**–**121**, 171–174 (2003).

95. Porz, L. *et al.* Mechanism of Lithium Metal Penetration through Inorganic Solid Electrolytes. *Adv. Energy Mater.* **7**, 1–12 (2017).

96. Raj, R. & Wolfenstine, J. Current limit diagrams for dendrite formation in solid-state electrolytes for Li-ion batteries. *J. Power Sources* **343**, 119–126 (2017).

97. Han, F. *et al.* High electronic conductivity as the origin of lithium dendrite formation within solid electrolytes. *Nat. Energy* **4**, 187–196 (2019).

98. Chen, Y. T. *et al.* Voltammetric Enhancement of Li-Ion Conduction in Al-Doped Li 7-x La 3 Zr 2 O 12 Solid Electrolyte. *J. Phys. Chem. C* **121**, 15565–15573 (2017).

99. Shin, B. R. *et al.* Comparative study of TiS2/Li-In all-solid-state lithium batteries using glass-ceramic Li3PS4and Li10GeP2S12 solid electrolytes. *Electrochim. Acta* **146**, 395–402 (2014).

100. Le Van-Jodin, L., Ducroquet, F., Sabary, F. & Chevalier, I. Dielectric properties,

conductivity and Li+ ion motion in LiPON thin films. *Solid State Ionics* **253**, 151–156 (2013).

101. Pfenninger, R., Struzik, M., Garbayo, I., Stilp, E. & Rupp, J. L. M. A low ride on processing temperature for fast lithium conduction in garnet solid-state battery films. *Nat. Energy* **4**, 475–483 (2019).

102. Maurya, D., Sardarinejad, A. & Alameh, K. Recent Developments in R.F. Magnetron Sputtered Thin Films for pH Sensing Applications—An Overview. *Coatings* **4**, 756–771 (2014).

103. Vouros, P. & Masters, J. I. Thin-Film Silver Halide Electrolyte Cells. *J. Electrochem. Soc.* **116**, 880 (1969).

104. Dudney, N. J. Solid-state thin-film rechargeable batteries. in *Materials Science and Engineering B: Solid-State Materials for Advanced Technology* **116**, 245–249 (2005).

105. Zhao, S., Fu, Z. & Qin, Q. A solid-state electrolyte lithium phosphorus oxynitride film prepared by pulsed laser deposition. *Thin Solid Films* **415**, 108–113 (2002).

106. Ohring, M. *Materials Science of Thin Films*. (Academic Press, 2001).

107. Jones, S. D. & Akridge, J. R. A thin film solid state microbattery. *Solid State Ionics* **53**–**56**, 628–634 (1992).

108. Marchand, R. Nitrogen-containing phosphate glasses. *J. Non. Cryst. Solids* **56**, 173–178 (1983).

109. Bates, J. Electrical properties of amorphous lithium electrolyte thin films. *Solid State Ionics* **53**–**56**, 647–654 (1992).

110. Bates, J. B. *et al.* Fabrication and characterization of amorphous lithium electrolyte thin films and rechargeable thin-film batteries. *J. Power Sources* **43**, 103–110 (1993).

111. Wang, B. *et al.* Characterization of Thin-Film Rechargeable Lithium Batteries with Lithium Cobalt Oxide Cathodes. *J. Electrochem. Soc.* **143**, 3203–3213 (1996).

112. Dudney, N. J. & Neudecker, B. J. Solid state thin-film lithium battery systems. *Curr. Opin. Solid State Mater. Sci.* **4**, 479–482 (1999).

113. Lacivita, V. *et al.* Resolving the Amorphous Structure of Lithium Phosphorus Oxynitride (Lipon). *J. Am. Chem. Soc.* **140**, 11029–11038 (2018).

114. Hood, Z. D. *et al.* Elucidating Interfacial Stability between Lithium Metal Anode and Li Phosphorus Oxynitride via In Situ Electron Microscopy. *Nano Lett.* **21**, 151–157 (2021).

115. Cheng, D. *et al.* Unveiling the Stable Nature of the Solid Electrolyte Interphase between Lithium Metal and LiPON via Cryogenic Electron Microscopy. *Joule* **4**, 2484–2500 (2020).

116. Zhu, Y., He, X. & Mo, Y. First principles study on electrochemical and chemical stability of solid electrolyte-electrode interfaces in all-solid-state Li-ion batteries. *J. Mater. Chem. A* **4**, 3253–3266 (2016).

117. Westover, A. S., Dudney, N. J., Sacci, R. L. & Kalnaus, S. Deposition and Confinement of Li Metal along an Artificial Lipon-Lipon Interface. *ACS Energy Lett.* **4**, 651–655 (2019).

118. Kalnaus, S., Westover, A. S., Kornbluth, M., Herbert, E. & Dudney, N. J. Resistance to fracture in the glassy solid electrolyte Lipon. *J. Mater. Res.* **36**, 787–796 (2021).

119. West, K., Zachau-Christiansen, B., Jacobsen, T. & Skaarup, S. Thin-film vanadium oxide electrodes for lithium batteries. *J. Power Sources* **43**, 127–134 (1993).

120. Front Edge Technology, Inc. (2014). Available at: http://frontedgetechnology.com/gen.htm. (Accessed: 20th April 2019)

121. Grady, S. e-poster 26-Steve Grady. *Cymbet Corporation* (2014). Available at: http://pwrsocevents.com/wp-content/uploads/2014-presentations/ep/e-poster 26-Steve Grady.pdf. (Accessed: 6th October 2022)

122. THINERGY® MEC202 Solid-State, Flexible, Rechargeable Thin-Film Micro-Energy Cell DS1015 v1.2 Product Data Sheet. *Infinite Power Solutions* (2012). Available at: https://media.digikey.com/pdf/Data Sheets/Infinite Power Solutions PDFs/MEC202.pdf. (Accessed: 6th October 2022)

123. EnFilm™ - rechargeable solid state lithium thin film battery. *STMicroelectronics* Available at: https://www.st.com/en/power-management/efl700a39.html. (Accessed: 10th September 2022)

124. Ko, J. & Yoon, Y. S. Lithium phosphorus oxynitride thin films for rechargeable lithium batteries: Applications from thin-film batteries as micro batteries to surface modification for large-scale batteries. *Ceram. Int.* **48**, 10372–10390 (2022).

125. Shepard, J. Infinite Power Solutions Selects Site for Thin-Film Battery Manufacturing Facility. *EE Power* (2006). Available at: https://eepower.com/news/infinite-power-solutions-selects-site-for-thin-film-battery-manufacturing-facility/#. (Accessed: 9th September 2022)

126. Lü, X. *et al.* Li-rich anti-perovskite Li 3 OCl films with enhanced ionic conductivity.

Chem. Commun. **50**, 11520–11522 (2014).

127. Takahashi, M., Hayashi, M. & Shodai, T. Characterization of all-solid-state secondary batteries with LiCoO2 thin films prepared by ECR sputtering as positive electrodes. *J. Power Sources* **189**, 191–196 (2009).

128. Tan, J. & Tiwari, A. Fabrication and Characterization of Li7La3Zr2O12 Thin Films for Lithium Ion Battery. *ECS Solid State Lett.* **1**, Q57–Q60 (2012).

129. Neudecker, B. J., Dudney, N. J. & Bates, J. B. "Lithium-Free" Thin-Film Battery with In Situ Plated Li Anode. *J. Electrochem. Soc.* **147**, 517 (2000).

130. Notten, P. H. L., Roozeboom, F., Niessen, R. A. H. & Baggetto, L. 3-D Integrated All-Solid-State Rechargeable Batteries. *Adv. Mater.* **19**, 4564–4567 (2007).

131. Xu, F. *et al.* Properties of lithium phosphorus oxynitride (Lipon) for 3D solid-state lithium batteries. *J. Mater. Res.* **25**, 1507–1515 (2010).

132. Moitzheim, S., Put, B. & Vereecken, P. M. Advances in 3D Thin-Film Li-Ion Batteries. *Adv. Mater. Interfaces* **6**, 1–17 (2019).

133. Oudenhoven, J. F. M., Baggetto, L. & Notten, P. H. L. All-solid-state lithium-ion microbatteries: A review of various three-dimensional concepts. *Advanced Energy Materials* **1**, 10–33 (2011).

134. Li, J., Ma, C., Chi, M., Liang, C. & Dudney, N. J. Solid Electrolyte: the Key for High-Voltage Lithium Batteries. *Adv. Energy Mater.* **5**, 1401408 (2015).

135. Aribia, A. *et al.* Unlocking Stable Multi-Electron Cycling in NMC811 Thin-Films between 1.5 – 4.7 V. *Adv. Energy Mater.* 2201750 (2022). doi:10.1002/aenm.202201750

136. Lin, J. *et al.* Promising Electrode and Electrolyte Materials for High-Energy-Density Thin-Film Lithium Batteries. *ENERGY Environ. Mater.* **5**, 133–156 (2022).

137. Chen, R., Liang, W., Zhang, H., Wu, F. & Li, L. Preparation and performance of novel LLTO thin film electrolytes for thin film lithium batteries. *Chinese Sci. Bull.* **57**, 4199–4204 (2012).

138. Chen, H., Tao, H., Zhao, X. & Wu, Q. Fabrication and ionic conductivity of amorphous Li–Al–Ti–P–O thin film. *J. Non. Cryst. Solids* **357**, 3267–3271 (2011).

139. Kalita, D. J., Lee, S. H., Lee, K. S., Ko, D. H. & Yoon, Y. S. Ionic conductivity properties of amorphous Li–La–Zr–O solid electrolyte for thin film batteries. *Solid State Ionics* **229**, 14–19 (2012).

140. Garbayo, I. *et al.* Glass-Type Polyamorphism in Li-Garnet Thin Film Solid State Battery Conductors. *Adv. Energy Mater.* **8**, 1702265 (2018).

141. Reckeweg, O., Blaschkowski, B. & Schleid, T. Li 5 OCl 3 and Li 3 OCl: Two Remarkably Different Lithium Oxide Chlorides. *Zeitschrift für Anorg. und Allg. Chemie* **638**, 2081–2086 (2012).

142. Zhao, Y. & Daemen, L. L. Superionic Conductivity in Lithium-Rich Anti-Perovskites. *J. Am. Chem. Soc.* **134**, 15042–15047 (2012).

143. Dawson, J. A., Famprikis, T. & Johnston, K. E. Anti-perovskites for solid-state batteries: recent developments, current challenges and future prospects. *J. Mater. Chem. A* **9**, 18746–18772 (2021).

144. Lü, X. *et al.* Antiperovskite Li3OCl Superionic Conductor Films for Solid-State Li-Ion Batteries. *Adv. Sci.* **3**, 1500359 (2016).

145. Braga, M. H., Ferreira, J. A., Stockhausen, V., Oliveira, J. E. & El-Azab, A. Novel Li 3 ClO based glasses with superionic properties for lithium batteries. *J. Mater. Chem. A* **2**, 5470–5480 (2014).

146. Braga, M. H., Murchison, A. J., Ferreira, J. A., Singh, P. & Goodenough, J. B. Glass-amorphous alkali-ion solid electrolytes and their performance in symmetrical cells. *Energy Environ. Sci.* **9**, 948–954 (2016).

147. Braga, M. H., Grundish, N. S., Murchison, A. J. & Goodenough, J. B. Alternative strategy for a safe rechargeable battery. *Energy Environ. Sci.* **10**, 331–336 (2017).

148. Braga, M. H. *et al.* Extraordinary Dielectric Properties at Heterojunctions of Amorphous Ferroelectrics. *J. Am. Chem. Soc.* **140**, 17968–17976 (2018).

149. Braga, M. H., M Subramaniyam, C., Murchison, A. J. & Goodenough, J. B. Nontraditional, Safe, High Voltage Rechargeable Cells of Long Cycle Life. *J. Am. Chem. Soc.* **140**, 6343–6352 (2018).

150. Braga, M. H., Murchison, A. J., Oliveira, J. E. & Goodenough, J. B. Low-Temperature Performance of a Ferroelectric Glass Electrolyte Rechargeable Cell. *ACS Appl. Energy Mater.* **2**, 4943–4953 (2019).

151. Braga, M. H., Oliveira, J. E., Murchison, A. J. & Goodenough, J. B. Performance of a ferroelectric glass electrolyte in a self-charging electrochemical cell with negative capacitance and resistance. *Appl. Phys. Rev.* **7**, 011406 (2020).

152. Hanghofer, I. *et al.* Untangling the Structure and Dynamics of Lithium-Rich Anti-Perovskites Envisaged as Solid Electrolytes for Batteries. *Chem. Mater.* **30**, 8134–

8144 (2018).

153. Bacelli, G., Ringwood, J. V & Iordanov, P. Impedance matching controller for an inductively coupled plasma chamber - L-type matching network automatic controller. in *Proceedings of the Fourth International Conference on Informatics in Control, Automation and Robotics, Signal Processing, Systems Modeling and Control, Angers, France, May 9-12, 2007* 202–207 (2007).

154. Park, H. Y. *et al.* Effects of sputtering pressure on the characteristics of lithium ion conductive lithium phosphorous oxynitride thin film. *J. Electroceramics* **17**, 1023–1030 (2006).

155. Hu, Z., Xie, K., Wei, D. & Ullah, N. Influence of sputtering pressure on the structure and ionic conductivity of thin film amorphous electrolyte. *J. Mater. Sci.* **46**, 7588–7593 (2011).

156. Uzakbaiuly, B., Mukanova, A., Kurmanbayeva, I. & Bakenov, Z. B. Optimization of deposition parameters for thin film lithium phosphorus oxynitride (LIPON). *Eurasian J. Phys. Funct. Mater.* **3**, 174–182 (2019).

157. Ko, J. & Yoon, Y. S. Effect of post-annealing on structural and electrochemical properties of lithium phosphorus oxynitride thin film. *Ceram. Int.* **46**, 14071–14077 (2020).

158. Birkl, C. R., McTurk, E., Roberts, M. R., Bruce, P. G. & Howey, D. A. A Parametric Open Circuit Voltage Model for Lithium Ion Batteries. *J. Electrochem. Soc.* **162**, A2271–A2280 (2015).

159. Cullity, B. D. & Stock, S. R. *Elements of X-ray Diffraction*. (Pearson, 2014).

160. SEM Resolution. *Thermo Fisher Scientific* (2022). Available at: https://www.thermofisher.com/uk/en/home/materials-science/learning-center/applications/sem-resolution.html#:~:text=SEM resolution is typically between,to create a magnified image. (Accessed: 16th February 2023)

161. The Difference Between SEM and Optical Microscopes. *Thermo Fisher Scientific* (2022). Available at: https://www.thermofisher.com/uk/en/home/materials-science/learning-center/applications/sem-optical-microscopes-difference.html. (Accessed: 16th February 2023)

162. Theory of scanning electron microscopy and X-ray microanalysis. *Naturhistorisches Museum Wien* (2022). Available at: https://www.nhm-wien.ac.at/en/research/central_research_laboratories/analytical_electron_microscopy/theory. (Accessed: 16th February 2023)

163. https://www.unl.edu/ncmn-cfem/xzli/em/volume.htm. *UNIVERSITY of NEBRASKA–LINCOLN* Available at: https://www.unl.edu/ncmn-cfem/xzli/em/volume.htm. (Accessed: 16th February 2023)

164. Temiz, C. Scanning Electron Microscopy. in *Electron Microscopy* (ed. Mhadhbi, M.) (IntechOpen, 2022). doi:10.5772/intechopen.103956

165. Liao, Y. Interaction Volumes for Generation of Characteristic X-Rays. in *Practical Electron Microscopy and Database* (GlobalSino).

166. EDS Principle. *Yale University* (2023). Available at: https://ywcmatsci.yale.edu/edx-principle. (Accessed: 16th February 2023)

167. X-ray Photoelectron Spectroscopy Electron spectroscopy for chemical analysis. *Thermo Fisher Scientific Inc.* (2022). Available at: https://assets.thermofisher.com/TFS-Assets/MSD/Flyers/xps-quick-guide-fl0163.pdf. (Accessed: 30th May 2022)

168. X-RAY PHOTOELECTRON SPECTROSCOPY 'X-RAY PHOTOELECTRON SPECTROSCOPY (PHI XPS VERSAPROBE III). *The Henry Royce Institute* (2022). Available at: https://www.royce.ac.uk/equipment-and-facilities/x-ray-photoelectron-spectroscopy-al-k-alpha-1486-ev/. (Accessed: 30th May 2022)

169. XPS / ESCA. *Physical Electronics, Inc. (PHI)* (2022). Available at: https://www.phi.com/surface-analysis-techniques/xps-esca.html#:~:text=XPS %2F ESCA,-Home %2F Techniques %2F XPS&text=PHI XPS instruments provide the,beam across the sample surface. (Accessed: 30th May 2022)

170. Jenkins, S. N. The development and application of a transmission X-ray photoelectron spectrometer (TXPS). (University of Surrey, 1993).

171. Introduction into X-- ray and UV Photoelectron Spectroscopy (XPS/UPS). *Helmholtz-Zentrum Berlin für Materialien und Energie* Available at: https://mmrc.caltech.edu/XPS Info/Intro to XPS Helmholtz.pdf. (Accessed: 6th October 2022)

172. Raman and FTIR Spectroscopy. *Thermo Fisher Scientific Inc.* (2018). Available at: https://assets.thermofisher.com/TFS-Assets/CAD/Application-Notes/Raman-FTIR-TechNote-Final.pdf. (Accessed: 31st May 2022)

173. Explainer: The difference between IR, FTIR, and ATR-FTIR. *Specac Ltd* (2022). Available at: https://specac.com/explain-difference-between-ftir-ir-and-atr/. (Accessed: 20th February 2023)

174. Exline, D. Comparison of Raman and FTIR Spectroscopy: Advantages and

Limitations. *Gateway Analytical LLC* (2013). Available at: https://www.gatewayanalytical.com/resources/publications/comparison-raman-and-ftir-spectroscopy-advantages-and-limitations/. (Accessed: 31st May 2022)

175. What Is FTIR Spectroscopy? *Agilent Technologies, Inc.* (2022). Available at: https://www.agilent.com/en/support/molecular-spectroscopy/ftir-spectroscopy/ftir-spectroscopy-basics-faqs. (Accessed: 31st May 2022)

176. Bradley, M. FTIR Basics. *Thermo Fisher Scientific Inc.* Available at: https://www.thermofisher.com/uk/en/home/industrial/spectroscopy-elemental-isotope-analysis/spectroscopy-elemental-isotope-analysis-learning-center/molecular-spectroscopy-information/ftir-information/ftir-basics.html. (Accessed: 31st May 2022)

177. Ausili, A., Sánchez, M. & Gómez-Fernández, J. C. Attenuated total reflectance infrared spectroscopy: A powerful method for the simultaneous study of structure and spatial orientation of lipids and membrane proteins. *Biomed. Spectrosc. Imaging* **4**, 159–170 (2015).

178. Q: How deep does the infrared light penetrate at the position of contact between the prism and sample during ATR measurements? *Shimadzu Corporation* (2022). Available at: https://www.shimadzu.com/an/service-support/faq/ftir/2/index.html. (Accessed: 31st May 2022)

179. Krosse, S. & van der Ven, P. ICP-OES. *Radboud University* (2022). Available at: https://www.ru.nl/science/gi/facilities-activities/elemental-analysis/icp-oes/. (Accessed: 1st June 2022)

180. ICP-OES Frequently Asked Questions. *Agilent Technologies, Inc.* (2022). Available at: https://www.agilent.com/en/support/atomic-spectroscopy/inductively-coupled-plasma-optical-emission-spectroscopy-icp-oes/icp-oes-instruments/icp-oes-faq. (Accessed: 1st June 2022)

181. Basics of Electrochemical Impedance Spectroscopy. *Gamry Instruments* (2022). Available at: https://www.gamry.com/application-notes/EIS/basics-of-electrochemical-impedance-spectroscopy/. (Accessed: 6th June 2022)

182. Evans, D. H., O'Connell, K. M., Petersen, R. A. & Kelly, M. J. Cyclic voltammetry. *J. Chem. Educ.* **60**, 290 (1983).

183. Palagonia, M. S., Erinmwingbovo, C., Brogioli, D. & La Mantia, F. Comparison between cyclic voltammetry and differential charge plots from galvanostatic cycling. *J. Electroanal. Chem.* **847**, 113170 (2019).

184. Turrell, S. J., Zekoll, S., Liu, J., Grovenor, C. R. M. & Speller, S. C. Optimization of a

potential manufacturing process for thin-film LiCoO2 cathodes. *Thin Solid Films* **735**, 138888 (2021).

185. Wang, Q. H. *et al.* Potential threshold of anode materials for foldable lithium-ion batteries featuring carbon nanotube current collectors. *J. Power Sources* **310**, 70–78 (2016).

186. Wang, X. *et al.* Lithium-Aluminum-Phosphate coating enables stable 4.6 V cycling performance of LiCoO2 at room temperature and beyond. *Energy Storage Mater.* **37**, 67–76 (2021).

187. Qi, Z. & Koenig, G. M. High-Performance LiCoO 2 Sub-Micrometer Materials from Scalable Microparticle Template Processing. *ChemistrySelect* **1**, 3992–3999 (2016).

188. Liang, G., Peterson, V. K., See, K. W., Guo, Z. & Pang, W. K. Developing high-voltage spinel LiNi0.5Mn1.5O4cathodes for high-energy-density lithium-ion batteries: Current achievements and future prospects. *J. Mater. Chem. A* **8**, 15373–15398 (2020).

189. Thin Film Considerations for High-Volume Manufacturing. *Denton Vacuum* (2022). Available at: https://www.dentonvacuum.com/thin-film-considerations-for-high-volume-manufacturing/. (Accessed: 21st February 2023)

190. Douglass, D. Thin-film Coatings: Thin-film manufacturing considerations for semiconductor lasers. *Laser Focus World* (2018). Available at: https://www.laserfocusworld.com/lasers-sources/article/16555241/thinfilm-coatings-thinfilm-manufacturing-considerations-for-semiconductor-lasers. (Accessed: 21st February 2023)

191. Jimbo, T., Kim, P. & Suu, K. Production Technology for Thin-film Lithium Secondary Battery. *Energy Procedia* **14**, 1574–1579 (2012).

192. Liao, C.-L. & Fung, K.-Z. Lithium cobalt oxide cathode film prepared by rf sputtering. *J. Power Sources* **128**, 263–269 (2004).

193. Zhu, X., Guo, Z., Du, G., Zhang, P. & Liu, H. LiCoO2 cathode thin film fabricated by RF sputtering for lithium ion microbatteries. *Surf. Coat. Technol.* **204**, 1710–1714 (2010).

194. Chiu, K.-F., Hsu, F. C., Chen, G. S. & Wu, M. K. Texture and Microstructure Development of RF Sputter-Deposited Polycrystalline Lithium Transition Metal Oxide Thin Films. *J. Electrochem. Soc.* **150**, A503–A507 (2003).

195. Xie, J. *et al.* Li-ion transport in all-solid-state lithium batteries with LiCoO2 using NASICON-type glass ceramic electrolytes. *J. Power Sources* **189**, 365–370 (2009).

196. Jeon, S.-W., Lim, J.-K., Lim, S.-H. & Lee, S.-M. As-deposited LiCoO2 thin film cathodes prepared by rf magnetron sputtering. *Electrochim. Acta* **51**, 268–273 (2005).

197. Pan, H. & Yang, Y. Effects of radio-frequency sputtering powers on the microstructures and electrochemical properties of LiCoO2 thin film electrodes. *J. Power Sources* **189**, 633–637 (2009).

198. Fragnaud, P., Brousse, T. & Schleich, D. M. Characterization of sprayed and sputter deposited LiCoO2 thin films for rechargeable microbatteries. *J. Power Sources* **63**, 187–191 (1996).

199. Benqlilou-Moudden, H., Blondiaux, G., Vinatier, P. & Levasseur, A. Amorphous lithium cobalt and nickel oxides thin films: Preparation and characterization by RBS and PIGE. *Thin Solid Films* **333**, 16–19 (1998).

200. Whitacre, J. F., West, W. C. & Ratnakumar, B. V. The influence of target history and deposition geometry on RF magnetron sputtered LiCoO2 thin films. *J. Power Sources* **103**, 134–139 (2001).

201. Park, H. Y. *et al.* Influence of sputtering gas pressure on the LiCoO2 thin film cathode post-annealed at 400 °C. *Korean J. Chem. Eng.* **23**, 832–837 (2006).

202. Tintignac, S., Baddour-Hadjean, R., Pereira-Ramos, J. P. & Salot, R. High performance sputtered LiCoO2 thin films obtained at a moderate annealing treatment combined to a bias effect. *Electrochim. Acta* **60**, 121–129 (2012).

203. Jan, D.-J., Lee, C.-C., Yu, Y.-J. & Chiang, H.-W. Evaluation of lithium cobalt oxide films deposited by radio frequency magnetron sputtering as thin-film battery cathodes. *Jpn. J. Appl. Phys.* **58**, 085501 (2019).

204. Wang, C. *et al.* LiCoO2 thin film cathode sputtered onto 500 °C substrate. *Electrochim. Acta* **354**, 136668 (2020).

205. Filippin, A. N. *et al.* Ni-Al-Cr superalloy as high temperature cathode current collector for advanced thin film Li batteries. *RSC Adv.* **8**, 20304–20313 (2018).

206. Park, H. Y., Lee, S. R., Lee, Y. J., Cho, B. W. & Cho, W. I. Bias sputtering and characterization of LiCoO2 thin film cathodes for thin film microbattery. *Mater. Chem. Phys.* **93**, 70–78 (2005).

207. Kumar, P. J. *et al.* HT-LiCoO2 Thin Film Positive Electrodes Prepared by RF Magnetron Sputtering. *AIP Conf. Proc.* **1349**, 381–382 (2011).

208. Ziebert, C. *et al.* Constitution, microstructure, and battery performance of magnetron sputtered Li-Co-O thin film cathodes for lithium-ion batteries as a function of the

working gas pressure. *Surf. Coatings Technol.* **205**, 1589–1594 (2010).

209. Wei, G., Haas, T. E. & Goldner, R. B. Thin films of lithium cobalt oxide. *Solid State Ionics* **58**, 115–122 (1992).

210. Bouwman, P. J., Boukamp, B. A., Bouwmeester, H. J. M., Wondergem, H. J. & Notten, P. H. L. Structural Analysis of Submicrometer LiCoO2 Films. *J. Electrochem. Soc.* **148**, A311 (2001).

211. Bohne, L., Pirk, T. & Jaegermann, W. Investigations on the influence of the substrate on the crystal structure of sputtered LiCoO2. *J. Solid State Electrochem.* **17**, 2095–2099 (2013).

212. Bates, J. B. *et al.* Preferred orientation of polycrystalline LiCoO2 films. *J. Electrochem. Soc.* **147**, 59–70 (2000).

213. Xie, J. *et al.* Orientation dependence of Li-ion diffusion kinetics in LiCoO2 thin films prepared by RF magnetron sputtering. *Solid State Ionics* **179**, 362–370 (2008).

214. Bohne, L., Pirk, T. & Jaegermann, W. Crystal Structure of Sputtered LiCoO 2 for Thin Film Lithium Ion Batteries. *ECS Trans.* **32**, 17–21 (2011).

215. Tintignac, S., Baddour-Hadjean, R., Pereira-Ramos, J. P. & Salot, R. Electrochemical properties of high rate bias sputtered LiCoO2 thin films in liquid electrolyte. *J. Power Sources* **245**, 76–82 (2014).

216. Trask, J. *et al.* Optimization of 10-μm, sputtered, LiCoO2 cathodes to enable higher energy density solid state batteries. *J. Power Sources* **350**, 56–64 (2017).

217. Wu, T. *et al.* Improved solid interfacial kinetics and electrochemical performance for LiCoO2(1 1 0) textured thin-film lithium batteries. *Appl. Surf. Sci.* **591**, 153174 (2022).

218. Bouwman, P. J., Boukamp, B. A., Bouwmeester, H. J. M. & Notten, P. H. L. Influence of diffusion plane orientation on electrochemical properties of thin film LiCoO2 electrodes. *J. Electrochem. Soc.* **149**, 699–709 (2002).

219. Dudney, N. J. & Jang, Y. Il. Analysis of thin-film lithium batteries with cathodes of 50 nm to 4 μm thick LiCoO2. *J. Power Sources* **119**–**121**, 300–304 (2003).

220. Song, S. W. *et al.* High rate-induced structural changes in thin-film lithium batteries on flexible substrate. *J. Power Sources* **195**, 8275–8279 (2010).

221. Rao Kosuri, Y., Rao Penki, T., Nookala, M., Morgen, P. & Rao Gowravaram, M. Investigations On Sputter Deposited LiCoO2 Thin Films From Powder Target. *Adv. Mater. Lett.* **4**, 615–620 (2013).

222. Tintignac, S., Baddour-Hadjean, R., Pereira-Ramos, J. P. & Salot, R. High rate bias sputtered LiCoO 2 thinfilms as positive electrode for all-solid-state lithium microbatteries. *Electrochim. Acta* **146**, 472–476 (2014).

223. Navone, C., Tintignac, S., Pereira-Ramos, J. P., Baddour-Hadjean, R. & Salot, R. Electrochemical behaviour of sputtered c-V2O5 and LiCoO2 thin films for solid state lithium microbatteries. *Solid State Ionics* **192**, 343–346 (2011).

224. Kim, H. S. *et al.* Characterization of Sputter-Deposited LiCoO2 Thin Film Grown on NASICON-type Electrolyte for Application in All-Solid-State Rechargeable Lithium Battery. *ACS Appl. Mater. Interfaces* **9**, 16063–16070 (2017).

225. Xiao, D.-L. *et al.* Improved performance of all-solid-state lithium batteries using LiPON electrolyte prepared with Li-rich sputtering target. *Solid State Ionics* **324**, 202–206 (2018).

226. Yoon, Y. S., Lee, S. H., Cho, S. B. & Nam, S. C. Influence of Two-Step Heat Treatment on Sputtered Lithium Cobalt Oxide Thin Films. *J. Electrochem. Soc.* **158**, A1313 (2011).

227. Xie, J. *et al.* Amorphous LiCoO2 thin films on Li1+x+yAl xTi2-xSiyP3-yO12 prepared by radio frequency magnetron sputtering for all-solid-state Li-ion batteries. *Electrochim. Acta* **55**, 5440–5445 (2010).

228. Polo da Fonseca, C. N., Davalos, J., Kleinke, M., Fantini, M. C. A. & Gorenstein, A. Studies of LiCoOx thin film cathodes produced by r.f. sputtering. *J. Power Sources* **81**–**82**, 575–580 (1999).

229. Theivaprakasam, S. *et al.* Passivation behaviour of aluminium current collector in ionic liquid alkyl carbonate (hybrid) electrolytes. *npj Mater. Degrad.* **2**, 13 (2018).

230. Melting point of aluminium. *thyssenkrupp Materials (UK) Ltd* (2022). Available at: https://www.thyssenkrupp-materials.co.uk/melting-point-of-aluminium. (Accessed: 21st February 2023)

231. Jeevan-Kumar, P., Jayanth-Babu, K., Hussain, O. M. & Julien, C. M. RF-sputtered LiCoO2 thick films: microstructure and electrochemical performance as cathodes in aqueous and nonaqueous microbatteries. *Ionics (Kiel).* **19**, 421–428 (2013).

232. Xie, J. *et al.* Kinetics investigation of a preferential (104) plane oriented LiCoO2 thin film prepared by RF magnetron sputtering. *Solid State Ionics* **178**, 1218–1224 (2007).

233. Smith, W. L. & Hobson, A. D. The structure of cobalt oxide, Co3O4. *Acta Crystallogr. Sect. B Struct. Crystallogr. Cryst. Chem.* **29**, 362–363 (1973).

234. Antaya, M., Cearns, K., Preston, J. S., Reimers, J. N. & Dahn, J. R. In situ growth of layered, spinel, and rock-salt LiCoO2 by laser ablation deposition. *J. Appl. Phys.* **76**, 2799–2806 (1994).

235. Douakha, N. *et al.* Nuclear and Magnetic Structure of Layered LiFe1−xCoxO2 (0≤x≤1) Determined by High-Resolution Neutron Diffraction. *J. Solid State Chem.* **163**, 406–411 (2002).

236. Gummow, R. ., Liles, D. & Thackeray, M. Spinel versus layered structures for lithium cobalt oxide synthesised at 400°C. *Mater. Res. Bull.* **28**, 235–246 (1993).

237. Jang, Y. Il, Dudney, N. J., Blom, D. A. & Allard, L. F. Electrochemical and electron microscopic characterization of thin-film LiCoO2 cathodes under high-voltage cycling conditions. *J. Power Sources* **119**–**121**, 295–299 (2003).

238. Julien, Mauger & Hussain. Sputtered LiCoO2 Cathode Materials for All-solid-state Thin-film Lithium Microbatteries. *Materials (Basel).* **12**, 2687 (2019).

239. Hayashi, M., Takahashi, M. & Shodai, T. Preparation and electrochemical properties of pure lithium cobalt oxide films by electron cyclotron resonance sputtering. *J. Power Sources* **189**, 416–422 (2009).

240. Akimoto, J., Gotoh, Y. & Oosawa, Y. Synthesis and Structure Refinement of LiCoO2Single Crystals. *J. Solid State Chem.* **141**, 298–302 (1998).

241. Liao, C.-L., Lee, Y.-H. & Fung, K.-Z. The film growth and electrochemical properties of rf-sputtered LiCoO2 thin films. *J. Alloys Compd.* **436**, 303–308 (2007).

242. Kim, H.-K. & Yoon, Y. S. Characteristics of rapid-thermal-annealed LiCoO2 cathode film for an all-solid-state thin film microbattery. *J. Vac. Sci. Technol. A Vacuum, Surfaces, Film.* **22**, 1182–1187 (2004).

243. HAYNES® Waspaloy alloy. *HAYNES® Waspaloy alloy* (2017). Available at: http://haynesintl.com/docs/default-source/pdfs/new-alloy-brochures/high-temperature-alloys/brochures/waspaloy.pdf?sfvrsn=e77229d4_24. (Accessed: 4th June 2020)

244. Chen, J. H., Rogers, P. M. & Little, J. A. Oxidation behavior of several chromia-forming commercial nickel-base superalloys. *Oxid. Met.* **47**, 381–410 (1997).

245. Dantzig, J. A. *Equilibrium Shapes for Crystalline Solids*. (2018).

246. Kramer, D. & Ceder, G. Tailoring the Morphology of LiCoO 2 : A First Principles Study. *Chem. Mater.* **21**, 3799–3809 (2009).

247. Hart, F. X. & Bates, J. B. Lattice model calculation of the strain energy density and other properties of crystalline LiCoO2. *J. Appl. Phys.* **83**, 7560–7566 (1998).

248. JEOL USA, I. Trusting Quantitative EDS Data. *AZoM* (2020). Available at: https://www.azom.com/article.aspx?ArticleID=19692. (Accessed: 19th February 2023)

249. Hafner, B. *Energy Dispersive Spectroscopy on the SEM: A Primer*. (2013).

250. Winchester, M. R., Butler, T. A. & Turk, G. C. Improving the High-Performance Inductively Coupled Plasma Optical Emission Spectrometry Methodology through Exact Matching. *Anal. Chem.* **82**, 7675–7683 (2010).

251. Reimers, J. N. & Dahn, J. R. Electrochemical and In Situ X-Ray Diffraction Studies of Lithium Intercalation in Li x CoO2. *J. Electrochem. Soc.* **139**, 2091–2097 (1992).

252. Ménétrier, M., Saadoune, I., Levasseur, S. & Delmas, C. The insulator-metal transition upon lithium deintercalation from LiCoO2: electronic properties and 7Li NMR study. *J. Mater. Chem.* **9**, 1135–1140 (1999).

253. Amatucci, G. G., Tarascon, J. M. & Klein, L. C. Cobalt dissolution in LiCoO2-based non-aqueous rechargeable batteries. *Solid State Ionics* **83**, 167–173 (1996).

254. Takahashi, Y. *et al.* Development of Lithium-Ion Batteries with a LiCoO[sub 2] Cathode Toward High Capacity by Elevating Charging Potential. *J. Electrochem. Soc.* **155**, A537 (2008).

255. Cao, H., Xia, B., Zhang, Y. & Xu, N. LiAlO-coated LiCoO as cathode material for lithium ion batteries. *Solid State Ionics* **176**, 911–914 (2005).

256. Tan, J. *et al.* Electrochemically Driven Phase Transition in LiCoO2 Cathode. *Materials (Basel).* **14**, 242 (2021).

257. Shu, J. *et al.* A New Look at Lithium Cobalt Oxide in a Broad Voltage Range for Lithium-Ion Batteries. *J. Phys. Chem. C* **114**, 3323–3328 (2010).

258. Turrell, S. J. *et al.* Fabrication of thin solid electrolytes containing a small volume of an Li 3 OCl-type antiperovskite phase by RF magnetron sputtering. *Mater. Adv.* (2022). doi:10.1039/D2MA00971D

259. Koedtruad, A., Patino, M. A., Ichikawa, N., Kan, D. & Shimakawa, Y. Crystal structures and ionic conductivity in Li2OHX (X = Cl, Br) antiperovskites. *J. Solid State Chem.* **286**, 121263 (2020).

260. Xiao, Y. *et al.* Understanding interface stability in solid-state batteries. *Nature Reviews Materials* **5**, 105–126 (2020).

261. Hood, Z. D., Wang, H., Samuthira Pandian, A., Keum, J. K. & Liang, C. Li2OHCl Crystalline Electrolyte for Stable Metallic Lithium Anodes. *J. Am. Chem. Soc.* **138**, 1768–1771 (2016).

262. Song, A. Y. *et al.* Protons Enhance Conductivities in Lithium Halide Hydroxide/Lithium Oxyhalide Solid Electrolytes by Forming Rotating Hydroxy Groups. *Adv. Energy Mater.* **8**, 1–11 (2018).

263. Persson, K. *Materials Data on Li3ClO (SG:221) by Materials Project*. (2016). doi:10.17188/1282131

264. Jain, A. *et al.* Commentary: The Materials Project: A materials genome approach to accelerating materials innovation. *APL Mater.* **1**, 011002 (2013).

265. Yamamoto, T. *et al.* Synthesis of the Metastable Cubic Phase of Li2OHCl by a Mechanochemical Method. *Inorg. Chem.* **59**, 11901–11904 (2020).

266. Zhang, Y., Zhao, Y. & Chen, C. Ab initio study of the stabilities of and mechanism of superionic transport in lithium-rich antiperovskites. *Phys. Rev. B - Condens. Matter Mater. Phys.* **87**, 1–8 (2013).

267. Emly, A., Kioupakis, E. & Van Der Ven, A. Phase stability and transport mechanisms in antiperovskite Li 3OCl and Li3OBr superionic conductors. *Chem. Mater.* **25**, 4663–4670 (2013).

268. Mouta, R., Melo, M. Á. B., Diniz, E. M. & Paschoal, C. W. A. Concentration of Charge Carriers, Migration, and Stability in Li 3 OCl Solid Electrolytes. *Chem. Mater.* **26**, 7137–7144 (2014).

269. Kim, K. *et al.* Exploring the Synthesis of Alkali Metal Anti-perovskites. *Chem. Mater.* **34**, 947–958 (2022).

270. Chen, M. H., Emly, A. & Van Der Ven, A. Anharmonicity and phase stability of antiperovskite Li3 OCl. *Phys. Rev. B - Condens. Matter Mater. Phys.* **91**, 1–8 (2015).

271. Wu, M., Xu, B., Lei, X., Huang, K. & Ouyang, C. Bulk properties and transport mechanisms of a solid state antiperovskite Li-ion conductor Li3OCl: Insights from first principles calculations. *J. Mater. Chem. A* **6**, 1150–1160 (2018).

272. Dawson, J. A. *et al.* Elucidating lithium-ion and proton dynamics in anti-perovskite solid electrolytes. *Energy Environ. Sci.* **11**, 2993–3002 (2018).

273. Serejo, J. A. S., Pereira, J. S., Mouta, R. & Rego, L. G. C. Sluggish anion transport provides good kinetic stability to the anhydrous anti-perovskite solid electrolyte Li3OCl. *Phys. Chem. Chem. Phys.* **23**, 6964–6973 (2021).

274. Dondelinger, M. *et al.* Electrochemical stability of lithium halide electrolyte with antiperovskite crystal structure. *Electrochim. Acta* **306**, 498–505 (2019).

275. Li, S. *et al.* Reaction mechanism studies towards effective fabrication of lithium-rich

anti-perovskites Li3OX (X = Cl, Br). *Solid State Ionics* **284**, 14–19 (2016).

276. Han, B. *et al.* Self-Regulated Phenomenon of Inorganic Artificial Solid Electrolyte Interphase for Lithium Metal Batteries. *Nano Lett.* **20**, 4029–4037 (2020).

277. Yang, Y., Han, J., DeVita, M., Lee, S. S. & Kim, J. C. Lithium and Chlorine-Rich Preparation of Mechanochemically Activated Antiperovskite Composites for Solid-State Batteries. *Front. Chem.* **8**, 3–9 (2020).

278. Dr Jari Liimatainen *et al.* Ultra Short Pulsed Laser Deposition Technology for Industrial Applications. *J. Mater. Sci. Eng. B* **5**, (2015).

279. Benetti, D. *et al.* Combined magnetron sputtering and pulsed laser deposition of TiO2 and BFCO thin films. *Sci. Rep.* **7**, 2–10 (2017).

280. Faraji, G., Kim, H. S. & Kashi, H. T. Severe Plastic Deformation Methods, Processing and Properties. in *Severe Plastic Deformation* 1–17 (Elsevier, 2018). doi:10.1016/b978-0-12-813518-1.00020-5

281. Howard, J., Hood, Z. D. & Holzwarth, N. A. W. Fundamental aspects of the structural and electrolyte properties of Li2OHCl from simulations and experiment. *Phys. Rev. Mater.* **1**, 1–13 (2017).

282. Song, A. Y. *et al.* Understanding Li-Ion Dynamics in Lithium Hydroxychloride (Li2OHCl) Solid State Electrolyte via Addressing the Role of Protons. *Adv. Energy Mater.* **10**, (2020).

283. Wang, F. *et al.* Dynamics of Hydroxyl Anions Promotes Lithium Ion Conduction in Antiperovskite Li2OHCl. *Chem. Mater.* **32**, 8481–8491 (2020).

284. Deng, Z. *et al.* Local structural changes and inductive effects on ion conduction in antiperovskite solid electrolytes. *Chem. Mater.* **32**, 8827–8835 (2020).

285. Lee, Y.-S., Jung, S.-Y. & Ryu, K.-S. Electrochemical Stability and Performance of Li2OHCl Substituted by F or Br as Solid-State Electrolyte. *J. Electrochem. Energy Convers. Storage* **18**, 1–12 (2021).

286. Liu, B. *et al.* Computational insights into the ionic transport mechanism and interfacial stability of the Li2OHCl solid-state electrolyte. *J. Mater.* (2021). doi:10.1016/j.jmat.2021.05.006

287. Watanabe, A. *et al.* Ambient Pressure Synthesis and H- Conductivity of LaSrLiH2O2. *Electrochemistry* **85**, 88–92 (2017).

288. Finch, G. I. & Fordham, S. The effect of crystal-size on lattice-dimensions. *Proc. Phys. Soc.* **48**, 85–94 (1936).

289. Powell, R. A. & Rossnagel, S. M. *PVD for microelectronics : sputter deposition applied to semiconductor manufacturing*. (Academic Press, 1999).

290. Hamon, Y. *et al.* Influence of sputtering conditions on ionic conductivity of LiPON thin films. *Solid State Ionics* **177**, 257–261 (2006).

291. Gao, Y. *et al.* Amorphous Dual-Layer Coating: Enabling High Li-Ion Conductivity of Non-Sintered Garnet-Type Solid Electrolyte. *Adv. Funct. Mater.* **31**, 1–10 (2021).

292. Su, Y. *et al.* LiPON thin films with high nitrogen content for application in lithium batteries and electrochromic devices prepared by RF magnetron sputtering. *Solid State Ionics* **282**, 63–69 (2015).

293. Boeuf, A. *et al.* Effects of M23C6 precipitation on the lattice parameter of AISI 304 stainless steel. *Mater. Lett.* **3**, 115–118 (1985).

294. Allen, J. D. T. Effect of chemistry and temperature on planar defects in superalloys. (UNIVERSITY OF BIRMINGHAM, 2019).

295. Morinaga, M. Local Lattice Strains Around Alloying Elements in Metals. in *A Quantum Approach to Alloy Design* 221–260 (Elsevier, 2019). doi:10.1016/B978-0-12-814706-1.00011-X

296. Table of X-ray Emission Lines. *Horiba Jobin Yvon* Available at: https://www.horiba.com/fileadmin/uploads/Scientific/Documents/XRay/emission_lines.pdf. (Accessed: 6th October 2022)

297. Introduction to Energy Dispersive X-ray Spectrometry (EDS). *University of California, Riverside* Available at: https://cfamm.ucr.edu/media/126/download?attachment. (Accessed: 6th October 2022)

298. Yan, C. *et al.* 4.5 V High-Voltage Rechargeable Batteries Enabled by the Reduction of Polarization on the Lithium Metal Anode. *Angew. Chemie* **131**, 15379–15382 (2019).

299. Eilbracht, C., Kockelmann, W., Hohlwein, D. & Jacobs, H. Orientational disorder in perovskite like structures of Li2X(OD) (X = Cl, Br) and LiBr·D2O. *Phys. B Condens. Matter* **234**–**236**, 48–50 (1997).

300. Schwering, G., Hönnerscheid, A., Van Wüllen, L. & Jansen, M. High lithium ionic conductivity in the lithium halide hydrates Li3-n(OHn)Cl (0.83 ≤ n ≤ 2) and Li3-n(OHn)Br (1 ≤ n ≤ 2) at ambient temperatures. *ChemPhysChem* **4**, 343–348 (2003).

301. Zhang, C. C., Gao, X. & Yilmaz, B. Development of FTIR Spectroscopy Methodology for Characterization of Boron Species in FCC Catalysts. *Catalysts* **10**, 1327 (2020).

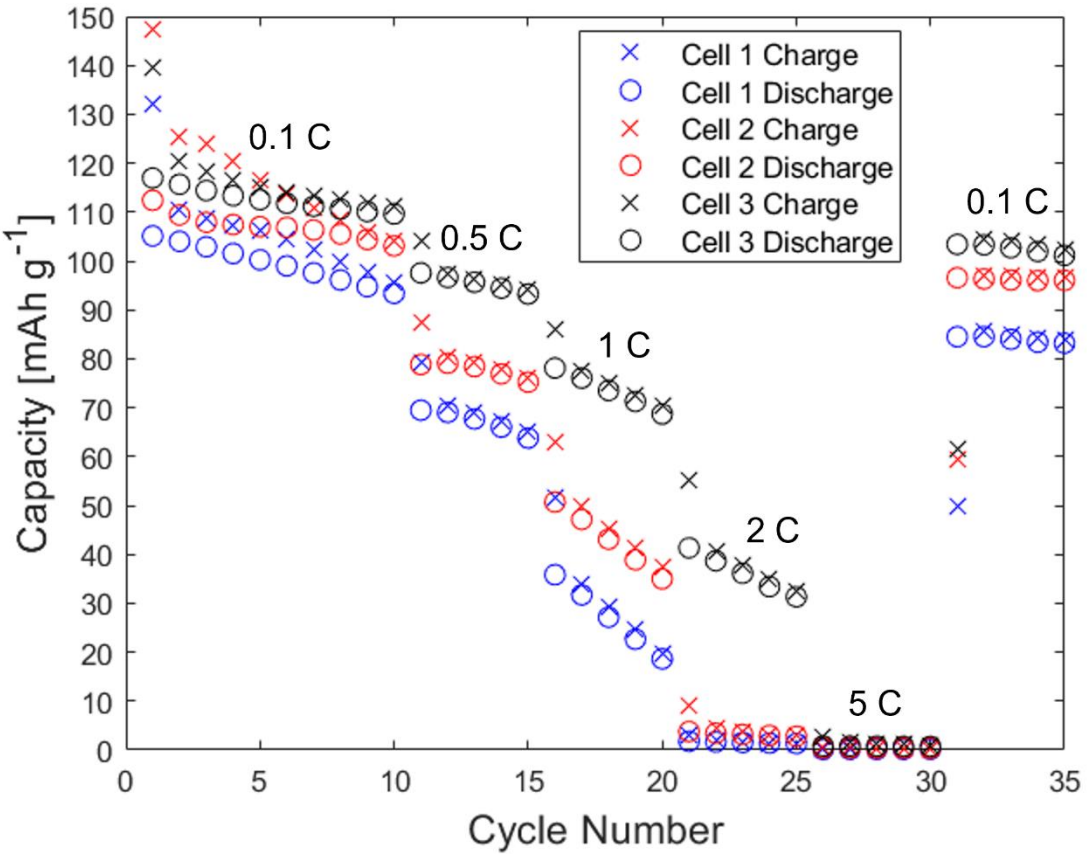
302. Dal Sasso, G., Asscher, Y., Angelini, I., Nodari, L. & Artioli, G. A universal curve of

apatite crystallinity for the assessment of bone integrity and preservation. *Sci. Rep.* **8**, 1–13 (2018).

Appendices

Appendix A: Variability of cycling performance between cells

The plot below shows the charge and discharge capacities over cycling of three cells tested in the experiment reported in Section 3.3.3.4. Cell 3 showed the best overall performance, and results from cycling this cell are shown in Figure 3.19. The masses of the LCO cathode films (prior to annealing) used in Cell 1 and Cell 2 were (1.3±0.1) mg and (1.1±0.1) mg, respectively. Although the same method of preparation was used for the 3 cells, the differences in as-deposited cathode mass could have been due to differences in the positioning of the substrates relative to the sputtering target and the degree of film exfoliation prior to weighing.



Appendix B: Equivalent Circuit Model Properties

The values of the equivalent circuit component properties used to fit the Nyquist plots shown in Figure 4.21 are listed in the tables below for each measurement temperature, T. Since the units of T depend on the value of P (which is dimensionless), for clarity the units are not stated in the tables below, but given that the unit of Z_{CPE} is the ohm (Ω), the units of T can be calculated using Equation 2.8 for Z_{CPE}. The values stated for the resistors are simply resistances, in Ω.

Film deposited from Li_2O + LiCl target

T / °C	R_i	R_e	R	R_{series}	CPE_{geom}		CPE_{int}		CPE	
					T	P	T	P	T	P
25	6.500×10^{4}	1.030×10^{5}	n/a	n/a	4.502×10^{-8}	0.65	1.5004×10^{-6}	0.600	n/a	
27	5.100×10^{4}	8.840×10^{4}	n/a	n/a	4.002×10^{-8}	0.66	1.4004×10^{-6}	0.610	n/a	
29	3.800×10^{4}	1.025×10^{5}	n/a	n/a	4.002×10^{-8}	0.67	1.6004×10^{-6}	0.600	n/a	
30	3.400×10^{4}	1.225×10^{5}	n/a	n/a	4.002×10^{-8}	0.67	1.7004×10^{-6}	0.607	n/a	
40	1.260×10^{4}	1.280×10^{5}	n/a	n/a	4.002×10^{-8}	0.70	3.2004×10^{-6}	0.600	n/a	
50	5.100×10^{3}	1.570×10^{5}	n/a	n/a	5.002×10^{-8}	0.66	4.5004×10^{-6}	0.590	n/a	
60	2.230×10^{3}	1.500×10^{6}	n/a	n/a	3.002×10^{-8}	0.68	3.0004×10^{-6}	0.630	n/a	
70	1.520×10^{3}	n/a	1.4×10^{4}	n/a	2.002×10^{-8}	0.69	2.3004×10^{-6}	0.770	2.1×10^{-6}	0.69
80	1.195×10^{3}	n/a	9.0×10^{3}	20	9.000×10^{-9}	0.78	1.1004×10^{-5}	0.800	9.1×10^{-6}	0.57
90	1.290×10^{3}	n/a	5.4×10^{3}	25	4.500×10^{-9}	0.80	1.1004×10^{-5}	0.813	9.1×10^{-6}	0.57

Film deposited from Li_2OHCl target

T / °C	R_i	R_e	R	CPE_{geom}		CPE_{int}		CPE	
				T	P	T	P	T	P
25	1.19×10^{5}	1.855×10^{4}	9.0×10^{4}	1.368×10^{-8}	0.900	2.9681×10^{-6}	0.600	5×10^{-8}	0.87
27	9.00×10^{4}	1.870×10^{4}	6.9×10^{4}	1.368×10^{-8}	0.893	2.9681×10^{-6}	0.630	5×10^{-8}	0.80
29	8.00×10^{4}	1.874×10^{4}	5.1×10^{4}	1.368×10^{-8}	0.890	2.9681×10^{-6}	0.600	5×10^{-8}	0.85
30	6.80×10^{4}	1.885×10^{4}	4.5×10^{4}	1.368×10^{-8}	0.890	2.9681×10^{-6}	0.600	5×10^{-8}	0.85
40	3.20×10^{4}	1.885×10^{4}	1.1×10^{4}	1.368×10^{-8}	0.850	2.9681×10^{-6}	0.700	5×10^{-8}	0.93
50	1.27×10^{4}	1.910×10^{4}	2.8×10^{3}	1.368×10^{-8}	0.841	2.5681×10^{-6}	0.700	5×10^{-8}	0.95
60	5.60×10^{3}	1.945×10^{4}	3.5×10^{2}	1.368×10^{-8}	0.790	1.0681×10^{-6}	0.770	5×10^{-8}	0.97
70	1.40×10^{3}	n/a	55	1.368×10^{-8}	0.810	6.0681×10^{-6}	0.670	5×10^{-8}	0.98
80	4.01×10^{2}	n/a	11	1.368×10^{-8}	0.850	1.7081×10^{-5}	0.665	5×10^{-8}	0.98
90	2.58×10^{2}	n/a	6	1.368×10^{-8}	0.850	2.2081×10^{-5}	0.665	5×10^{-8}	0.98
100	1.66×10^{2}	n/a	3	1.368×10^{-8}	0.850	2.7081×10^{-5}	0.665	5×10^{-8}	0.98

Appendix C: Electrical Contact Area Measurements

The areas of overlap between the top and bottom electrical contacts of the samples used for through-plane impedance measurements in Section 4.3.4 are shown in the table below. Full precision is provided, since these values were used in the calculations of ionic conductivity.

Sample	Electrical contact overlap area / cm^2	Method of area measurement
Film deposited from Li_2O + LiCl target (Ni contacts, small circle design)	0.016218229	PFIB used for SEM imaging of top contact in surface view. Circular measurement tool used to measure diameter of top contact, allowing calculation of its area (which is equal to the overlap area). Imaging and measurement performed by Marco Siniscalchi.
Film deposited from Li_2OHCl target (Pt contacts, overlapping strip design)	0.0183	SEM used to image contacts in surface view. Widths of top and bottom contacts measured as close to the region of overlap as possible and multiplied together to obtain the overlap area.